UNIVERSITÀ degli STUDI di CATANIA

Dipartimento di Scienze
Biologiche, Geologiche e Ambientali

PhD Course in "Earth and Environmental Science"

Dottorato di Ricerca in "Scienze della Terra e dell'Ambiente"

XXXIII Cycle

WHAT COULD BE DONE TO BETTER MONITOR AND UNDERSTAND THE EVOLUTION OF ETNA FAULTS?

MONITORING AND ANALYSIS OF SURFACE DEFORMATION USING COMPARATIVE GEODETIC AND TOPOGRAPHIC TECHNIQUES. CASE STUDY OF THE EASTERN SLOPE OF THE ETNA VOLCANO

Francesco Carnemolla

Advisor:
Prof. Giorgio De Guidi

Co-advisor:
Prof. Pierre Briole

Coordinator:
Prof. Agata Di Stefano

Ph. D. attended during 2019/2020

Index

ABSTRACT

The volcano - tectonic domains represent complex systems within the framework of geodynamic models studied by the international scientific community. We define these systems as complex because they represent the interaction between regional tectonic processes related to the geodynamics of the area and the volcanic processes generated by the dynamics of the volcano complex system. In these domains it is in fact necessary to define: i) the tectonic domain, ii) the current dynamics (tectonic-regional and volcanic process induced, iii) the main structural features of tectonic origin, iv) the main structural elements of volcanic origin and v) determine a model of relationship between regional and volcanic tectonic processes.

In the active geological processes, the kinematic and mechanical behaviour of the geological body affected by deformation is extremely variable and depends on various factors that interfere in the process (geometric and physical variability of the geomechanical parameters, thermal disturbances, internal structure, water content, etc.) but in particular the deformation follows a process that has geodynamics as its origin, which is the source of the forces that translate into a regional and local stress.

The role of the scientific community is to analyse this process in both directions: from the deformation to the source and vice versa, in order to be able to understand through criteria and mechanical physics law, how and when the complex system develops. The multidisciplinary approach is obviously the one that can best fulfil this system. The main goal is to obtain the knowledge of the mode and the velocity of deformation of the geological body affected by active geological processes. Therefore it is essential to identify the crucial points where to observe these dynamics in order to distinguish the main deformation systems from the associated ones and to evaluate the hierarchy of structures.

Since 2014, the research group of the GEODynamics & GEOMatic Laboratory of the University of Catania, as part of a multidisciplinary project oriented to the study of active geological structures, has identified natural open-air laboratories where deformation phenomena could be recorded, analysed and modelled at different space-time scales. Nowadays, these laboratories have been identified in the areas of the mud volcanoes present in Sicily, along the coseismic shear zones of the Umbro-Marchigiano Apennines, in the interseismic extensional domain of southern Calabria and along the active shear zones of the eastern flank of the Etna volcanic complex.

In particular, the orientation of the research group is to respond to the main criteria and models of deformations of geological body with elastic and plastic behaviour, concentrating in

particular on the terminal areas of the discontinuities where most of the concentration of the stresses occurs and trying to detect the deformation by discriminating the main structures from those associated with them.

The first structure of the Etna volcanic laboratory that the research group identified to start the experimentation is the shear system of San Gregorio - Acitrezza, which for its peculiar characteristics and development represents the ideal prototype for the study in progress. This structure, in fact, develops along the southern edge of the portion of the eastern slope of Etna considered unstable, and is made up of right lateral kinematic shear segments with associated extensional structures and aseismic creep deformation mode, which affect the inhabited centres of San Gregorio and Acitrezza. After a detailed morphostructural, geological-structural survey accompanied by geophysical investigations, the GEOD & GEOM Lab research group designed the first network of the "Etna Laboratory" for discrete geodetic-topographical monitoring of deformation along the active shear zones present on the volcano.

Geodetic-topographic benchmarks have been installed to record their precise coordinates, between the shear zone of San Gregorio – Acitrezza Fault, through campaigns measurement. After that, this network has been extended to almost all the shear structures on the eastern flank of the volcano, called UNICT-Net.

From several decades, one of the most sophisticated and multi-specialist monitoring systems in the world has already created on the Etna volcanic complex by the INGV-OE (National Institute of Geophysics and Volcanology - Etna Observatory). The idea of the GEOD & GEOM laboratory is therefore to concentrate the monitoring and analysis of deformation on the behaviour of the shear zones by integrating and without overlapping the existing monitoring network. Currently the permanent and discrete geodetic network ideated, installed and managed by the INGV allows to store, analyse and model the information of the ongoing deformation processes, making it possible to discriminate the distinct volcano tectonic phases that occur during eruptive cycles, seismic crises and everything that can be classified as an "active geological process".

Since 2019, the GEODynamics & GEOMatic Laboratory of the University of Catania started to collaborate with the Laboratoire de Géologie de École Normale Supérieure in Paris and with the INGV-OE of Catania in order to improve the research methods and share data related to campaign and permanent GNSS registrations, which integrated with those of the GEODynamics & GEOMatic Laboratory of the University of Catania will serve to structure a more complete database for the research object.

In this Ph.D. thesis, the time series developed by GNSS registrations on the benchmarks of the UNICT-Net network (2014 - 2020) and on the benchmarks of the ETNA@NET network managed by the INGV-OE will be analysed together with the time series of Permanent Scatters (PS) obtained through P-SBAS (2016 - 2019) tool. The deformation of the south-eastern sector of the unstable flank of Etna will be analysed in order to obtain with maximum resolution the deformation scenario acting in the area with particular attention to the faults already known in literature, including Belpasso-Ognina Lineament, Tremestieri-San Gregorio-Acitrezza Fault, Trecastagni Fault and Fiandaca-Nizzeti Fault.

All this in order to discriminate the behaviour of each fault in relation to the deformation that involves them based to the elastic or plastic response of the layer involved. Another aspect is to analyse for each fault the offset that it generates through PS time series in order to outline the stress state to which the structure was subjected during the period analysed.

The final objective of the thesis is to provide useful information to improve the monitoring of the above mentioned structures through the creation of new permanent GNSS stations in the most useful sites in order to improve the current state of knowledge on some structures on the unstable side of Mount Etna, as well as on their kinematic, rheological behaviour in relation to the substrate of Mount Etna.

DISSERTATION STRUCTURE

This dissertation is composed by five chapters.

The first chapter contains a detailed introduction to the eastern Sicily tectonic and volcanic system relationships. The first part of this chapter is dedicated to the description of the tectonics domain in eastern Sicily that influenced the volcanic activity at Mount Etna. The second part is dedicated to the description volcano tectonic framework of Mount Etna, in particular the faults of the south eastern flank were described considering their morphological signature and displacement carried out by geological survey, GNSS data and InSAR data from bibliographic research.

In the second chapter, collection and processing of GNSS data from permanent and campaign stations at Mount Etna are presented. The GNSS networks managed by Istituto Nazionale Geofisica e Vulcanologia and by Università degli Studi di Catania are descrived.

The third chapter is dedicated to present GNSS time series realized by GipsyX for the permanent and campaign stations. In the second part of this chapter, the reference frame used in this dissertation is defined and finally the velocity field.

The fourth chapter presents the deformation results derived by InSAR interferometry using the PBAS (Parallel Small Baseline Subset) Sentinel-1 processing on-demand services, realized by CNR-IREA of Naples. In this chapter, the alignment between GNSS and InSAR data is shown together with the deformation map for the east and up component of the Permanent Scatter located on the south eastern flank of Mount Etna. By the analysis of Permanent Scatter the off set of each fault located on the area of interest are shown in order to analysed the deformation related of each fault.

The fifth chapter consists in the final summary, discussion, conclusions and proposal for the future in order to improve the monitoring of ground deformation on the Mount Etna.

CHAPTER 1

VOLCANO-TECTONIC DOMAINS

1.1 Eastern Sicily framework

Mt. Etna is located in eastern Sicily within the geodynamic context of the central Mediterranean. The central Mediterranean presents a complex geodynamic frame, which is still the subject of research for several scientists around the world. In this context different structural domains coexist due to the presence of various microplate which appeared and developed as the results of Neogene-Quaternary collisional tectonic processes induced by relative Eurasian and African convergence (Figure 1. 1).

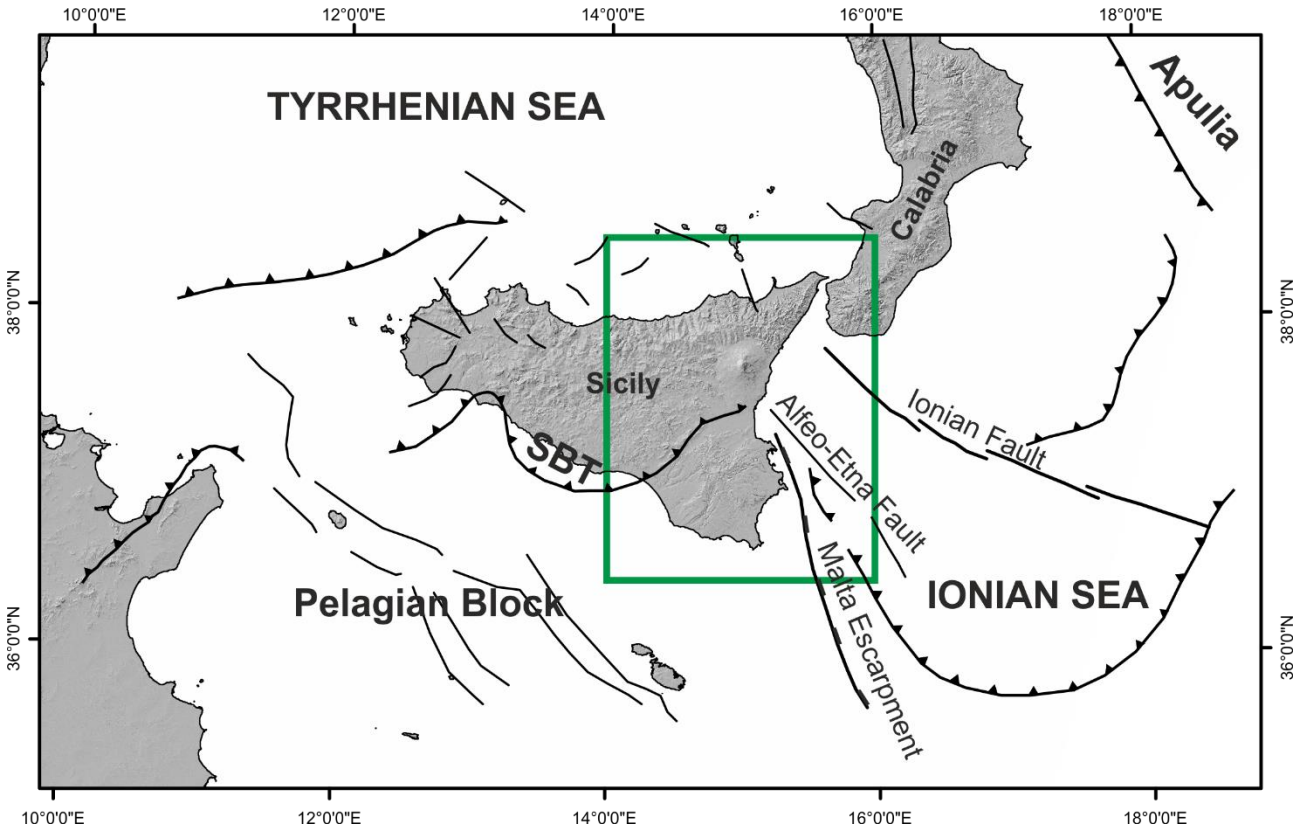

Figure 1. 1 - Location of Sicily in the geodynamic framework of the central Mediterranean. The green box is the Figure 1. 2.

Eastern Sicily consists of three structural domains (Lentini and Carbone, 2014):

- the Hyblean foreland which is part of the Pelagian Block (northern margin of the African plate) and it is constituted by undeformed carbonate rocks;
- the Appenninc-Maghrebian chain which is a Neogene-Quartenary collisional belt formed by the fold and thrust system involving the foreland domain;
- the Catania-Gela foredeep (Bousquet and Lanzafame, 2004)which is a Plio-Pliostocene basin, filled by the sediments of the Catania plain due to the bending of the foreland below the chain.

In eastern Sicily the major tectonic structures are (Figure 1. 1; Figure 1. 2):

- the Sicilian Basal Thrust (SBT) which represents the outermost basal thrust plane of the chain, which dates back to Plio-Pleistocene times with some evidence of Holocene activity (De Guidi et al., 2015; Lavecchia et al., 2007);
- the Malta Escarpment, a large Mesozoic boundary reactivated during the Quaternary, which separates the Ionian oceanic crust from the Pelagian continental crust (Hirn et al., 1997; Makris et al., 1986; Scandone, 1981);
- the North Alfeo and the South Alfeo Fault Sustem (the Alfeo-Etna fault System of Polonia et al., 2016) which is interpreted as a upper plate deformation belt of a Subduction Transform Edge Propagator (STEP) fault (Gutscher et al., 2016) at the lateral termination of the Ionian subduction zone, and which in its North-Western sector joins the fault system of the eastern flank of Mount Etna (Barreca et al., 2018a);

the Ionian Fault, which together with the Tindari Fault is alternatively interpreted as the south-western edge of the Ionian Subduction system (Barreca et al., 2019).

In Eastern Sicily two dynamic tectonic regimes coexist (Palano et al., 2012):

1. a compression with approximately N-S orientation due to the Africa-Europe convergence, which has caused the development of the Sicilian-Maghrebian fold and Thrust belt; active convergence is well evident in the growth of fold structures at the chain front, such as the Catania anticline (De Guidi et al., 2015) which shows an uplift rate of about 10 mm/yr, related to a convergence rateof about 5 mm/yr (Mattia et al., 2012; Palano et al., 2012);
2. a WNW-ESE oriented extension coupled with tectonic uplift interpreted as: (i) isostatic response to the passive subduction of the detached Ionian slab (Westaway, 1993); (ii) the result of roll back of the slab and consequent asthenospheric flow at its western lateral edge (Faccenna et al., 2011; Hirn et al., 1997; Schellart, 2010); (iii) due to the counter clockwise rotation of the Adriatic microplate which generated a tensile stress field along its western margin (D'Agostino et al., 2008; D'Agostino and Selvaggi, 2004);

(iv) related to a Middle Pleistocene tectonic plate reorganization in the southern-central Mediterranean driven by the stalling of the Calabrian roll-back/subduction (Goes et al., 2004). The WNW-ESE regional extensional regime manifests itself since 700 ka ago by the activity of a normal fault belt system running roughly N–S for about 370 km from southern Calabria to eastern Sicily (Monaco and Tortorici, 2000; Tortorici et al., 1995). The extensional regime has been accompanied by late Quaternary and Holocene tectonic and volcano-tectonic uplift, affecting with differential magnitude, all the coasts of eastern Sicily (Antonioli et al., 2003; Bousquet and Lanzafame, 1986; Firth et al., 1996; De Guidi et al., 2003; Kershaw, 2000; Ristuccia et al., 2013; Rust and Kershaw, 2000; Spampinato et al., 2012; Stewart et al., 1997).

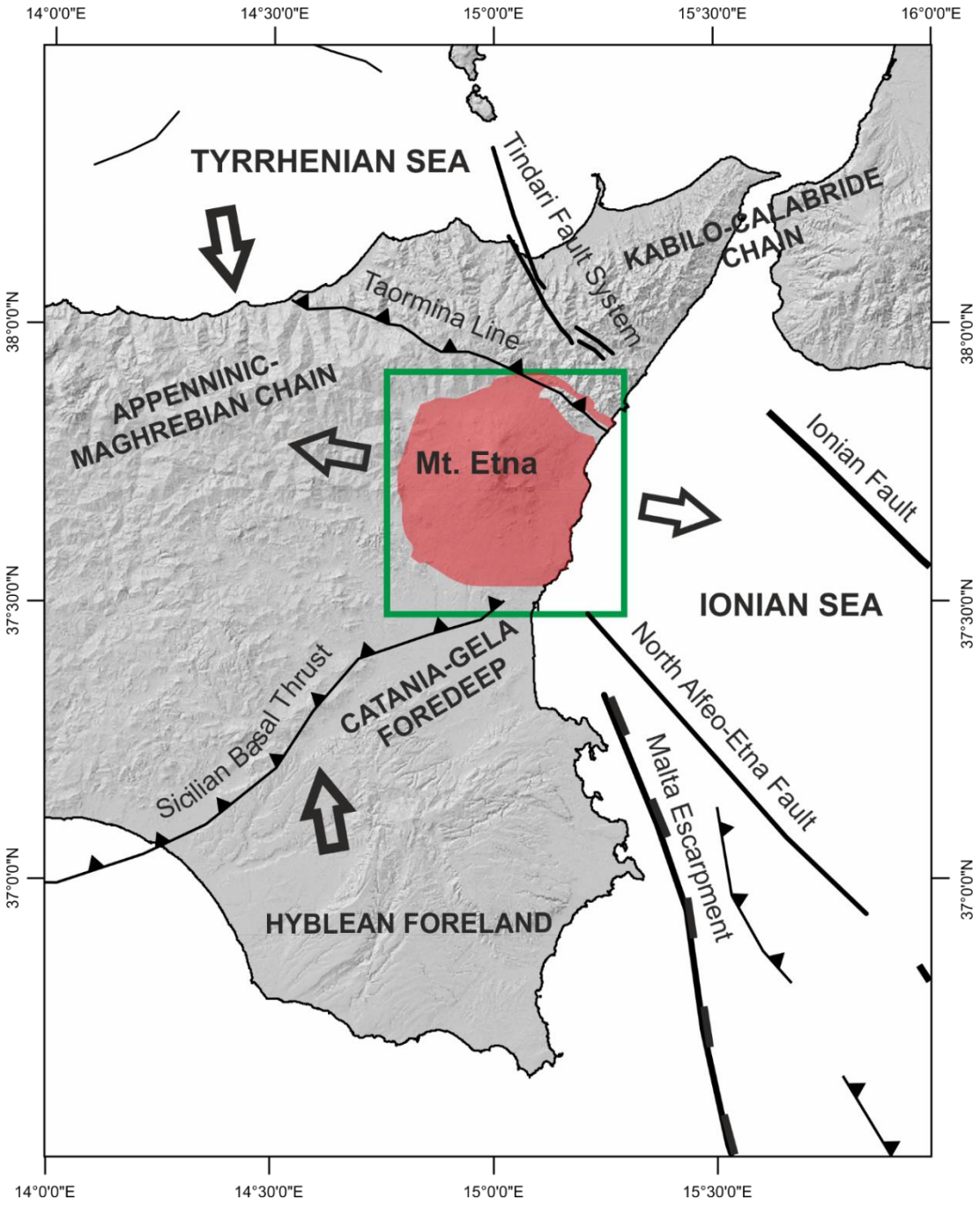

Figure 1. 2 - Location of Mount Etna in the geodynamic framework of eastern Sicily. The black arrows represent the extension and compressional regims direction The green box is the Figure 1. 3.

1.2 Volcano-tectonic framework of Mount Etna

Mount Etna is a late Quaternary polygenic volcano located between the Gela-Catania foredeep and the frontal nappes of the Sicilian-Maghrebian collision zone (Figure 1. 2). The volcanic edifice has grown within a geodynamic framework involving the major tectonic structures of

the area (see above), and its activity is believed related to the occurrence of a regional-scale tectonic boundary extending from the central sector of the Aeolian archipelago to the Ionian coast of Sicily (the Aeolian-Tindari-Letojanni fault system, Palano et al., 2012), presumably joining to a series of offshore fault systems: the Malta escarpment (Hirn et al., 1997; Nicolich et al., 2000); the North Alfeo Fault (Gutscher et al., 2016) or the Alfeo - Etna Fault (Polonia et al., 2016).

This major boundary accommodates the lithospheric tearing of the south-western edge of the Ionian slab subducting beneath the Calabrian Arc and the Tyrrhenian basin, whose detachment favored the progressive south-eastward migration of the Calabrian Arc (Govers and Wortel, 2005; Neri et al., 2012). Accordingly, in the last 500 ka, crustal faulting and associated fracturing favored magma ascent through the lithosphere along the Ionian coast of Sicily where volcanic products have accumulated above a Neogene-Quaternary sedimentary clayey basement to form a composite stratovolcano (Barreca et al., 2018b).

Within this complex tectonic frame, authors proposed various hypothesis concerning the origin and the evolution of the Mount Etna:

1) the consequence of the intersection of three main fault zones with different trends (Cristofolini et al., 1977; Lo Giudice and Rasà, 1992);
2) Ellis and King (1991) explain the common occurrence of volcanoes on the footwall of normal faults through a flexing plate model.
3) Monaco et al. (1997), following Ellis and King, (1991), relate Etna magmatism to dilatational strain on the footwall of an east-facing, crustal-scale normal fault system, (SCRZ). They also define the local stress field, suggesting a WNW–ESE roughly oriented regional extension.
4) Hirn et al. (1997) relate Mt. Etna evolution to rifting coupled with the slab windows at the lateral edge of the Ionian slab.
5) Similary Gvirtzman and Nur (1999) and Doglioni et al. (2001) propose the voluminous melting process under Mt. Etna as the result from “suction” of asthenospheric material below the African plate in a process of “rollback” of the descending Ionian slab. They recognize a differential rollback process of the Apennine subduction: the larger retreat of Ionian lithosphere would account for a “window” allowing decompression and melting in the lower lithosphere (or in the upper asthenosphere). Schellart (2010) presents a geodynamic model that indicates that the east-directed rollback of the Ionian

slab results in mantle upwelling around the southern slab edge causing decompression melting of upper mantle material and accounting for Mt. Etna and Hyblean volcanism.

6) Finally, some authors (Clocchiatti et al., 1998; Patanè et al., 2006; Tanguy et al., 1997) suggest the existence of a "hot spot" origin for the Etnean volcanism.

In addition to the regional extensional faults system of eastern Sicily, volcano-tectonics lineaments and gravitational sliding affect unstable eastern flank of Mount Etna.

Normal faults are present mostly on the eastern flank of Mt. Etna, along the Ionian coast, where they form a 30 km long system dipping towards the Ionian Sea (Figure 1 .3).

To the north, Late Quaternary fault segments run along the Ionian coastline, strongly uplifting the onshore, reaching the Straits of Messina to continue along the Tyrrhenian side of the Calabrian Arc (Catalano and De Guidi, 2003; Monaco and Tortorici, 2000; Stewart et al., 1997).

The system trends SSW-NNE on the lower north-eastern flank, where the Piedimonte-Fiumefreddo fault system occurs, interpreted as a synthetic geometry of transfer zones that connects the southern end of the Taormina Fault (Catalano and De Guidi, 2003; De Guidi et al., 2003) with the northern termination of the southeaster Sicily seismogenic fault belt (Piedimonte fault of Monaco et al., 1997). The NNE-SSW direction of Piedimonte Fault bends to NNW-SSE direction on the lower eastern south-eastern flanks, where the Sant'Alfio-Guardia, San Leonardello-Trepunti, Acireale-Santa Venerina and Acicatena-Valverde fault systems show a slight right- lateral component of motion (Azzaro, 1999, 2004; Lo Giudice and Rasà, 1986, 1992; Lanzafame et al., 1996; Monaco et al., 1995, 1997).

Southwards, this normal fault system extends offshore where it bounds NNW trending Late Quaternary wedge-shaped basins, as shown by reflection seismic profiles (Bianca et al., 1999; Hirn et al., 1997; Monaco et al., 1995).

The fault segments control the present topography and drainage network of lower eastern flank of Mount Etna and show steep escarpments (Timpe) with very fresh, mostly Late Pleistocene to Holocene, morphology. The most impressive scarps, up to 200 m high, extend discontinuously for about 20 km from Sant'Alfio to Acireale , where they affect sedimentary and volcanic rocks ranging in age from Early Pleistocene to historical times, as the 396 B.C., IX century, 1284, 1329, 1408, 1689 lava flows (AA and VV, 1979; Corsaro et al., 2002; Monaco et al., 1997; Tanguy and Kieffer, 1993). In this sector, normal faulting is associated with shallow depth (<5 km) seismicity and the occurrence of several earthquakes with M~4.5 (Azzaro et al., 2000).

Secondary structures are represented by the NW-SE striking Linera and Fiandaca faults, that extend up slope with poor morphologic evidence. In the southern flank of the volcano, between

Nicolosi and Catania, a less pronounced fault system occurs, composed of NW-SE striking segments (Tremestieri-Trecastagni fault system), characterized by a component of dextral displacement.

To the west, the isolated N-S striking Ragalna fault also shows oblique-dextral component of motion. The normal fault system occurring in the eastern flank of Mt. Etna is confined to the north by the WNW- ESE striking left-lateral Pernicana fault and to the south by the Acitrezza fault. These structures transfer most of the extension to the east toward the master faults of the Siculo-Calabrian Rift Zone (Monaco et al., 1997).

The Pernicana, Timpe and Tremestieri Trecastagni fault system, define the unstable eastern flank of Etna complex characterized by movement to the Ionian Sea with velocity at still one order of magnitude greater than the area surrounding the volcano.

In such a geodynamic context, the area between the southern edge of the Mt. Etna volcanic edifice and the Hyblean Plateau (the Catania Plain) represents the remnant of a foredeep domain, filled by Pleistocene sediments and volcanics, and by Holocene alluvial-coastal deposits (Torelli et al., 1998)

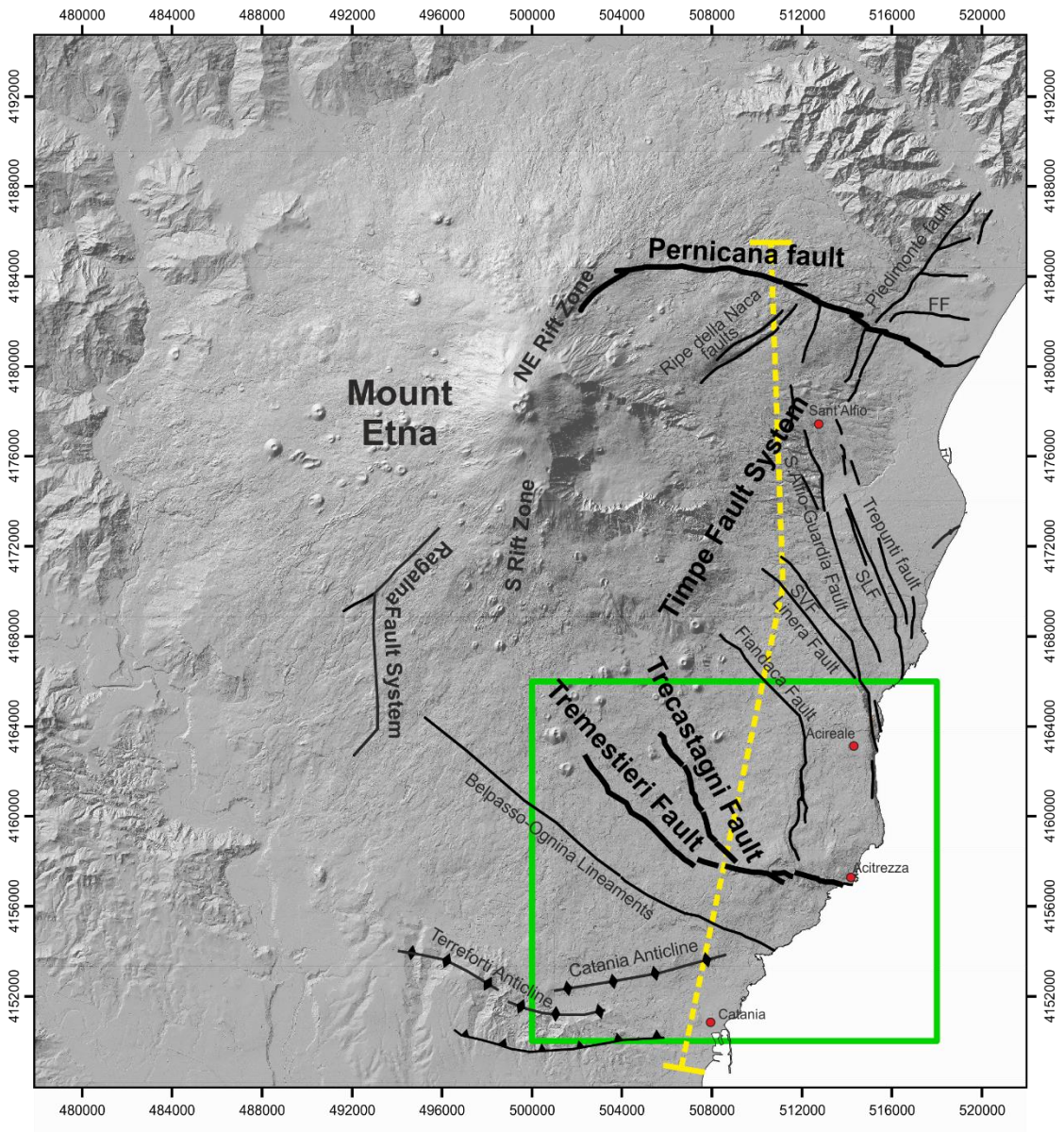

Figure 1. 3 – Tectonic framework on the Mount etna volcano. Yellow dashed line represents the traces of cross section in Figure 1. 4. The boundary structures of unstable flank are represented by thick lines. The acronyms are: SVF = Santa Venerina Faults; SLF = San Leonardello Fault; FF = Fiumefreddo Fault. Green box represents the Figure 1. 5.

The S-N crustal structural geological section (Figure 1. 4) with superimposed volcano-tectonics frame has been carried out Etna based on published data (Barreca et al., 2018a; Bigi et al., 1992; Branca et al., 2011b; Branca and Ferrara, 2013; Chiarabba et al., 2000; Gross et al., 2016; De Guidi et al., 2015; Lavecchia et al., 2007; Lentini and Carbone, 2014; Monaco et al., 2010; Palano, 2016). It extends along eastern slope of Etna volcano for about 40 and 7 km in length and depth respectively. It shows from the east point of view Northwards, the foreland crust deepens under the chain between the northern coast of Sicily and Mount Etna.

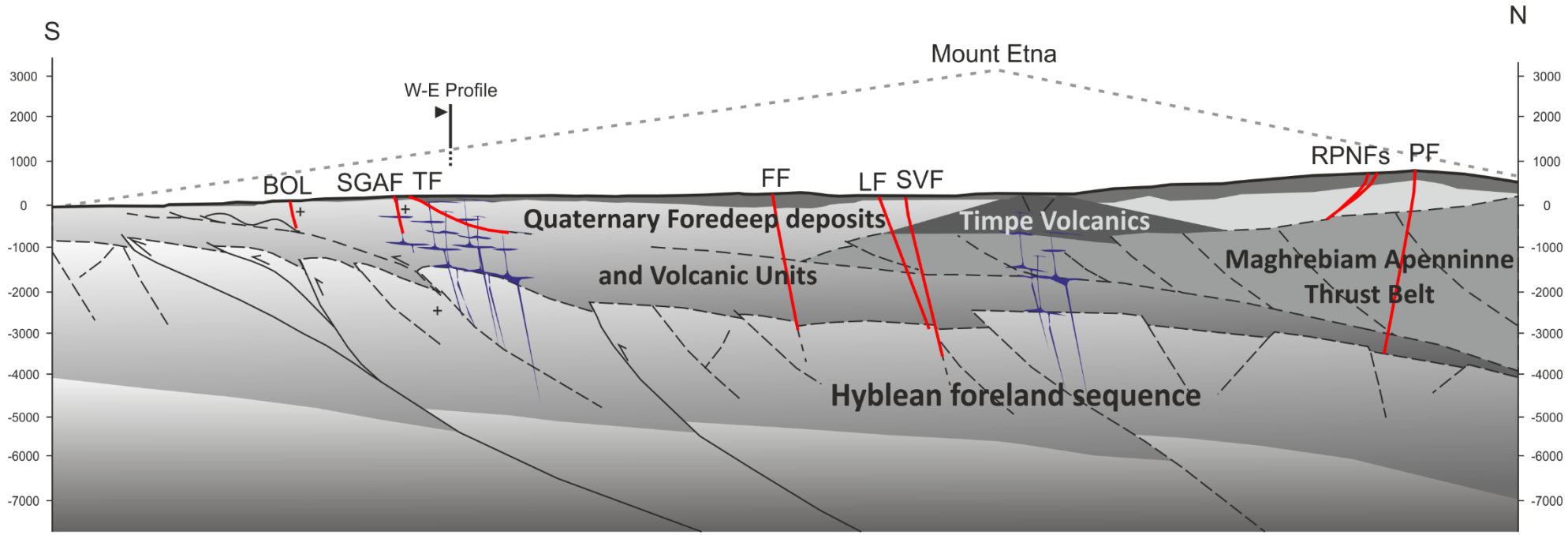

Figure 1. 4 – South -North schematic cross section, 40 km long. Faults of the volcano-tectonic framework are represented by red lines (BOL = Belpasso-Ognina Linements; SGAF = San Gregorio-Acitrezza Fault; FF = Fiandaca Fault; LF = Linera Fault; SVF = Santa Venerina Fault; RPNFs = Ripe della Naca Faults; PF = Pernicana Fault). Dyke intrusion belong to the Timpe volcanics and Basal Tholeiitic volcanics are represented in blue. The reconstruction of geological section was carried out with the bibliographic information.

1.3 Etna South Eastern Flank

Geological, seismological, and geophysical evidence indicates that the eastern complex fault system is controlled by an eastward motion confined within two ~E-W oriented boundaries. The northern one is well defined, while the southern one is less evident and the observed deformation is more distributed. The geological deformation rates (~200 kyr) are characterized by values in the order of few mm/yr (Barreca et al., 2018a; Branca et al., 2014; De Guidi et al., 2014; Monaco et al., 1997; Scudero et al., 2015); on the other hand GNSS measurements over the last decades suggest a short-term deformation rate in the order of cm/yr, reaching even faster velocities in some localized places or periods, sometimes in association with eruptive episodes. In particular, the GNSS velocities have a clear predominant horizontal component with increasing intensity moving eastwards.

In the southern flank of the volcano, between Nicolosi and Catania, there is a complex system of active faults, affected by a component of dextral displacement (Figure 1. 5).

The southernmost structure is the Belpasso-Ognina lineaments (BOL). The location and the activity is well imaged by InSAR (Bonforte et al., 2011; Froger et al., 2001; Solaro et al., 2010) and confirmed by in-situ geochemical surveys (Bonforte et al., 2013a). However it does not show any morphological feature and together with Tremesteri-San Gregorio-Acitrezza Fault and Trecastagni, bound to the south the unstable flank by extensional movements with a minor dextral component. According to some authors, the Belpasso-Ognina Lineament shows a constant deformation rate between August 1996 and January 1998 of about 4 mm/yr (Froger et al., 2001), Bonforte et al., 2011 suggest that BOL produces a eastward velocity increase, from South to North of about 5 mm/yr.

To the north the next structures are the Tremestieri Fault (TMF) and the San Gregorio-Aci Trezza (SGAF) Fault, that form together an unique system of faults. The 3 km-long, TMF is characterized by a 10 m high scarp in its northern sector, whereas in the Tremestieri town it shows minor morphological evidences, even though several building are damage by recent activity (Azzaro et al., 2012; Monaco et al., 2010). According to Azzaro (2004) the TMF extends to the NW without morphological evidences. According to Froger et al. (2001), the TMF shows a deformation rate of about 6 mm/yr; moreover, according to Solaro et al. (2010) this structure produces a velocity increase of about 5 mm/yr on the east block. The vertical movement progressively decrease from west (4 mm/yr) to the east (0 mm/yr) and, in fact TMF is

characterized, on its east sector, by a mainly transcurrent kinematics, from transtensive to purely right lateral on moving from west to the east (Bonforte et al., 2013c).

Based on geological survey, the SGAF is a 5 km long fracture zone without morphologic evidence, being characterized by various discontinuous segments showing prevalent right-lateral motion (Monaco et al., 2010). According to Azzaro et al. (2012), the SGAF presents a 10 m high scarp close to Mt. Catira and a 2 m high scarp in the urban area of S. Gregorio. Historically, this structure is characterized by creep deformation normally linked to the volcano-tectonic activity of Mt. Etna.

De Guidi et al. (2018) installed a local GNSS network taking into account existing geological and geophysical surveys (Imposa et al., 2015) along the SGAF. This GNSS network was designed to determinate the deformation rate which occurs along this structure. By analyzing the first available data, they found a value of average velocity of about 13 mm/yr on the western part of SGA and 28 mm/yr on the eastern part. Moreover, De Guidi et al. (2018) estimate an extensional component of about 15 mm/yr along the E-W direction that it is accommodated by the NNE-SSW trending Nizzeti fault. According to Bonforte et al. (2011b), from 1995 until 2000, along the coastline the SGAF produces a sudden increase of eastward motion of almost 15 mm/yr.

The Trecastagni Fault (TF) extends with NNW-SSE direction until San Giovanni la Punta village whereas it joins with the San Gregorio-Aci Trezza Fault. It forms ~10 m high scarp, partially mantled by the 1408 lava flow that in turn is offset by recent activity. Froger et al. (2001) and Solaro et al. (2010) found a value of 5 mm/yr using InSAR . During the October to January 2010 period, the creep rate of the TF reached up to 5.5 to 7.0 mm/yr and this was accompanied by several shallow, low magnitude earthquakes (Gambino et al., 2011). This fault shows a main vertical kinematics, producing the strongest effect on the vertical velocity pattern, with an evident downthrow of the hangingwall (on the eastern side) at a rate of about 4 mm/yr and its activity is related to the flank dynamics of the volcano , whose stress field affects only the shallowest part the crust (Bonforte et al., 2013a).

To the east, another major structure, shaping the flank of the volcano, is the Nizzeti fault (NF). This fault steps to the right with respect to the Fiandaca Fault. The linear, up to 100 m high cumulative scarp of this fault, together with a minor parallel conjugate structure upslope, truncates the Timpe volcanics deposits. To the north, this structure links to southern end of the

Fiandaca fault by a system of east-dipping normal fault splays (the Acicatena fault) with direction between N-S and SSW-NNE (Monaco et al., 2010). According to De Guidi et al. (2018). The NF accommodates the extensional component of about 15 mm/yr along the E-W direction created by the SGAF. The NF is linked to the southern end of the Fiandaca fault (FF) where the 26 December 2018 earthquake (Mw = 4.9) occurred (Bonforte et al., 2019; INGV-OE, 2018). The FF is a 5 km long and NNW-SSE striking fault; it is characterized by minor morphological evidence and extensional motion with oblique-dextral component. Ground ruptures and building damage have been detected also on this fault during seismic events in the last two centuries (Monaco et al., 2010).

To the east, the Acireale Fault forms a NNW-SSE striking, up to 200 m hight, rectilinear scarp between Santa Tecla and Capo Mulini where it offsets a volcanic sequence mostly made of the 200 to 100 Ka-old Timpe Volcanics (Corsaro et al., 2002; Monaco et al., 2010). This is implies a vertical slip rate of 1.1 -1.9 mm/yr (Monaco et al., 1997), yet other authors find different values of vertical displacement rate of about 4.3 mm/yr (Azzaro et al., 2012) and 3 mm/yr (Branca et al., 2014).

To the south, external to eastern flank, between Misterbianco and Catania, two contractional structures occur: the Terreforti anticline and the Catania anticline (Catalano et al., 2011; De Guidi et al., 2015; Labaume et al., 1990; Ristuccia et al., 2013). There are several interpretations for their origin. Some authors suggest that they have grown due the load of the volcanic edifice (Borgia et al., 2000) while others interpreted them as a thrust propagation folds at the front of the chain, related to the migration of the thrust belt, as a response to the regional NNW-SSE compressive tectonic regime (Palano et al., 2012). Solaro et al. (2010) suggest that the growing of anticline is due to both the tectonic compressional regime and the load of Mt. Etna. Using morphological, seismological and geodetic data, De Guidi et al. (2015) suggest an uplift of 10 mm/yr for the anticline and a shorting of 5 mm/yr due the activity of a possible low-angle blind thrust.

Using InSAR data, Bonforte et al. (2011) and Froger et al. (2001) suggest an upraises of about 5 mm/yr while Borgia et al. (2000), using GPS and InSAR, data suggest a relative uplift between the GPS station of Nicolosi, Centuripe and Misterbianco of about 7 mm/yr and an absolute value of uplift of about 15-20 mm/yr; moreover, Borgia et al. (2000) suggest a shortening of 12 mm/yr due the load of the volcano onto the weak sub etnean clays.

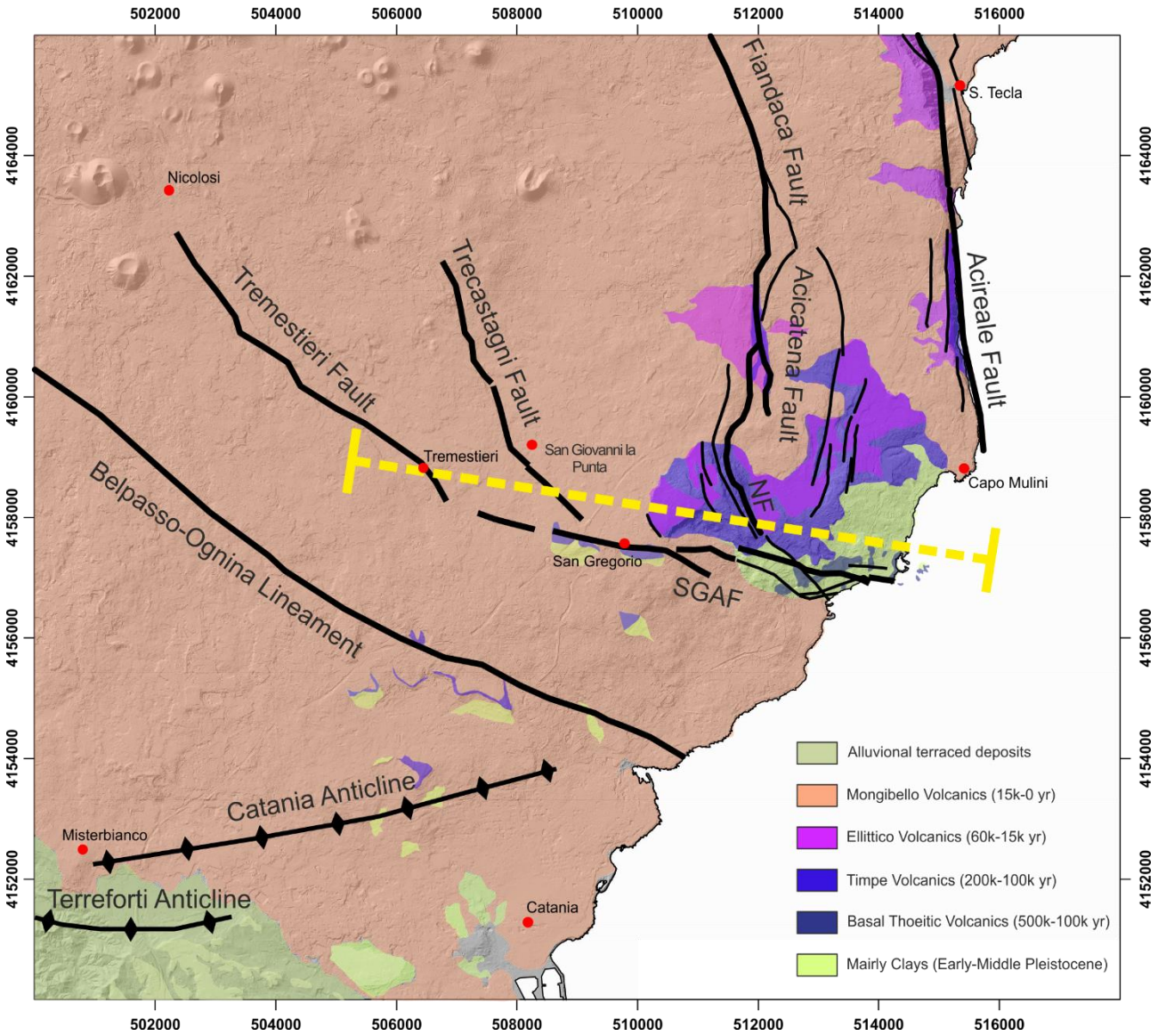

Figure 1. 5 – Tectonic framework and schematic geological succession of the south eastern flank of Mount Etna. Major structures are represented by larger black lines. Yellow dashed line represents the E-W geological section of Figure 1. 6.

A E-W crustal-structural geological section (Figure 1. 6) with superimposed volcano-tectonics frame has been carried out based on published data (Barreca et al., 2018a; Bigi et al., 1992; Branca et al., 2011b; Branca and Ferrara, 2013; Chiarabba et al., 2000; Gross et al., 2016; De Guidi et al., 2015; Lavecchia et al., 2007; Lentini and Carbone, 2014; Monaco et al., 2010; Palano, 2016). It extends along eastern slope of Etna volcano for about 15 and 5 km in length and depth, respectively. It shows from the south point of view the architecture of volcano-tectonics structures and shallower foredeep quaternary sediments covered to the west by the last products of lava flow and intruded by the first phase of volcanic activities dating from 500 ka

to the east. The dashed red line represents the interpreted decollement plane (Palano, 2016) which matching with the top of reconstructed top of the foreland crust deepens under the chain.

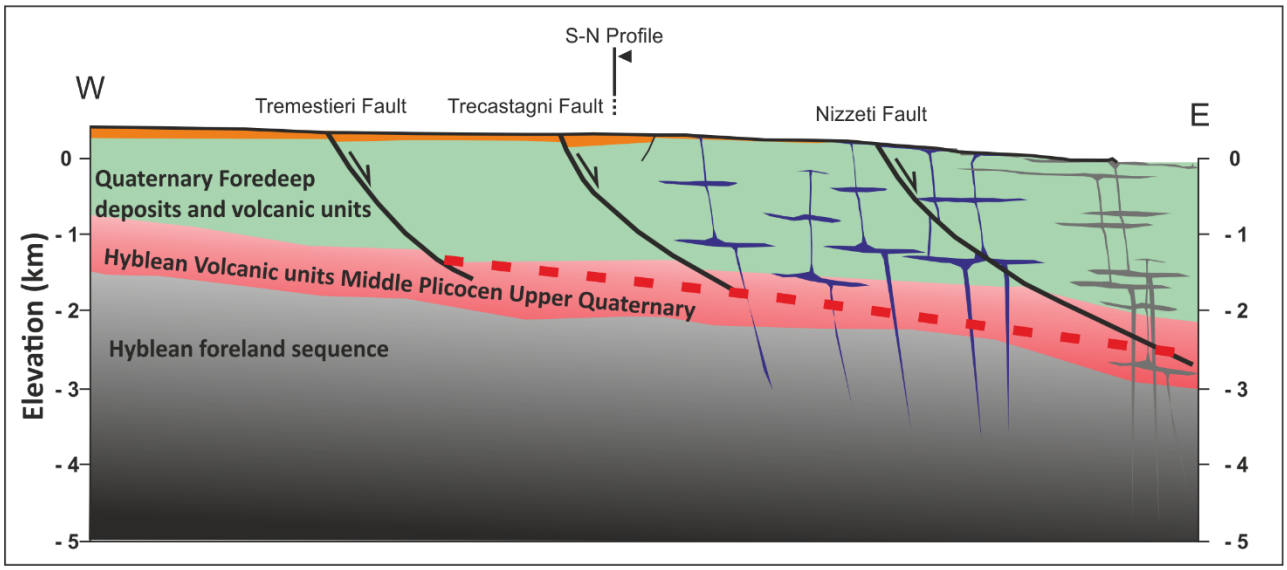

Figure 1. 6 – East – West schematic geological section of the south eastern flank of Mount Etna. Dyke intrusions are represented in blue (Timpe volcanics) and in grey (Basal Tholeiitic volcanics). The lava succession is represented in orange. Black lines represent the faults present on the south eastern flank. Red dashed line represents the decollement plane define by Palano (2016).

1.4 Faulting and shallow earthquakes at Etna

Historically, earthquakes have been common on Etna volcano, systematic observations of seismic activity at Mt. Etna began in 1967, with a mechanical seismometer permanently deployed on the southern flank of the volcano, near the Astrophysical Observatory at Serra la Nave (Bottari and Riuscetti, 1967). Previous investigations were limited to macroseismic observations and/or sporadic analyses of seismograms collected by an observatory in Catania (Caloi et al., 1948). A new improvement for seismic observations came in 1978 when a short-period, telemetered network was set up permanently by the University of Catania (Gresta and Patané, 1987). For several years, five to nine analogue stations transmitted seismic signals which were recorded on paper drums and analogue magnetic tapes. From the early 1980's on, seismic experiments have been carried out for specific studies on source parameters, wave propagation, and volcano tomography, boosting dramatically the information collected at the permanent network especially with the use of temporary digital arrays (Castellano et al., 1989, 1993) operating in local recording mode on event-trigger detection (Patanè et al., 2004).

Nowadays about 40 seismic stations are deployed on the Mount Etna, operated by INGV-OE (Istituto Nazionale Geofisica e Vulcanologia, Osservatorio Etneo). The seismicity at Mount Etna (Figure 1. 7), as in other volcanic areas, is defined as seismo-volcanic activity (Patanè et al., 2004). There is the general agreement that most earthquakes with origin in active volcanoes are ultimately related to volcanic processes. A large class of earthquakes at Mt. Etna shares similar characteristics to those of seismic events in a tectonic environment, such as the nearby areas of the Peloritan-Calabrian arc and the Hyblean plateau. In spite the large variety of seismic signals recorded at Mt. Etna, the seismic signals can be divided into two main groups. The first group includes volcano-tectonic earthquakes generated by fracturing processes induced by tectonic stress and/or by stress generated by magma upwelling in the Earth's crust (Chouet, 1996; Patanè et al., 1994, 1997). The second group includes the seismic manifestation related to fluid dynamics (eruption episodes, magma overflow and explosive activity).

The upper part of the volcano is commonly affected by earthquake swarms, often related to magma movement towards the surface, through dyke propagation (Gambino, 2004; Patanè et al., 2003a).

Conversely, the western flank of the volcano is mainly characterized also by relatively deeper earthquakes (h>10 km), showing an average NNW–SSE maximum compressive stress (Cocina et al., 1998; Patanè et al., 2003b), in agreement with the regional one.

Finally, there are earthquakes affecting the medium-lower eastern flank of the volcano. Those events are mainly linked to regional tectonics.

Some authors make distinctions between the regional tensile stress field and a local one related to gravity-induced sliding or spreading (Alparone et al., 2013b; Lo Giudice and Rasà, 1992; Walter, 2005). Other authors relate both regional and local stresses to the extensional forces acting on eastern Sicily (Catalano et al., 2008). In all cases, the main feature of the seismic activity in the eastern flank is the fact that the seismicity is shallow, with more than 80% of earthquakes not deeper than 5 km (Gresta et al., 1998) and magnitude rarely above M=4.0. Despite their low magnitude, those earthquakes can produce destructive effects (epicentral macroseismic intensity I0 up to IX) in narrow macro-seismic area, sometimes accompanied by visible surface ruptures (Azzaro et al., 1989; Lo Giudice and Rasà, 1992; Gresta et al., 1997).

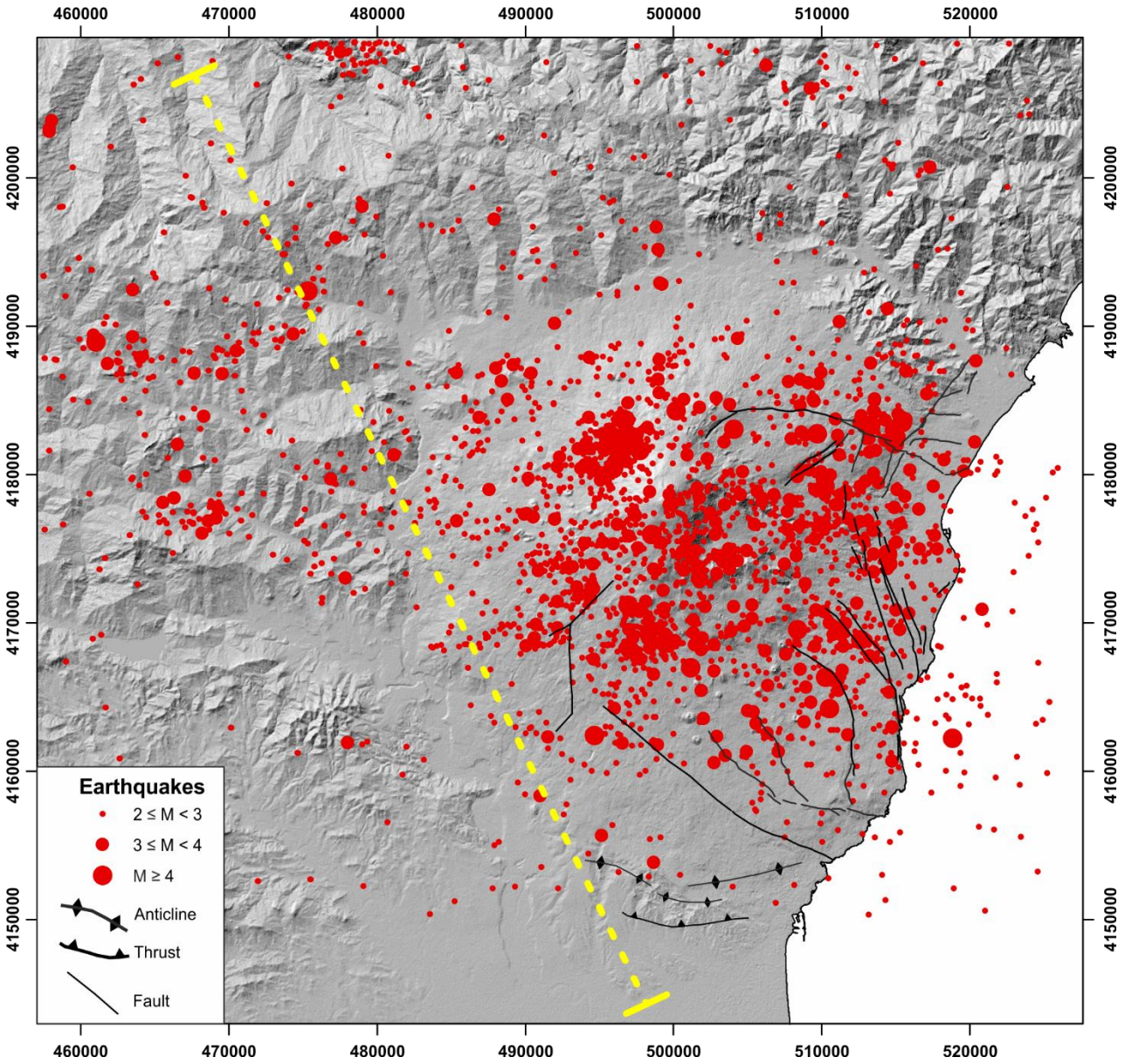

Figure 1. 7 – Earthquakes distribution occurred from 1999 until 2020 with M > 2 (ISIDe Working Group, 2007). Yellow dashed line is the cross section of Figure 1. 8.

De Guidi et al. (2015) analysed the seismological dataset (Gruppo Analisi Dati Sismici, 2020) selecting 1900 earthquakes occurred on the southern and western sectors of the volcano, with magnitude between 1 and 4.8, recorded between in 1999-2012. The distribution of the earthquakes shows a clear trend from very shallow hypocentres in the area south of Mt Etna to deeper (35 km) in the northern area (Figure 1. 8). Analysing the orientation of P-axes of the focal mechanism, the cluster of earthquakes located west of the summit craters shows P-axis striking mostly about WNW-ESE, southward, earthquakes at 10-15 km of depth have a P-axes quite uniformly NE-SW oriented and the P-axes for the deeper events have a NW-SE orientation. De Guidi et al. (2015) suggest that at the intermediate depth (10-15 km) the seismicity is related

to local process (magmatic processes) while at greater depth the regional dynamics is the main driving force with the stress NW-SE oriented connected to the Europe-Africa collision (Scarfi et al., 2013).

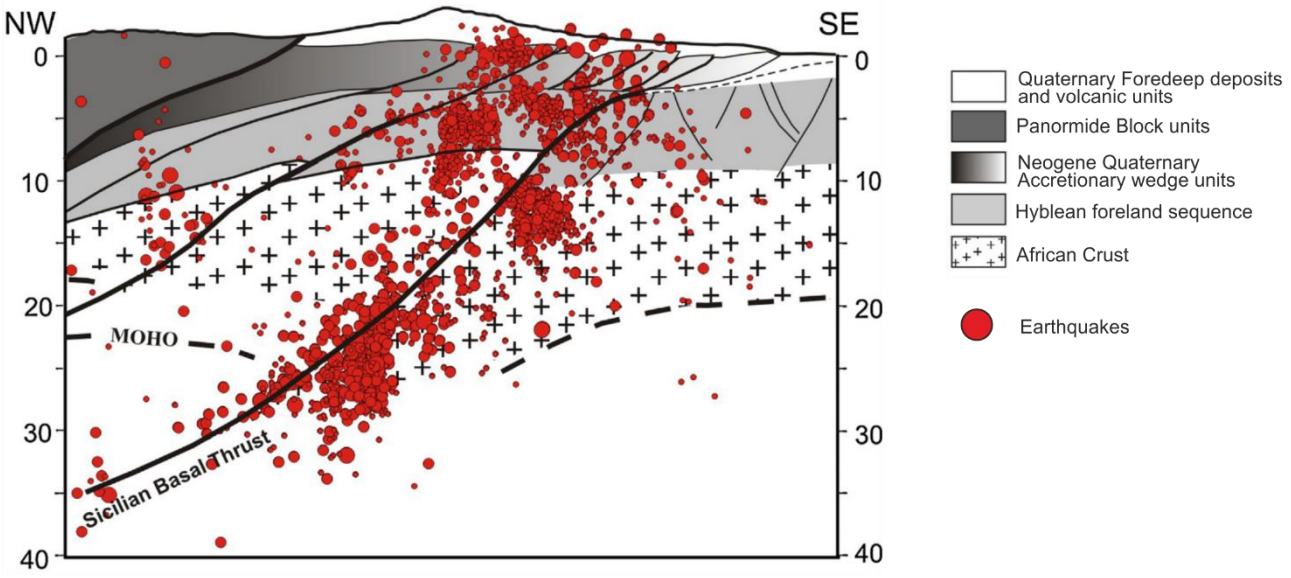

Figure 1. 8 – Schematic crustal section with the projection of the hypocentral distribution. Earthquakes recorded between 1999 and 2012 (from De Guidi et al., 2015).

The seismic events that occur in the eastern portion of the volcano are characterized by hypocenters localized at shallow depths (maximum 5 km), (Gresta et al., 1998) many of this events can be connected to the activity of surface extensional structures that control the deformation of the etnean eastern side (Figure 1. 8) (Alparone et al., 2013a; Azzaro et al., 2013). During the last 20 years, most of the earthquakes that occurred on the eastern flank of the volcano have been linked to the volcanic activity. According to De Guidi et al., (2012), fault segments on the lower eastern flank of Mt. Etna affect a shallow, brittle-deforming crust, whereas offshore fault segments are deeper rooted. The observed minimum magnitude producing ground effect is fairly low and generally coseismic effects accompany earthquakes greater than a magnitude of 5. A reduced thickness of the brittle seismogenic crust below the eastern side of Mt. Etna would explain why the value of the minimum earthquake magnitude associated with sudden surface faulting is around 2.5. Local thinning of the seismogenic layer below the eastern flank of Mt. Etna, probably is due to the influence of the heat on rock rheology. Historical data evidence the correlation between lateral eruptions and seismicity on the eastern falnk. For instance, the eruptions of 2002 and 2018 were preceded by seismic activity.

During these eruptions, it was observed that seismic swarms in the summit area preceded the aperture of eruptive fractures and when they were created suddenly the seismic activity decreased; after that the faults of eastern flank generated strong earthquakes triggered by rising magma. In 2002 the flank instability was probably induced by the dynamic effect (lateral push) due the emplacement of the dikes (Battaglia et al., 2011), which also generated strong earthquakes on eastern flank (Azzaro and D'Amico, 2019; Gruppo Analisi Dati Sismici, 2020; ISIDe Working Group, 2007; Monaco et al., 2005).

Similar behaviour was observed during the eruption of December 2018 (Bonforte et al., 2019; De Novellis et al., 2019) (Figure 1. 9). As in 2002-2003, this eruption was preceded by a seismic swarm. Strong shallow seismicity (depth max=5.3 km b.s.l.; Mmax=4.2 october 2002, (Monaco et al., 2005) and depth of about 0.8 km; Mmax=4.9 december 2018 are consistent with modelled seismogenic thickness and regression curves obtained for the Mt. Etna area (De Guidi et al., 2012). One of the peculiarities of this seismic swarm is that many volcano-tectonic structures on the flanks of the volcano were active. Most of the earthquakes occurred below the upper SE flank, beneath the 1989 fracture on an area that already showed seismic and ground deformation activity during recent eruptions (Bonforte et al., 2009, 2013b). Furthermore, also the Pernicana Fault System, at NE, and Ragalna Fault System (Neri et al., 2007), at SW, were activated. Beside from the seismic swarm localised beneath the upper part the volcano, a Mw = 4.9 earthquake struck the lower SE flank of Mt Etna on December 26th at 02:19 GMT, activating the Fiandaca fault. The seismic swarm lasted for several days, with a continuously decreasing. The peculiar characteristic of the 2018 intrusion is the simultaneous activation of several faults during the same intrusive event, which was never observed since DInSAR is used on Etna (Bonforte et al., 2019). The 2018 December Mt. Etna eruption shows that the eccentric upraise of a large magma body carries a potential energy on structurally complex volcanoes that can be released by activating peripheral faults (Bonforte et al., 2019).

Similar behaviour was observed during the eruption of December 2018 (Figure 1. 9). As in 2002-2003, this eruption was preceded by a seismic swarm. Strong shallow seismicity (depth max=5.3 km b.s.l.; Mmax=4.2 october 2002, (Monaco et al., 2005) and depth of about 0.8 km; Mmax=4.9 december 2018 are consistent with modelled seismogenic thickness and regression curves obtained for the Mt. Etna area (De Guidi et al., 2012). One of the peculiarities of this seismic swarm is that many volcano-tectonic structures on the flanks of the volcano were active. Most of the earthquakes occurred below the upper SE flank, beneath the 1989 fracture on an area that already showed seismic and ground deformation activity during recent

eruptions (Bonforte et al., 2009, 2013b). Furthermore, also the Pernicana Fault System, at NE, and Ragalna Fault System (Neri et al., 2007), at SW, were activated. Beside from the seismic swarm localised beneath the upper part the volcano, a Mw = 4.9 earthquake struck the lower SE flank of Mt Etna on December 26th at 02:19 GMT, activating the Fiandaca fault. The seismic swarm lasted for several days, with a continuously decreasing energy. The peculiar characteristic of the 2018 intrusion is the simultaneous activation of several faults during the same intrusive event, which was never observed since DInSAR is used on Etna (Bonforte et al., 2019). The 2018 December Mt. Etna eruption shows that the eccentric upraise of a large magma

body carries a potential energy on structurally complex volcanoes that can be released by activating peripheral faults (Bonforte et al., 2019).

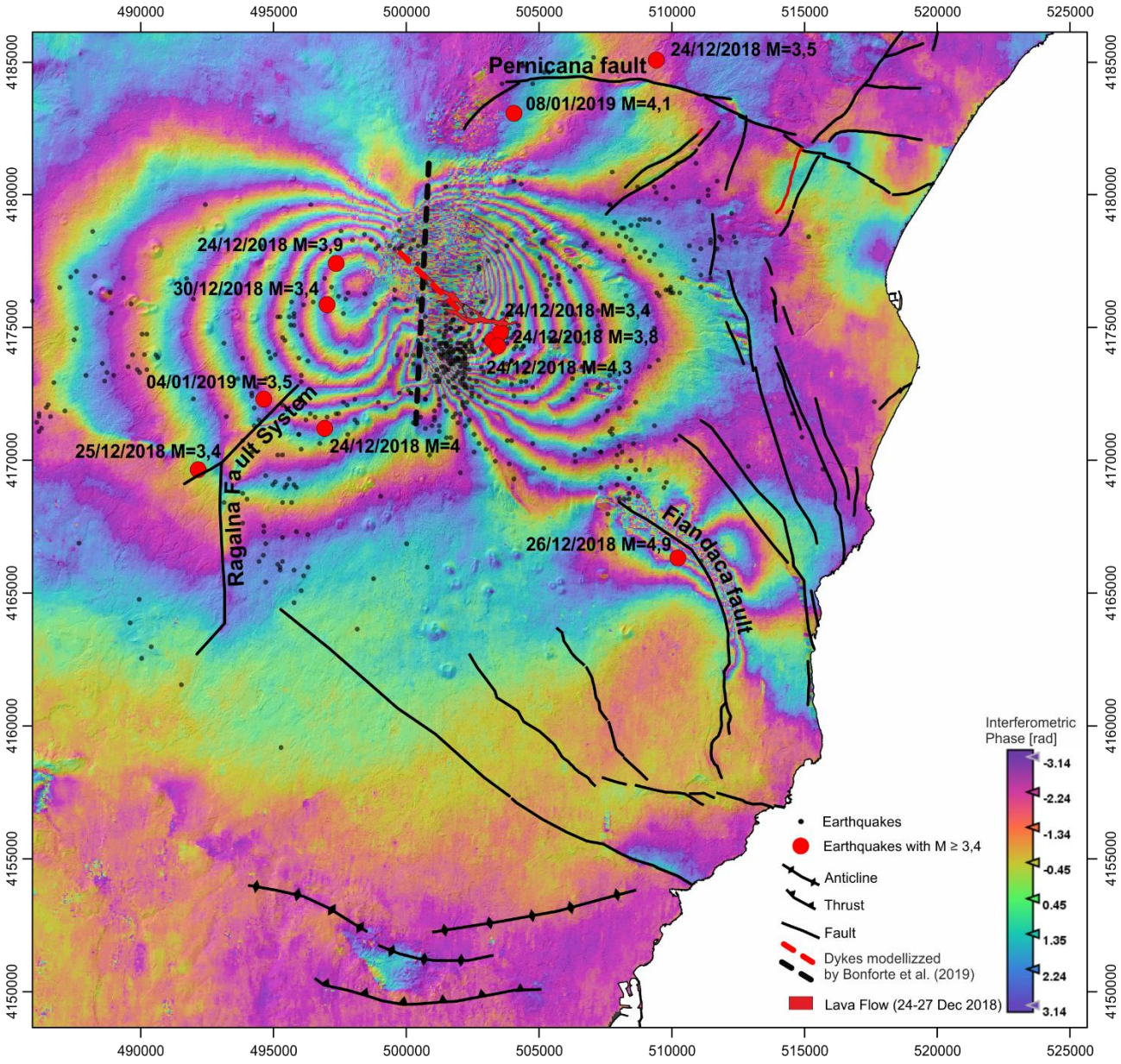

Figure 1. 9 – Descending Sentinel 1A/B interferogram (22/12/2018 – 28/12/2018) produced by SNAP using the online Geohazards-Thematic Exploitation Platform (ESA, 2015). Red circles represent the major earthquake (M>3.4) occurred between 20 December 2018 and 31 January 2019 on the Mount Etna. Black and red dashed lines are the modelized dykes by (Bonforte et al., 2019). The lava flow of 24-27 December 2019 is represented.

1.5 Stratigraphic succession

Recent stratigraphic and geochronological studies have made it possible to reconstruct the evolution of volcanism in the Etna region (De Beni et al., 2011; Branca et al., 2011a), highlighting how the structure of Mount Etna is the result of a long and complex eruptive history. The volcanic products of Etna volcano are related to the activity of five main volcano stratigraphic units (Figure 1. 10): Basal Tholeiitic volcanics, Timpe volcanics, Valle del Bove volcanics, Ellittico volcanics and Mongibello volcanics (Azzaro et al., 2012; Branca et al., 2004, 2008, 2011a, 2011b; Monaco et al., 2010).

1.5.1 Basal Tholeiitic volcanics (500-200 ka)

The Basal Tholeiitic volcanics represent the first volcanic manifestation in the Mount Etna area. The oldest volcanic products were injected in the shallow clays sediments or emplaced on the seafloor of the Gela-Catania Foredeep around 500ka ago. This volcanism produced the pillow lava and volcaniclastic breccia that now outcrop for example in the Acitrezza village. It is associated to the occurrence of effusive-type eruptions with associated minor hydromagmatic activity. Around 300 ka, the volcanic activity moved to Adrano and Paternò area, with the emission of thin lava flows generated by scattered fissure-type eruption. In this period, due the regional uplift in this area (Branca et al., 2014); the paleoenviromental change to a transitional one to a subarial. After the emplacement of this thin lava flows, a period of inactivity starded and lasted 100kr.

1.5.2 Timpe volcanics (200-100 ka)

During this phase, a primitive lava shield was built characterized by a sub-alkaline composition. The eruptive activity was strictly influenced by the extensional tectonics of the NNW trending Timpe fault system (Branca et al., 2008). The repetitive occurrence of effusive eruptions along N-S fissures build a lava shield 22 km long on a NNW-SSE axis, from Acireale to the Ripe della Naca area. During the growth of this shield volcano, eruptive activity occurred also on the lower southwestern and the south eastern area of the Etna volcano. Differently to the basal tholeiitic

volcanics, the volcanic activity was almost continuous as a consequence of a more efficient magma ascent from the mantle (Branca et al., 2011a).

1.5.3 Valle del Bove volcanics (100-60 ka)

In this phase an important change in volcanic activity occurred, it changed from a fissural-type activity to a central-type one. This phase is characterized by the construction of the earliest central-type polygenetic volcanoes on the etnean area at least from about 110 ka (Branca et al., 2011a). Volcanics of this period had a composition from hawaiitic to benmoreitic. This phase was characterized by effusive and explosive activity.

1.5.4 Ellittico volcanics (60-15 ka)

After the construction of the volcanoes of the Valle del Bove, the volcano plumbing system shifted by about 4 km NNW. This activity was characterised by the definitive construction of the present bulk of Etna edifice that took place: the Ellittico volcano, the main eruptive centre recognized in the Etna region, ranging in composition from alkali-basalts to trachytes with mugearites (Corsaro and Pompilio, 2004). Ellittico volcano began its growth about 57 ka ago (De Beni et al., 2011) on the northwest flank of the Valle del Bove edifices, reaching a maximum elevation of about 3600 m. This volcano was characterized by both explosive and effusive activity, mostly from the summit vents and subordinately from flank fissures. The Ellittico volcano ended its activity with four plinian eruptions, occurred between 15.5 -15 ka ago, which produced the collapse of the summit area.

1.5.5 Mongibello volcanics (15-0 ka)

After the Ellittico collapse up to the present, a new volcanic edifice was emplaced which produced the actual edifice, namely Mongibello volcano. The Mongibello lavas range in composition from hawaiite to mugearite, even though after 1970, the erupted products are different from all previous historical Etnean lavas in being enriched in potassium and other alkalis and are mainly classified as K-trachybasalts (Corsaro and Cristofolini, 1996).

Since the first stage of Mongibello volcano activity, several lava flows generated by lower fissures reached the Ionian coast, the Alcantara valley and the present Simeto river floor, causing several dam phenomena. A strong explosive activity also took place at the summit craters starting from about 12 ka ago (Coltelli et al., 2000) and producing several strombolian to subplinian events. The morpho structural arrangement of the Mongibello volcano was

radically modified about 10 ka ago by a catastrophic flank collapse that involved the eastern flank of the Etna edifice producing the wide depression of the Valle del Bove (Calvari et al., 2004; Guest et al., 1984; Kieffer, 1985).

Since the second half of 17th century eruptive activity of Mongibello volcano was characterized by both periods of explosive activity at the summit craters, from strombolian to lava fountain with sporadic short-lived subplinian events, and the occurrence of flank eruptions which appear to have no systematic relationship with the central activity.

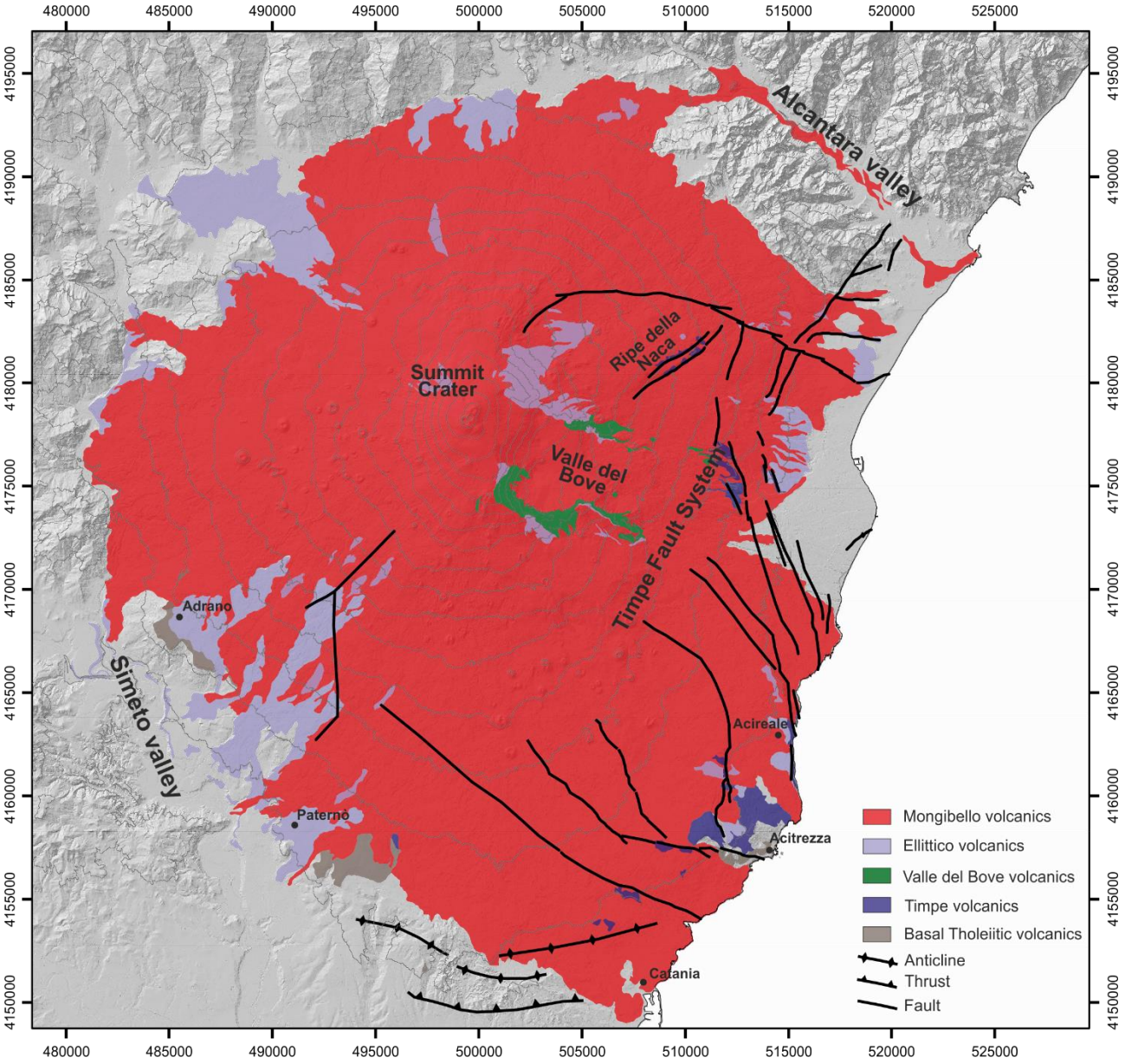

Figure 1. 10 – Schematic geological map of Mount Etna. The main five volcano stratigraphic units are represented.

1.6 Existence of transient deformations (Slow Slip Events)

Since 2000, the deployment of continuous GPS (CGPS) stations allowed to improve the monitoring of the deformation of Mount Etna. In particular GPS permitted to detect episodic aseismic slip events, named slow-slip events (SSEs) (Bruno et al., 2017; De Guidi et al., 2018; Mattia et al., 2015; Palano, 2016).

A seismic creep is a well-know phenomena on Mt Etna, field observation detected very slow aseismic slip along faults on the eastern flank of the Etna volcano. Rasà et al. (1996) detected 16 creep sites where aseismic creep occurs using field observation and historical data. According to Rasà et al. (1996), creep rates range from 0.5 to 2.3 cm/yr and the local creep histories are complex, eruptive crises rarely appear to have triggered fault creep. Moreover Rasà et al. (1996) did not find an obvious relationship between eruptions and creep activity.

Since mid-2008, SSEs have been observed on the lower part of the eastern flank of Mount Etna. In particular they are clearly recognizable from GPS data (Mattia et al., 2015).

Mattia et al. (2015) show that between the end of March and end of May 2009 and from March to August 2012 the CGPS of Etna volcano measured significant ground accelerations, particularly at the stations on its lower flank. The SSEs can be distinguished into two types: the first one is characterized by sudden changes on the linear trend of the GPS time series, linked to the brittle behaviour and the second one is characterised by change with respect to the long-term trend (gentle slope changes) on the GPS time series (Mattia et al., 2015; Palano, 2016).

Mattia et al. 2015 detect fifteen SSEs recorded by the CGPS station of ELAC (Lachea island), ESAL (Sant'Alfio) and EPOZ (Pozzillo) from 2009 until mid-2013.

SSE_ID	Date	GPS Station
SSE1	31/03/2009	ESAL
SSE2	09/04/2009	EPOZ
SSE3	14/04/2009	ELAC
SSE4	24/05/2009	ELAC
SSE5	31/03/2010	ESAL
SSE6	15/04/2010	ELAC
SSE7	24/05/2011	ESAL
SSE8	02/07/2011	ELAC

SSE9	18/07/2011	ESAL
SSE10	13/03/2012	ESAL
SSE11	17/03/2012	ELAC
SSE12	24/06/2012	ELAC
SSE13	12/08/2012	ESAL
SSE14	23/08/2012	EPOZ
SSE15	23/05/2013	EPOZ

This SSEs lasted 1 or 2 days, had a maximum displacement up to 2 cm and were not correlated to any particular volcanic event in this period and to concurrent earthquakes occurring on the volcano or elsewhere and any possible instability of the pillar on which GPS antenna is mounted has been excluded. Moreover according to Mattia et al. (2015) analysing the seismic, well and geochemical data, suggest that hot fluids circulate at shallow depth (0-3 km) beneath the highly fractured eastern flank and facilitate slip.

Palano (2016) investigate SSEs occurring on Mt. Etna from mid-2009 until 2016, he detects seven SSE with a duration ranging from 2 to 71 days on the time series of ELAC, EPOZ and MASC (now ERIP) stations (Figure 1. 11).

SSE_ID	DATE	Duration [days]	Magnitude
SSE1	04/04/2009	71	5.6
SSE2	24/03/2010	39	5.3
SSE3	16/03/2012	8	5.2
SSE4	14/05/2012	15	5.4
SSE5	07/08/2012	42	5.2
SSE6	09/02/2014	2	5.1
SSE7	26/10/2015	11	5.3

The author inverted the GPS data to define a shallow decollement surface beneath the contact between the lava pile and the sedimentary basement. It is ~25 km length and ~20 km width with an eastward dipping of 4° (Figure 1. 11). Moreover, SSEs are not correlated to any volcanic activity and shallow earthquakes.

Finaly De Guidi et al. (2018) detect at least three SSEs recorded by the GPS stations of ELAC. They are characterized by a duration from 1 to 5 days and by slips ranging from ~0.6 up to ~15 mm on the east component.

SSE_ID	Date	Station
SSE1	14/01/2016	ELAC
SSE2	28/04/2016	ELAC
SSE3	10/10/2016	ELAC

Bruno et al. 2017 suggest that the sources of the stresses that encourage SSEs includes both gravitation spreading and tectonic forces, but it is facilitated by magmatic fluids.

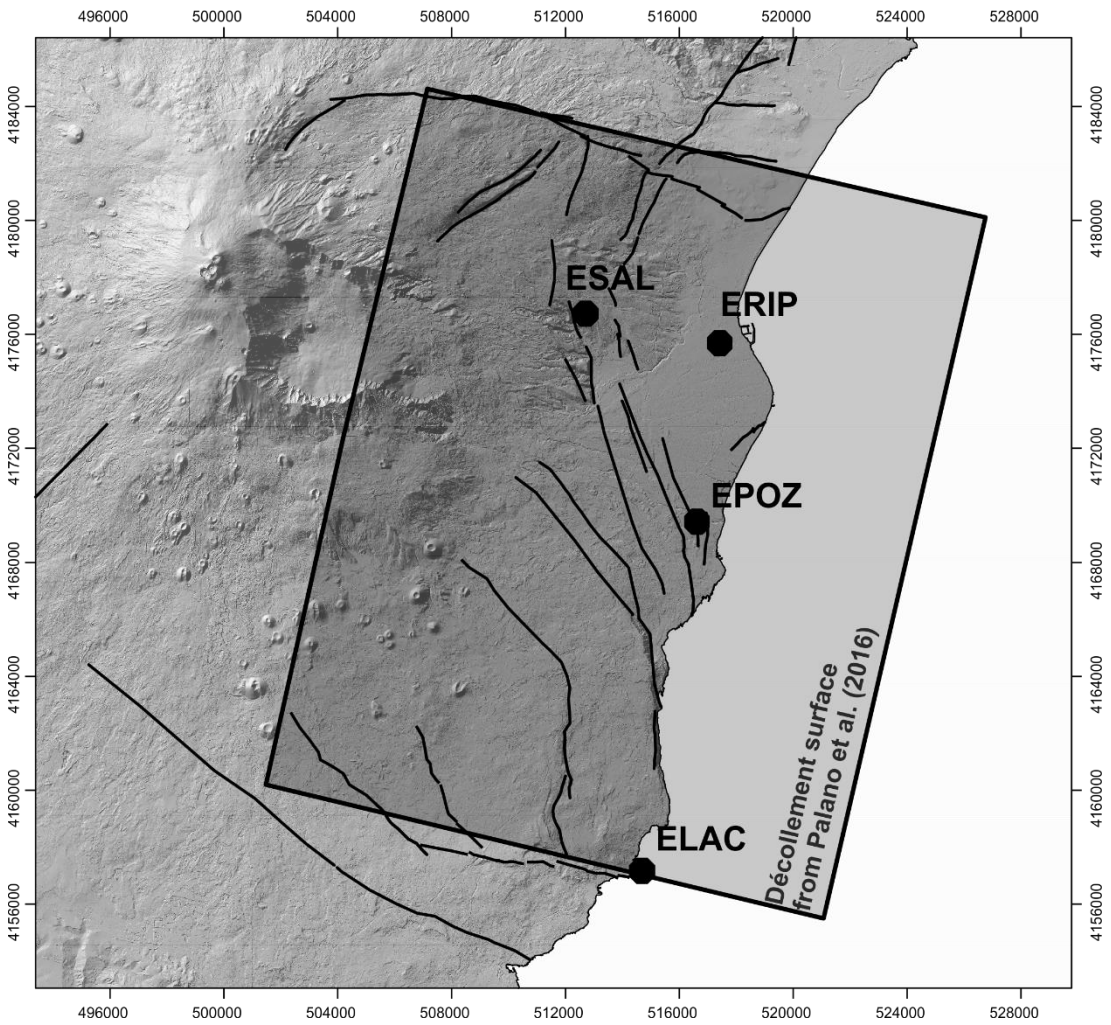

Figure 1. 11 – The décollement surface modeled by Palano (2016) is shown together with the GNSS permanent station used to detect the SSEs.

CHAPTER 2

GPS SURVEYS AND PROCESSING

2.1 Introduction

Geodetic observation of volcano deformations started during the nineteenth century in Italy with the monitoring of the vertical movements of the Phlegraean Fields since 1819 (Berrino et al., 1984) and in Japan, when the first geophysicists created levelling lines for convention geodetic purpose (Mogi, 1958; Omori, 1911). At the beginning of the twentieth century, the first geodetic networks were set up on the Japanese and Hawaiian volcanoes.

Ground deformation studies are important to understand the dynamics on the volcano edifice. Currently Etna is one of the most monitored volcanoes in the world. Various methodologies are used involving various disciplines which are important to improve the knowledge and above all the understanding of a volcanic system on which an important urban fabric has developed.

On Etna, during the 1970s, a geodimetric trilateration network was created (Murray et al., 1977; Villari, 1977; Wadge et al., 1975) along the eastern side (Ionian network) and along the NE rift of Etna. The EDM (Electromagnetic Distance Measurement) technique was used to measure the distances between the benchmark and therefore the horizontal deformations with very high precision (5mm + 1 ppm).

These early networks provided important data relevant to eruptions taking place near the summit of the volcano, related to the eruptions of North East crater between the 1974 and 1978 (Murray and Guest, 1982; Wadge, 1976, 1977).

Subsequently, due to important limitations both for technical reasons (prohibitive environmental condition, absence of good roads or observatories and for the maintenance of the network itself (benchmarks were frequently destroyed during eruptions), three EDM networks on the intermediate flanks, on the north-eastern (in 1978), south-western (in 1980) and southern (in 1983) sides of the volcano were built.

A levelling line was installed in 1980 around the volcano at a quote between 1500 and 1800 meters above sea level (Luongo et al., 1989). These networks, mentioned above, were surveyed at least one time for year and more frequently during eruptions.

The first GPS measurement campaign took place in 1988 (Briole et al., 1992).Based on the experience acquired over the previous 15 years, and in order to improve the existing networks,

the 9 GPS sites were surveyed for the first time on Mt. Etna. With the introduction of GPS techniques begins a new era in geodetic monitoring on Etna, operation and application of geodetic survey completely change, it was possible to obtain 3D coordinates with approximately centimetre accuracy by using a single type of instruments during one single type of survey (Puglisi et al., 2004). Moreover, the procedure to obtain the coordinates was unique and global, in contrast with the complexity of computing the combined data collected on the several levelling and trilateration networks.

2.2 GNSS System

A satellite navigation system is a system that uses satellites to provide autonomous geo-spatial positioning. It allows small electronic receiver receivers to determinate their location (longitude, latitude and altitude/elevation) to high precision (within a few centimetres to meters) using time signals transmitted along a line of sight by radio from satellites. The system can be used for providing position, navigation or for tracking the position of something fitted with a receiver (satellite tracking). The signals also allow the electronic receiver to calculate the current local time to high precision, which allows time synchronisation. These uses are collectively known as Positioning, Navigation and Timing (PNT). Satnav systems operate independently of any telephonic or internet reception, though these technologies can enhance the usefulness of the positioning information generated.

A satellite navigation system with global coverage may be termed a global navigation satellite system (GNSS). As of June 2020, the United States' Global Positioning System (GPS), Russia's Global Navigation Satellite System (GLONASS) and China's BeiDou Navigation Satellite System (BDS) are fully operational GNSSs, with the European Union's Galileo scheduled to be fully operational by 2020. Japan's Quasi-Zenith Satellite System (QZSS) is a GPS satellite-based augmentation system to enhance GPS's accuracy, with satellite navigation independent of GPS scheduled for 2023. The Indian Regional Navigation Satellite System (IRNSS) plans to expand to a global version in the long term. Global coverage for each system is generally achieved by a satellite constellation of 18–30 medium Earth orbit (MEO) satellites spread between several orbital planes. The actual systems use orbital inclinations of >50° and orbital periods of roughly twelve hours (at an altitude of about 20,000 kilometres).

The GNSS concept is based on time and the known position of GNSS specialized satellites. The satellites carry very stable atomic clocks that are synchronized with one another and with the ground clocks. Any drift from time maintained on the ground is corrected daily. In the same

manner, the satellite locations are known with great precision. GNSS receivers have clocks as well, but they are less stable and less precise.

Each GNSS satellite continuously transmits a radio signal containing the current time and data about its position. Since the speed of radio waves is constant and independent of the satellite speed, the time delay between when the satellite transmits a signal and the receiver receives it is proportional to the distance from the satellite to the receiver. A GNSS receiver monitors multiple satellites and solves equations to determine the precise position of the receiver and its deviation from true time. At a minimum, four satellites must be in view of the receiver for it to compute four unknown quantities (three position coordinates and clock deviation from satellite time).

In the case of the GPS constellation, each satellite contains an oscillator of high precision and long-term stability, with a fundamental frequency f_0 = 10.23 MHz, from which are derived the two carrier waves of the signal, called L1 and L2 with a frequency respectively at 154 times f_0 (f_1 = 1575 MHz and λ_1 = 19.05 cm) and 120 times f_0 (f_2 = 1227.60 MHz and λ_2 = 24.45 cm) which allow to determinate the influence of the ionosphere and troposphere on the propagation time of the signals.

The carrier wave L1 is modulated in two codes: Course Acquisition (C/A code) and Precise (P code); C/A code is the type of signal that consumer GPS units receive, is has a frequency of 1/10 f_0 (1.023 MHz), a wavelength of 293 m and a period of 1 ms. Each satellite has a different C/A code that allow to recognize every satellite (Pseudo Randome Code, PRN). The P code provides highly precise location information, the U.S. military is the primary user of P-code transmission and it uses an encrypted form of the data (Y-code) so only special receivers can access the information. The P code has a frequency of 10.23 MHz (λ = 29.3 cm) and a period of 267 days, divided in 38 segments of one week each.

The carrier wave L2 is modulated only in P code with a frequency of 1227.60 MHz.

There is also the navigation data code (D code) with a frequency of 50 Hz with a period of 12.5 min that contains the Ephemeris parameters, needed to compute the satellite coordinates with enough accuracy, the Time parameters and Clock Corrections, to compute satellite clock offsets and time conversions, the Service Parameters with satellite health information (used to identify the navigation data set), Ionospheric parameters model needed for single frequency receivers, and the Almanacs, allowing the computation of the position of ”all satellites in the constellation”, with a reduced accuracy (1 - 2 km of 1-sigma error), which is needed for the

acquisition of the signal by the receiver. The ephemeris and clocks parameters are usually updated every two hours, while the almanac is updated at least every six days.

Range measurements from GNSS constellations are based on the detection of the phase of transmitted electromagnetic signals. The physical observable is the difference between the reference phase of the receiver at the time of signal reception.

The observables are defined in terms of clock differences since the reference phase at the receiver is derived from the receiver clock and the reference phase at the transmitter is derived from the space vehicle clock. For both carrier phase and pseudo range the computed observable is given by the theoretical difference between the space vehicle and receiver clocks plus a bias term. The clock difference is accumulated as the sum of five components: i) the difference between receiver clock time and proper time at the receiver; ii) the difference between proper time and coordinate time at the receiver; iii) the difference between the coordinate time of signal emission and the coordinate time of signal reception; iv) the difference between coordinate time and proper time at the transmitter spacecraft; v) the difference between proper time at the transmitter and transmitter spacecraft clock time.

These terms are readily interpreted. The first term is referred to as a receiver clock error and the fifth term is referred to as a transmitter clock error. The second and fourth terms are general relativistic time transformations. The third term is the solution to the light time equation connecting the events of signal emission and signal reception. Of these five contributions the third term is normally dominant. This term is also referred to as the geometric range between transmitter and receiver, whence the use of “range” in referring to GPS observables. Delays due to the troposphere and first order ionospheric effects will always be removed by performing measurements at two frequencies. The observables are assumed to have been calibrated to remove the effects of instrumental delays. A detailed model for instrumental phase delay is not provided, but a bias term is included in the definition of both data types.

This bias might account for:

1. an unknown integer number of cycles of phase,
2. an uncalibrated offset in the absolute phase of an oscillator,
3. uncalibrated delays within transmitter or receiver electronics, or an uncalibrated offset between the phase reference used for signal detection and the phase reference used for time-tag generation within a receiver.

The GNSS measurements can be essentially grouped into two categories obtaining two distinct levels of accuracy: pseudo ranges and carrier phase.

The pseudo ranges method consists to calculate distance measurements from the unknown ground point (Xp, Yp, Zp) to known position satellites (Xs, Ys, Zs). The propagation time of an impulse transmitted by the satellite to earth multiplied by the propagation speed of the electromagnetic wave provides the distance between satellite and receiver, called pseudo ranges because it is affected by numerous uncertainties and therefore inaccurate. Each measure generates an equation with the three unknowns coordinates a fourth unknown related to the time delay between the satellite clock and the receiver one: therefore four satellites are necessary to obtain four equations to determine the position of the point.

The main uncertainties that make this method inaccurate concern the orbital ephemeris of satellites and the speed of signal propagation in the atmosphere, whose behaviour is significantly different in the ionosphere and troposphere.

Observed pseudo-range is given by

$$R^O = c\,(\tilde{t}_3 - \tilde{t}_2)$$

where the times $\widetilde{t_3}$ and $\widetilde{t_2}$ are the actual times kept by the receiver and transmitter clocks, respectively. Correlation of the received pseudo-random code (PRN code for GPS) generated and transmitted by the space vehicle with a local copy of the code within the receiver allows for direct conversion between the detected received phase and clock readings.

Computed pseudo-range is given by

$$R^C = c\,(\tilde{t}_3 - \tilde{t}_2 + B_R) + \rho_{trop}$$

where now the times $\widetilde{t_3}$ and $\widetilde{t_2}$are the modelled times of, respectively, the receiver and transmitter clocks, B_R is the bias for pseudo-range measurements and ρ_{trop} is the delay due to troposphere.

The carrier phase method consists in comparing the carrier phase transmitted by the satellite with the signal of the same frequency generated by the receiver; the shifting between this two signals represent a part of the distance between the satellite and the receiver that is less than an integer number of N cycles (called "ambiguity"), which is unknown.

The measurement is performed following the satellite for some time without losing contact with it. In this case, an equation with 5 unknowns is generated (3 unknown for the 3D

coordinates, one for the time and one for the ambiguity): therefore, five satellites are needed to obtain five equations and determine the position of the point. Even here the same uncertainty factors regarding the measurement of pseudo-ranges remain, but it possible to reduce their effects thanks to differential techniques (single, double, triple differential equations), with which we use two observations of two receivers in two moments (epochs) with two satellites without losing contact with them.

Observed carrier phase is given by

$$P^O = -\frac{c}{w_n}(\Phi_{trn} - \Phi_{rec})$$

where Φ_{trn} is the received radio frequency (RF) phase of the space vehicle signal at time $\tilde{t}_3$, Φ_{rec} is the receiver reference phase at time $\tilde{t}_3$, and w_n is the nominal value for both the transmitted frequency of the space vehicle signal and the receiver mixing frequency.

The computed carrier phase is given by

$$P^C = c\left(\tilde{t}_3 - \tilde{t}_2 + B_{trn,geo}\right) + \frac{c}{w_n}\Delta\Phi_{geo} + \rho_{trop}$$

where $\widetilde{t_3}$ and $\widetilde{t_2}$are the modelled times of, respectively, the receiver and transmitter clocks, $B_{trn,geo}$ is carrier phase bias, $\Delta\Phi_{geo}$ is geometrical correction (misalignment between transmitter and receiver antennas due to the rotation independent of the change in geometrical range).

2.3 GPS Survey

Currently in the Etna area there are about 40 permanent GNSS stations, installed and managed by the Istituto Nazionale di Geofisica e Vulcanologia – Osservatorio Etneo (INGV-OE) and about 80 campaign that are occupied annually on average, and occasionally during seismic or volcanic crisis.

For this research project, permanent and campaign stations data from the INGV-OE GNSS network have been processed (Bonforte et al., 2016). The permanent stations processed are: EMFN, ERIP, EBAG, ELEO, EPOZ, ESPC, EC10, ELIN, ETEC, EBDA, ENIC, EPED, ELAC and EIIV (Figure 2. 1). In particular to define the velocity field of the southern eastern flank of Mount Etna, the stations ELAC, ENIC, EPED, ETEC, EBDA and EIIV have been used (Figure 2. 2).

The campaign stations are: ACID (1998-1999), CASL (1997-1998), EMSC (2007-2019), EPEL (2005-2019), ESGR (2012-2019), MDGR (1997-2019), MPL0 (1994-2007), PDAP (2001-2019), MTSE (1997-2005) (Figure 2. 3). Many campaign stations, over the years, have either been destroyed or have been replaced with permanent stations.

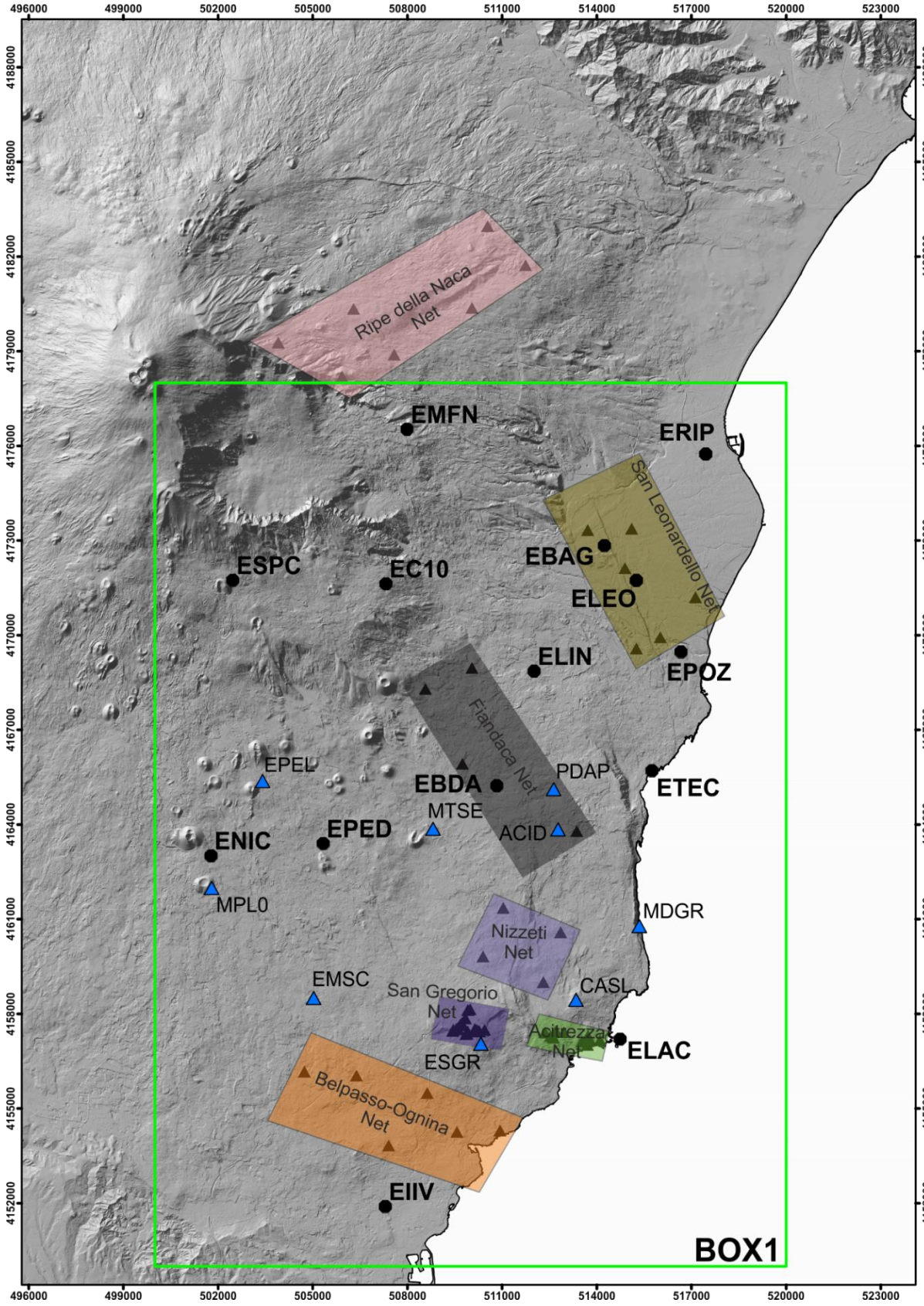

Figure 2. 1 - Map of the distribution of GNSS permanent (black circles) and campaign (blue triangles) stations belong to INGV-OE. The local networks, belonging to the UNICT-Net, are represented by coloured rectangle. The green rectangle represents the area where the velocity field was defined in the next chapter.

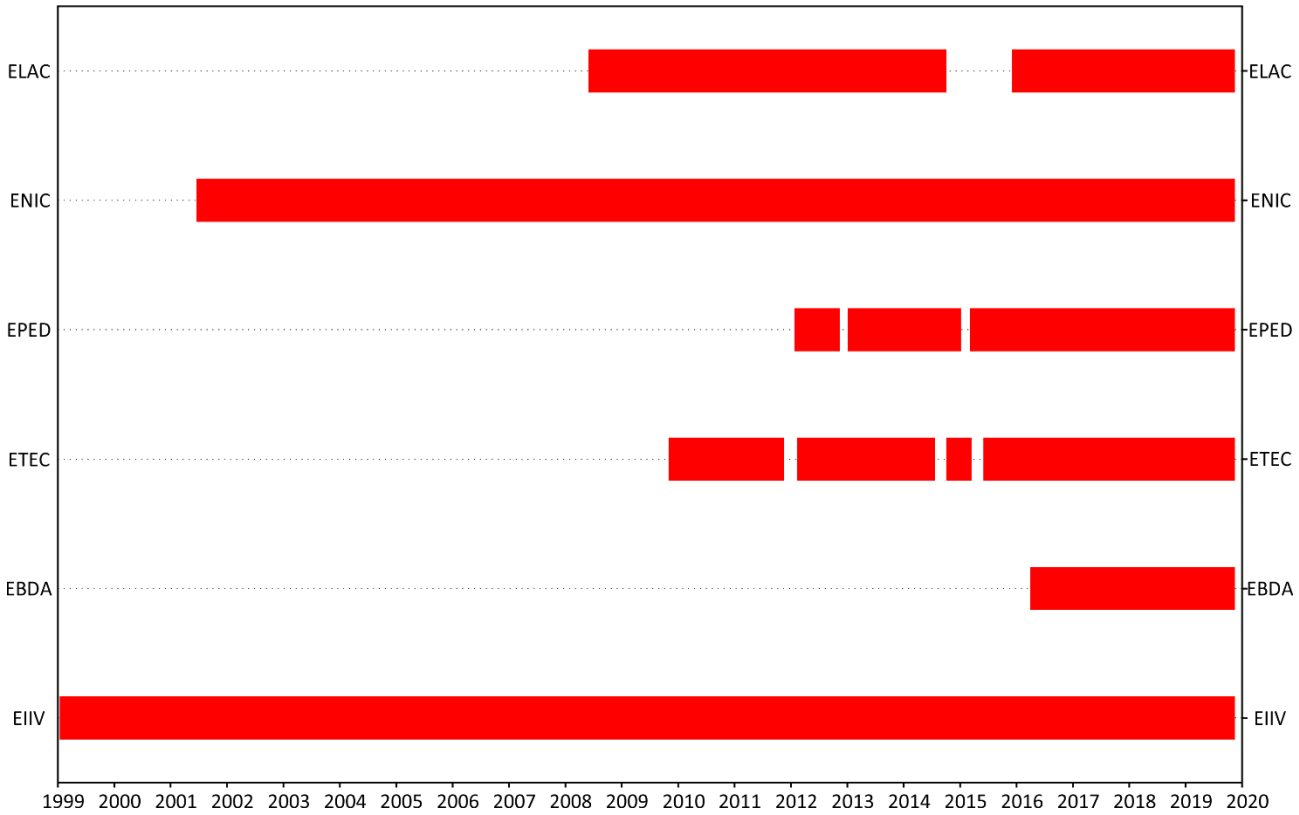

Figure 2. 2 - Occupation time of the GNSS permanent station belong to the INGV-OE, used to define the velocity field, from 1999-2020.

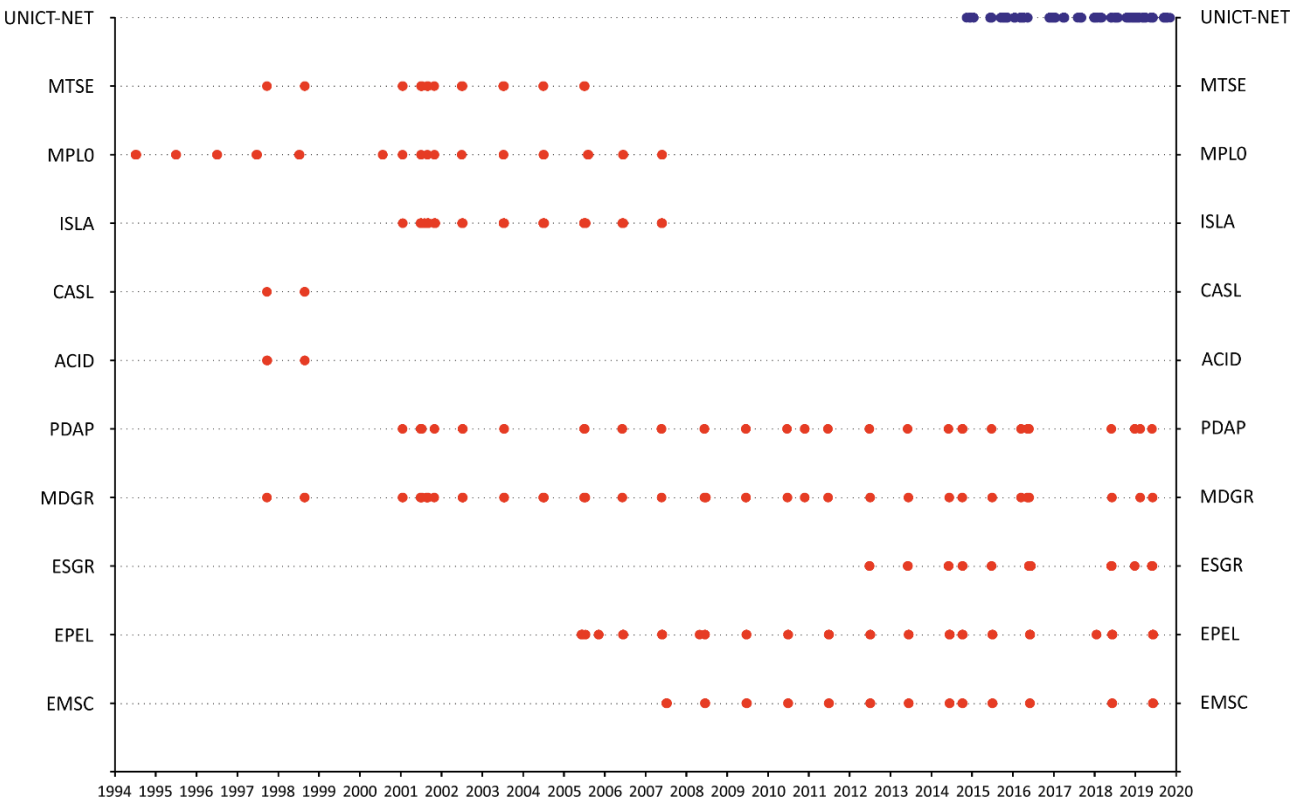

Figure 2. 3 - Occupations of the campaign stations of INGV-OE from 1994 until 2020 (red points) and the occupations of the all campaign stations belong to the UNICT-Net between 2014 and 2020.

2.3.1 UNICT-Net

Since 2014 the research group of GEODynamics & GEOMatic Laboratory of the University of Catania has started the design and implementation of a GNSS network, called UNICT-Net, with the aim of monitoring the deformation due to tectonic stress acting along the active faults.

Over the years, the UNICT-Net network has been continuously expanded. Currently there are sub-networks that extend in central Sicily to monitor the deformation of the mud volcano Santa Barbara in Caltanissetta, in the Umbro-Marchigiano Apennines (built after the seismic event of August 24, 2016) and along the eastern slope of Etna.

In this research project the GNSS stations located on the eastern slope of Etna have been realized, surveyed and processed because of the strong anthropization and the presence of numerous structures that form the south-eastern faults system.

The aim of the research group is to analyse the ground deformation in the fault area, for this reason the geometry of the various sub-nets follows the trend of the studied faults. In particular, the collation of benchmarks, along the active faults, is very useful to determine the speed of the footwall block and the hanging wall block, moreover considering the extension along the fault,

it is also possible determine the velocity differences along the same block and consequently the accelerations. In general the choice of the site on which to build the geodetic monument is made with care according to the following criteria that have already been defined in (De Guidi et al., 2017):

1. tectonic network of the area;
2. distribution of already existing GNSS stations both permanent and discrete;
3. lack of gravitation instabilities on the site.

In general, once that the site was chosen, fast building the GNSS monument (Figure 2. 4) on the UNICT-Net follows these steps:

1. stability and solidity of the location, normally it could be a rocky outcrop or a man-made monument with foundation;
2. implementation of the hole for housing the bushing and checks of its stability. It is realized through small-size battery powered equipment (Makita DHR243 hammer drill);
3. fixing and anchoring the knurled steel bushing (length 67 mm and diameter 20 mm); after the cementation to the artefact or to rocky outcrop, a male-male threaded bar is screwed in until the end of the stroke.

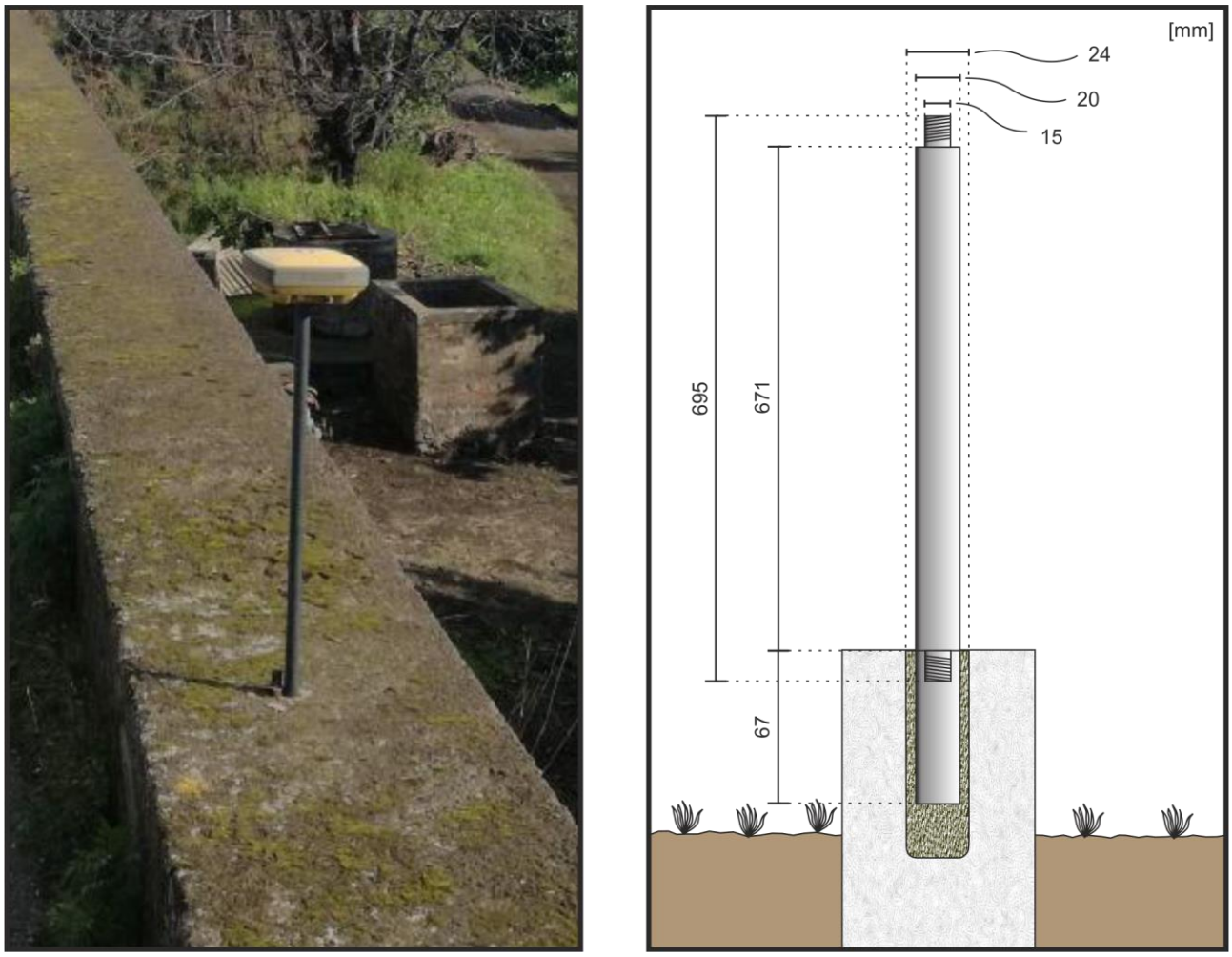

Figure 2. 4 – On the left, picture of a GNSS (Topcon Hiper SR) during an occupation. On the right sketch of the fast building self-centering benchmark.

For the early UNICT-Net sub networks, the monument was built differently from the general guide lines described in De Guidi et al., 2017. For the Acitrezza Net, the benchmarks consist of a concrete pillar monument anchored to exposed bedrocks or to large mass of concrete set within a pit in soil. Concrete pillars have a 20 x 20 cm section and variable height (usually 150 cm) (Figure 2. 5). A stainless-steel rod with external thread is drowned to the top of the pillar (De Guidi et al., 2018).

In the San Gregorio Net, the benchmarks, located on paved roads or along sidewalks, are built with specifically design, by a steel pillar drowned in the concrete at depth of 40 cm within a 25 x 25 cm trench and covered with a cast iron cover (Figure 2. 5). The benchmarks on the outcropping rocks are built with a 25 cm rod embedded in a vertically drilled hole (100 mm x 35 mm). The rods, with external thread at the outer end, are anchored with quick set concrete (De Guidi et al., 2018).

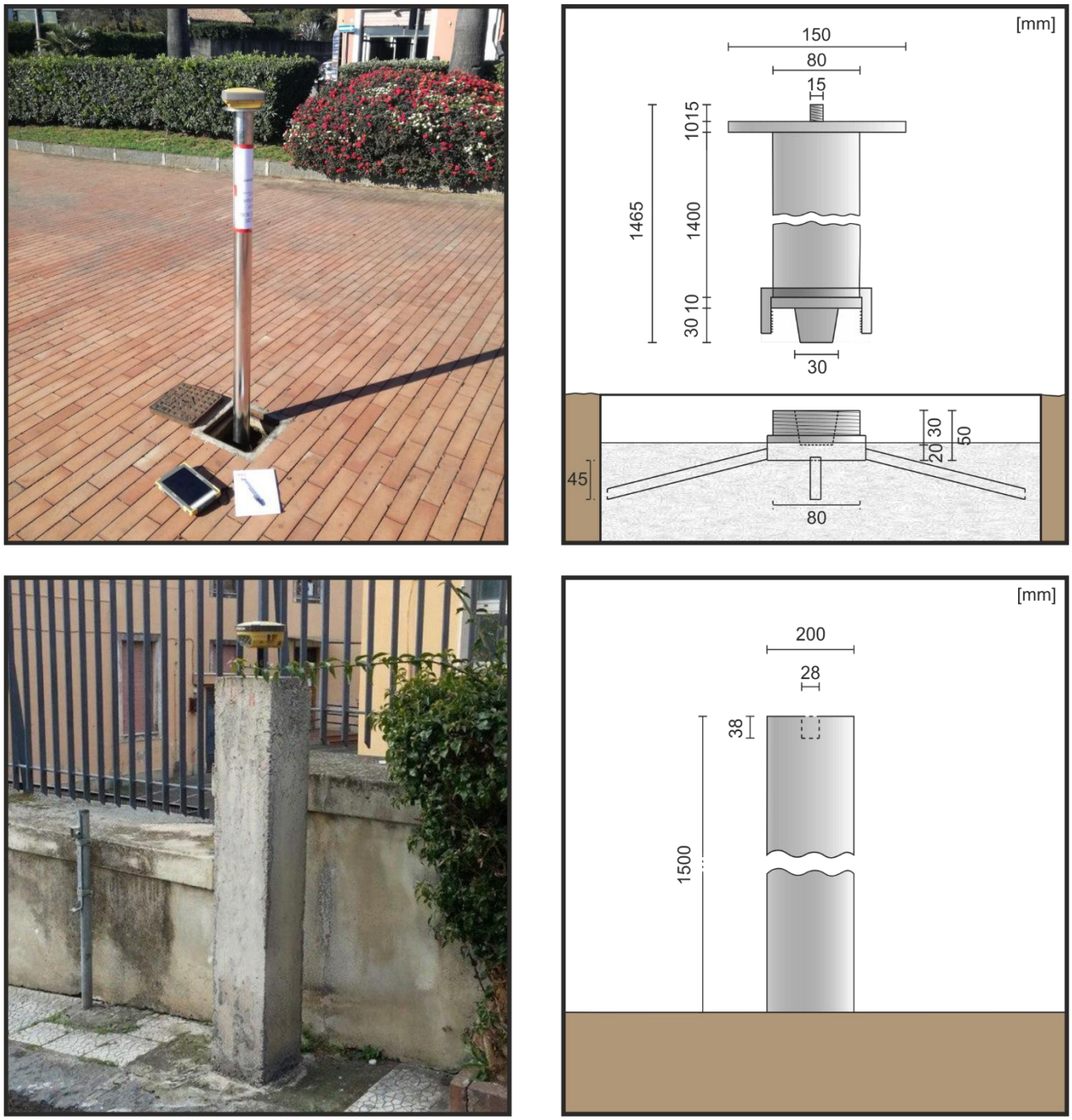

Figure 2. 5 – On the top, picture of a GNSS (Topcon Hiper SR) during an occupation on a benchmark belong to the San Gregorio Net and the scheme of the self-centering benchmark used on the San Gregorio Net. On the bottom, picture of a GNSS (Topcon Hiper V) during a measurement on a benchmark belong to the Acitrezza Net and the scheme of the pillar built on the Acitrezza Net.

The geodetic monitoring, started in 2014 and is still going on now, initially two nets were built in the town of San Gregorio and Acitrezza (San Gregorio Net and Acitrezza Net, Figure 2. 6) (De Guidi et al., 2018) after the network was expanded to include the area of the municipality of

Giarre in the summer of 2017 (San Leonardello Net, Figure 2. 6), in the autumn of 2017 the network along the Ripe della Naca (Ripe della Naca Net, Figure 2. 6) was built, in September/October 2018 two networks were created: the first one along the Nizzeti Fault (Nizzeti Net, Figure 2. 6) and the second one along the Belpasso-Ognina Lineaments (Belpasso-Ognina Net, Figure 2. 6) and finally in December 2018, following the earthquake of Fleri on December 26, 2018, a small network was built along the Fiandaca Fault to monitor the post-seismic deformation of this fault (Fiandaca Net, Figure 2. 6).

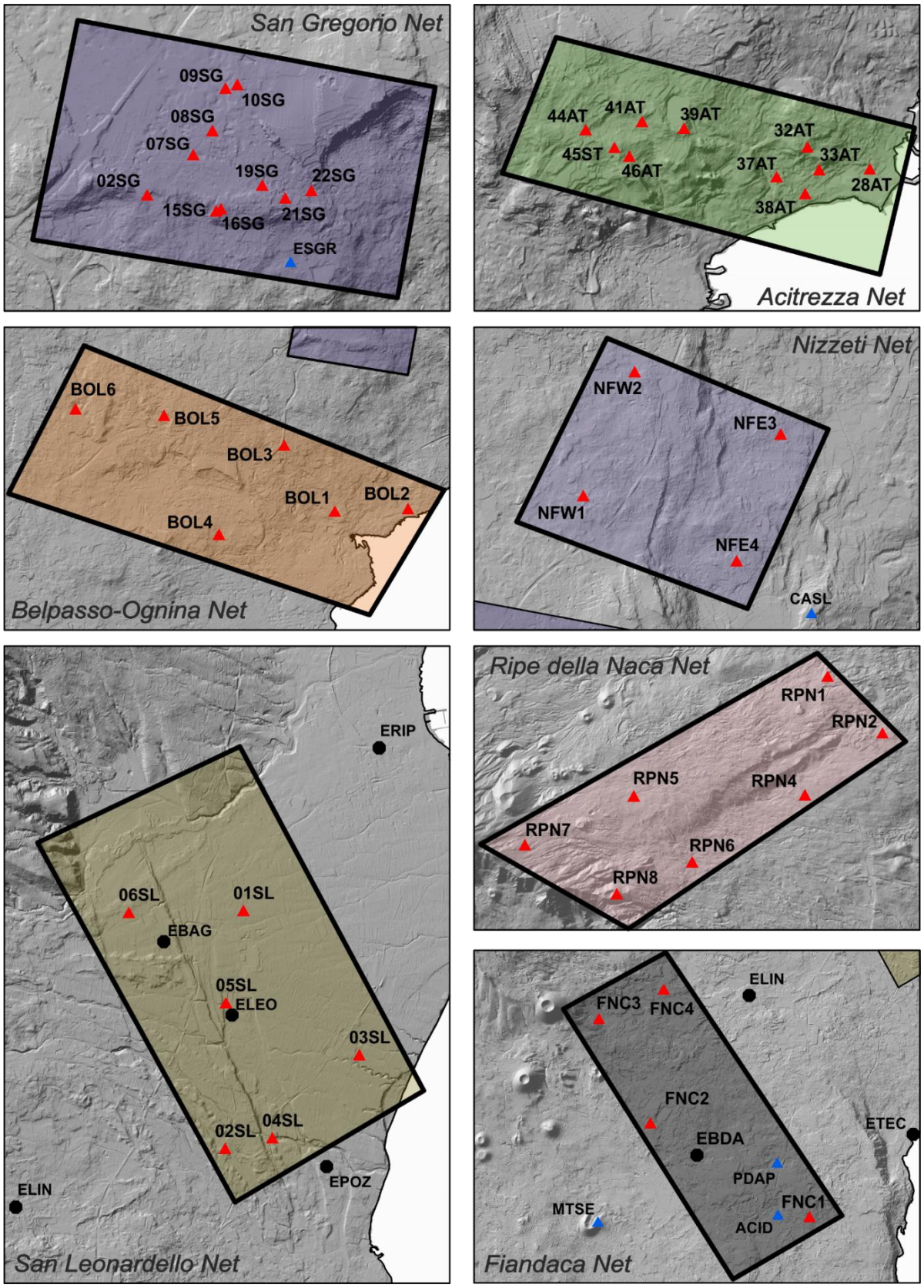

Figure 2. 6 – Maps of the various UNICT-Nets built on Mount Etna from 2014. The permanent (black circle) and the discrete (blue triangles) GNSS stations of INGV-OE are shown.

Actually, the UNICT-Net counts 45 benchmarks, that are surveyed periodically (Figure 2. 6; Figure 2. 7), every six months on average, to adequately detect patterns and rate variations of the ground deformation. However after a seismic event on the volcano, almost all the benchmark are surveyed again. Unfortunately, depending on the weather conditions and/or human resources, some benchmarks have been occupied less time compare to the others.

Each occupation lasted between 5 and 12 hours, manly depending on the logistic conditions; the employed instruments are two dual-frequency GNSS TOPCON receiver with integrated antenna: two receivers HiPer V and three receiver HiPer SR.

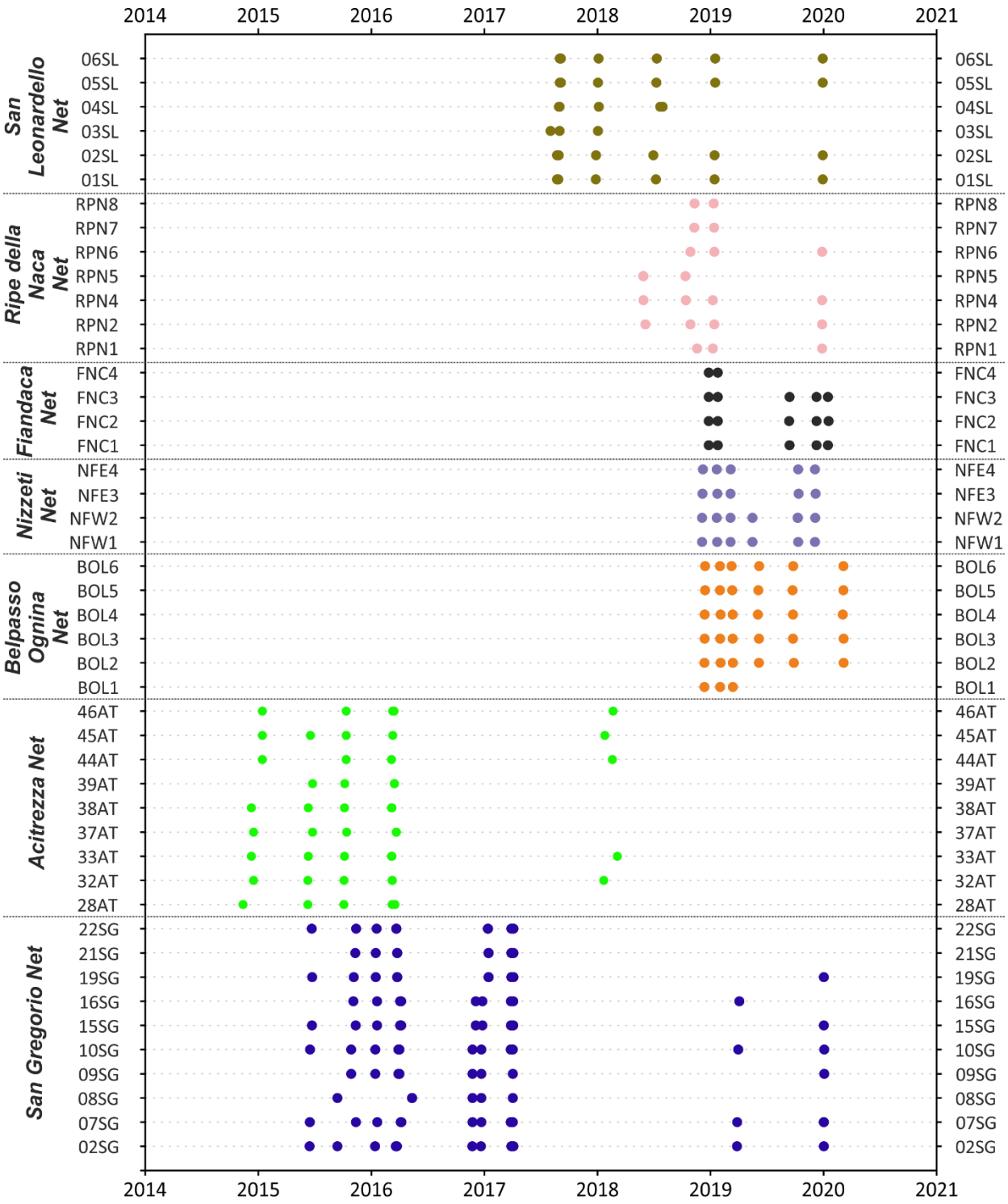

Figure 2. 7 – Occupations of the benchmarks belong to the UNICT-Net from 2014 until 2021.

2.4 GipsyX Processing

The pre-processing of the data consists of converting the raw files into RINEX (Receiver INdipendent Exchange format) using Teqc software (Estey and Meertens, 1999). The Rinex files have been realized considering only the satellites belonging to the GPS system, thus excluding

the satellites belonging to the GLONASS system and moreover the observable L1, L2, C1 and P2 have been chosen and decimated at 30 seconds. After the conversion phase, a pre-processing of all the data was carried out for a double-check of the RINEX data, in particular to verify that there were no errors on the instrument height, station names etc.

Data post-processing was carried out by GipsyX-1.3 Release (https://gipsy-oasis.jpl.nasa.gov) development at the Jet Propulsion Laboratory (JPL), California institute of Technology (Bertiger et al., 2020). GipsyX/RTGx is the JPL's next generation software package for positioning, navigation, timing and Earth science using three geodetic techniques: Global Navigation Satellite System (GNSS), Satellite Laser Ranging (SLR) and Doppler Orbitography and Radiopositioning Integrated by Satellite (DORIS); with Very Long Baseline Interferometry (VLBI) under development. The software facilities combined estimation of geodetic and geophysical parameters using a Kalman filter approach on real or simulated data in both post-processing and in real-time. The estimated parameters include station coordinates and velocities, satellite orbits and clocks, Earth orientation, ionospheric and tropospheric delays. The software is also capable of full realization of a dynamic terrestrial reference through analysis and combination of time series of ground station coordinates (Bertiger et al., 2020).

Gipsy's core computational engines were written in Fortran with glue and automation in C-Shell, Bourne-Shell and Perl. Gipsy is used to process data came from full GNSS system (GPS, GLONASS, BeiDou, Galileo and QZSS), SLR (Satellite Laser Ranging), DORIS (Doppler orbit determination and Radiopositioning Integrated by Satellite) and VLBI (Very Long Baseline Interferometry).

Precise orbits and clock information referred to the satellite to the satellite coordinates and clock correction information were used. Absolute IGS antenna phase center and atmospheric zenith delay models were used, and Global Mapping Functions. The absolute coordinate (ITRF2014) were used to elaborate time series for each station.

GipsyX is organized according to various modules that perform different operations.

Several of Gipsy executables are configured by a single interface called tree. A tree is a text file with a hierarchical structure identified using Python-like indentations that consist of root (the highest level), branches, and leaves (the lowest level). The input tree is divided in 4 main root: i) Self, ii) Global, iii) Station info and iv) Satellite info. Here I show an example of trees used to process a rinex data of station 02SG.

```
Self
  Metadata On
  File debug.tree
```

```
GEOPFILE == GNSSinitValues/GNSS.eo
GNSSORB_POS  == GNSSinitValues/GNSS.pos
GNSS_WLPB    == GNSSinitValues/GNSS.wlpb
GNSS_ANT_OFF_PCM == GNSSinitValues/GNSS.pcm
GNSSXYZ_FILE==/home/francesco/goavar/etc/antennaCalsGNSS/igs14_1958.xyz
GNSSLIST     == gnssList.txt
XYZFILE_STATIONS == allStations.xyz
STATIONLIST == stations.txt
GLOBAL_EPOCH == 495484680            # 2015-09-14 06:38:00.000000
FILTER_STOP  == 495500850            # 2015-09-14 11:07:30.000000
DATARECORD_FILE == dataRecordFile.gz
STA_DB == /home/francesco/Scrivania/etnaest/02sg/2015/rinexStaDb
OCEANLOAD == Off
StationCovOnOff == Off

SMOOTHPOS == smooth0_0.pos
SMOOTHTDP == smooth0_0.tdp
TDP_INPUT == GNSSinitValues/GNSS.tdp

GLOBAL_DATA_RATE == 300
```

The previous variables of self root are defined by gd2e (Geodetic Data to Estimate) configuration. The first two lines are referred to the satellite, GEOP (Earth Orientation Parameter Table) file consists on the satellite coordinate transformation from the inertial reference frame to ECEF (Earth-Fixed-Earth-Centered) reference frame. This transformation depends by the complex Earth rotation in an inertial reference system and it follows IERS (International Earth Rotation and Reference) convention. The second GNSSORB_POS file consists in the position of satellite. Each file is processed by OI (Orbit Integrator) module of GipsyX. GNSS_WLBD file has the information about wide lane and phase bias information from network. It is used to compute ambiguity when it is used only one receiver. GNSS_ANT_OFF_PCM is a piecewise constant model parameter file, it is meant to hold information related to ground or satellite platforms which change in a piecewise constant function. GNSSXYZ_FILE is the phase antenna correction, in this case is referenced to the 1958 GPS week (igs14_1958.xyz). This file gives the change in phase center as a function of azimuth (clockwise sense angle respect the north and) and elevation (the angle between the receiver and the local horizon). GnssList is the list of satellite seen by the receiver and their block and model. XYZFILE_STATIONS is the phase antenna correction used for the processed station. STATIONLIST is the list of the processed station. GLOBALEPOCH and FILTERSTOP are the first and the last observation in seconds of the antenna. DATARECORD_FILE is a file created automatically and contains the information of each signal path through the space. STA_DB is the Station Database file, it is ASCII text file containing various information about stations like position, antenna and receiver configuration. OCEANLOAD and StationCovOnOff are two option that the users can change. SMOOTHPOS is the solution file for the satellites position.

SMOOTHTDP is the solution file, normally after a precise number of interaction, GipsyX creates a SmooFinal.tdp (the extension .tdp means Time Dependent Parameter). It is an ASCII text file that contains the solutions and parameters used for the calculation ordered by time. GLOBAL_DATA_RATE defines the interval time for the tdp file, in this case is set at 300 seconds.

```
Global
   Logging
     Alert   cerr
     Warn    cout
     Event   cout
```

This part is dedicated to the errors, the software has to print a list of error and a message.

```
     Filter
       Start $GLOBAL_EPOCH
       Stop  $FILTER_STOP
```

Start and stop indicated the begging and the end time of the filter (if there are epoch before or after the filter will not consider the data

```
     MeasGather
       DecimateSmoothInterval $GLOBAL_DATA_RATE
       HonorEditorFlags On

       Type DATARECORD
       FileName $DATARECORD_FILE
```

Here there are the parameters, like output name and decimal rate in second, for GDE (GNSS Data Editor) to create the data record file. The output will be marked as good to be used in the range smoothing process.

```
     DataTypes
       PostSmoothEditGlobals
         MaxIteration 5

       IonoFreeL_1P_2P
         DataLinkSpec_LC_GPS
           PostSmoothEdit 2e5 2e4 0.125 0.1 0.05 .025
           ElDepWeight SqrtSin
           #ElMin 7
           SignalPath
             Platforms .* GPS.*
           DataBias
             StochasticAdj 3.0e8 3.0e8 DATADRIVEN WHITENOISE
               UseItOrLoseItInterval 3600

       IonoFreeC_1P_2P
         DataLinkSpec_PC_GPS
           SignalPath
```

```
    Platforms .* GPS.*
  PostSmoothEdit 2e5 2e4 12.5 10 5 2.5
  ElDepWeight SqrtSin
  #ElMin 7
```

This part is dedicated to the data type specification for phase and range. In this case it is set to process ionospheric free phase carrier (IonoFreeL) and pseudo range (IonoFreeC) for the GPS platform.

```
FilterConfig
  Parallel
    NumThreads 1
  SmootherFormalError
   SigmaRegex ^\.
  SmootherCovariance
    Station $StationCovOnOff
    CalculationMethod InverseSriRows
  SmootherPostProcess
    Smoother On
    TdpFile $SMOOTHTDP
    CovarianceFilename smoothFinal.cov
       TerminalEpochOnly On
  FilterParametersAddRemove
    LinkBias Off
```

FilterConfig consists of the configuration parameter of SRIF (Square Root Information Filter), it calculates the sigmas corresponding to parameter name that match the regex (Regular Expression) and to calculates the covariance matrix by the inverse SRI matrix. Finally, the SRIF does smoothing as a post processing step after RTGX finished to process all data and creates the final output file: the covariance matrix file and the time depending file.

```
EarthOrientation
  GeopTable $GEOPFILE
```

The geopfile contains a time series of TAI-UTC (International Atomic Time – Coordinated Universal Time), pole tidal model epoch for the Earth Orientation parameter partials.

```
Input
  TimeDepParms
    NameFilter
      Satellite\.[A-Z]\w*.*\.Clk\.Bias
        Degree 0
        Strict On
          MaxDx 1.0e-6
        MaxFormalError 0.12
      Station\..*\.Trop.*
    File
      Path $TDP_INPUT
      BufferTime 3600
      MaxExtrap 0
```

This is the input configuration section. There are indicated the parameters that the filter has to read according to the regular expressions and formal errors cut off for input tdp data. It is indicated the path for the input file and some parameters for the buffer memory.

```
Output
  Residual
    Prefit
      File prefitResiduals.out
    Postfit
      File postfitResiduals.out
  TimeDepParms
    NameFilter ^\.
    EstimatedOnly Off
    File filter.tdp
```

This is the output configuration section that consists on the prefit and/or postfit residual to file. The output parameters are defined by regular expression (in this case: ^\. indicates that the filter will use all the parameter that begin with a point). Finally the filter will write all the estimated and not in the output file.

```
AmbRes On

    OutputConstraintsFile constraints.txt

    StatsFile ambres.stats

    Mode inSmoother

    SettingsForGround
        SmootherIterations 1
        MinOverlap 3600.0

        WidelaneMaxDistanceToNearestInt 0.3
        WidelaneInflation 0.1
        BackgroundLevel  0.5
        WidelaneConfidence  0.750
        WidelaneMaxSigma 1.0

        NarrowlaneMaxDistanceToNearestInt 0.2
        NarrowlaneInflation 1.5
        NarrowlaneConfidence 0.99
        NarrowlaneMaxSigma 0.1
        InputWlpb
            File $GNSS_WLPB
        Priority 0

        GlobalNarrowLaneSigmaFactor 6.0
        UseNLOverlapSigmas
        ComputeAllNLSigmas
```

Configuration option for the Ambiguity Resolution section, in this case the operation mode for the ambiguity resolution is set insmoother mode. Insmoother mode the process determinate which double differences have to be constrained is done during the smoother. The result is a

file with the constrains that be applied. In the second part of the ambiguity resolution section, there are the widelane and narrowlane double difference are configurated, even according to the WLPB file (Widelane Phase Bias information file for a network).

```
# Station info:
# Solve for constant position
GRN_STATION_CLK_WHITE ==
    State
      Pos
        ConstantAdj 10.0
    Clk
      Model On
      Bias  0.0
        StochasticAdj 3.0e8 $GLOBAL_DATA_RATE WHITENOISE
    Trop
      Model   On
      Mapping GMF
      WetZ    0.1
        StochasticAdj 0.5 5e-5 $GLOBAL_DATA_RATE RANDOMWALK
      GradEast 0.0
        StochasticAdj 1.0 5e-6 $GLOBAL_DATA_RATE RANDOMWALK
      GradNorth 0.0
        StochasticAdj 1.0 5e-6 $GLOBAL_DATA_RATE RANDOMWALK
    Tides
      All On
      OceanLoad $OCEANLOAD
      OceanLoadFile
$GOA_VAR/sta_info/ocnld_coeff_cm_got48ac_wtpxo8ofunc_qlflinn
    Antennas
      Antenna1
        XyzFile $XYZFILE_STATIONS

Station `cat $STATIONLIST`
Station `staDb2TreeIn.py -s $STATIONLIST -y2kSecs $GLOBAL_EPOCH -d
$STA_DB`
```

Station info is the third branch off the tree; in the sub-branch there is the configuration for the station position in particular the priori sigma for the coordinates (State). In the clock sub-branch, modelling and computation of partial is on to estimate white noise clock according to the time rate defined in global data rate. In trop sub-branch, the tropospheric delay modelling uses the Global Mapping Function (GMF) (Boehm et al., 2006) to define the atmospheric refractivity. In tides it is sett the ocean tide model. In antenna, the python executable StaDb2TreeIn.py updates the tree using the station database.

```
# Satellite info
GPS_Common_Settings ==
    State
      SatelliteTimeSeries
        Strict On # Do not interpolate over unequal time steps in
input orbit
```

```
                  # Use extreme care if you change this especially if
processing data
                  # that span multiple 30-hour (JPL products) or 24-
hour (IGS products)
        BufferTime 10800
        InterpOrder 11
        ShadowFinder On
        PosGOAQuaternions Off
        PosGOAFile $GNSSORB_POS
    Clk
      Model On
      Bias  0.0
    Antennas
      Antenna1
        XyzFile $GNSSXYZ_FILE

GPS_BlockI_Model ==
      AttitudeModel gpsBlockI

GPS_BlockII_Model ==
      AttitudeModel gpsBlockII

GPS_BlockIIA_Model ==
      AttitudeModel gpsBlockII

GPS_BlockIIR_Model ==
      AttitudeModel gpsBlockIIR

GPS_BlockIIF_Model ==
      AttitudeModel gpsBlockIIF

GPS_BlockIII_Model ==
      AttitudeModel gpsBlockIIF

BDS_IGSO_MEO ==  # IGSO/MEO
    State
      SatelliteTimeSeries
        Strict On # Do not interpolate over unequal time steps in
input orbit
        BufferTime 10800
        InterpOrder 11
        ShadowFinder On
        PosGOAQuaternions Off
        PosGOAFile $GNSSORB_POS
    Clk
      Model On
      Bias  0.0
    Antennas
      Antenna1
        XyzFile $GNSSXYZ_FILE
    Models
      AttitudeModel yawNormal

BDS_GEO ==  # GEO
    State
      SatelliteTimeSeries
        Strict On # Do not interpolate over unequal time steps in
input orbit
        BufferTime 10800
        InterpOrder 11
        ShadowFinder On
        PosGOAQuaternions Off
```

```
        PosGOAFile $GNSSORB_POS
    Clk
      Model On
      Bias  0.0
    Antennas # Currently no cal for BDS, but expected in the future
      Antenna1
        XyzFile $GNSSXYZ_FILE
    Models
      AttitudeModel orbitNormal

GLONASS_Common_Settings ==
    State
      SatelliteTimeSeries
        Strict On # Do not interpolate over unequal time steps in
input orbit
        BufferTime 10800
        InterpOrder 11
        ShadowFinder On
        PosGOAQuaternions Off
        PosGOAFile $GNSSORB_POS
    Clk
      Model On
      Bias  0.0
    Antennas
      Antenna1
        XyzFile $GNSSXYZ_FILE

GLO_M_Model ==
      AttitudeModel glonassM

GLO_K1_Model ==
      AttitudeModel glonassM

GALILEO_Common_Settings ==
    State
      SatelliteTimeSeries
        Strict On # Do not interpolate over unequal time steps in
input orbit
        BufferTime 10800
        InterpOrder 11
        ShadowFinder On
        PosGOAQuaternions Off
        PosGOAFile $GNSSORB_POS
    Clk
      Model On
      Bias  0.0
    Antennas
      Antenna1
        XyzFile $GNSSXYZ_FILE

GAL_IOV_Model ==
      AttitudeModel galileoIOV

GAL_FOC_Model ==
      AttitudeModel galileoIOV # needs revising

QZSS_Common_Settings ==
    State
      SatelliteTimeSeries
        Strict On # Do not interpolate over unequal time steps in
input orbit
        BufferTime 10800
```

```
          InterpOrder 11
          ShadowFinder On
          PosGOAQuaternions Off
          PosGOAFile $GNSSORB_POS
      Clk
        Model On
        Bias  0.0
      Antennas
        Antenna1
          XyzFile $GNSSXYZ_FILE

QZSS_001_IGSO_Model ==
      AttitudeModel yawNormal
        Cutover 20.0

QZSS_002_IGSO_Model ==
      AttitudeModel gpsBlockIIR # "yaw steering"

QZSS_003_GEO_Model ==
      AttitudeModel orbitNormal

QZSS_004_IGSO_Model ==
      AttitudeModel gpsBlockIIR # "yaw steering"

Satellite `cat $GNSSLIST`

Satellite `pcm.py -file $GNSS_ANT_OFF_PCM -epoch $GLOBAL_EPOCH -sat
$GNSSLIST -param Antenna1`

  Common
    YawBiasFile $GOA_VAR/etc/yawBiasTable.pcm
    YawRateFile $GOA_VAR/etc/nominalYawRates.pcm
      TimeDepParms .Global.Input.TimeDepParms
          BufferTime 108000
          MaxExtrap  108000
```

The satellite info part contains the information for each type of satellites like orbits attitude models (solar radiation model). They are divided for satellite system (GPS, BEIDU, GLONASS, GALILEO and QZSS), and for each block.

After this phase, the next step was to compute GPS time series thought GipsyX. To obtain time series the first step is to create the .gdcov file from the terminal epoch file covariance file and tdp file for each doy. The gdcov file contains the parameter estimated for the single measurement, normally contains the tree coordinate (X, Y, Z) with time and their sigma. After all the single gdcov file must be merged in a single gdcat file by the executable netSplit.py that converts from one gdcov per day to one gdcat file per site.

```
netSpit.py -i *.gdcov
```

where the argument -i indicates the input file for netSpit.py.

Once the gdcat file has been created, the next step is to fit the time series with the executable staFit.py that takes the data in a gdcat file and turns it into a solution in a gdcov file that contains position, velocity and correlations.

```
staFit.py -i 02SG.gdcat -o 02SG.gdcov -v 2015-06-16
```

where the arguments -i indicates the gdcat to read, -o indicates the gdcov output name and -v indicates the epoch of the position and velocity solution (normally the first measurement for the station).
Next step is to compute the time series by the command staSeries.py.

```
staSeries.py -r 02SG.gdcov -i 02SG.gdcat
```

where the argument -r is referred to the output gdcov solution and -i to the input gdcat file.
the staSeries.py command produces time series, model, residual and a summary file for a single station. Once the time series was computed, it is important to check it to verify that there are outliers in the components, break or seasonal variation. In this case GipsyX gives the possibly to detect breaks by the command staBreaks.py set with a precise value for the Ftest, and to detect outliers by the command staEdit.py set with a maximum value for sigma and a maximum value for outliers formal error.

2.5 Geodetic Reference Frame on Mount Etna

On Mount Etna, the use of a consistent and stable reference frame to correctly isolate ground deformation has become critically important since the first GPS measurements were carried out on the volcano edifice and surrounding areas. To isolate volcano deformation, the researchers have referred GNSS measurements to: i) an external network located outside the volcanic area (Palano et al., 2008 and reference therein); ii) a specific station located inside the volcanic area (Aloisi et al., 2003; Bonaccorso et al., 2002; Murray, 1994; Patanè et al., 2005); iii) NOT0/NOT1 GNSS station located about 90 km south of Mount Etna (Houlié et al., 2006).
Considering that Mount Etna is located close to the Eurasia-Nubia plate boundary, GNSS sites located in Sicily show a residual velocity considering both Eurasian reference frame and Nubian reference frame. In the Eurasian reference frame the GNSS sites have an average velocity of about 5 mm/yr and 2 ,mm/yr in a Nubian reference frame (Palano et al., 2010), it is clear that

both the Eurasia and Nubia reference frame are not suited to correctly isolate the volcanic ground deformation from the background geodynamic pattern.

Palano et al. (2010) defined a geodetic reference frame for the GNSS network of Mount Etna, named Etn@ref. This geodetic reference frame was realized to isolate volcanic ground deformation from the background geodynamic pattern. They estimated the Euler vector parameters (latitude and longitude of the pole, rotation rate) for the rigid block. Palano et al. (2010) used for their computation 13 fiducial benchmarks located outside the volcanic area. These benchmarks are prevalently located on eastern Sicily, two benchmarks are located on Malta and Lampedusa islands and three benchmarks are located on central and western Sicily (Figure 2. 8).

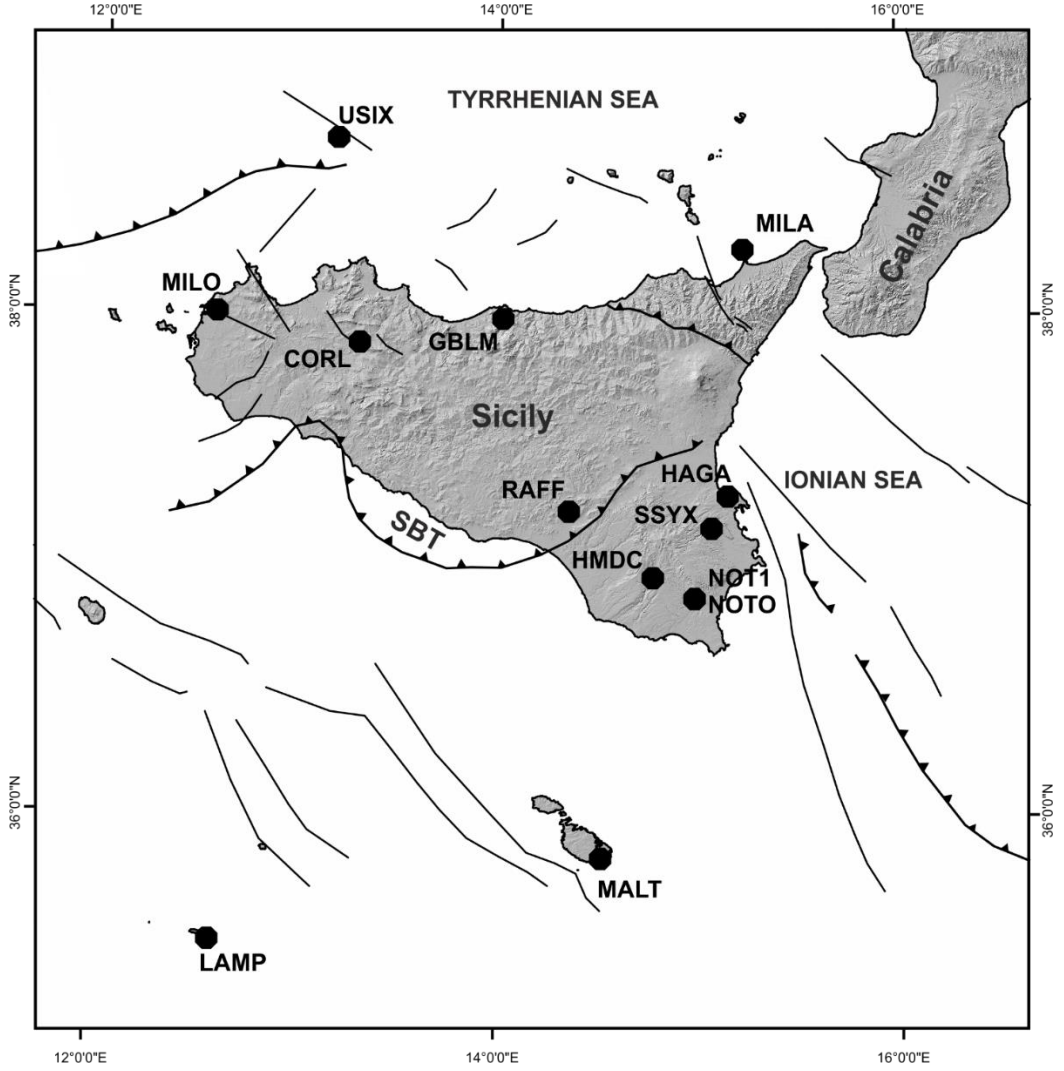

Figure 2. 8 – Location of the 13 fiducial sites used to estimate the Eurel pole in Palano et al. (2010).

CHAPTER 3

TIME SERIES AND VELOCITY FIELD

3.1 Introduction

The geodetic data are analyzed through time series. A time series is a series of coordinates of a permanent or campaign GNSS station, sorted as function of time, normally from a time (T_0). It can be represented in a graph. Each dot in the graph of a time series represents the position of a GNSS site in the east, north and vertical axis. Usually, there is one dot for each day or for the campaign stations there is a dot for each survey. The slope of the dots shows the direction of the GNSS site's movement. If a line has a slope of zero, the site is not moving in that dimension. On the North plot, north is positive and south is negative. If the slope is positive, the site is moving northward. If the slope is negative, the site is moving southward. In the time series, the starting number on the plot does not matter. We are not actually interested in where the site is, we are interested in how the site moves. We are always interested in the difference between one position and another, not the number associated with the position. It is important to know the reference frame of the GNSS data. In this thesis, the coordinates are given in the ITRF2014 reference frame (Altamimi et al., 2016)

From the time series it is possible to obtain the velocity vectors. The velocity vector shows the direction and velocity of the motion of a GNSS site during a given period of time. The magnitude of the velocity vector is the rate of motion, usually measured in millimetres per year; a vector is described in in three dimensions: east-west, north-south and up-down, however on maps the GNSS velocity vector shows only two of these dimensions: north-south and east-west which are shown with one arrow. On the maps, the GNSS site is at the tail of the vector and the site is moving in the direction of the arrow, longer arrow indicates the faster motion (UNAVCO and GPS Reflections Research Group, 2020).

3.2 Time Series

After GNSS data processing, the GipsyX outcomes are four files for each station:

1. Series file
2. Model file

3. Redisual file
4. Sum file.

The station series file is the observed east, north and up position of the station referred to the reference epoch used like input. It is composed by 17 columns, each column represents a calculated value, from left to right, of: 1) decimal year; 2) east displacement in meters; 3) north displacement in meters; 4) up displacement in meters; 5) sigma east in meters; 6) sigma north in meters; 7) sigma up in meters; 8) correlation east-north; 9) correlation east-up; 10) correlation north-up; 11) julian seconds past January 1, 2000 11:59:47 UTC; 12) year; 13) month; 14) day; 15) hour; 16) minute; 17) seconds.

Here the station series file for the 02SG is shown:

```
2015.45483497 0.001171 -0.009441 0.019714 0.003501 0.006057 0.006498 0.318135 -
0.715629 -0.265247 487717500.00 2015 6 16 9 5 0
2015.70121777 0.004084 0.000457 0.025393 0.003424 0.006029 0.006472 0.328332 -
0.751572 -0.267417 495492750.00 2015 9 14 8 52 30
2016.03533063 0.017175 0.003532 0.006648 0.003296 0.005263 0.005712 0.295807 -
0.614163 -0.308784 506036550.00 2016 1 14 9 42 30
2016.21889022 0.024636 0.006332 -0.009762 0.002531 0.004864 0.005133 0.343886 -
0.859439 -0.202989 511829250.00 2016 3 21 10 47 30
2016.22692315 0.023153 0.001943 -0.006037 0.003027 0.005520 0.005858 0.326459 -
0.774028 -0.224124 512082750.00 2016 3 24 9 12 30
2016.89489695 0.040627 0.011839 -0.016197 0.002720 0.004691 0.005000 0.305297 -
0.684570 -0.240641 533162400.00 2016 11 23 8 40 0
2016.97155677 0.044631 0.008797 -0.020898 0.002766 0.004675 0.005049 0.317055 -
0.696641 -0.289935 535581600.00 2016 12 21 8 40 0
2017.24045555 0.053703 0.010614 -0.007169 0.003357 0.005728 0.006033 0.279801 -
0.620784 -0.195115 544067400.00 2017 3 29 13 50 0
2017.25960624 0.058768 0.006984 -0.002347 0.003354 0.005588 0.005993 0.297977 -
0.645370 -0.263983 544671750.00 2017 4 5 13 42 30
2019.23613012 0.103835 0.021310 -0.014117 0.002953 0.005213 0.005545 0.313571 -
0.719815 -0.232392 607046100.00 2019 3 28 11 55 0
2020.00582744 0.139991 0.018900 0.005758 0.002696 0.004650 0.005013 0.325032 -
0.728813 -0.283899 631335900.00 2020 1 3 15 5 0
```

The same format is also used for output model and residual file. The model file is the modelled relative East, North and Up position of the station; the resid (redisual) file is the difference between the observed and modelled position. Finally the sum file provides a summary file of the fit in both XYZ and ENV coordinates. Here the sum file for the 02SG is shown:

```
XYZ 02SG STA 4887415.744351 1319346.350345 3867435.084778 0.003466 0.001428
0.002558
XYZ 02SG VEL -12.294845 27.448713 2.705784 1.357227 0.560327 0.994806
ENV 02SG STA 15.106778968 37.564137937 370.561445 0.001649 0.002885 0.003091
ENV 02SG VEL 29.704402 5.020091 -2.088904 0.646342 1.126004 1.208315
ENV 02SG REP 0.003631 0.003529 0.013162
```

The station sum file is composed by 9 columns: 1) cartesian (XYZ) or geodetic (ENV) parameter summary; 2) site name; 3) parameter code, it could be cartesian coordinates (STA), velocities (VEL), repeatability (REP) and other parameters; 4) X or East value for the coordinate or velocity; 5) Y or North value for the coordinate or velocity; 6) Z or Up value for the coordinate or velocity; 7) Sigma X or East; 8) Sigma Y or North; 9) Sigma Z or Up.

3.2.1 Permanent GNSS Station Time Series

In this paragraph, the Time Series of permanent GNSS station belonging to the ETNA@NET of INGV, locate in BOX2, are shown. The permanent stations shown are:

- EIIV site on the roof of the seat of INGV in Catania
- EBDA, Bosco di Aci, north of the Santa Maria la Stella
- ELAC, Lachea island localized in front of the village of Acitrezza
- ENIC, localized in the town of Nicolosi
- EPED, localized in the town of Pedara
- ETEC, localized in the village of Santa Tecla.

The GNSS reference frame is ITRF2014 (Altamimi et al., 2016).

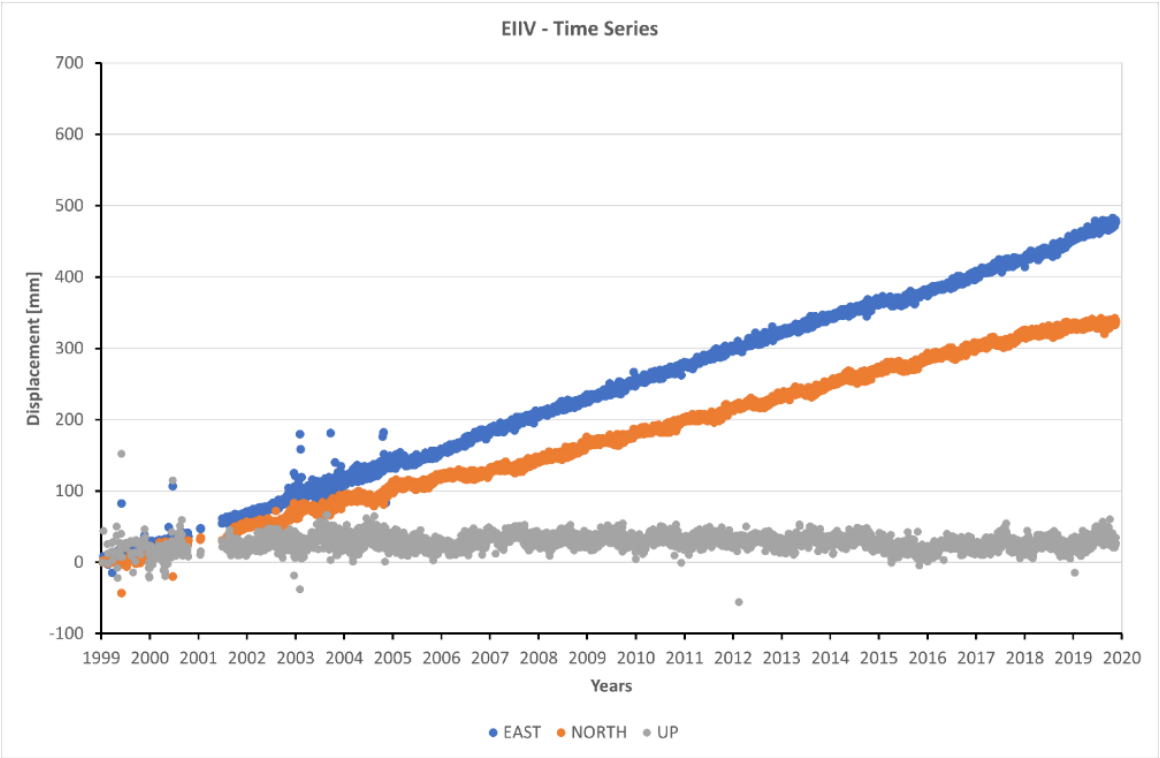

Figure 3. 1 – Time series between 1999 and 2019 of EIIV permanent station.

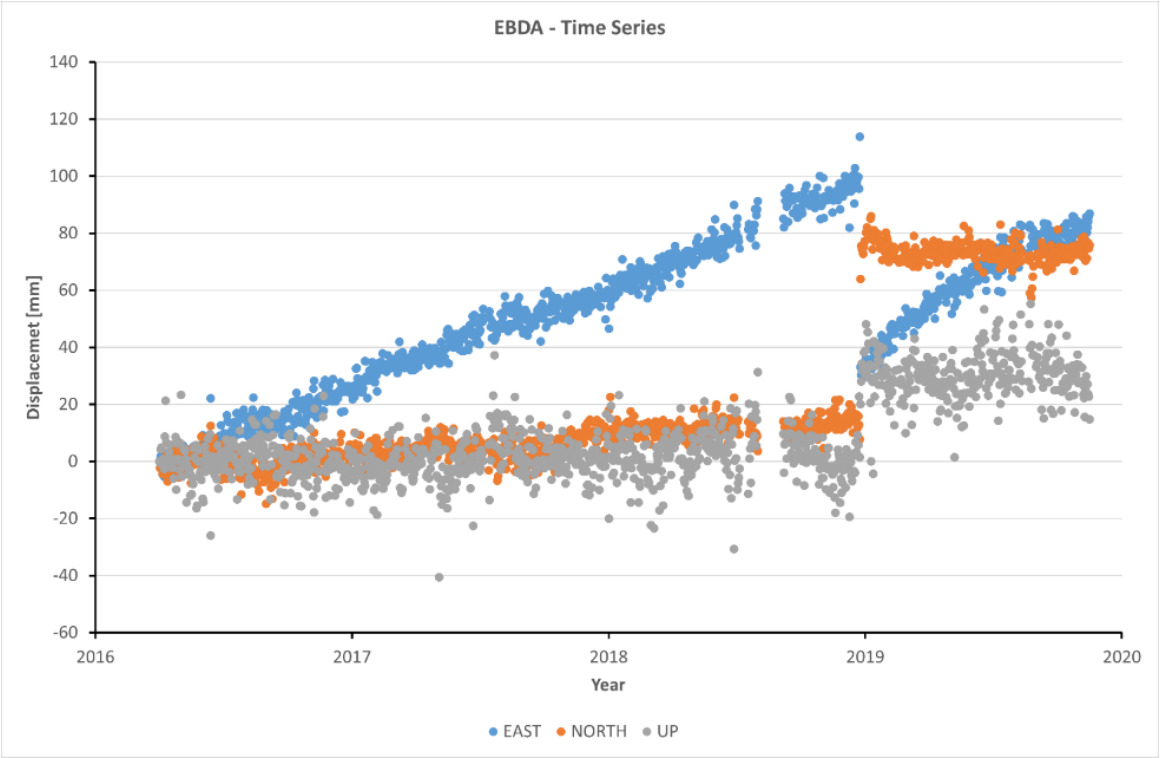

Figure 3. 2 – Time series between 2016 and 2019 of EBDA permanent station.

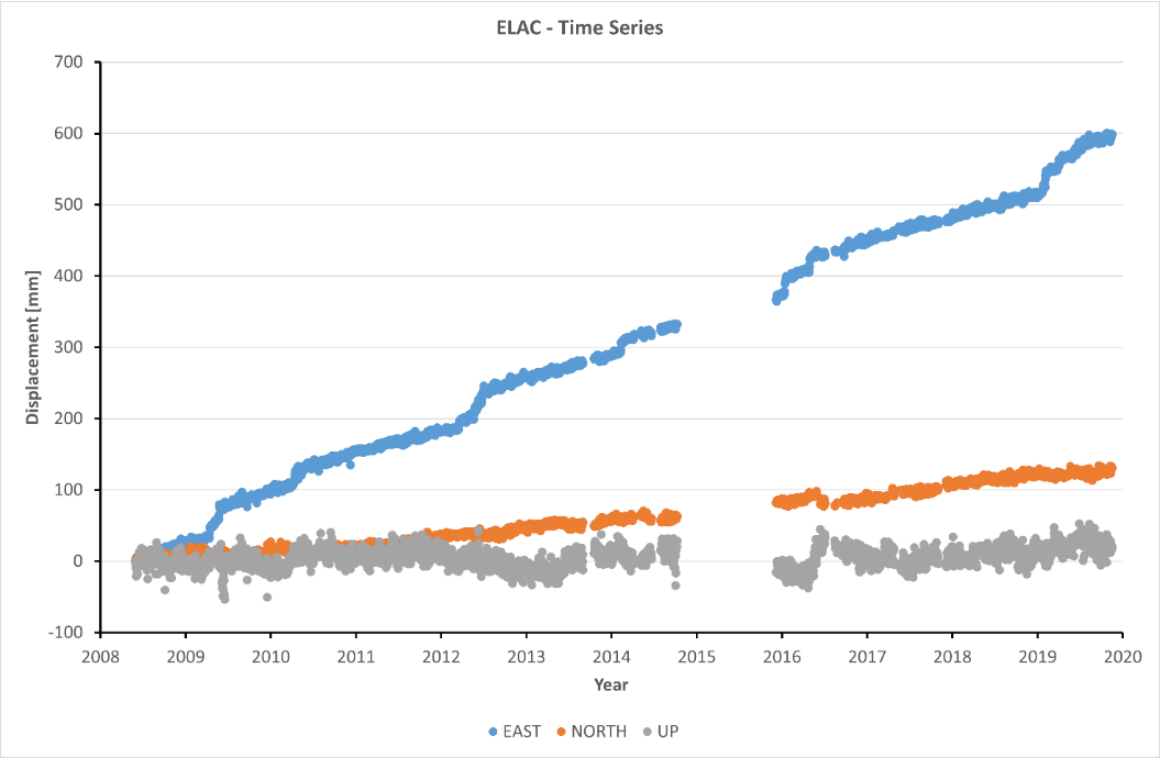

Figure 3. 3 - Time series between 2008 and 2019 of ELAC permanent station.

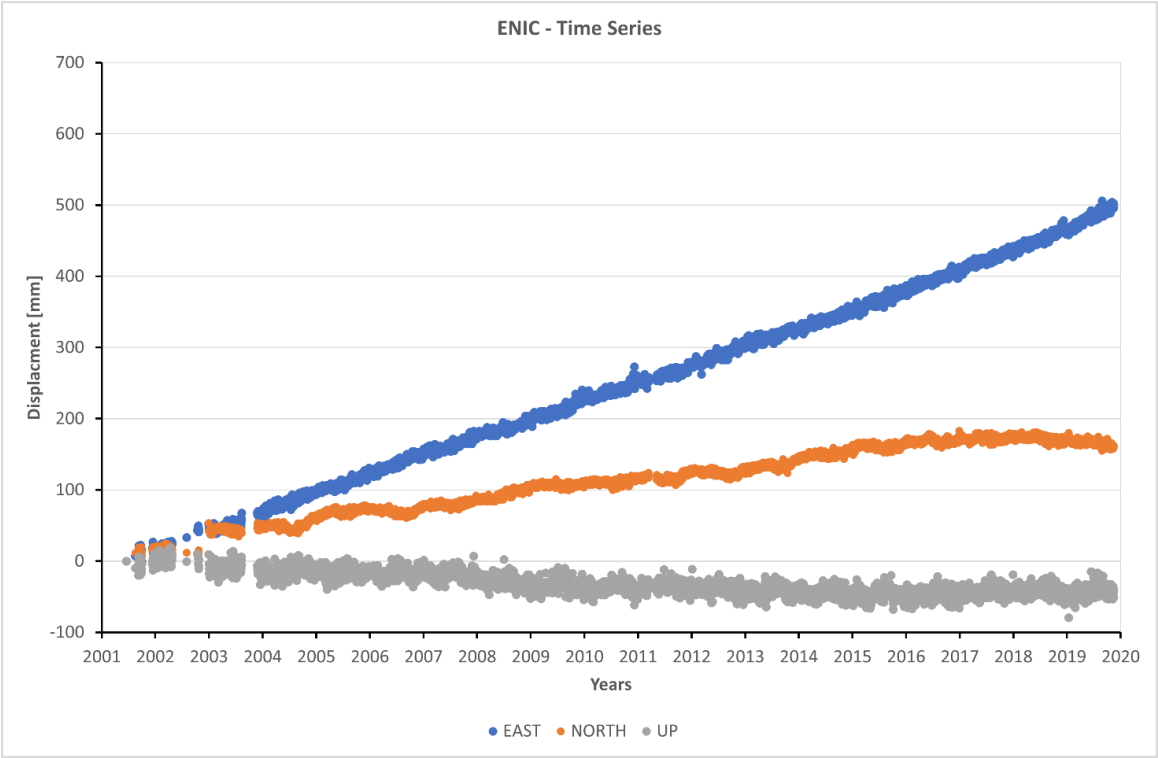

Figure 3. 4 - Time series between 2001 and 2019 of ENIC permanent station.

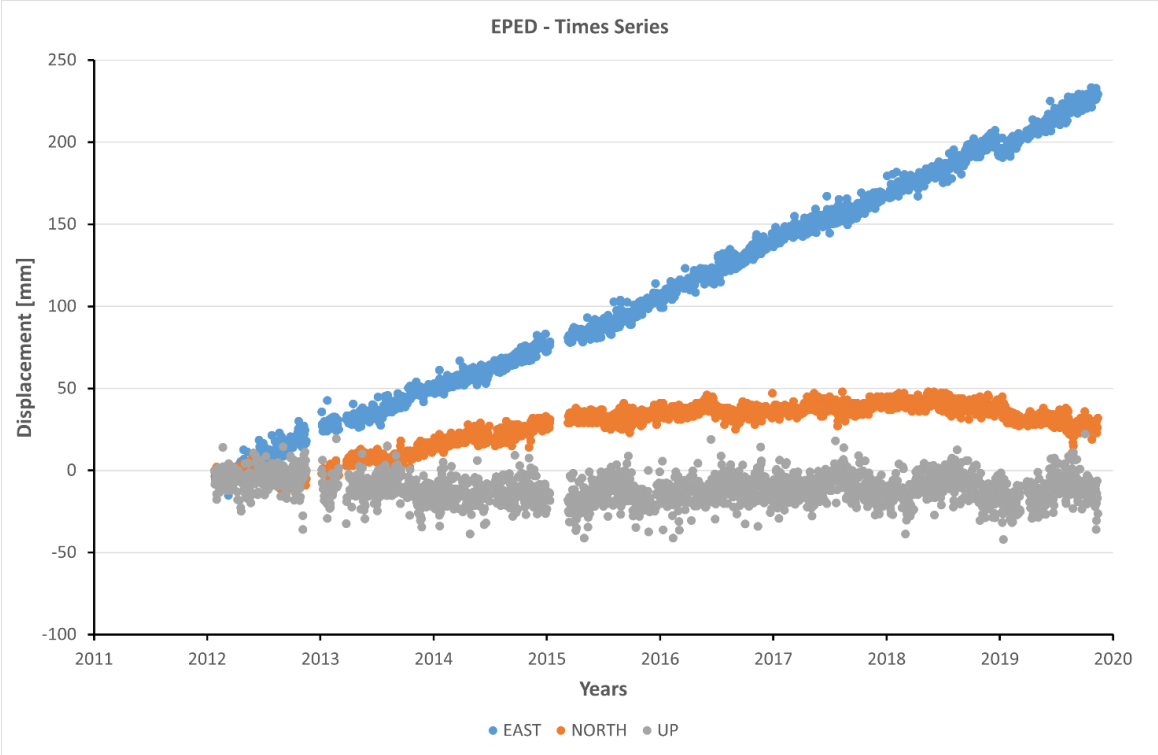

Figure 3. 5 - Time series between 2012 and 2019 of EPED permanent station.

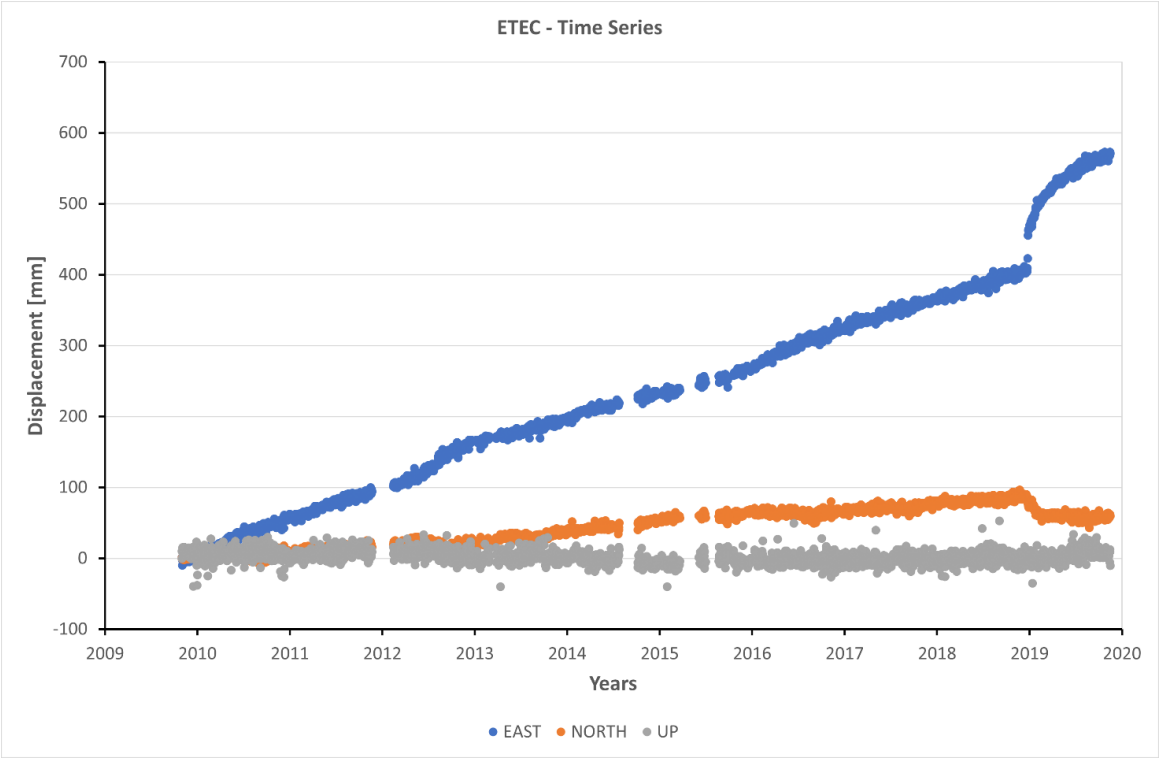

Figure 3. 6 - Time series between 2009 and 2019 of ETEC permanent station.

3.2.2 Campaign GNSS station of INGV

In this paragraph, the time series of the campaign GNSS station belonging to the "Ionica" sub-network of INGV, locate in BOX2, are shown. The discrete stations shown are:

STATION	NAME
~~ACID~~	~~Acireale~~
~~CASL~~	~~Casalotto~~
EMSC	Mascalucia
EPEL	Mompeloso
ESGR	San Gregorio
MDGR	Madonna delle Grazie
MPL0	Mompelieri
PDAP	Piano Api
MTSE	Monte Serra

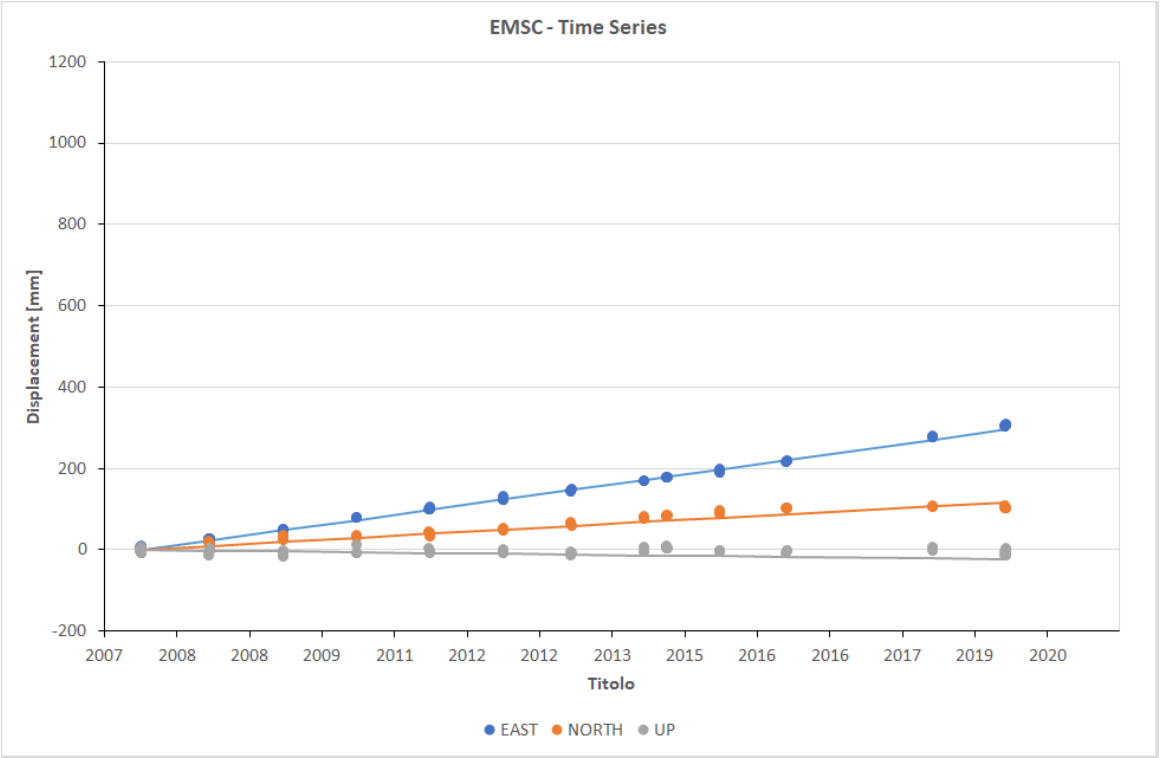

Figure 3. 7 - Time series between 2007 and 2019 of EMSC campaign station.

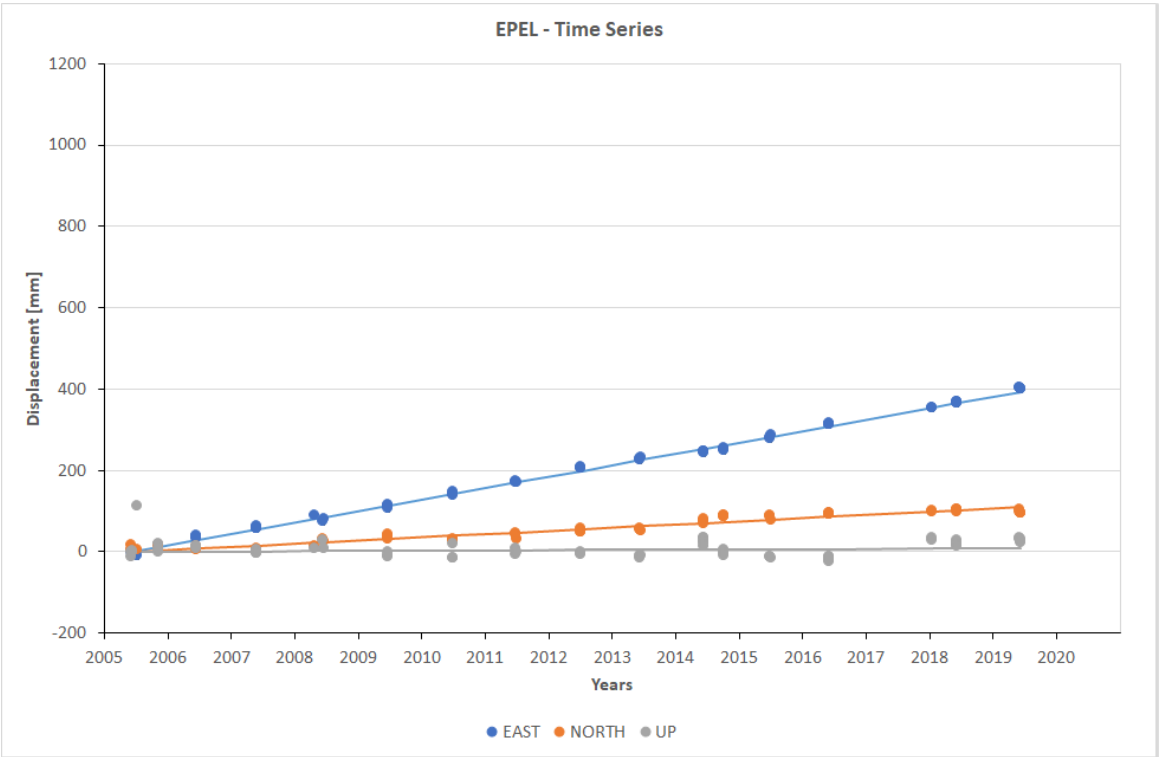

Figure 3. 8 - Time series between 2005 and 2019 of EPEL campaign station.

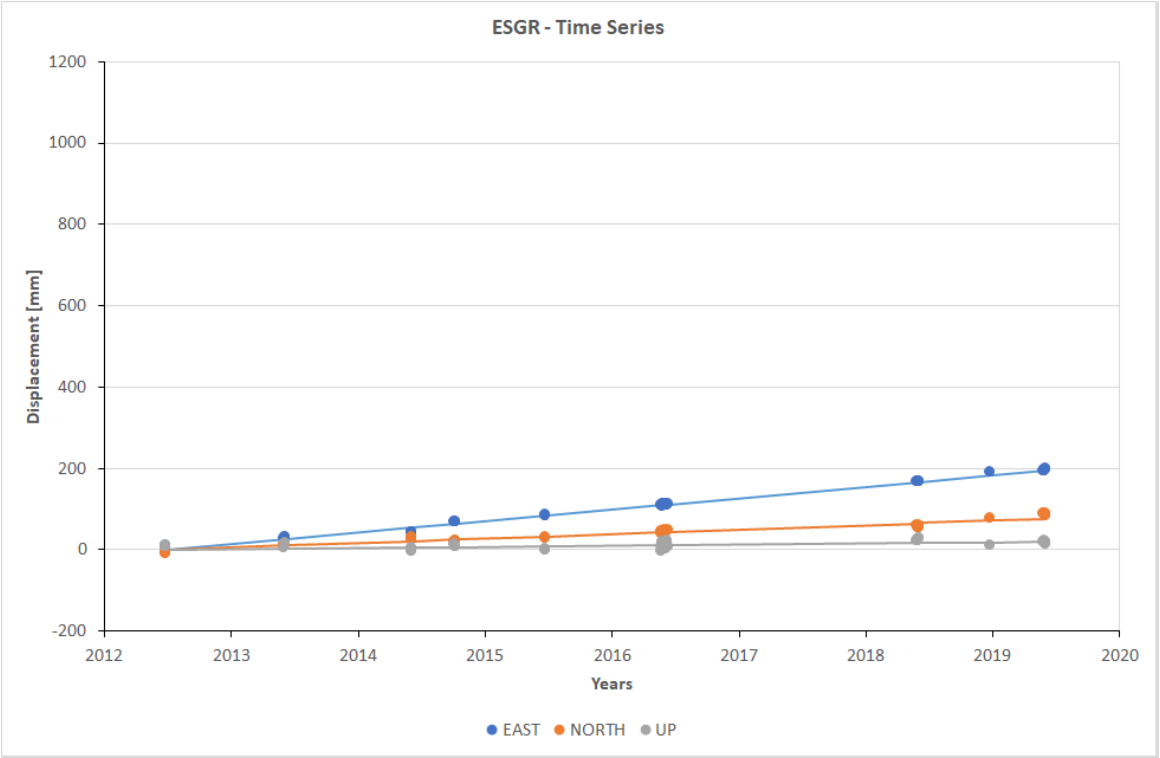

Figure 3. 9 - Time series between 2012 and 2019 of ESGR campaign station.

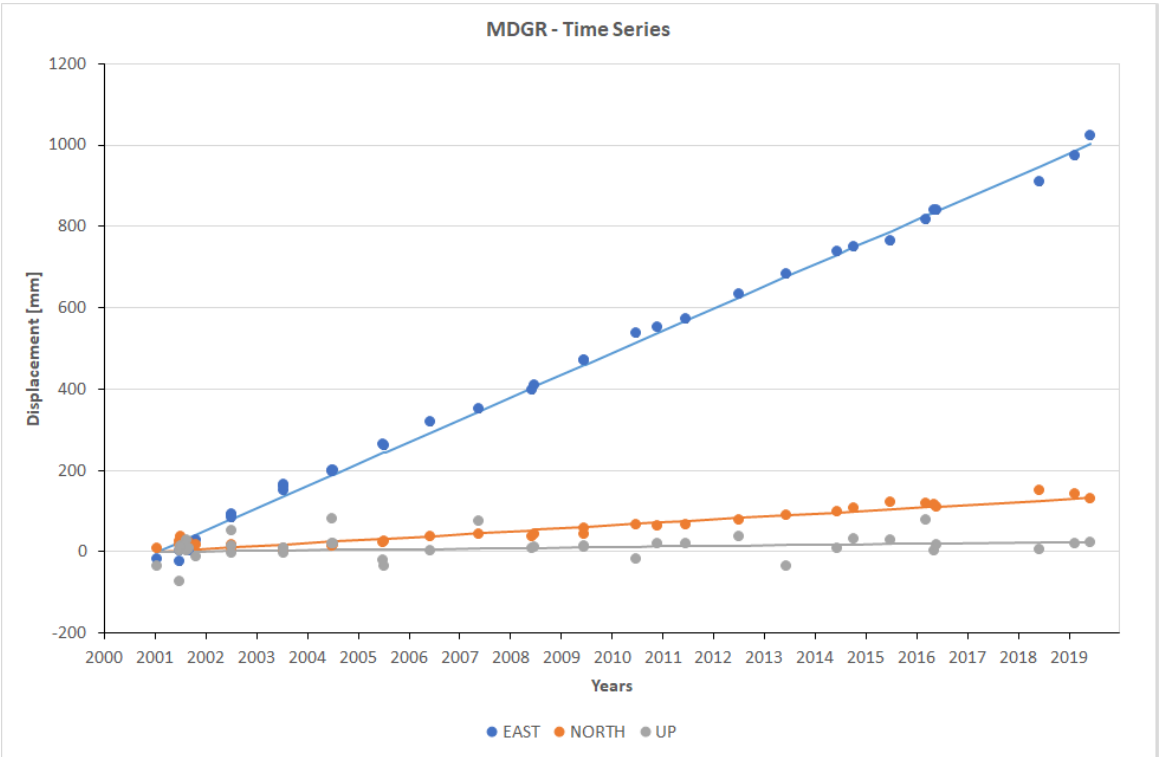

Figure 3. 10 - Time series between 2001 and 2019 of MDGR campaign station.

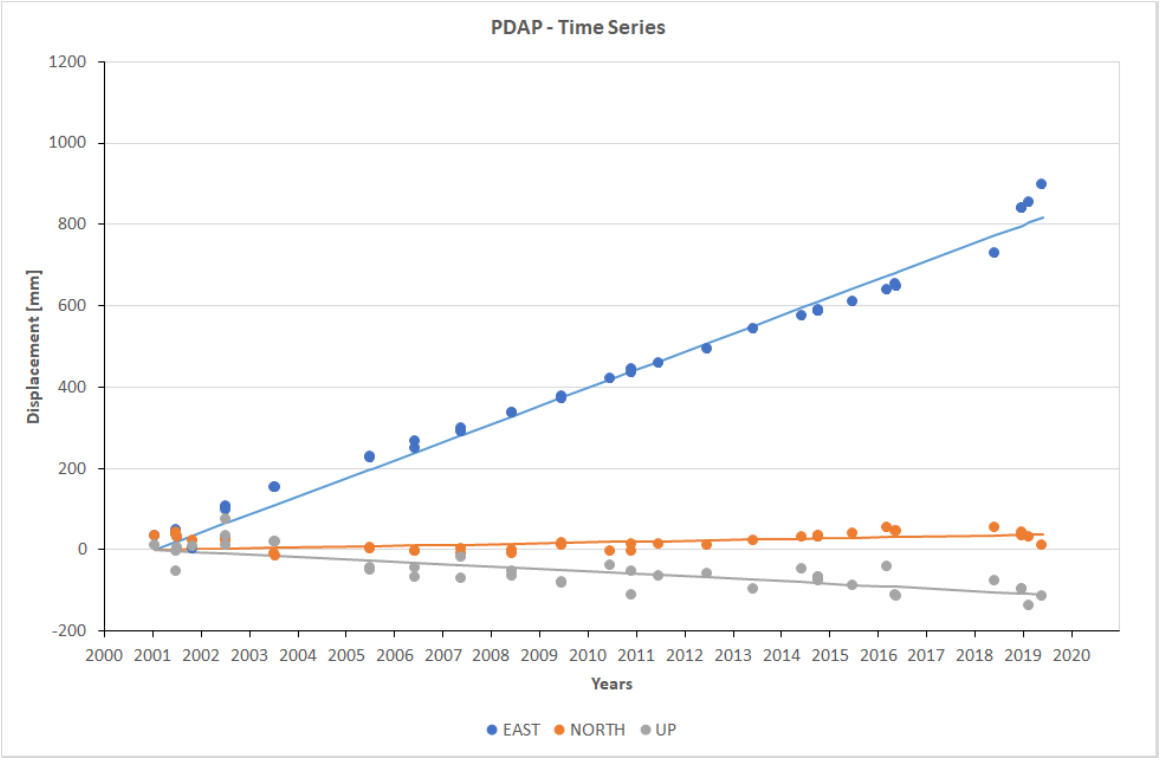

Figure 3. 11 - Time series between 2001 and 2019 of PDAP campaign station.

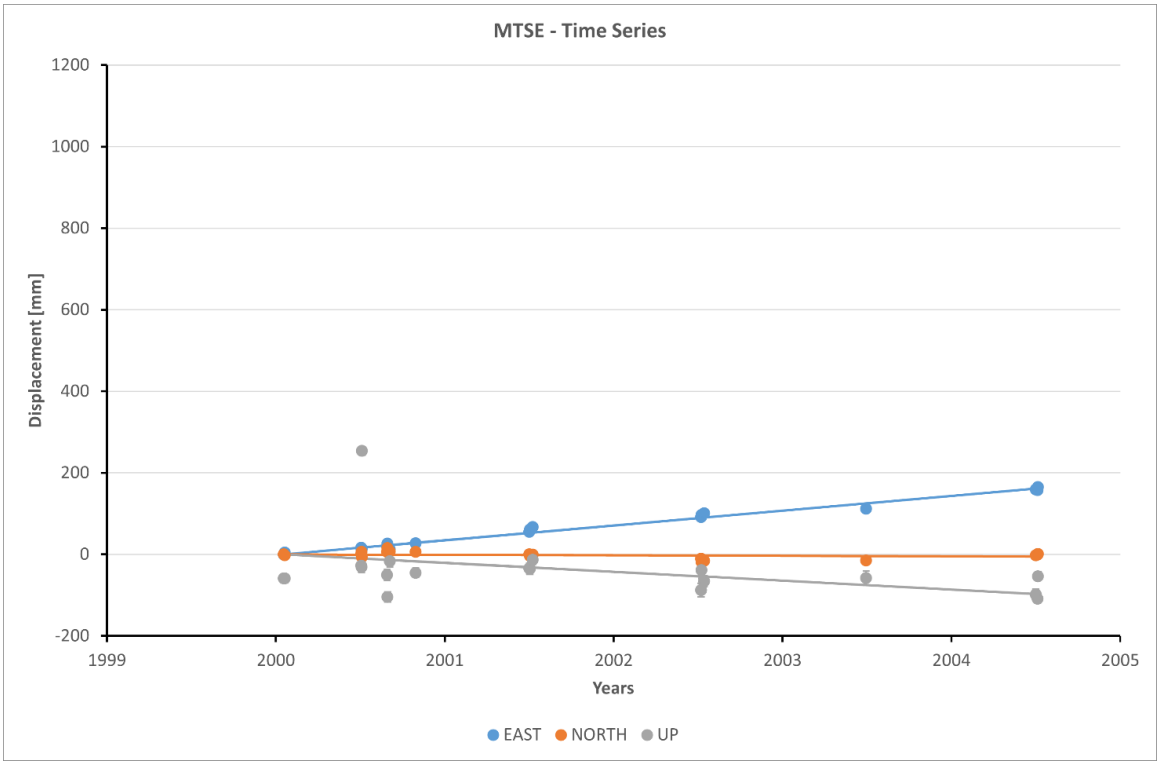

Figure 3. 12 - Time series between 2007 and 2019 of EMSC campaign station.

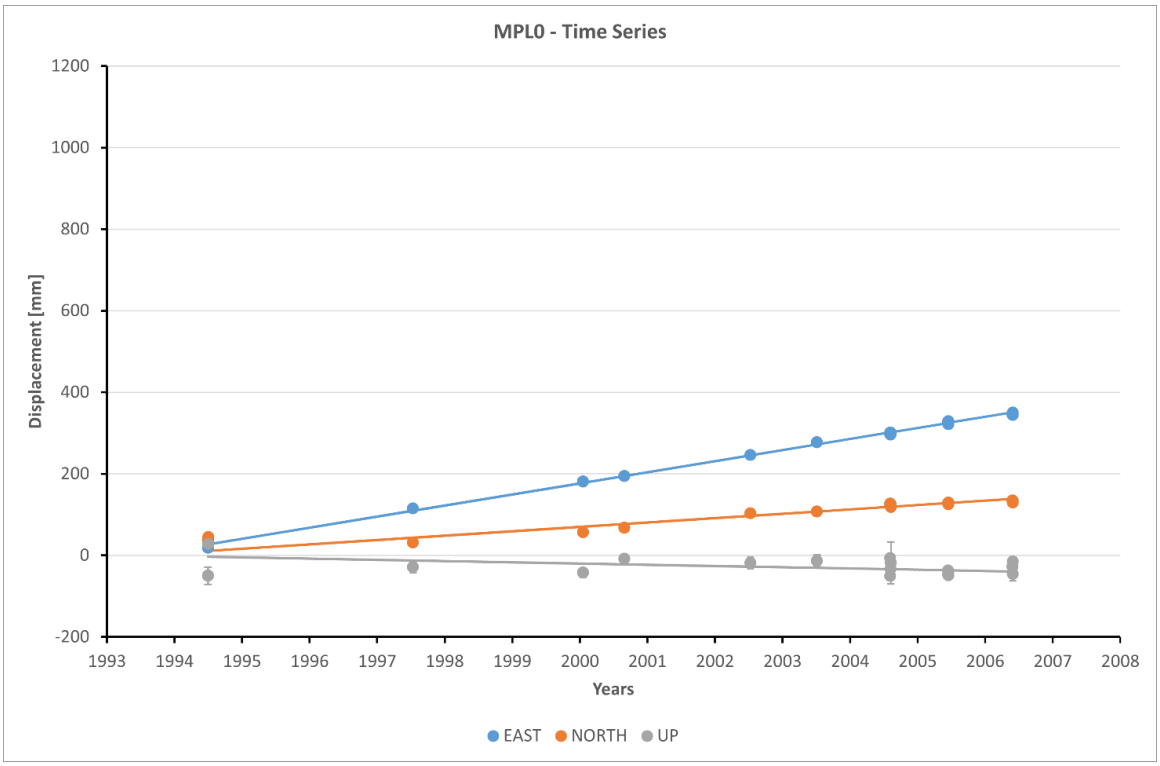

Figure 3. 13 - Time series between 2007 and 2019 of MPL0 campaign station.

3.2.3 Campaign GNSS stations of the San Gregorio network of the University of Catania

In this paragraph, the time series of campaign GNSS station belonging to the sub network San Gregorio Net operated by the University of Catania are shown. The campaign stations shown are:

STATION	NAME
02SG	Caduti in guerra
07SG	Margherita
08SG	Repubblica
09SG	Via Turi Ferro Ovest
10SG	Via Turi Ferro Est
15SG	Villa Comunale S
16SG	Via Zizzo
19SG	Bellini 20
21SG	Scuderi Est
22SG	Santantonio

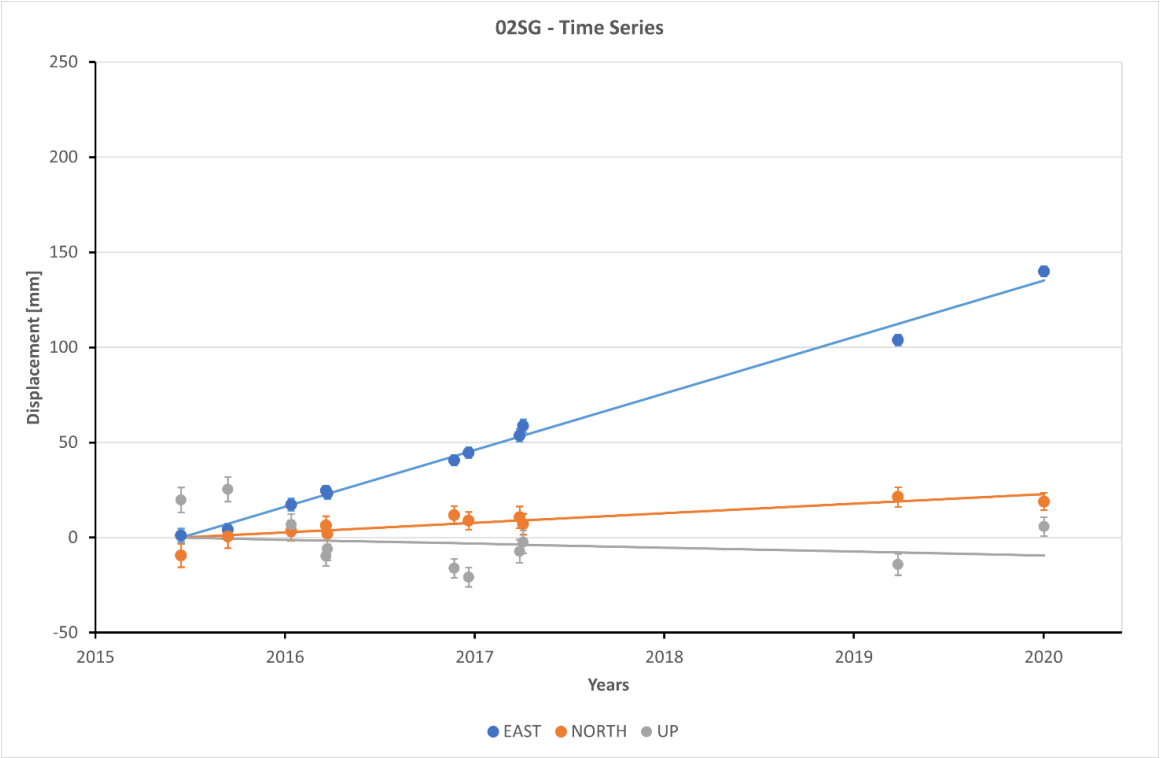

Figure 3. 14 - Time series between 2015 and 2020 of 02SG campaign station.

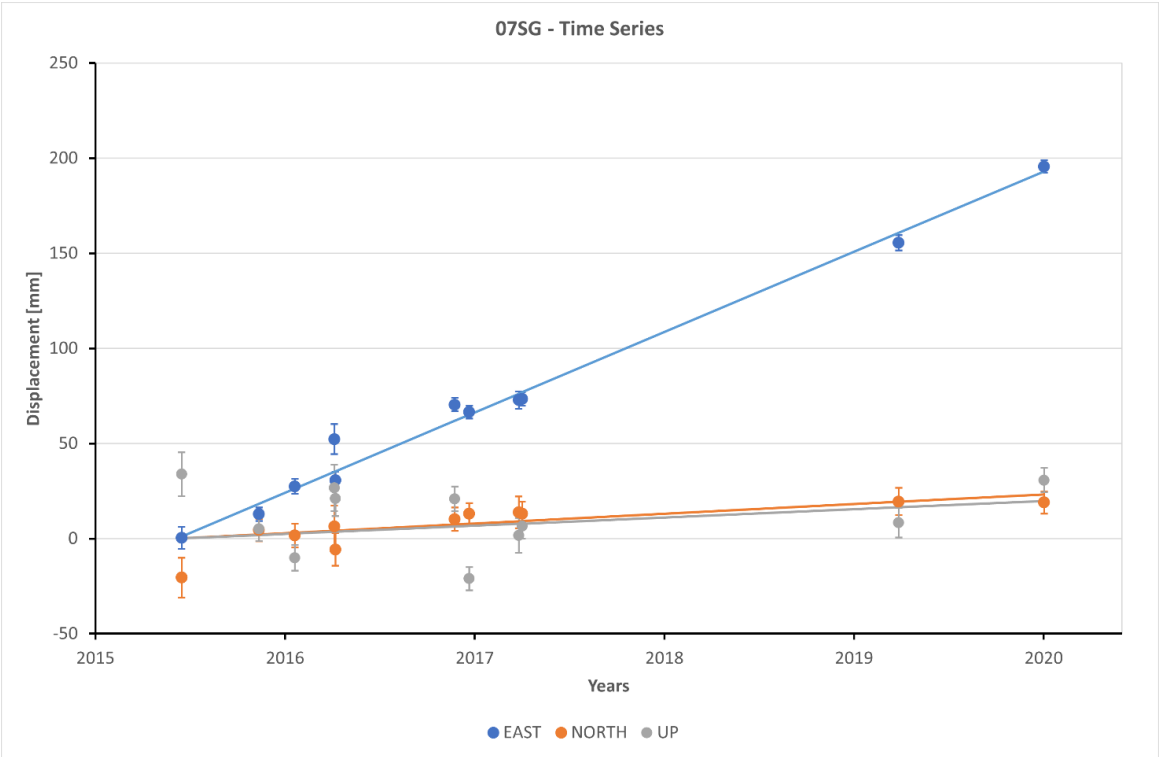

Figure 3. 15 - Time series between 2015 and 2020 of 07SG campaign station.

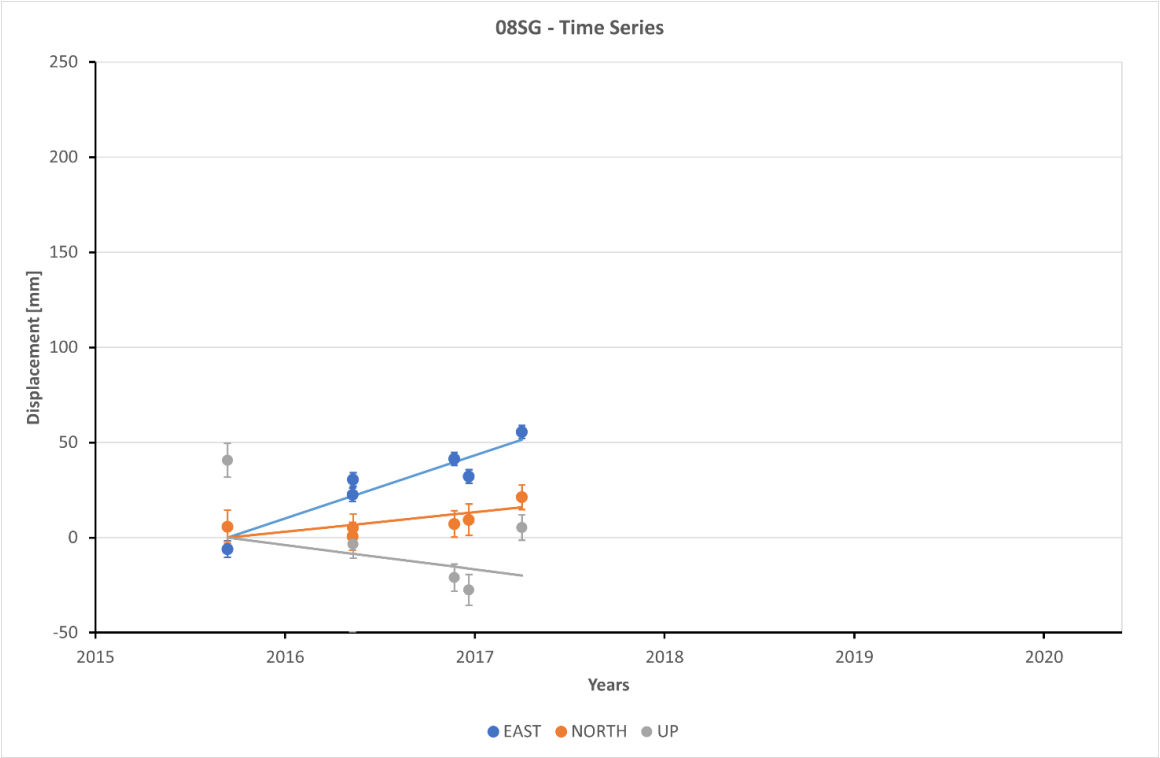

Figure 3. 16 - Time series between 2015 and 2020 of 08SG campaign station.

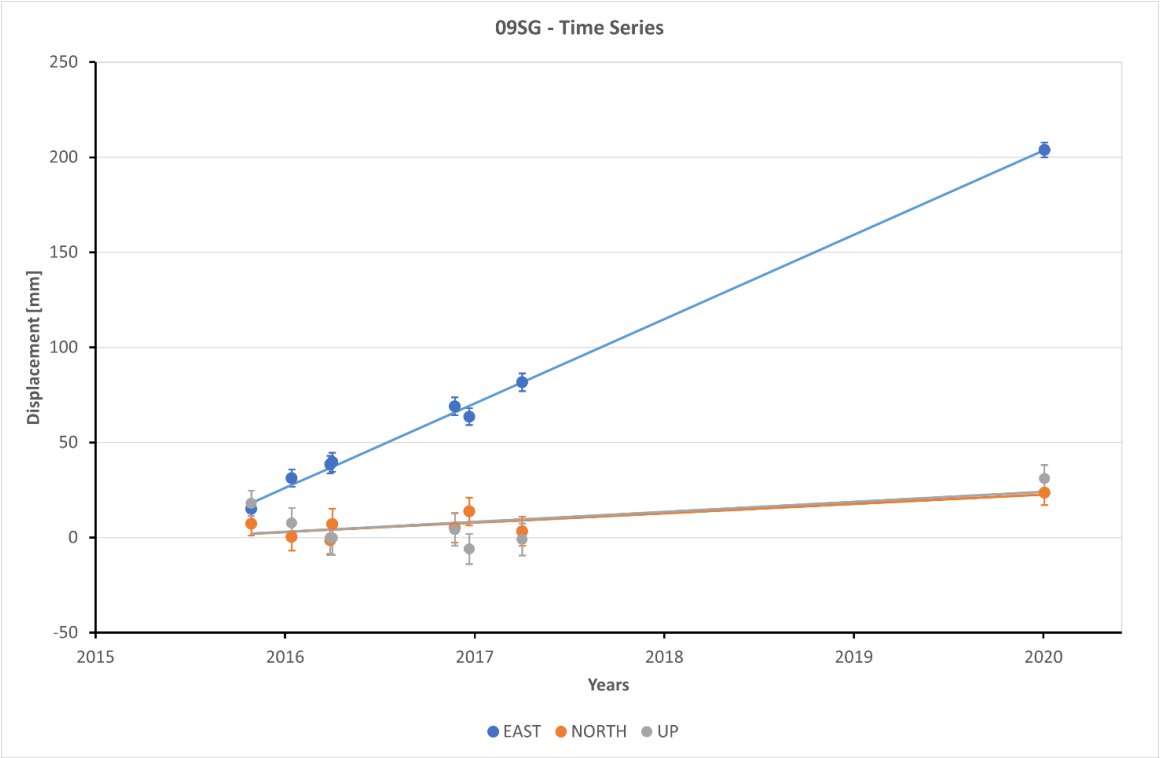

Figure 3. 17 - Time series between 2015 and 2020 of 09SG campaign station.

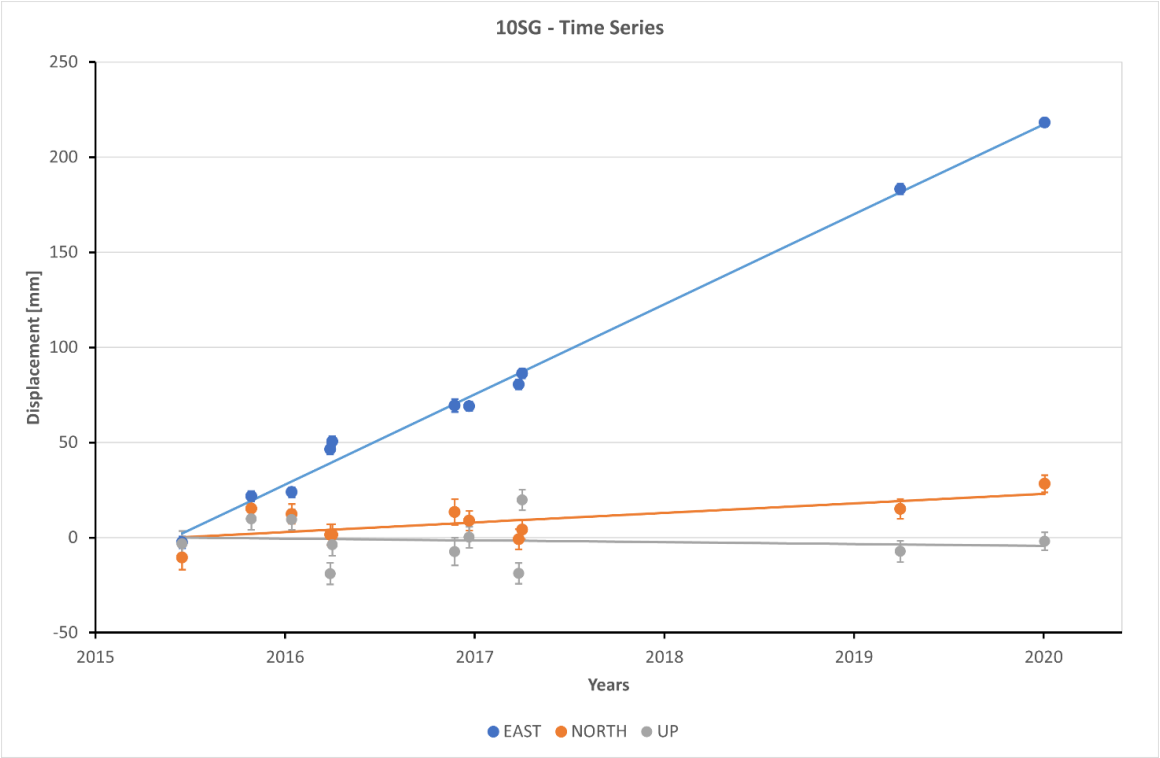

Figure 3. 18 - Time series between 2015 and 2020 of 10SG campaign station.

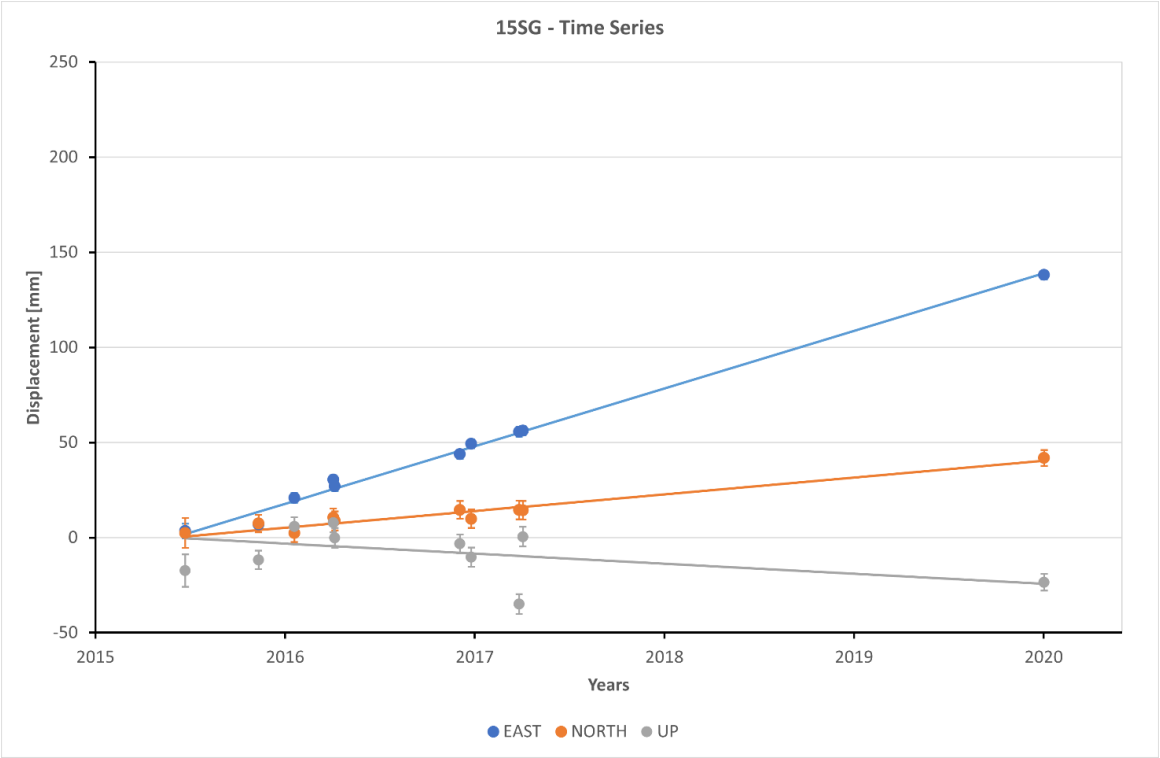

Figure 3. 19 - Time series between 2015 and 2020 of 15SG campaign station.

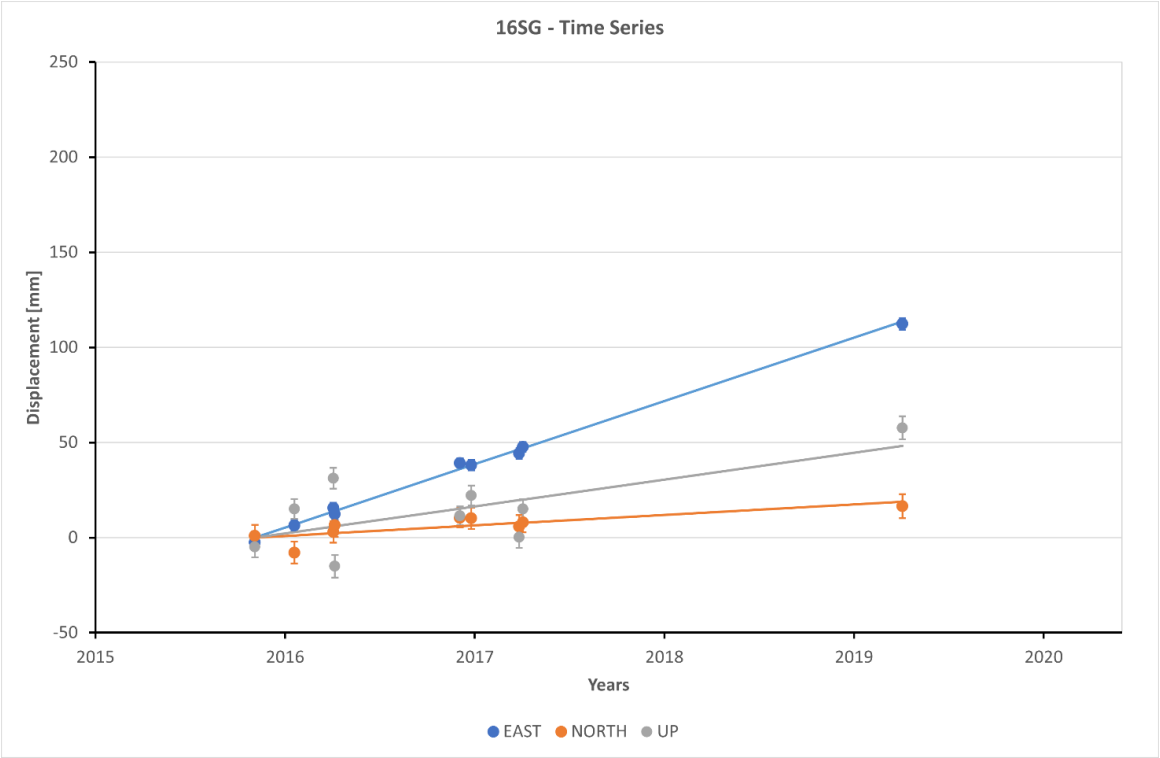

Figure 3. 20 - Time series between 2015 and 2020 of 16SG campaign station.

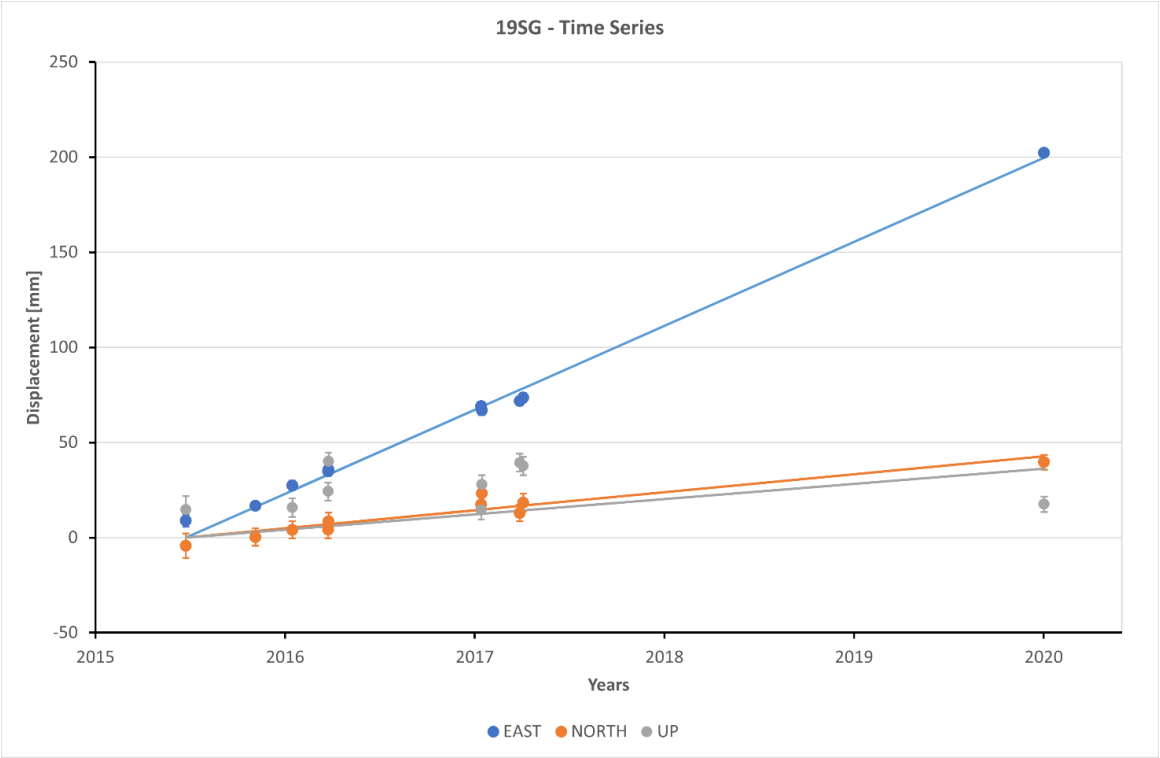

Figure 3. 21 - Time series between 2015 and 2020 of 19SG campaign station.

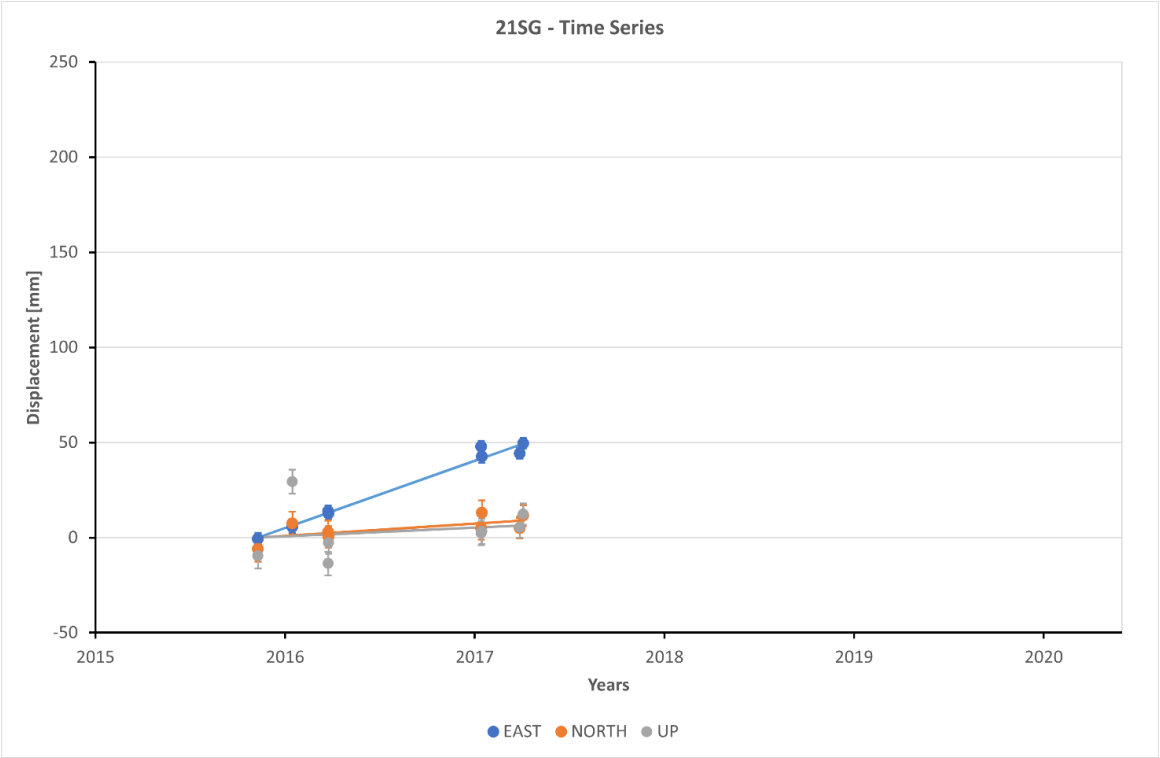

Figure 3. 22 - Time series between 2015 and 2020 of 21SG campaign station.

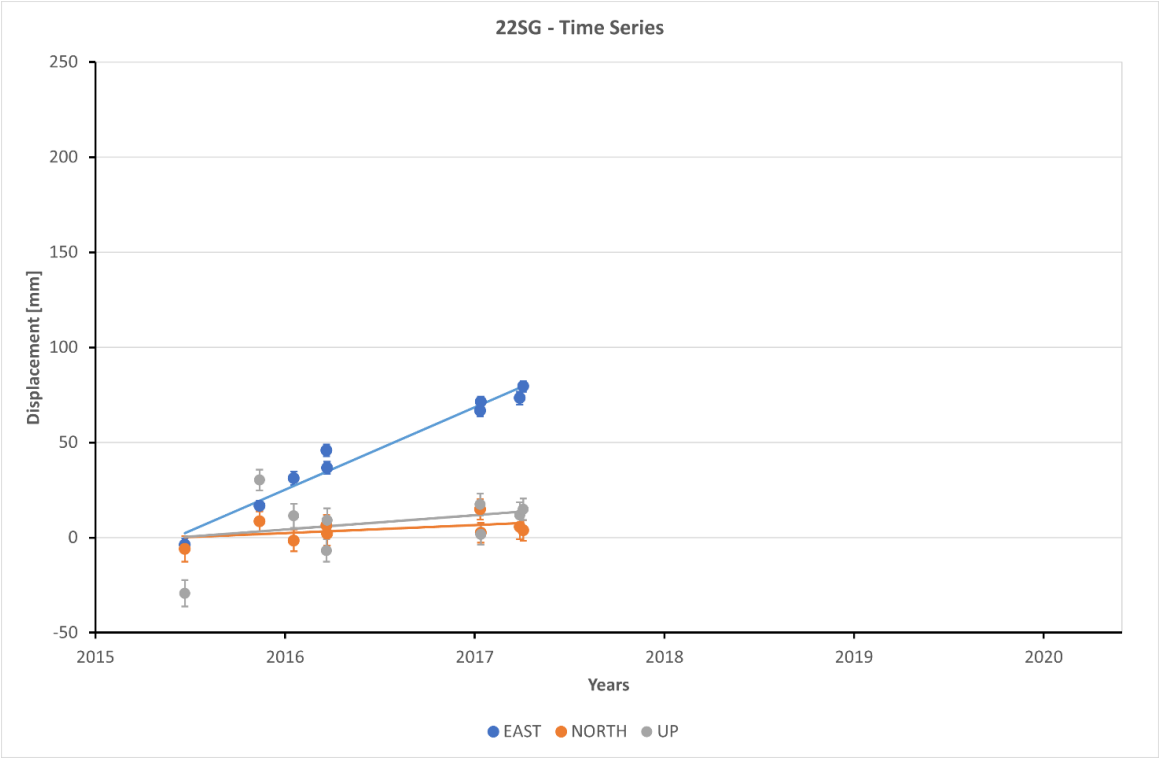

Figure 3. 23 - Time series between 2015 and 2020 of 22SG campaign station.

The most reliable stations, so far, are 02SG, 07SG, 09SG, 10SG, 15SG, 16SG and 19SG because they have the longest time series in the San Gregorio Net.

3.2.4 Acitrezza Net GNSS Station

In this paragraph, the Time Series of discrete GNSS station belonging to the sub network Acitrezza Net are shown. The discrete stations shown are:

STATION	NAME
28AT	Scuola Acitrezza
32AT	Via G M Frontini
33AT	Via Malavoglia E
37AT	Residence Ciclopi
38AT	Via Malavoglia S
39AT	Stadio
~~41AT~~	Campagna Terreforti
44AT	Via Monterosso W
45AT	Park Terreforti
46AT	Tennis Terrefori

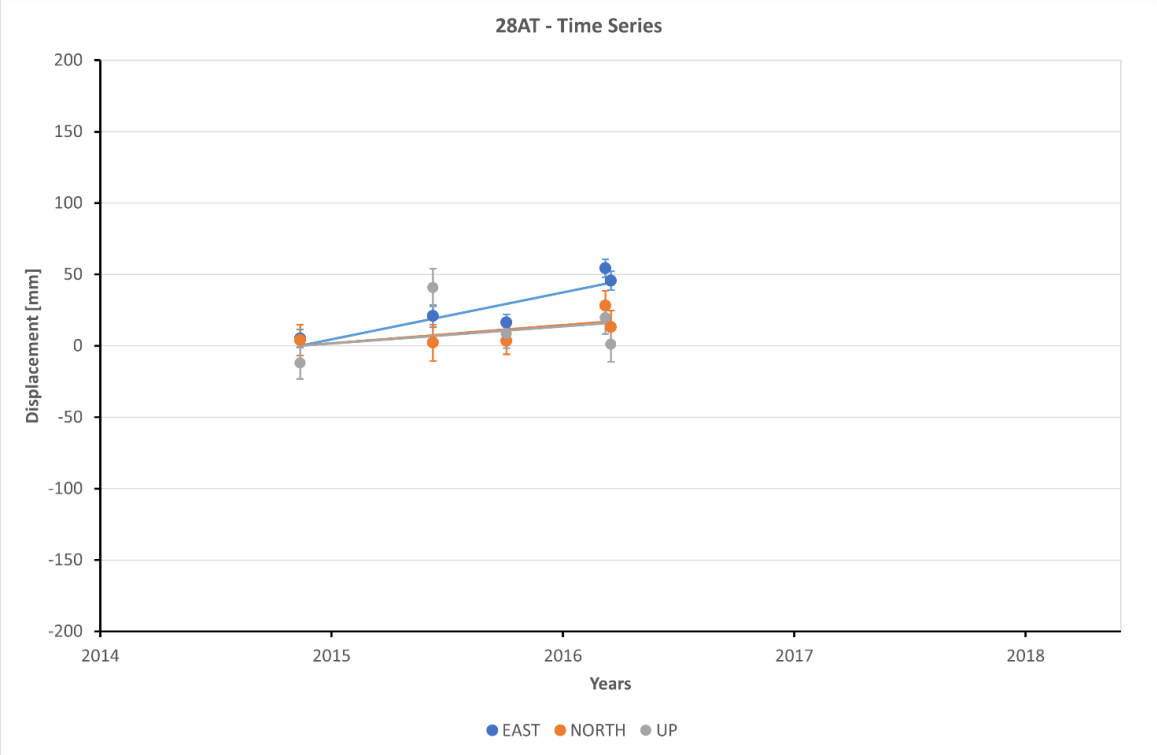

Figure 3. 24 - Time series between 2014 and 2020 of 28AT campaign station.

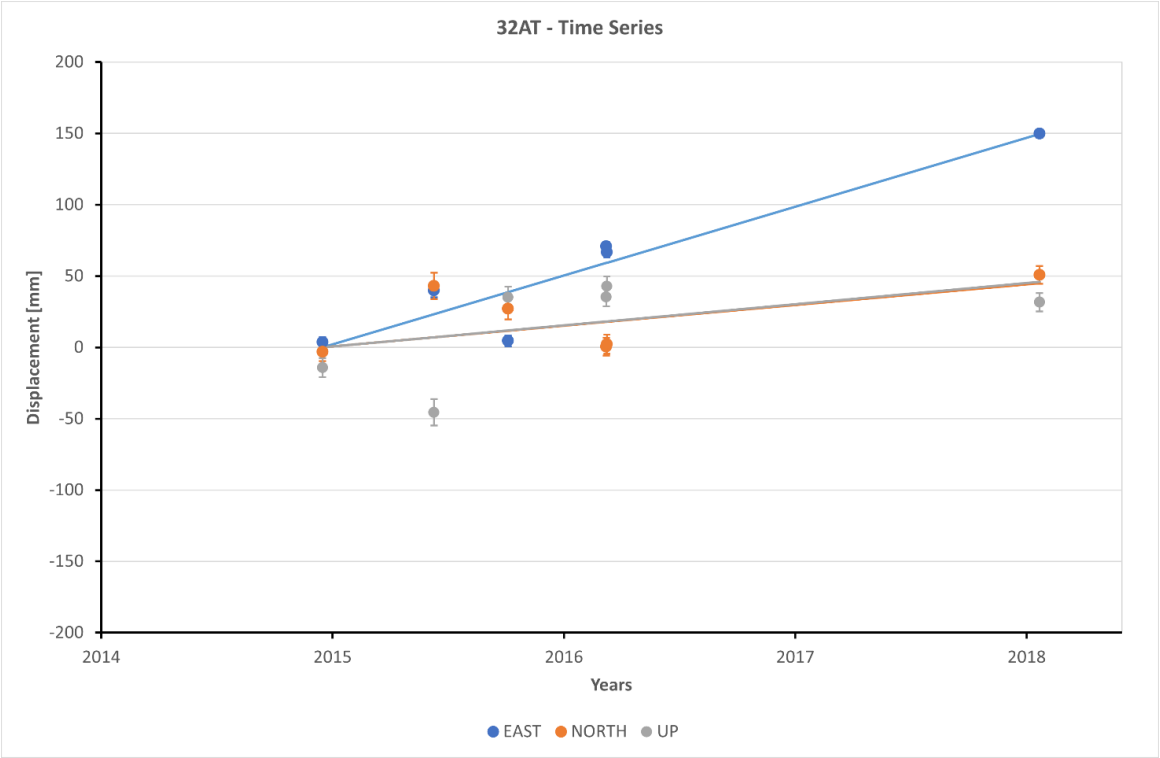

Figure 3. 25 - Time series between 2014 and 2020 of 32AT campaign station.

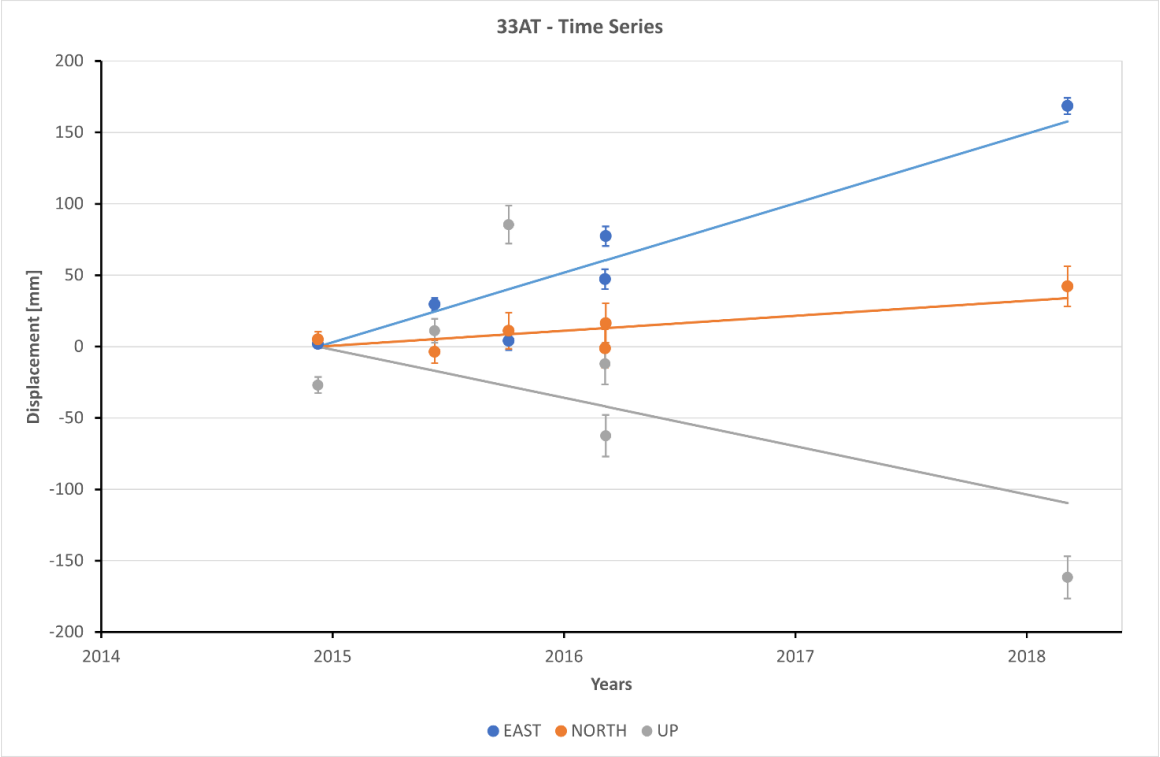

Figure 3. 26 - Time series between 2014 and 2020 of 33AT campaign station.

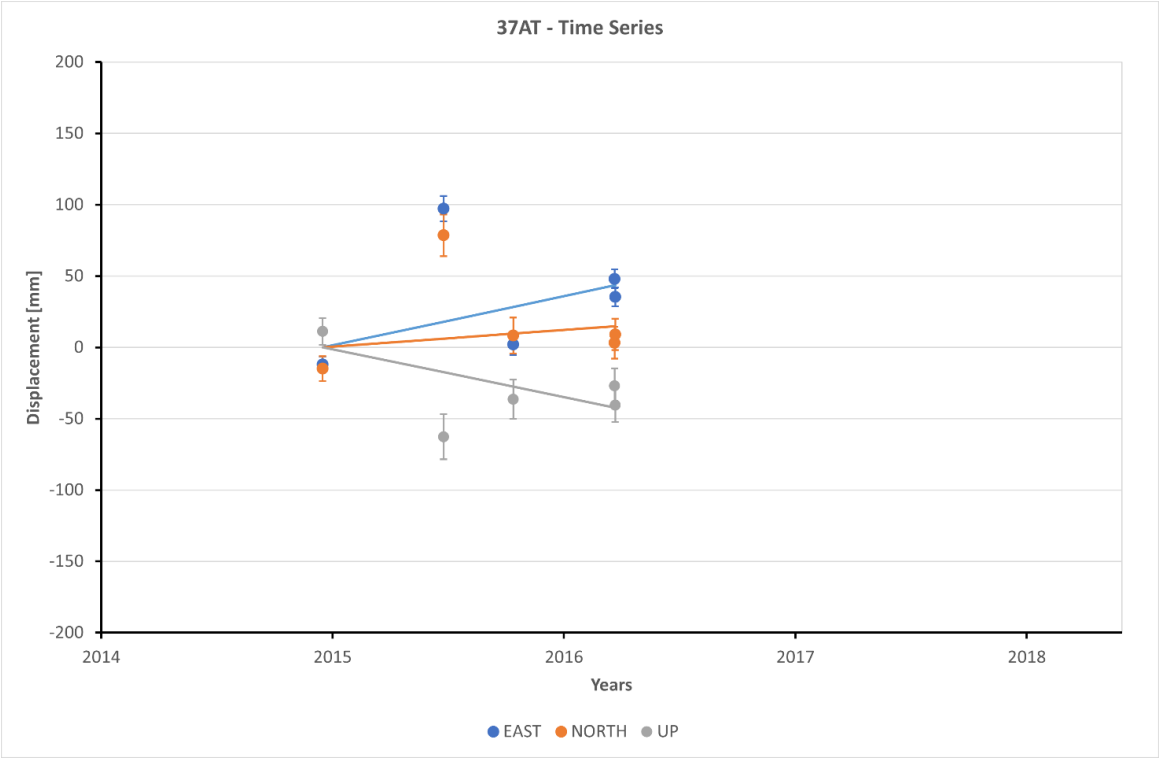

Figure 3. 27 - Time series between 2014 and 2020 of 37AT campaign station.

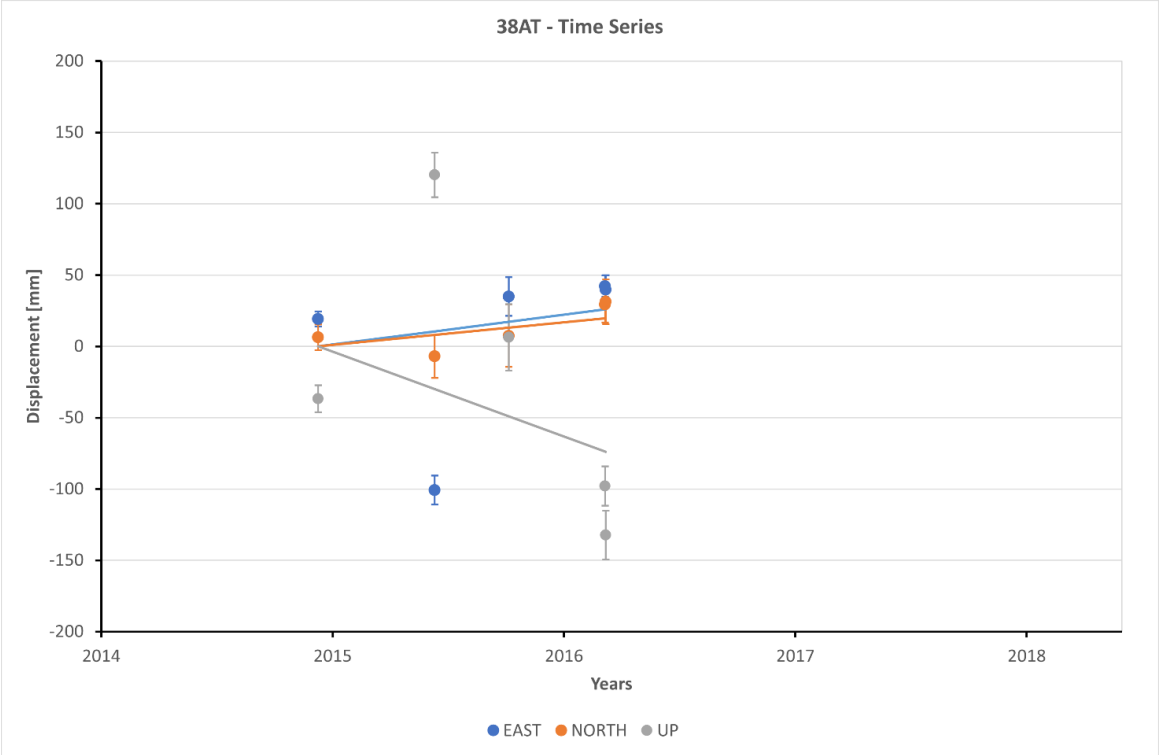

Figure 3. 28 - Time series between 2014 and 2020 of 38AT campaign station.

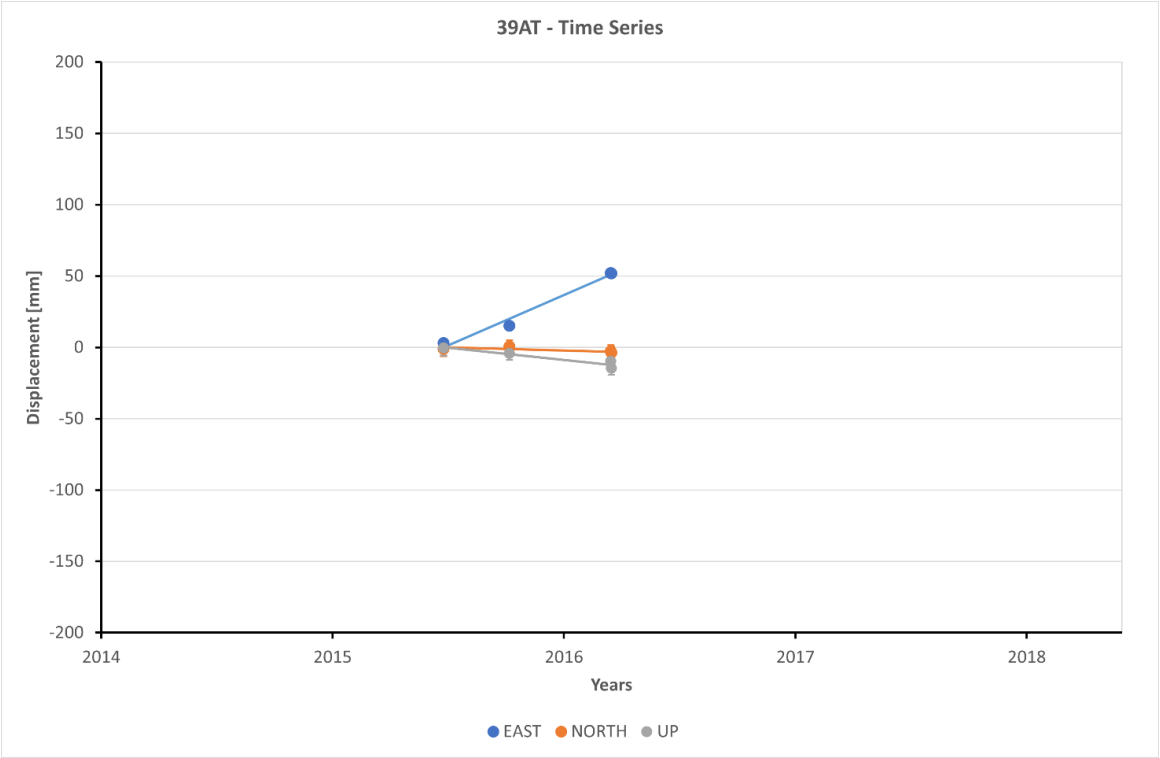

Figure 3. 29 - Time series between 2015 and 2020 of 39AT campaign station.

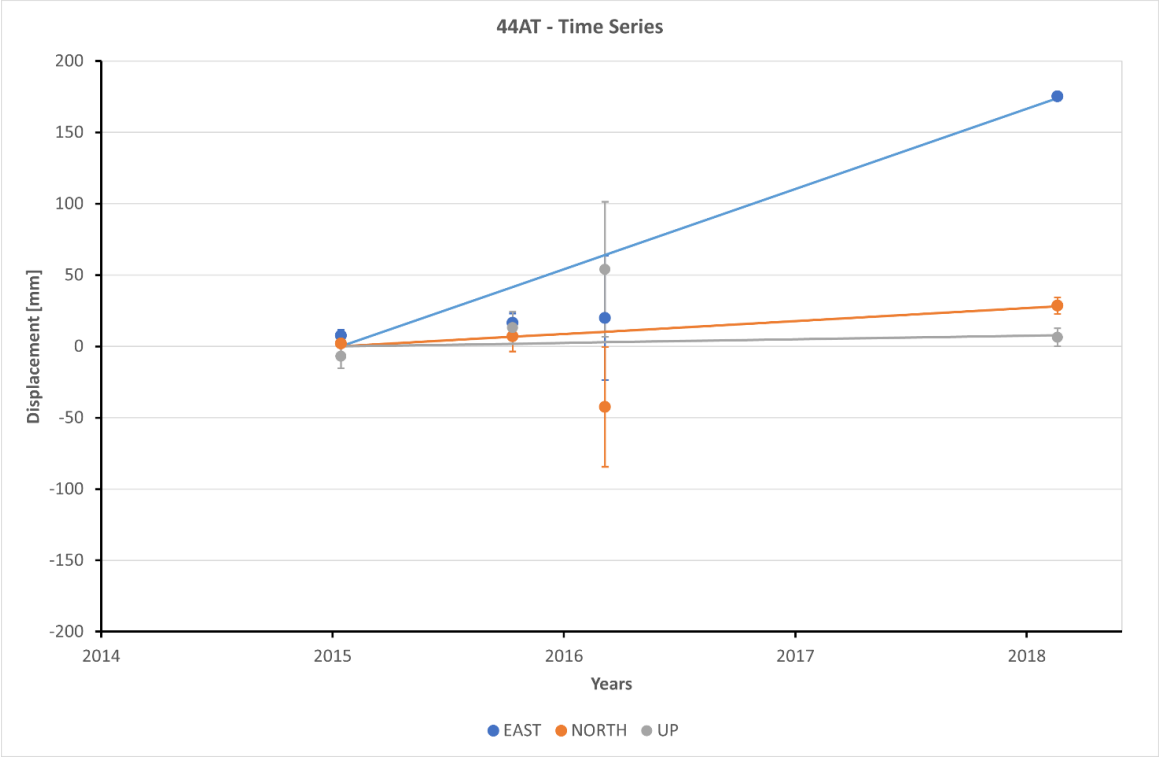

Figure 3. 30 - Time series between 2015 and 2020 of 44AT campaign station.

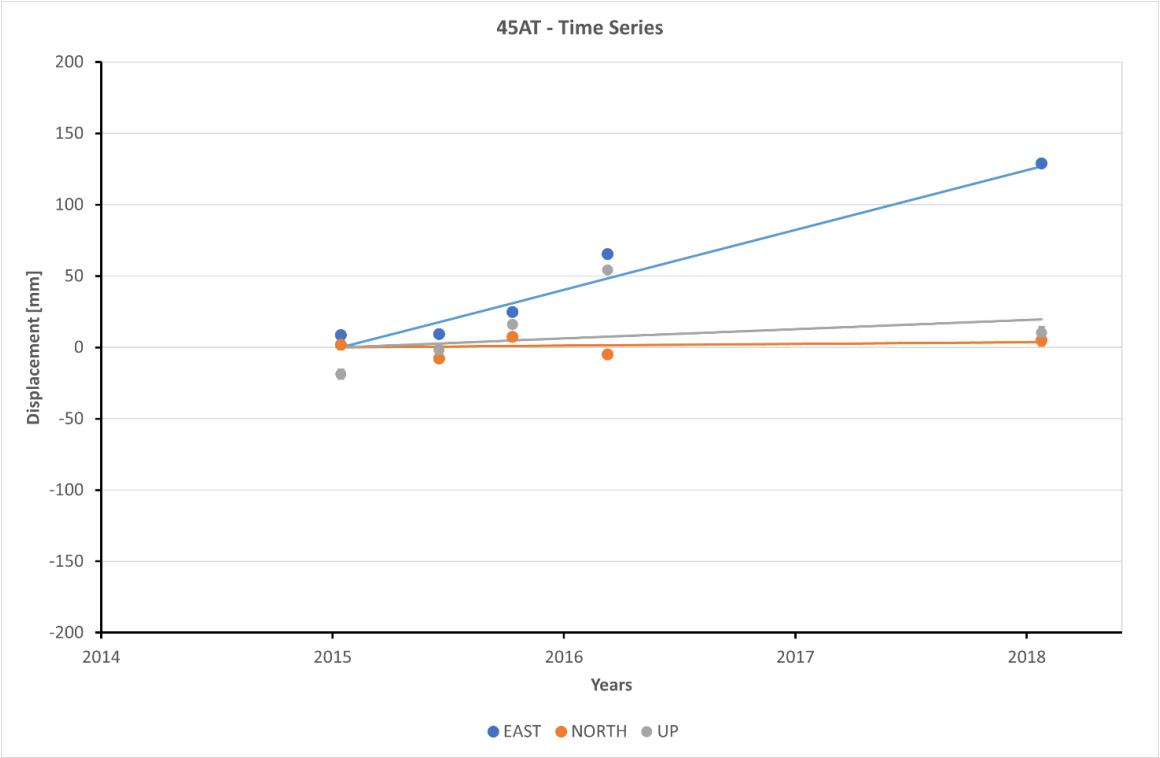

Figure 3. 31 - Time series between 2015 and 2020 of 45AT campaign station.

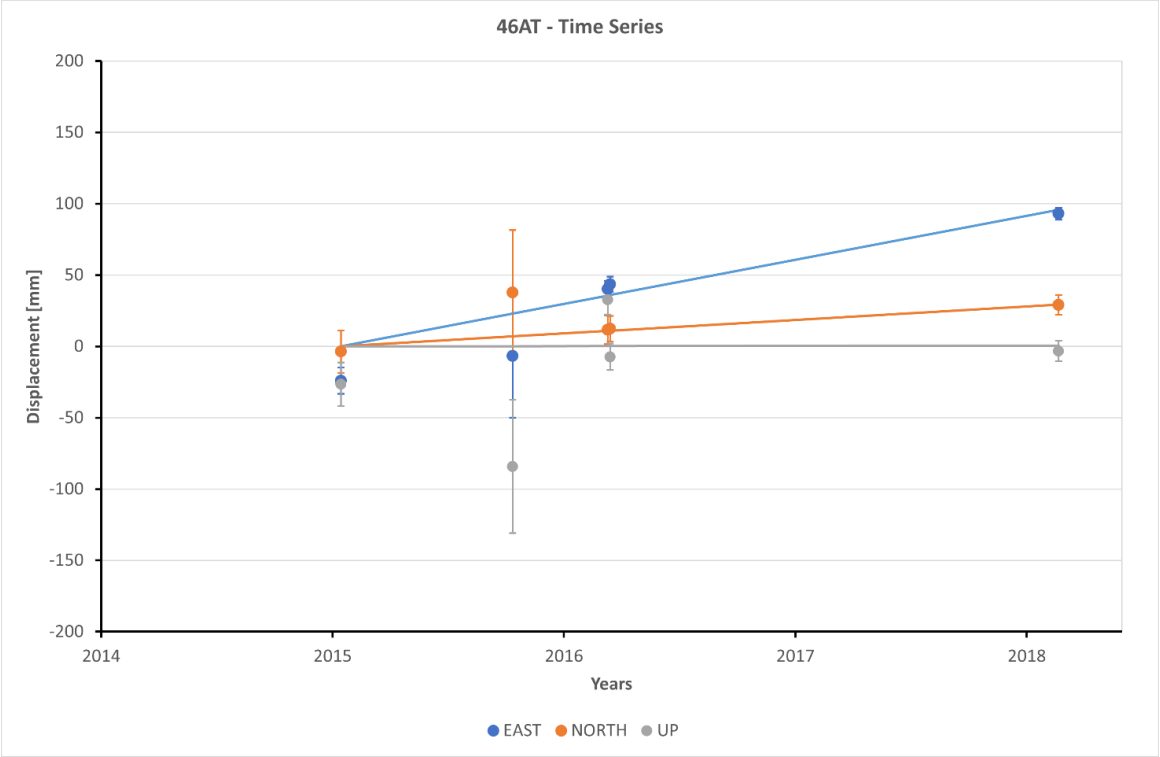

Figure 3. 32 - Time series between 2015 and 2020 of 46AT campaign station.

In the Acitrezza Net, many stations show an unstable temporal evolution. Some measurements have large errors. Moreover some time series are very short. In that network the most reliable stations are: 32AT, 33AT, 44AT, 45AT and 46AT.

3.2.5 Belpasso–Ognina Net GNSS Station

In this paragraph, the time series of campaign GNSS station belonging to the sub network Belpasso-Ognina Net operated by the University of Catania are shown. The discrete stations shown are:

STATION	NAME
~~BOL1~~	~~Viale Lainò~~
BOL2	Via Teseo
BOL3	Via Giuseppe Parini
BOL4	Via Cardinale Nava
BOL5	Gravina San Paolo
BOL6	Via Guardia

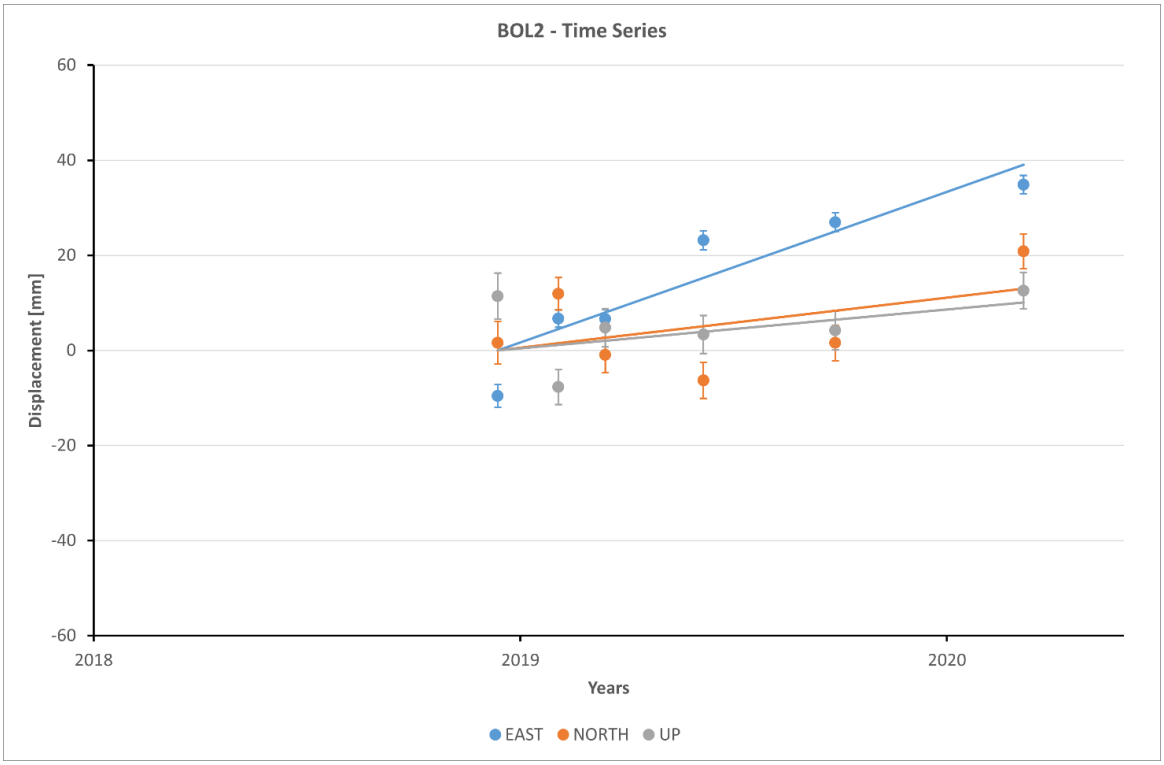

Figure 3. 33 - Time series between 2019 and 2020 of BOL1 campaign station.

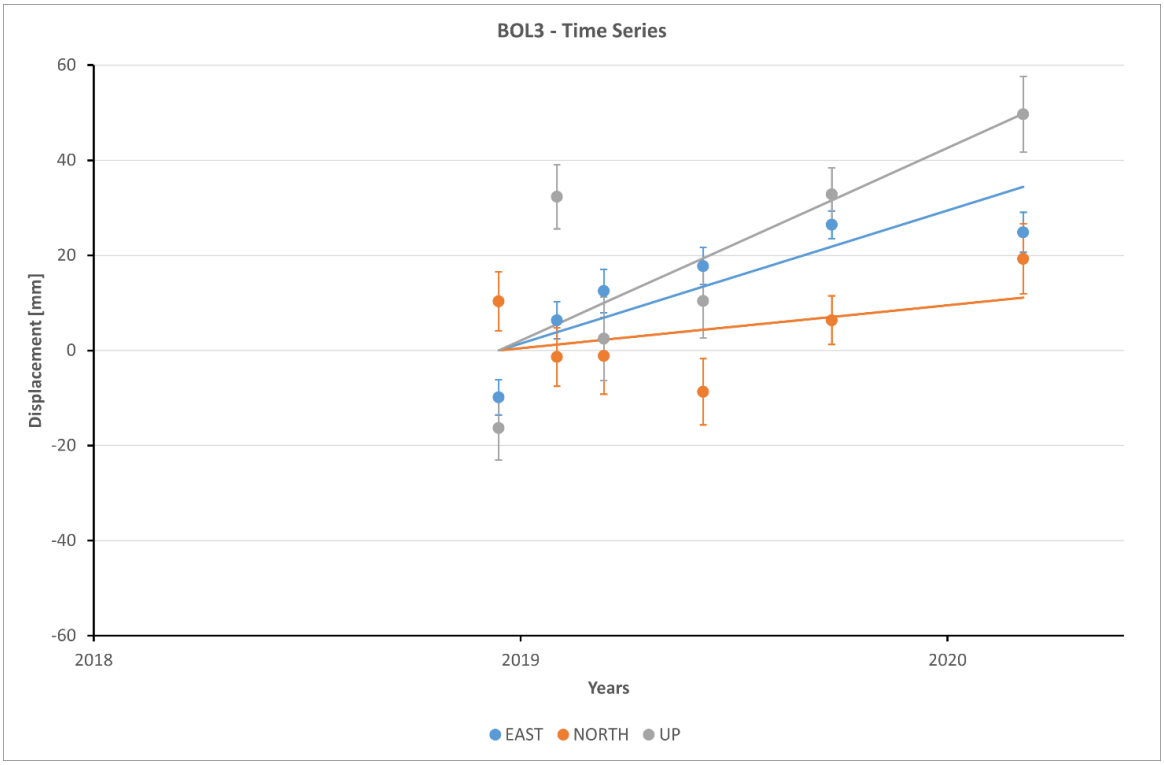

Figure 3. 34 - Time series between 2019 and 2020 of BOL3 campaign station.

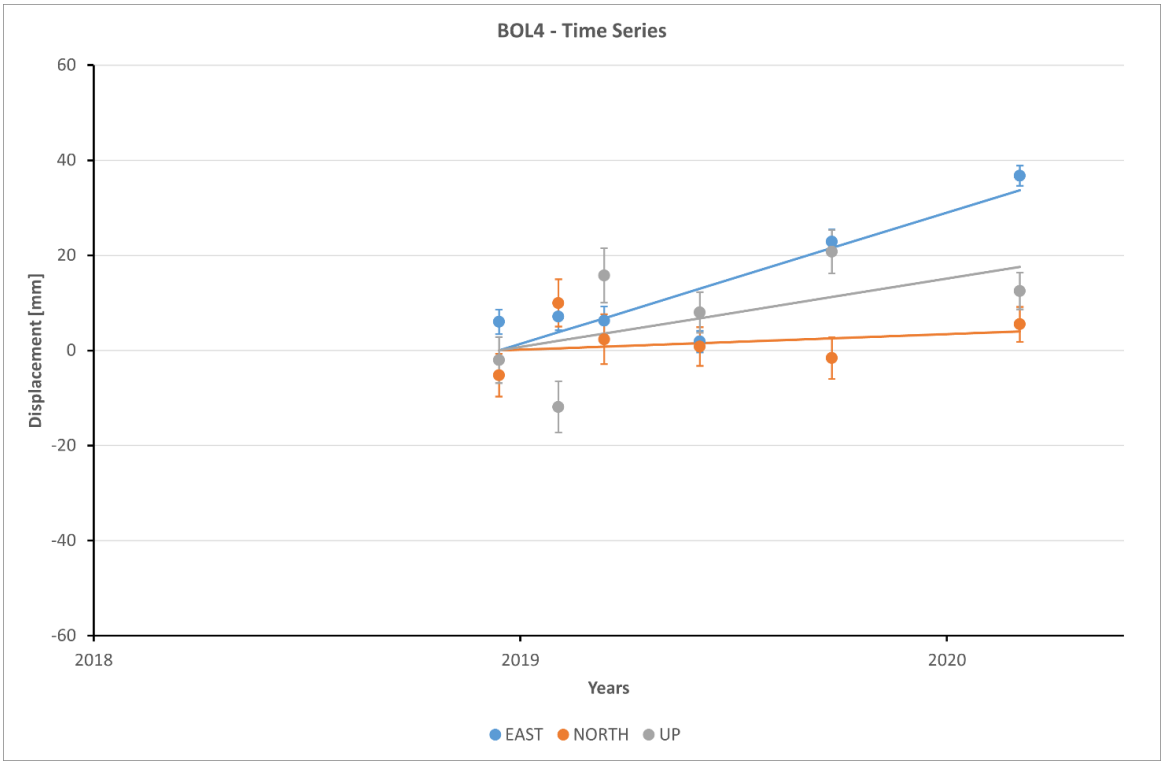

Figure 3. 35 - Time series between 2019 and 2020 of BOL4 campaign station.

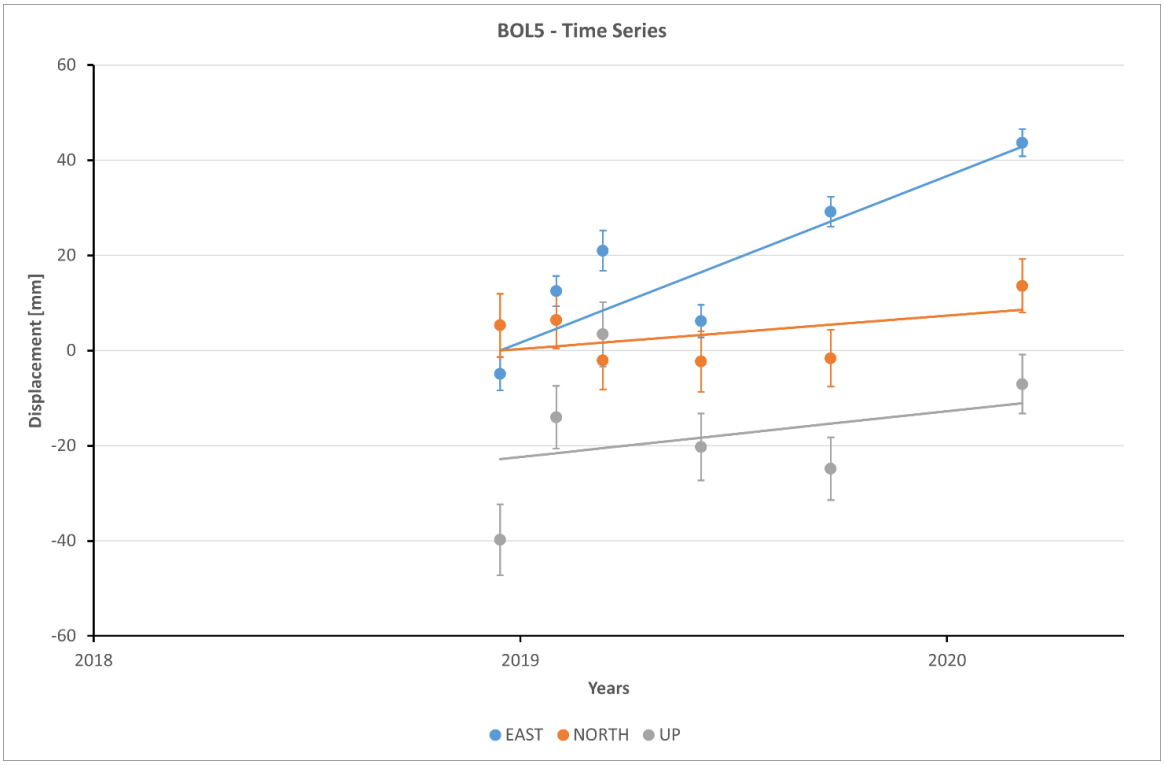

Figure 3. 36 - Time series between 2019 and 2020 of BOL5 campaign station.

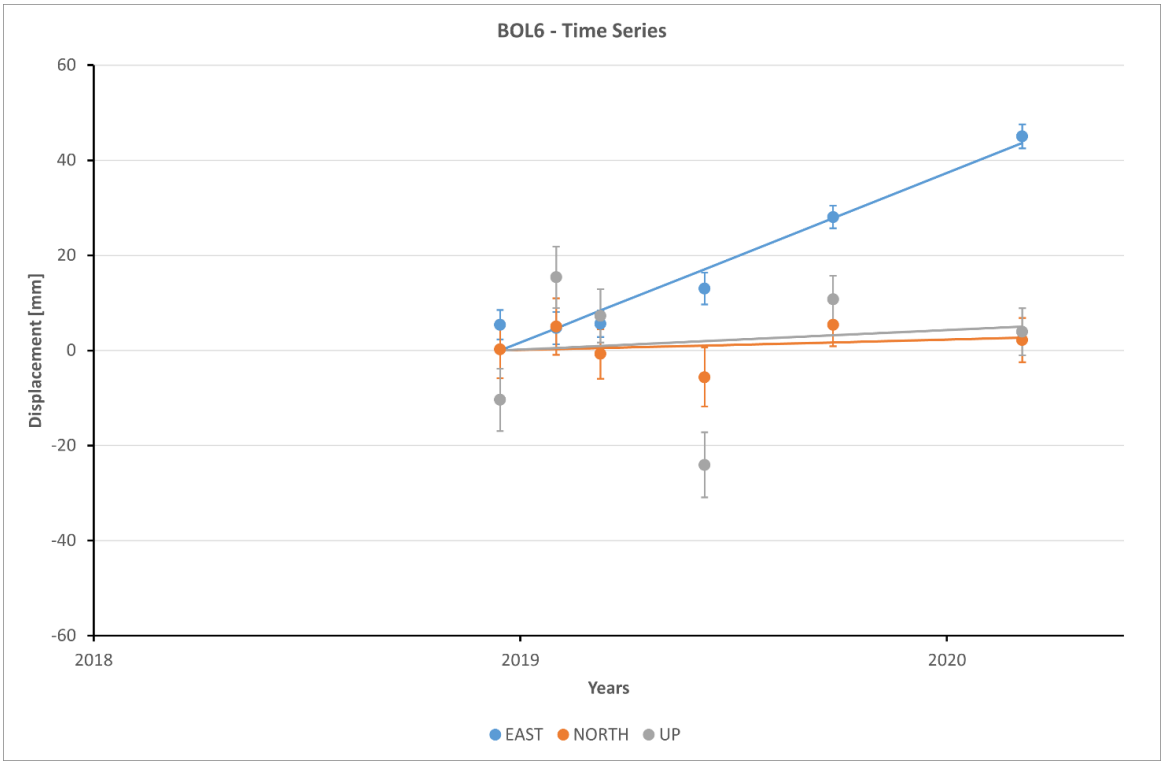

Figure 3. 37 - Time series between 2019 and 2020 of BOL6 campaign station.

The station BOL1 was destroyed just after its realization.

3.2.6 Nizzeti Net GNSS Station

In this paragraph, the time series of campaign GNSS station belonging to the sub network Nizzeti Net operated by University of Catania are shown. The campaign stations shown are:

STATION	NAME
NFW1	Via Pizzo Maugeri
NFW2	Marchese Casalotto
NFE3	Via Franca
NFE4	Via Nizzeti

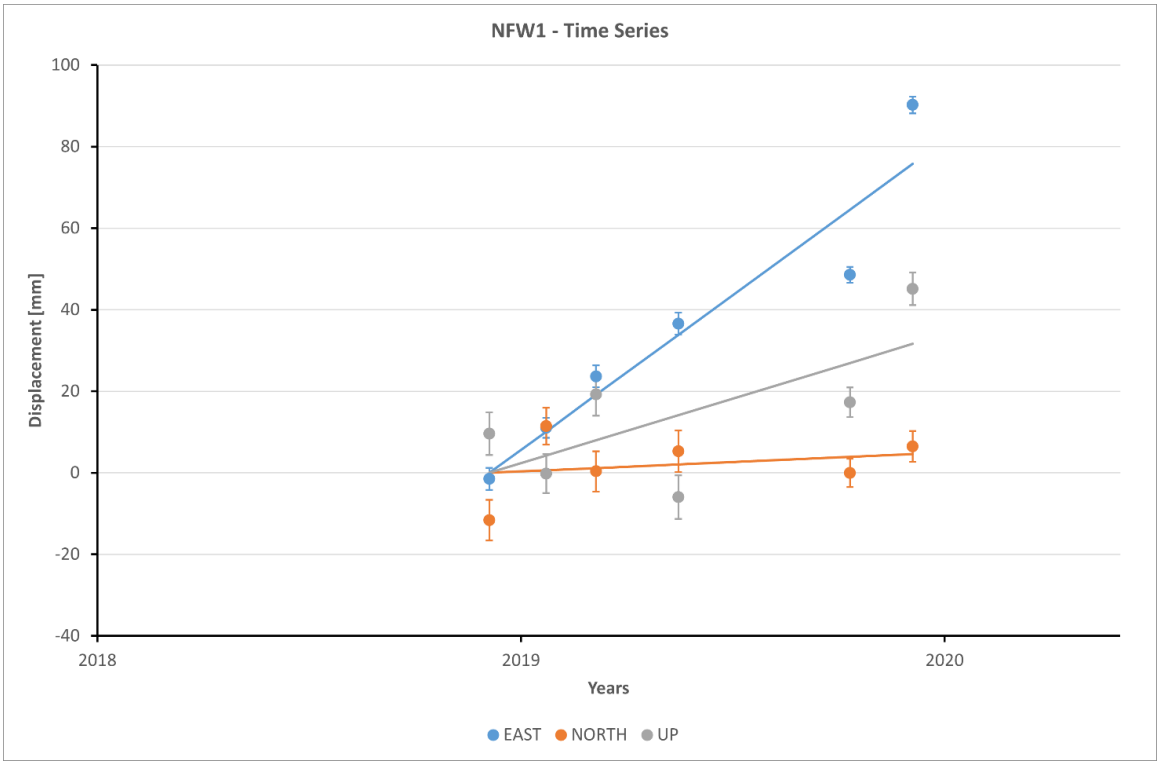

Figure 3. 38 - Time series between 2019 and 2020 of NFW1 campaign station.

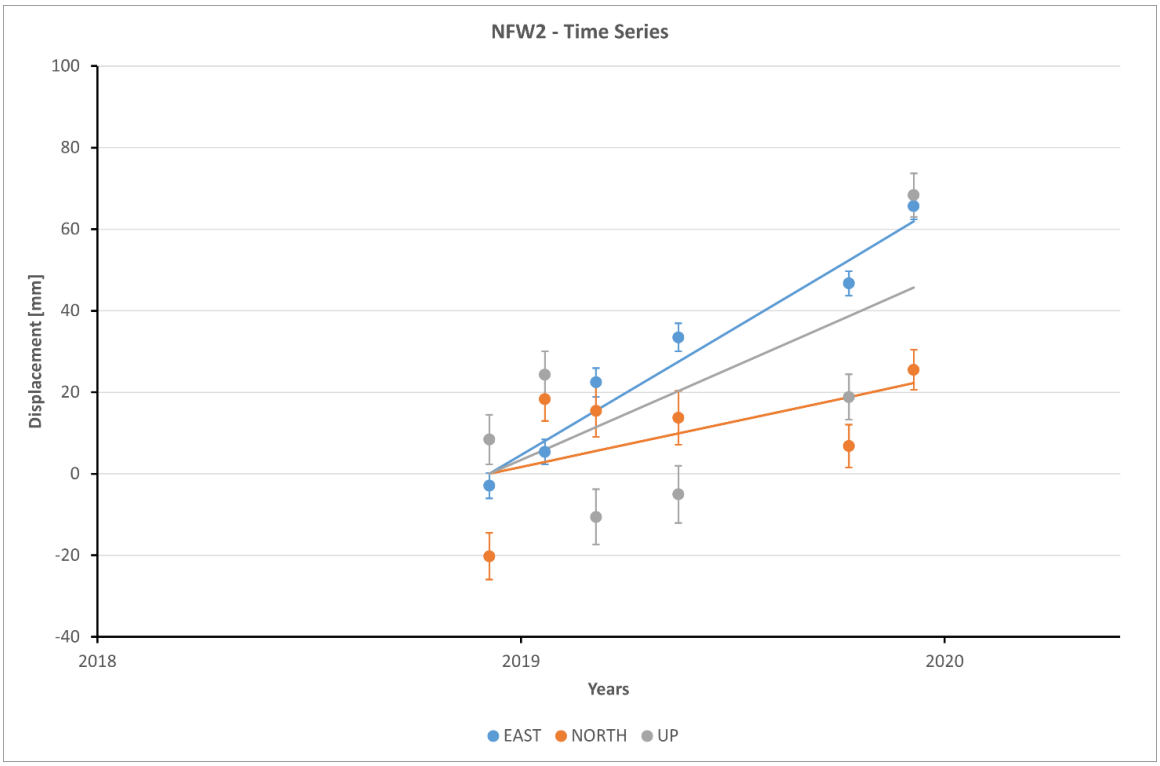

Figure 3. 39 - Time series between 2019 and 2020 of NFW2 campaign station.

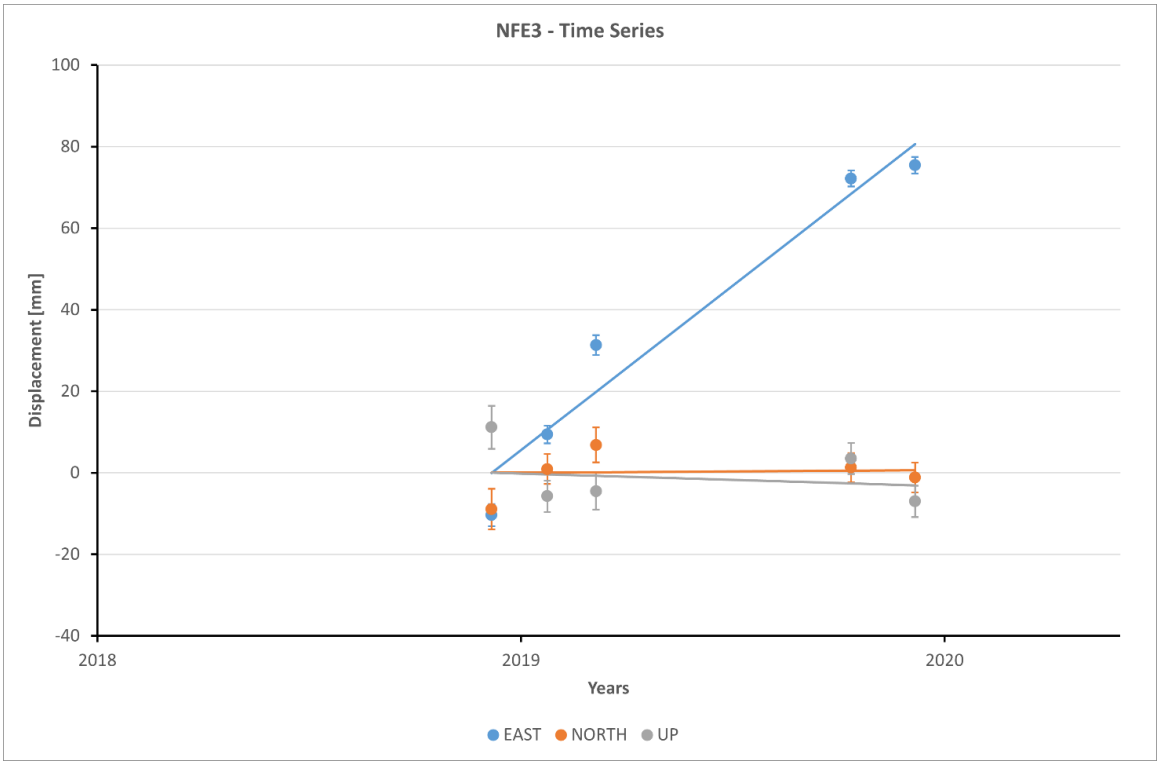

Figure 3. 40 - Time series between 2019 and 2020 of NFE3 campaign station.

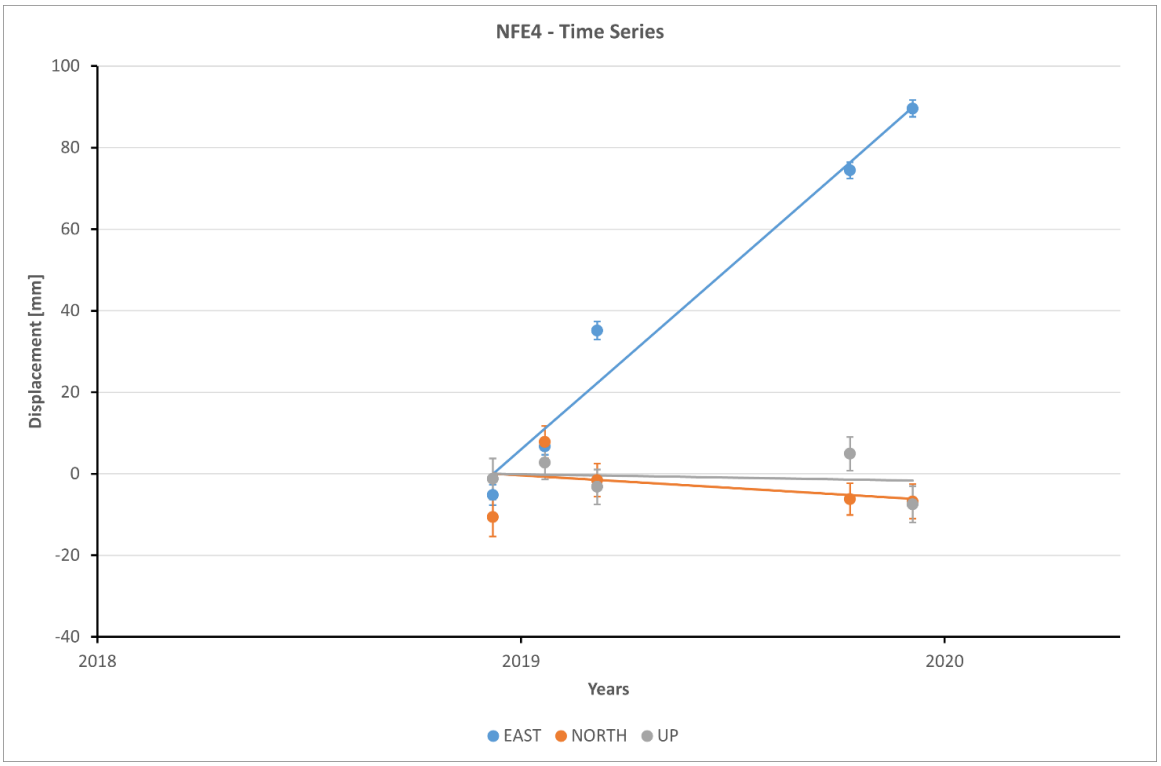

Figure 3. 41 - Time series between 2019 and 2020 of NFE4 campaign station.

3.3 Velocity field

3.3.1 Velocities

The velocities are tied to the ITRF2014 reference frame (Altamimi et al., 2016). The stations were selected according to the number of the occupation and to their reliability. The most reliable stations are the permanent stations due to their operation time. The velocities of the permanent stations in ITR2014 reference frame are:

Site	vE	vN	sigma
Unit	mm/yr	mm/yr	mm/yr
EIIV	21.5	19.5	0.3
ELAC	49.2	11.5	0.2
ENIC	26.1	9.0	0.1
EBDA	26.1	16.1	2.2
ETEC	45.6	9.5	0.3
EPED	29.6	5.3	0.4
ELIN	39.1	2.8	1.0
EPOZ	57.7	5.7	0.2
EC10	32.2	5.2	0.6
ELEO	61.7	-1.2	7.0
ESPC	31.2	9.4	0.1
EBAG	45.0	3.6	0.4
ERIP	51.4	7.8	0.7
EMFN	41.9	2.6	0.4

The velocities, in ITRF2014 reference frame, of the campaign stations belonging to the INGV-OE are:

STATION	**Ve [mm/yr]**	**Vn [mm/yr]**	**σE [mm/yr]**	**σN [mm/yr]**
~~ACID~~	~~169~~	~~-6~~	/	/
~~CASL~~	~~39~~	~~-3~~	/	/
EMSC	24.42	10.68	0.06	0.10
EPEL	28.13	7.84	0.05	0.09
ESGR	28.09	11.02	0.15	0.28
MDGR	54.60	7.26	0.13	0.24
MPL0	27.20	10.73	0.15	0.18
PDAP	44.48	2.05	0.10	0.18
MTSE	36.30	-1.17	0.39	0.41

The ACID and CASL are not plotted in the velocity field map because their operation time is too short, only two year from 1998 until 1999 for ACID and from 1997 until 1998 for CASL.

The velocities, in ITRF2014 reference frame, of the campaign stations belonging to the UNICT-Net are:

	STATION	Ve [mm/yr]	Vn [mm/yr]	σE [mm/yr]	σN [mm/yr]
San Gregorio Net	02SG	29.70	5.02	0.65	1.13
	07SG	42.20	5.07	0.86	1.50
	08SG	33.17	10.26	3.07	6.18
	09SG	44.35	4.95	1.12	1.88
	10SG	47.36	5.03	0.57	1.12
	15SG	30.26	8.80	0.64	1.17
	16SG	33.28	5.54	1.03	2.00
	19SG	44.14	9.46	0.58	1.11
	21SG	35.38	6.46	1.94	3.86
	22SG	43.28	4.16	1.63	3.13
Acitrezza Net	28AT	32.95	12.78	5.74	9.72
	32AT	48.28	14.55	1.33	2.75
	33AT	48.70	10.48	1.90	4.35
	37AT	34.48	11.73	5.63	9.17
	38AT	21.00	15.95	6.51	10.65
	39AT	70.69	-4.12	4.08	7.53
	~~41AT~~	/	/	/	/
	44AT	56.22	9.04	1.53	2.96
	45AT	41.92	1.25	1.04	1.88
	46AT	30.91	9.46	2.48	4.11
Nizzeti Net	NFW1	75.86	4.58	2.53	4.65
	NFW2	61.82	22.22	3.47	5.89
	NFE3	80.70	0.60	2.47	4.39
	NFE4	90.66	-6.15	2.40	4.70
Belpasso-Ognina Net	~~BOL1~~	/	/	/	/
	BOL2	31.69	10.55	1.95	3.65
	BOL3	27.99	9.03	3.79	6.49
	BOL4	27.63	3.30	2.31	4.02
	BOL5	35.02	7.02	3.03	5.78
	BOL6	35.66	2.17	2.66	4.97

3.3.2 Reference Frame

In order to analyse geophysically the local deformation, a local reference frame was created considering as stable the GNSS stations located in eastern Sicily. The aim of the realization of a local reference frame is to isolate the volcanic deformation and the tectonic deformation actives on the eastern flank of the volcano. Considering that the eastern Sicily is located close to Eurasian-Nubia plate boundary, the Eurasian and the Nubian reference frame are not suitable to correctly isolate the volcanic ground deformation from the background geodynamic pattern. The more suitable solution is considering the stations located both on the Nubian and Eurasia plates. Moreover, considering that in the etnean area the GNNS velocities reach hight values (at least one order of magnitude higher compare to the regional velocity field), it is useless computed an Eurel pole but it is better to obtain an average velocity field of east Sicily assuming that the velocity differences for each stations located on east Sicily are small. Considering this hypothesis and a short period (e.g. few years), it is possible to consider that the regional velocity has a linear trend thank to the little different of the GNSS velocities. In this case the regional velocity was detrended to the GNSS velocity of Mount Etna.

Eight GNSS permanent stations were chosen, six stations are located on the hyblaean area (Foreland) and two are located on north-east Sicily (Appenninic-Maghrebian chain). The chosen stations are:

1. HLNI (Scordia) belonging to the INGV-OE network;
2. SSYX (Sortino) belonging to the INGV-OE network;
3. HAGA (Brucoli) belonging to the INGV-OE network;
4. HMDC (Ragusa) belonging to the RDN (Rete Dinamica Nazionale) manage by Istituto Geografico Militare (IGM);
5. HAV1 (Avola) belonging to the INGV-OE network;
6. NOT1 (Noto) belonging to the IGS Network (International GNSS Service);
7. GALF (Gagliano) belonging to the RING (Rete Integrata Nazionale GNSS) network manage by INGV-SI;
8. MNOV (Novara di Sicilia) belonging to the INGV-OE network;

STATION	NAME	LONG [°]	LAT [°]	Ve [mm/yr]	Vn [mm/yr]	σE [mm/yr]	σN [mm/yr]
HLNI	Scordia	14.872	37.349	21.5	19.1	0.16	0.17
SSYX	Sortino	15.076	37.158	21.6	19.6	0.14	0.15
HAGA	Brucoli	15.155	37.286	21.9	19.5	0.15	0.14
HMDC	Ragusa	14.783	36.959	21.2	19.4	0.23	0.16
HAV1	Avola	15.122	36.960	21.5	19.8	0.17	0.15
NOT1	Noto	14.99	36.876	21.2	19.5	0.21	0.16
GALF	Gagliano	14.567	37.711	21.3	19.0	0.25	0.22
MNOV	Novara di Sicilia	15.136	38.029	20.8	19.6	0.20	0.35

The average velocity of the eight stations is Ve = 21.4 ± 0.3 mm/yr and Vn = 19.4 ± 0.3 mm/yr. This velocity represents the best solution to isolate the volcanic deformation from the regional deformation. Considering only the stations located on the hyblaean area and also the station located on North-East Sicily (GALF and MNOV), they show a consistent velocity within 0.3 mm/yr.

Moreover, for the San Gregorio Net and Acitrezza Net, the velocities for this sub-network are referred for a local reference frame, called San Gregorio reference frame. In this case the station 02SG is considered stable and the velocities for the benchmarks belonging to the San Gregorio and Acitrezza Net are also calculated in this reference frame.

3.3.3 Velocity Field

The velocity fields analysis has been divided into concentric areas, in each box proceeding from the largest to the smallest, the velocity of the permanent stations has been considered up to the discrete stations of the local networks with a smaller time interval for the small boxes. All this to facilitate the strain analysis and to allow an easier visualization of the velocity fields.

In this paragraph the velocity fields are listed. The reference frame is calculated considering the south eastern Sicily stable. The velocity of south eastern Sicily is Ve = 21.4 ± 0.3 mm/yr and Vn = 19.4 ± 0.3 mm/yr i.e. the average velocity of the eight stations listed in the previous section.

STATION	NAME	LONG [°]	LAT [°]	Ve [mm/yr]	Vn [mm/yr]	σE [mm/yr]	σN [mm/yr]
HLNI	Scordia	14.872	37.349	0.12	-0.34	0.46	0.47
SSYX	Sortino	15.076	37.158	0.22	0.16	0.44	0.45
HAGA	Brucoli	15.155	37.286	0.52	0.06	0.45	0.44
HMDC	Ragusa	14.783	36.959	-0.18	-0.04	0.53	0.46
HAV1	Avola	15.122	36.96	0.12	0.36	0.47	0.45
NOT1	Noto	14.99	36.876	-0.18	0.06	0.51	0.46
GALF	Gagliano	14.567	37.711	-0.08	-0.44	0.55	0.52
MNOV	Novara di Sicilia	15.136	38.029	-0.58	0.16	0.5	0.65
EIIV	Catania	15.082	37.514	1.2	-1.8	0.45	0.45

In Figure 3. 42 the velocity field of the station located in eastern Sicily are shown, the station EIIV show the faster velocity compared to the others due the influence of Etna volcano, the tectonic features located on the eastern flank of the volcano and especially the compressional structures located on the north-east of EIIV.

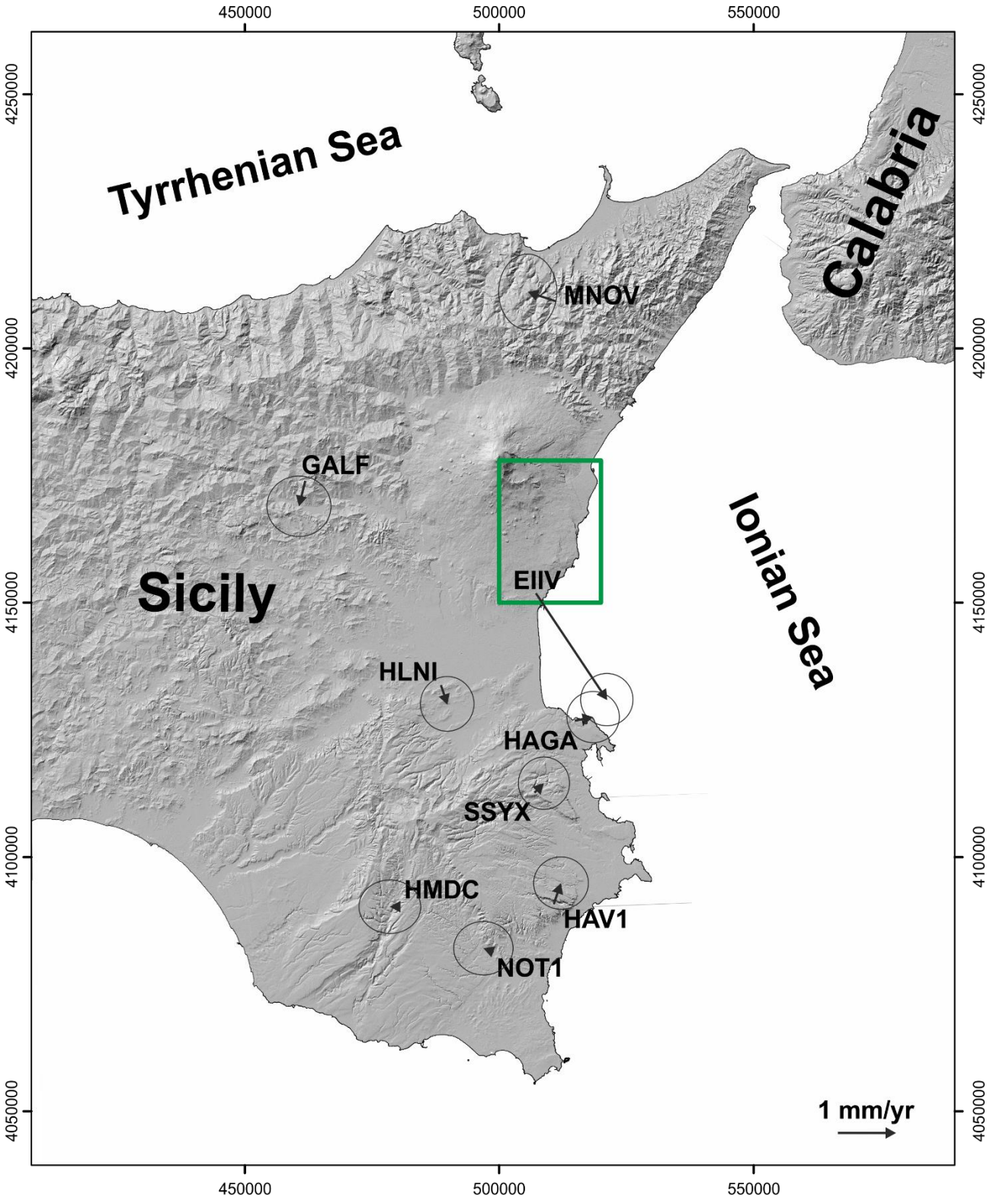

Figure 3. 42 - Velocity field of eastern Sicily. The GNSS permanent stations used for the calculation are shown. The green box is the Figure 3. 43.

STATION	NAME	LONG [°]	LAT [°]	Ve [mm/yr]	Vn [mm/yr]	σ [mm/yr]
EIIV	Catania	15.082	37.514	1.2	-1.8	0.45
ELAC	Isola Lachea	15,166	37,561	27.8	-7.9	0.5
ENIC	Nicolosi	15.019	37.614	4.7	-10.4	0.4
EBDA	Bosco di Aci	15.122	37.634	4.7	-3.3	2.5
ETEC	Santa Tecla	15.178	37.638	24.2	-9.9	0.6
ELIN	Linera	15.136	37.667	17.7	-16.6	1.3
EPOZ	Pozzillo	15.189	37.672	36.3	-13.7	0.5
EC10	/	15.083	37.692	10.8	-14.2	0.9
ELEO	S. Leonardello	15.172	37.692	40.3	-20.6	7.3
ESPC	Monte Serra Pizzuta Calvarina	15.027	37.693	9.8	-10	0.4
EBAG	Baglio	15.161	37.702	23.6	-15.8	0.7
ERIP	Riposto	15.197	37.729	30	-11.6	1
EMFN	Monte Fontana	15.090	37.736	20.5	-16.8	0.7
EPED	Pedara	15.06	37.617	8.2	-14.1	0.7

In Figure 3. 43 the velocity field of only the permanent stations belonging of INGV-OE are listed, there are represented only the stations located on the middle and south eastern flank of Mt Etna. In this reference frame the long-term velocity field of the flanks of Etna is represented, which show the general SE-E movement of the eastern flank.

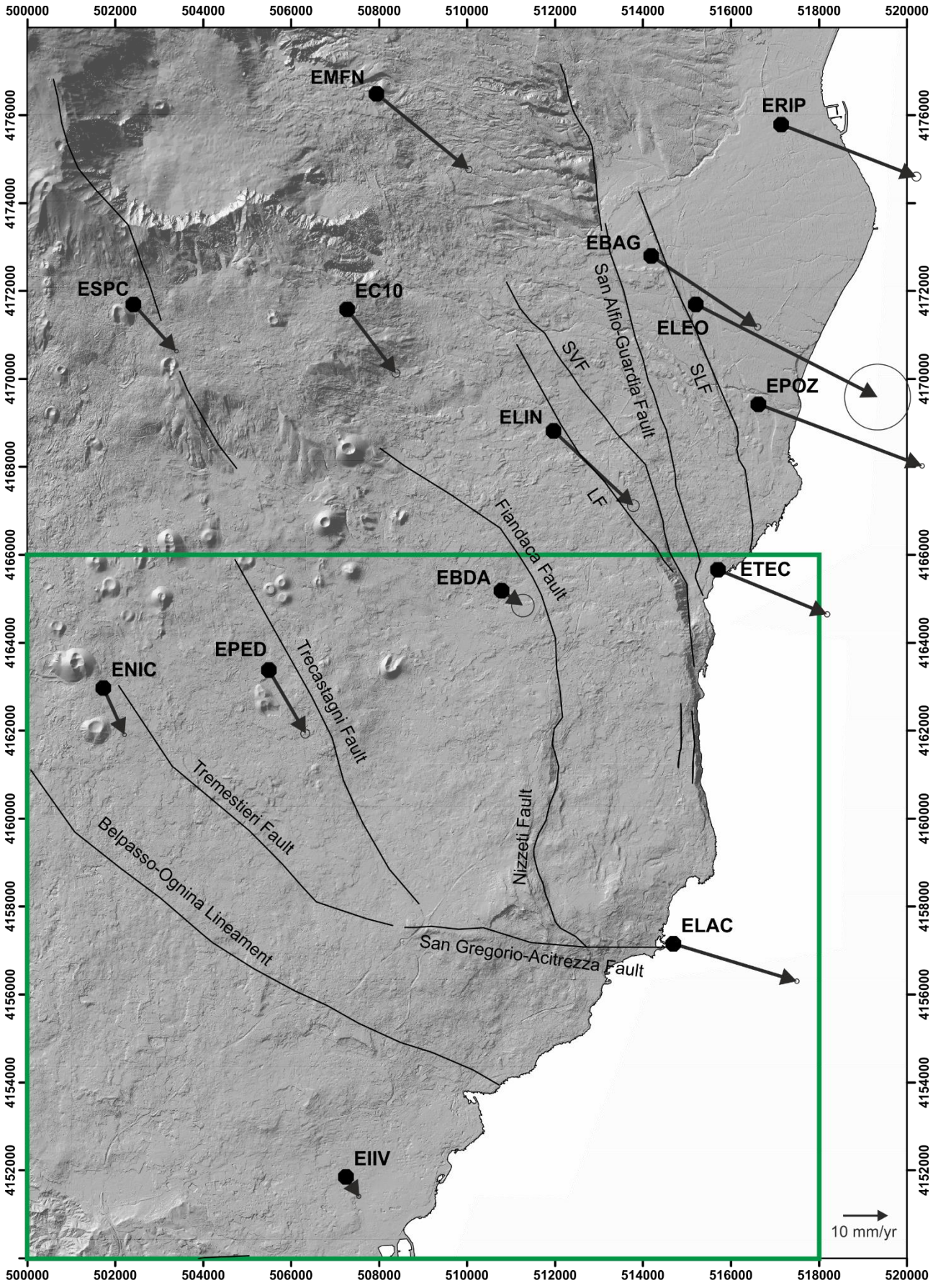

Figure 3. 43 – Velocity field of the eastern flank of Mount Etna. Black circles are the GNSS permanent stations. The green box is the Figure 3. 44.

STATION	NAME	Ve [mm/yr]	Vn [mm/yr]	σE [mm/yr]	σN [mm/yr]
~~ACID~~	~~Acireale~~	~~147.6~~	~~-25.4~~	/	/
~~CASL~~	~~Casalotto~~	~~17.6~~	~~-22.4~~	/	/
EMSC	Mascalucia	3.02	-8.72	0.36	0.40
EPEL	Mompeloso	6.73	-11.56	0.35	0.39
ESGR	San Gregorio	6.69	-8.38	0.45	0.58
MDGR	Madonna delle Grazie	33.20	-12.14	0.43	0.54
MPL0	Mompelieri	5.80	-8.67	0.45	0.48
PDAP	Piano Api	23.08	-17.35	0.40	0.48
MTSE	Monte Serra	14.90	-20.57	0.69	0.71

	STATION	NAME	Ve [mm/yr]	Vn [mm/yr]	σE [mm/yr]	σN [mm/yr]
Nizzeti Net	NFW1	Via Pizzo Maugeri	54.46	-14.82	2.83	4.95
	NFW2	Marchese Casalotto	40.42	2.82	3.77	6.19
	NFE3	Via Franca	59.30	-18.80	2.77	4.69
	NFE4	Via Nizzeti	69.26	-25.55	2.70	5.00
Belpasso-Ognina Net	~~BOL1~~	~~Viale Lainò~~	/	/	/	/
	BOL2	Via Teseo	10.29	-8.85	2.25	3.95
	BOL3	Via Giuseppe Parini	6.59	-10.37	4.09	6.79
	BOL4	Via Cardinale Nava	6.23	-16.10	2.61	4.32
	BOL5	Gravina San Paolo	13.62	-12.38	3.33	6.08
	BOL6	Via Guardia	14.26	-17.23	2.96	5.27

In Figure 3. 44 the velocity field of the station in the BOX2 are show. The permanent and discrete stations of INGV-OE and the stations of Nizzeti Net and Belpasso Net, belonging to the UNICT-Net are shown. The stations of UNICT-Net shown the short-term velocity that it is affected by transient deformation during the post seismic period after the 26 December 2018 Earthquake.

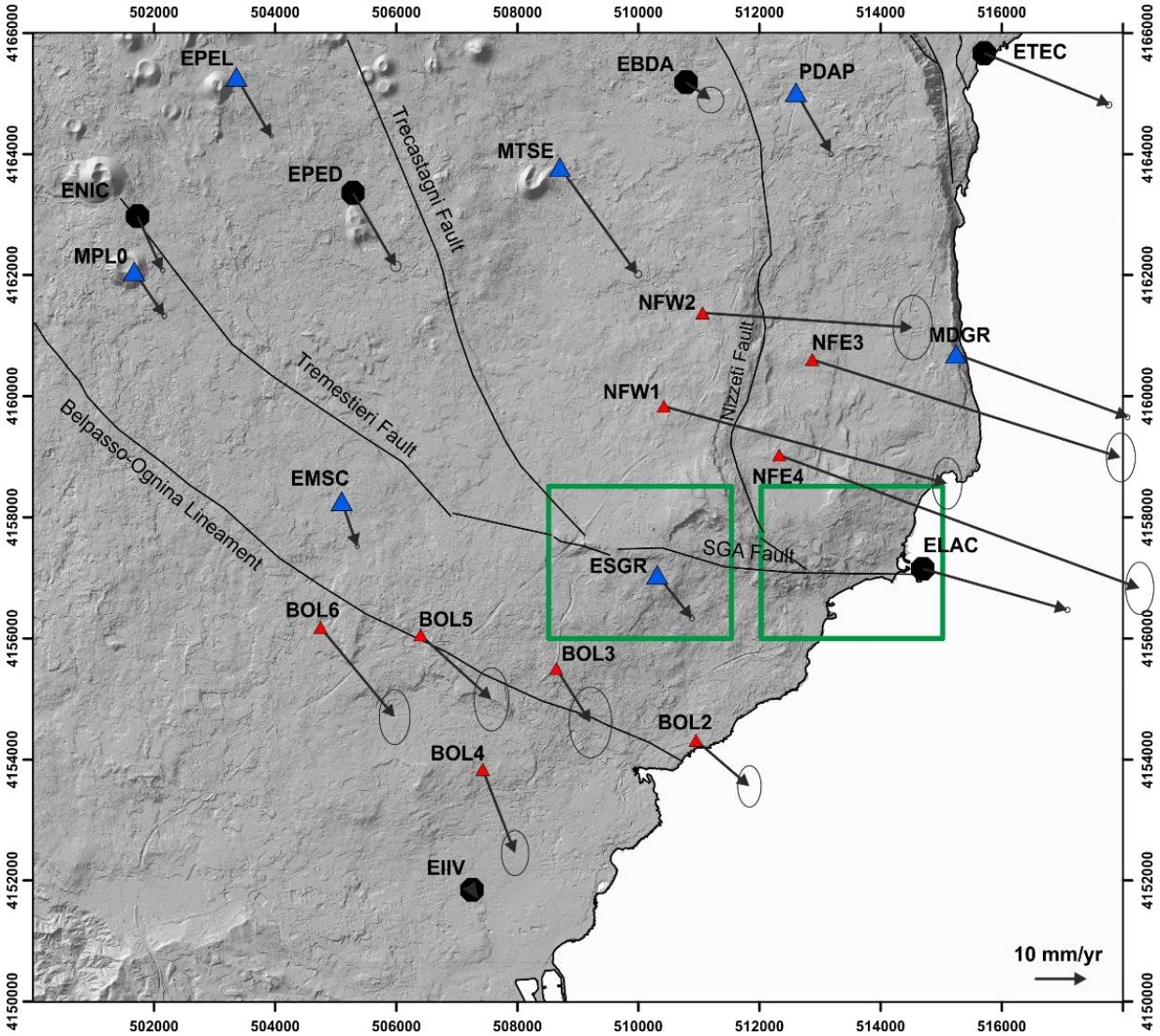

Figure 3. 44 – Velocity field of south eastern flank of Mount Etna. The permanent (black circles) and campaign (blue triangles) stations belong to the INGV-OE. Red triangles are the campaign GNSS stations belong to the UNICT-NET. Green boxes are the Figure 3. 45.

		EASTERN SICILY STABLE				02SG STABLE			
	STATION	**Ve [mm/yr]**	**Vn [mm/yr]**	**σE [mm/yr]**	**σN [mm/yr]**	**Ve [mm/yr]**	**Vn [mm/yr]**	**σE [mm/yr]**	**σN [mm/yr]**
San Gregorio Net	02SG	8.30	-14.38	0.95	1.43	0.00	0.00	1.89	2.85
	07SG	20.80	-14.33	1.16	1.80	12.50	0.05	2.11	3.22
	08SG	11.77	-9.14	3.37	6.48	3.47	5.24	4.31	7.91
	09SG	22.95	-14.45	1.42	2.18	14.65	-0.07	2.37	3.60
	10SG	25.96	-14.37	0.87	1.42	17.65	0.01	1.82	2.85
	15SG	8.86	-10.60	0.94	1.47	0.56	3.78	1.88	2.90
	16SG	11.88	-13.86	1.33	2.30	3.58	0.52	2.27	3.72
	19SG	22.74	-9.94	0.88	1.41	14.43	4.43	1.83	2.84
	21SG	13.98	-12.94	2.24	4.16	5.67	1.44	3.19	5.59
	22SG	21.88	-15.24	1.93	3.43	13.58	-0.86	2.88	4.86
Acitrezza Net	28AT	11.55	-6.62	6.04	10.02	3.25	7.76	6.98	11.45
	32AT	26.88	-4.85	1.63	3.05	18.58	9.53	2.58	4.47
	33AT	27.30	-8.92	2.20	4.65	19.00	5.46	3.15	6.07
	37AT	13.08	-7.67	5.93	9.47	4.78	6.71	6.87	10.89
	38AT	-0.40	-3.45	6.81	10.95	-8.71	10.93	7.75	12.38
	39AT	49.29	-23.52	4.38	7.83	40.98	-9.14	5.32	9.25
	~~41AT~~	/	/	/	/	/	/	/	/
	44AT	34.82	-10.36	1.83	3.26	26.51	4.02	2.78	4.69
	45AT	20.52	-18.15	1.34	2.18	12.21	-3.77	2.29	3.61
	46AT	9.51	-9.94	2.78	4.41	1.20	4.44	3.72	5.83

In Figure 3. 45, the velocity fields of San Gregorio and Acitrezza Net are shown. The velocities are referred to the Eastern Sicily reference frame and also, locally, to the 02SG reference frame. In the first case the velocities are still showing the global deformation of Mt. Etna while in the second one, the velocities, referred to the benchmark 02SG, show the different movement of the two blocks of the San Gregorio Acitrezza Fault. In that local reference frame, it is clear that the northern block is moving toward east with respect to the southern block and that the east velocity is increasing toward east.

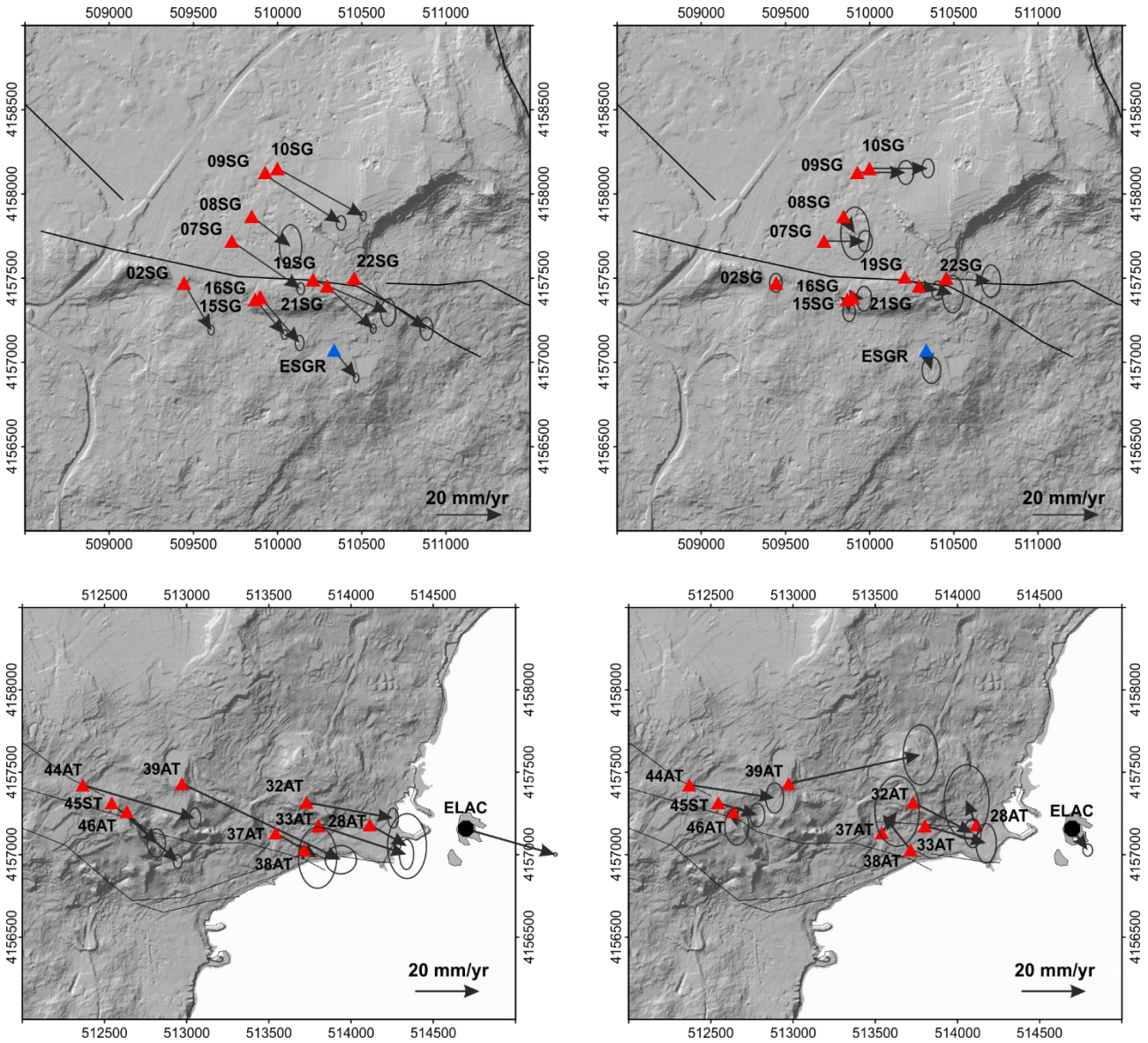

Figure 3. 45 – On the top, the velocity field of the San Gregorio Net and on the bottom the velocity field of the Acitrezza Net are shown. On the left the velocity field is referred to the eastern Sicily while on the right the velocity field is referred to the benchmarks 02SG. GNSS campaign stations belong to the UNICT-NET are represented by red triangles, GNSS stations belong to the INGV-OE are represented by blue triangles (campaign stations) and by red circles (permanent stations).

CHAPTER 4

INTERFEROMETRY

4.1 Introduction

Synthetic Aperture Radar (SAR) is a microwave imaging system. It has cloud penetrating capabilities because it uses microwaves. It has day and night operational capabilities because it is an active system. Its 'interferometric configuration', Interferometric SAR or InSAR, allows accurate measurements of the variations of the radiation travel path because it is coherent. Measurements of travel path variations as a function of the satellite position and time of acquisition allow generation of Digital Elevation Models and measurement of centimetric surface deformations of the terrain. One of the major difficulties of the InSAR technique is the fact that it is not the travel path that is measured, but the travel phase modulo, an integer number of half-wavelengths of the carrier phase.

In 1991, ESA launched the first European Remote Sensing satellite (ERS 1) and started building a catalogue of interferometric data covering the whole Earth. ERS 2 was launched in 1995, to continue and expand the work. For nine months in 1995/1996, the two satellites undertook a 'tandem' mission, in which they orbited Earth only 24 hours apart. The image pairs acquired provide much greater interferogram coherence than is normally possible, allowing scientists to generate detailed digital elevation maps and observe changes over a very short space of time.

In March 2000, ERS-1 ended operations. ERS-2 continued to operate until its end in September 2012. In 2002, ERS-2 was joined by Envisat (Enviromental Satellite), the largest Earth observation satellite ever built. Envisat and ERS-2 images are compatible for interferometry processing purposes and the satellites continue to work together, adding to the ever growing set of interferometric data. The Envisat's mission has been declared concluded on 9 May 2012. The Envisat mission has been followed by the Sentinel constellation of satellites on 3 April 2014. The Sentinel-1 mission is composed of a constellation of two satellites, SENTINEL-1A and SENTINEL-1B, sharing the same orbital plane. The SENTINEL-1 mission includes C-Band (ν = 5.405 GHz and λ = 5.546 cm) imaging operating in four exclusive imaging mode with different resolution (down to 5 m) and coverage (up to 400 km). It provides dual polarisation capability, short revisit times (12 days for each satellite, thus 6 days combining both) and fast product delivery. For each observation, precise measurements of spacecraft position (based on on board GNSS data) and altitude are available.

Sentinel-1 includes a right-looking active phased array antenna providing fast scanning in elevation and azimuth, data storage capacity of 1410 Gb and 520 Mbit/s capacity.

The C-SAR instrument supports operation in dual polarisation (HH+HV, VV+VH) implemented through one transmit chain (switchable to H or V) and two parallel receive chains for H and V polarisation. Dual polarisation data is useful for land cover classification and sea-ice applications. SENTINEL-1 operates in four exclusive acquisition modes:

- Stripmap (SM)
- Interferometric Wide swath (IW)
- Extra-Wide swath (EW)
- Wave mode (WV).

Stripmap imaging mode is provided for continuity with ERS and Envisat missions. Stripmap provides coverage with a 5 m by 5 m resolution over a narrow swath width of 80 km. One of six imaging swaths can be selected by changing the beam incidence angle and the elevation beamwidth. The Interferometric Wide swath (IW) mode allows combining a large swath width (250 km) with a moderate geometric resolution (5 m by 20 m). The IW mode images three sub-swaths using Terrain Observation with Progressive Scans SAR (TOPSAR). With the TOPSAR technique, in addition to steering the beam in range as in SCANSAR, the beam is also electronically steered from backward to forward in the azimuth direction for each burst, avoiding scalloping and resulting in a higher quality image. Interferometry is ensured by sufficient overlap of the Doppler spectrum (in the azimuth domain) and the wave number spectrum (in the range domain). The TOPSAR technique ensures homogeneous image quality throughout the swath. The IW mode is the default acquisition mode over land. The Extra Wide swath imaging mode is intended for maritime, ice and polar zone operational services where wide coverage and short revisit times are demanded. The EW mode works similarly to the IW mode employing a TOPSAR technique using five sub-swaths instead of three, resulting in a lower resolution (20 m by 40 m). The EW mode can also be used for interferometry as with the IW mode. SENTINEL-1 Wave mode, in conjunction with global ocean wave models, can help determine the direction, wavelength and heights of waves on the open oceans. Wave mode acquisitions are composed of stripmap imagettes of 20 km by 20 km, acquired alternately on two different incidence angles. Wave imagettes are acquired every 100 km, with imagettes on the same incidence angle separated by 200 km (ESA, 2020).

Differential SAR (Synthetic Aperture Radar) Interferometry (DInSAR) is one of the most used remote sensing techniques for the investigation of Earth's surface deformation phenomena (Massonnet and Feigl, 1998).

It permits the retrieval of surface deformation maps with centimetre to millimetre accuracy, starting from the phase difference (interferogram) of SAR image pairs relevant to the same area of interest but acquired at different epochs and with a significantly small orbital spatial separation (baseline) (Franceschetti and Lanari, 2018; Gabriel et al., 1989).

Originally, DInSAR was developed to analyse single deformation episodes, such as earthquakes (Massonnet et al., 1993), but it has subsequently evolved towards the study of temporal behaviour of the detected displacements. This evolution has been possible thanks to (a) the availability of temporally extended SAR data archives (b) the implementation of the multi-temporal DInSAR (Berardino et al., 2002; Crosetto et al., 2005; Ferretti et al., 2001; Hooper et al., 2004; Kampes, 2006; Mora et al., 2003; Sansosti et al., 2010; Werner et al., 2003) that permit the generation of surface deformation time series and the corresponding mean velocity maps of and an observed area through the exploitation of a sequence of interferograms (Lanari et al., 2004).

The SBAS approach relies only on small spatial and temporal baseline interferograms, which define a system of equations that can be inverted to retrieve the deformation time series, through a method based on Singular Value Decomposition (SVD). Thanks to the above-mentioned small baseline constraint, it is possible to drastically mitigate the noise phenomena affecting the DInSAR interferograms, referred to as decorrelation effects, thus maximizing the number of reliably analysed SAR pixels. A parallel implementation of the SBAS algorithm (Casu et al., 2014), referred to as P-SBAS, which the generation of deformation time series in a very short time by taking advantage of distributed computing systems, has been presented (de Luca et al., 2015 and reference therein).

4.2 Geohazards TEP and Sentinell-1 P-SBAS tool

4.2.1 Geohazard Thematic Exploitation Platform

The online Geohazards-Thematic Exploitation Platform (TEP) (ESA, 2015) was used for the interferometric analysis. The Geohazards Exploitation Platform or GEP aims to support the exploitation of satellite EO for geohazards. It follows the Supersites Exploitation Platform (SSEP), originally initiated in the context of the Geohazard Supersites & Natural Laboratories initiative (GSNL). The geohazards platform has been expanded to address broader objectives

of the geohazards community. It is a contribution to the CEOS WG Disasters to support its Seismic Hazards Pilot and terrain deformation applications of its Volcano Pilot. The geohazards platform and SSEP are sourced with elements (data, tools, and processing including INSAR) relevant to the Geohazards theme and related exploitation scenarios. Today the GEP has primary focus on mapping hazard prone land surfaces and monitoring terrain deformation. It allows users to access and exploit large collections ENVISAT ASAR and ERS SAR data hosted in the ESA (European Space Agency) clusters and in ESA's Virtual Archive. A large collection of ENVISAT ASAR and ERS SAR are available in the platform. In 2014 an additional 40 Terabytes of ERS and ASAR data was added in response to requirements of the CEOS Pilot on Seismic Hazards. The GEP is also be used to gradually access Sentinel-1A data. The activity also intends to support access to other EO missions' data than from ESA such as from other space agencies and mission owners and operators.

4.2.2 P-SBAS Sentinel-1 processing on-demand

Within the GEP platform, the web tool P-SBAS Sentinel-1 processing on-demand has been used (Casu et al., 2014; de Luca et al., 2015; Manunta et al., 2019). It was created by the CNR -IREA (Consiglio Nazionale delle Ricerche – Istituto per il Rilevamento Elettromagnetico dell'Ambiente) of Naples. This service is based on the implementation of the DInSAR algorithm referred to as Parallel Small Baseline Subset (P-SBAS) approach and produce surface deformation mean velocity maps and time series in an unsupervised manner. Such results are obtained by exploiting the available huge ERS and ENVISAT SAR data archives.

In 2019, Manunta et al. present a new implementation of P-SBAS web tool (P-SBAS Sentinel-1 processing on-demand) for the efficient generation of deformation time series from Sentinel-1 (S-1) interferometric wide (IW) swath SAR data sets. This tool is based on a processing chain that it is implemented within the original P-SBAS approach (Casu et al., 2014).

The processing chain developed to efficiently process the S-1 IW multitemporal SAR data sets is divided into nine steps. The first step concern the ingestion and unpacking operations performed on the input SAR data: i) sequence of temporally separated S-1 IW SLC images, ii) corresponding orbital information and iii) precise digital elevation model (DEM) of the overall investigated area.

The second step performs a series of sequentially operations: i) selection of the master image used as a reference geometry for registration of the entire SAR data set, ii) the area of interest common to the whole Single Look Complexs (SLCs) and iii) the bursts to be processed.

The third step is the conversion of the available DEM into the radar (azimuth and range) coordinates through the range-Doppler equations (Curlander and McDonough, 1991) followed by the estimation of both range and azimuth target to sensor distances with respect to the master orbital position.

The fourth step is the interferogram generation that consists in the coregistration of each burst of the SLC images with respect the master acquisition geometry and also a spatial complex average (multilook) operation is carried out to mitigate the decorrelation noise effects.

In the fifth step, the corrected multilook interferograms and corresponding spatial coherence maps of adjacent bursts are accurately put together through an interferogram mosaicking operation.

In the sixth step, the interferogram noise filtering procedure is executed according to a pixel granularity parallelization level.

The seventh step is the network selection that consists in the selection of an optimized reduced network of time redundant interferograms forming a triangulation in the temporal/perpendicular baseline.

The eighth step is the unwrapping phase operation by applying the EMCF (Extension of the Minimum Flow Cost algorithm) (Pepe and Lanari, 2006).

The final step consists in the generation of time series and the corresponding mean deformation velocity maps. This step performs the inversion of the retrieved sequence of unwrapped interferograms by searching for a least square solution, in addition this step computes the temporal coherence factor to provide a measurement of the reliability of the achieved results and filters out possible undesired atmospheric artifacts from the displacement time series.

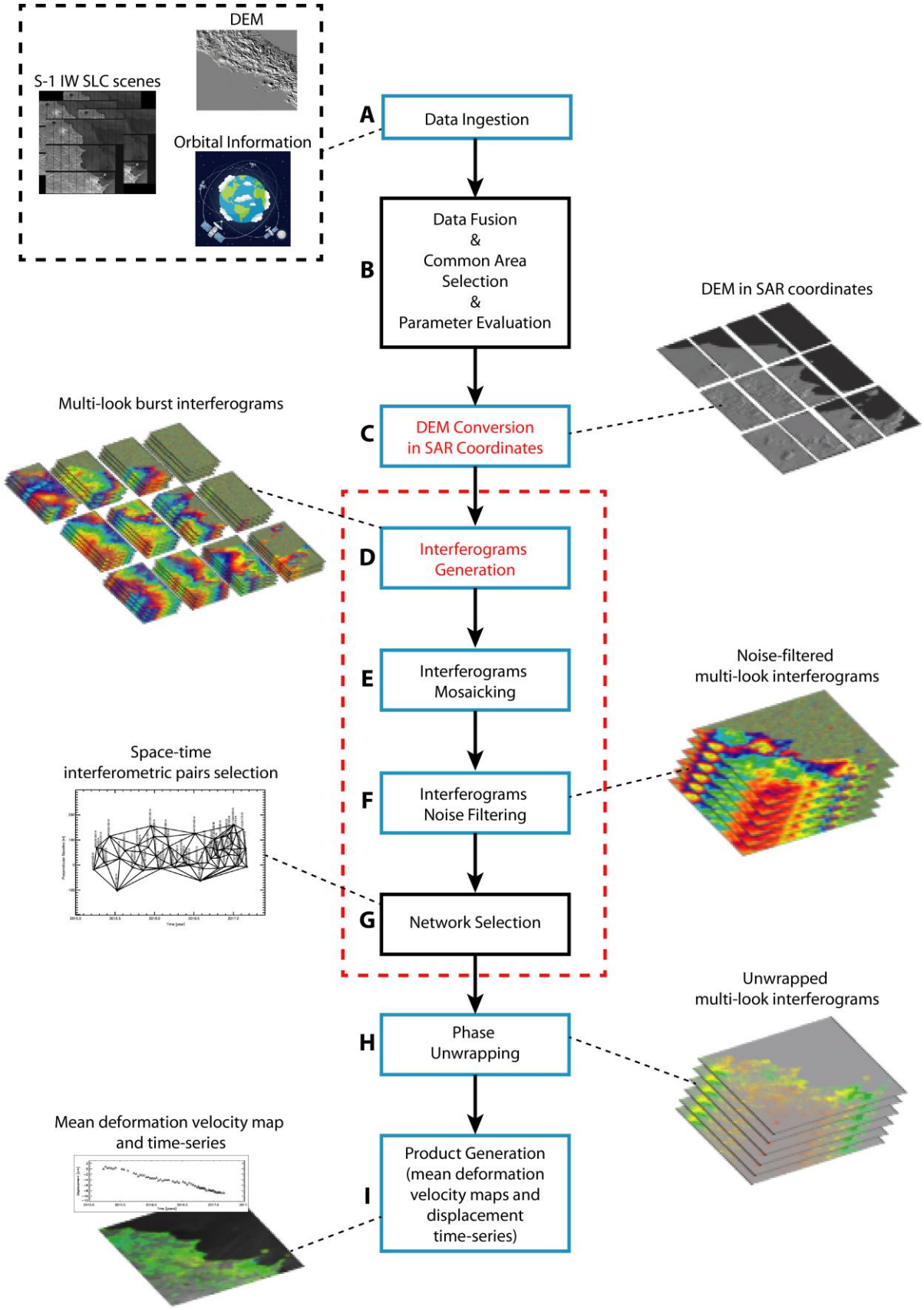

Figure 4. 1 – Sentinel -1 P-SBAS processing chain workflow. The black blocks represent the sequentially executed steps, whereas the blue ones indicate the parallel computed operations; the procedures that benefit from a burst granularity parallelization level are highlighted in red (from Manunta et al., 2019) .

4.3 P-SBAS Processing

The main user actions, to submit a job for the CNR-IREA P-SBAS Sentinel-1 (S1) processing on-demand service, are the following:

1. select the input SAR SLC data to be processed;
2. optionally define the area of SAR data to be processed;
3. set input parameters (e.g. reference point, polarization, processing mode, DEM type and Temporal Coherence Threshold) for P-SBAS DInSAR processing.

The considered data set includes the track 44 for the ascending orbit and the track 124 for the descending orbit. The software version of the P-SBAS Sentinel-1 web tool is 28, the DEM used is the 1-arcsec Shuttle Radar Topography Mission (SRTM) to remove the topography phase components. The number of look azimuth direction and range direction are respectively 5 and 20. The pixel dimension is 90x90 meters on the ground. The spatial filter Goldstein was applied with a value of 0.5. Finally an Area of Interest that represent the etnean area was used.

The displacements rates for the four years 2016, 2017, 2018 and 2019 have been calculated, using are reference point a coherent pixel next to the GNSS station EIIV located on the roof of the headquarters of the Istituto Nazionale di Geofisica e Vulcanologia in Catania, Piazza Roma 2. Indeed thanks to the existence of this GNSS station we have the knowledge of the absolute motion of this pixel.

For the P-SBAS processing, the following parameters were used:

Year	2016		2017		2018		2019	
Orbit	Asc.	Desc.	Asc.	Desc.	Asc.	Desc.	Asc.	Desc.
Product Code	BQPY	SDRG	MBSJ	YM53	AQNI	ZR00	RQQ2	FVPM
Date Start	19/01/16	13/01/16	07/01/17	13/01/17	02/01/18	02/01/18	21/01/19	09/01/19
Date End	14/12/16	26/12/16	27/12/17	21/12/17	28/11/18	28/11/18	06/09/19	30/10/19
Super Master	05/07/16	23/07/16	12/07/17	12/06/17	19/06/18	25/06/18	03/05/19	27/05/19
Number of date	26	26	48	28	53	45	38	45
Reference Date	19/01/16	13/01/16	07/01/17	13/01/17	02/01/18	02/01/18	21/01/19	09/01/19
Reference Point Long.	15.07874	15.08959	15.04226	15.10504	15.06308	15.09543	15.06780	15.097643
Reference Point Lat.	37.54148	37.49157	37.49701	37.53134	37.49449	37.5251	37.505149	37.520026
Interferograms used	65	66	132	74	145	122	103	121

The total number of processed S-1 acquisition is 309 and 828 differential interferograms have been produced characterized by a perpendicular baseline average value between 104 and -95 m and an average maximum temporal separation 170 days.

From here on the temporal/perpendicular baseline plane are shown, the graphics are made for each orbit and each year.

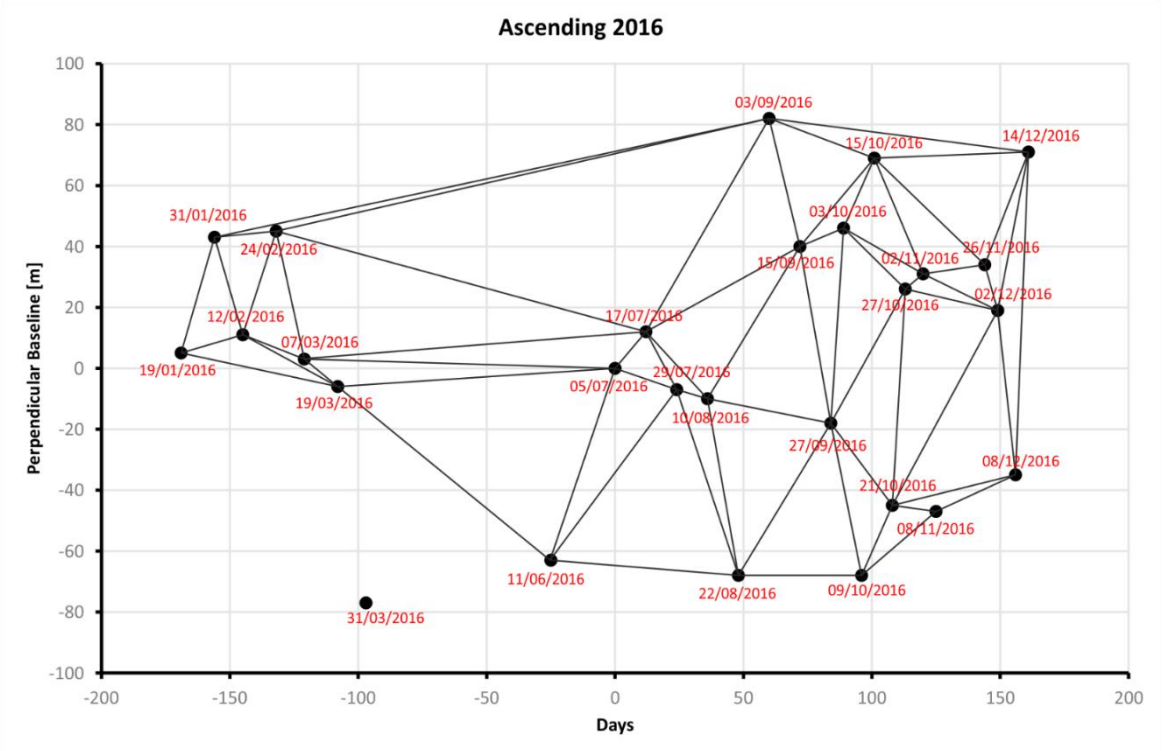

Figure 4. 2 – Distribution of the employed SAR dataset (Ascending 2016) in the temporal/perpendicular baseline plane.

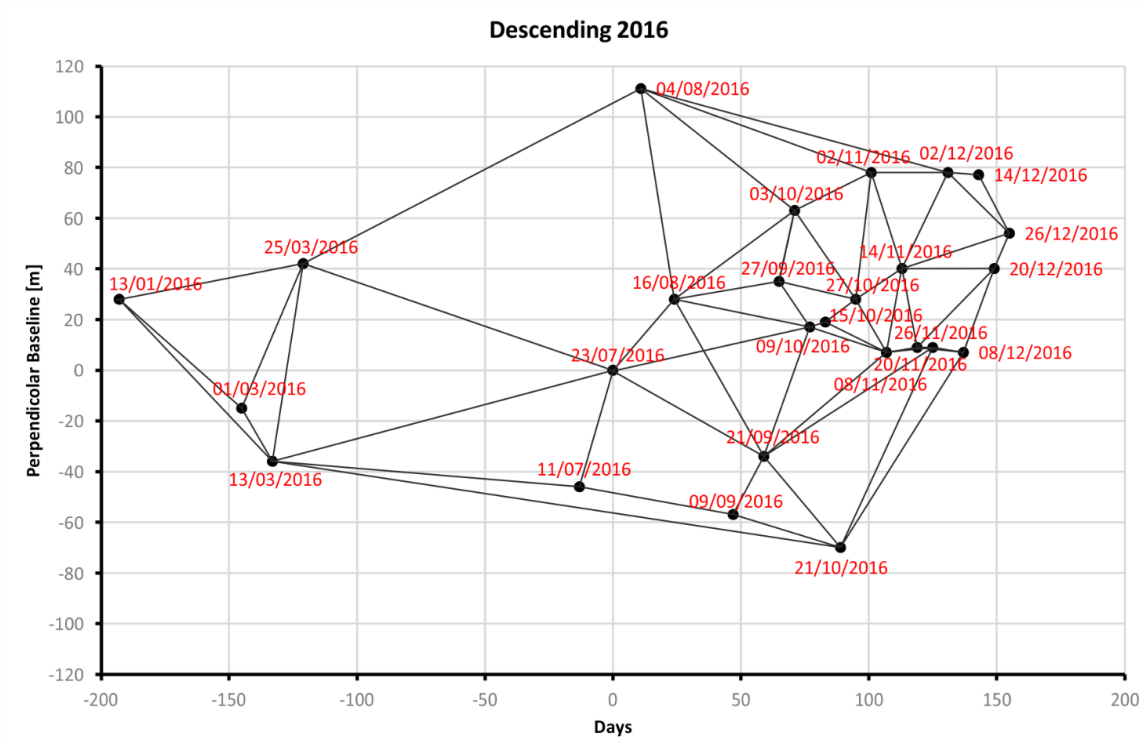

Figure 4. 3 - Distribution of the employed SAR dataset (Descending 2016) in the temporal/perpendicular baseline plane.

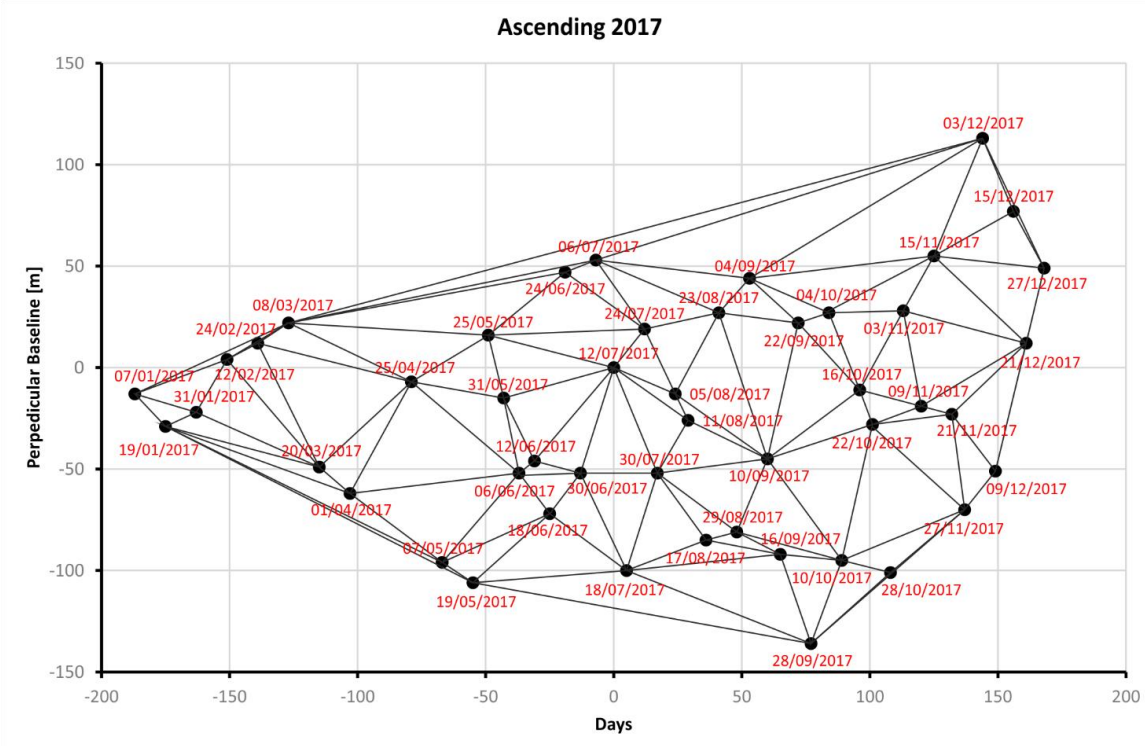

Figure 4. 4 - Distribution of the employed SAR dataset (Ascending 2017) in the temporal/perpendicular baseline plane.

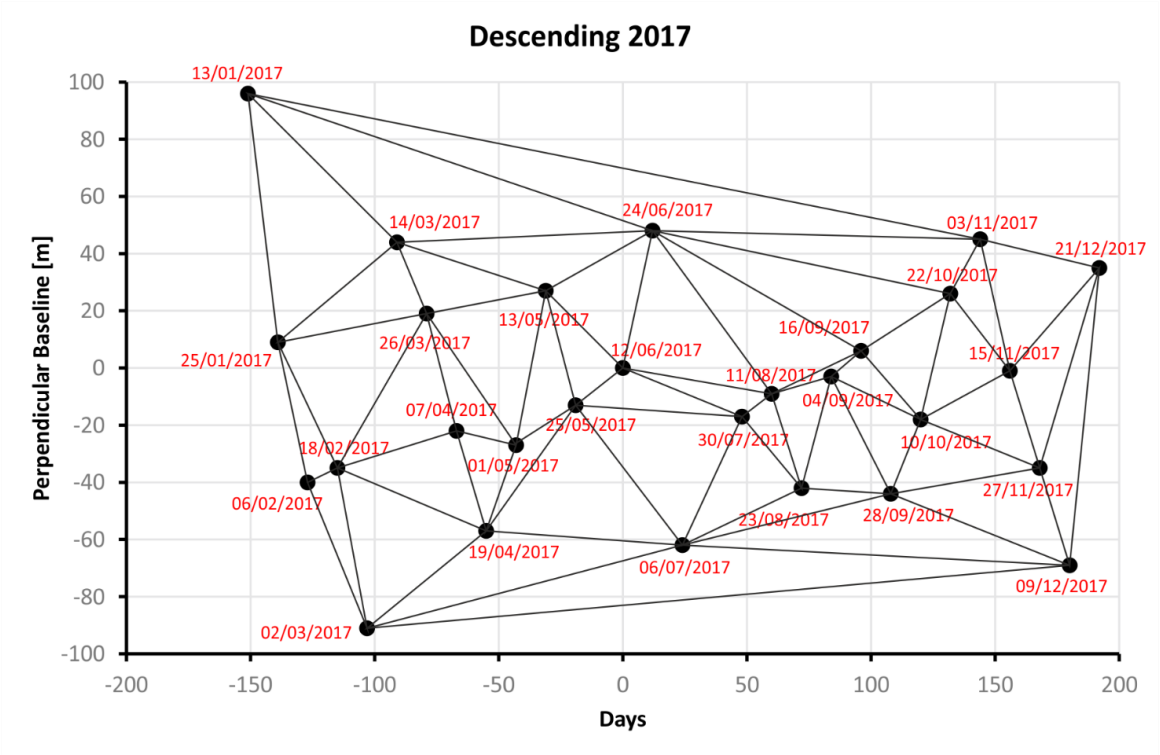

Figure 4. 5 - Distribution of the employed SAR dataset (Descending 2017) in the temporal/perpendicular baseline plane.

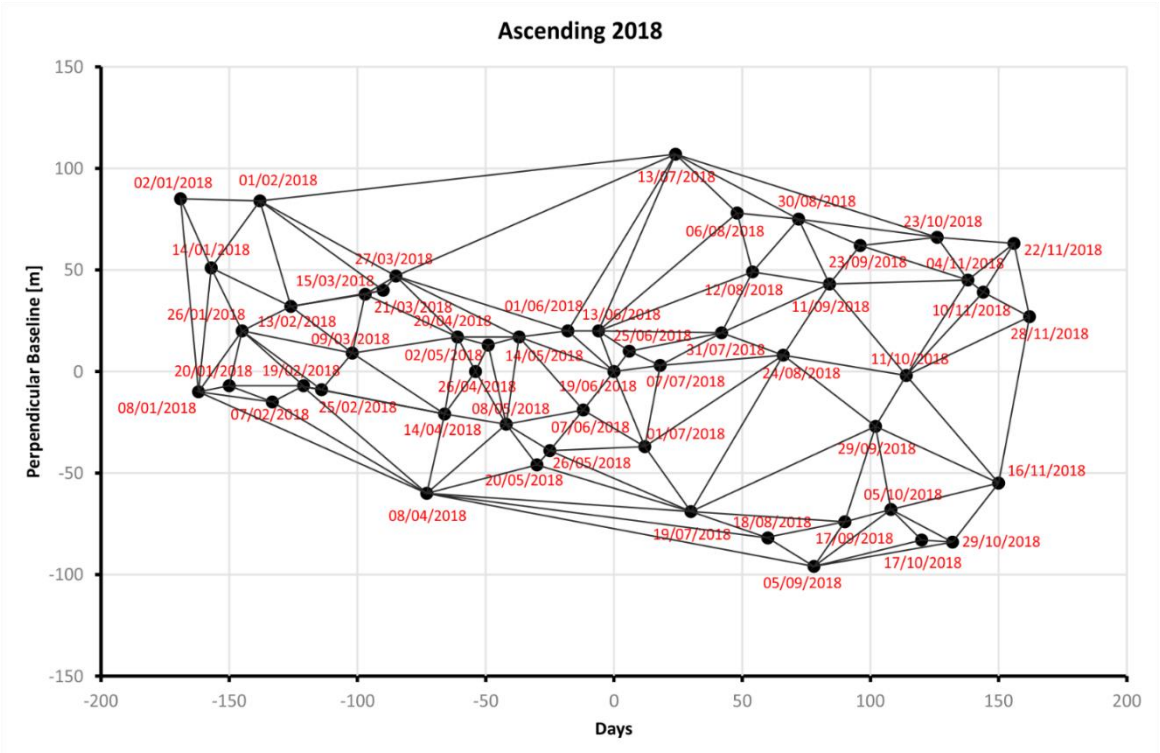

Figure 4. 6 - Distribution of the employed SAR dataset (Ascending 2018) in the temporal/perpendicular baseline plane.

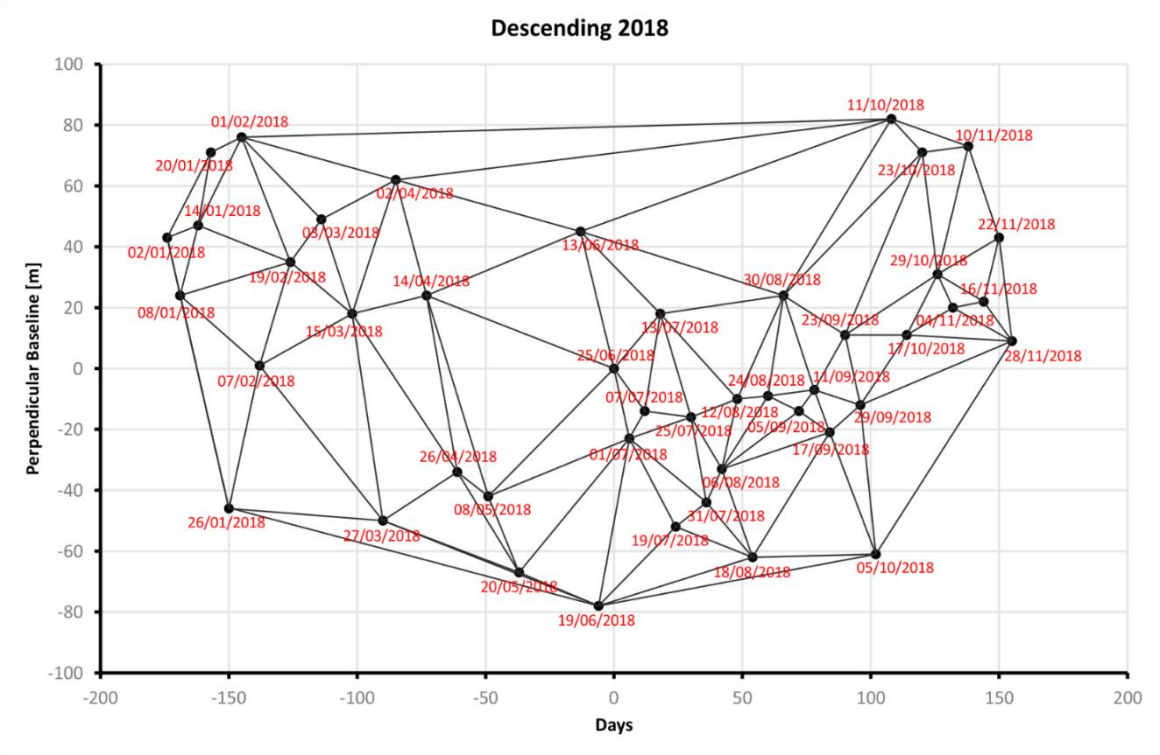

Figure 4. 7 - Distribution of the employed SAR dataset (Descending 2018) in the temporal/perpendicular baseline plane.

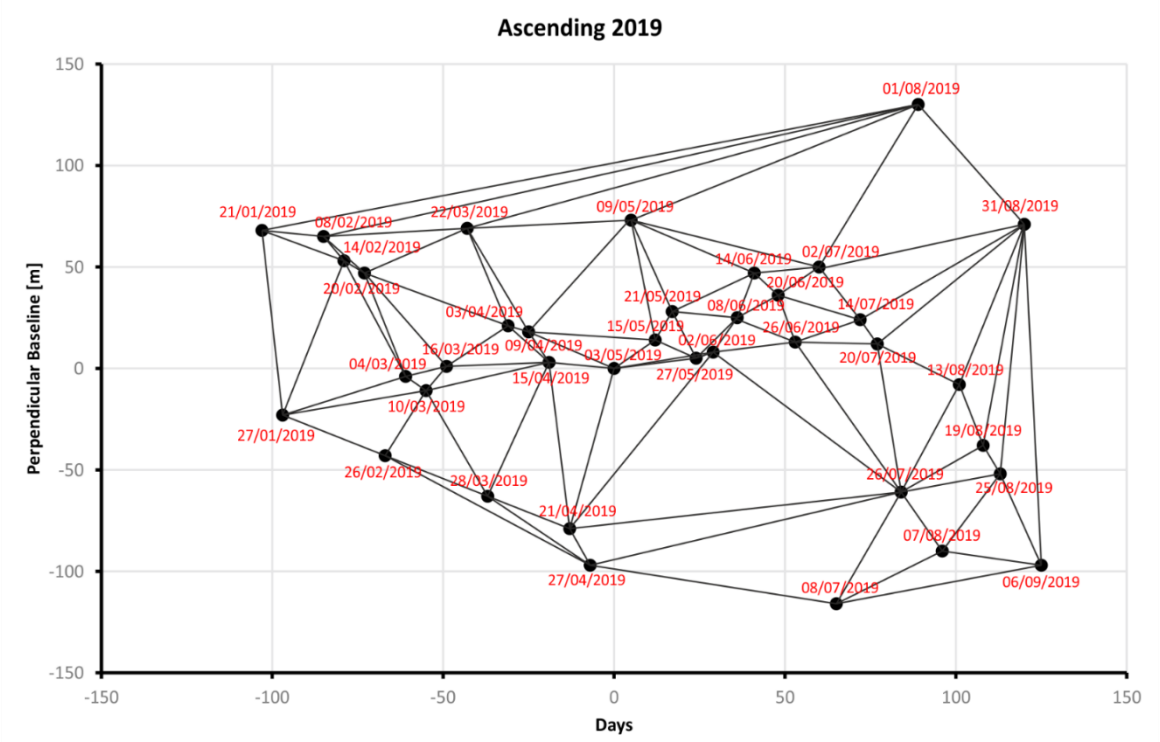

Figure 4. 8 - Distribution of the employed SAR dataset (Ascending 2019) in the temporal/perpendicular baseline plane.

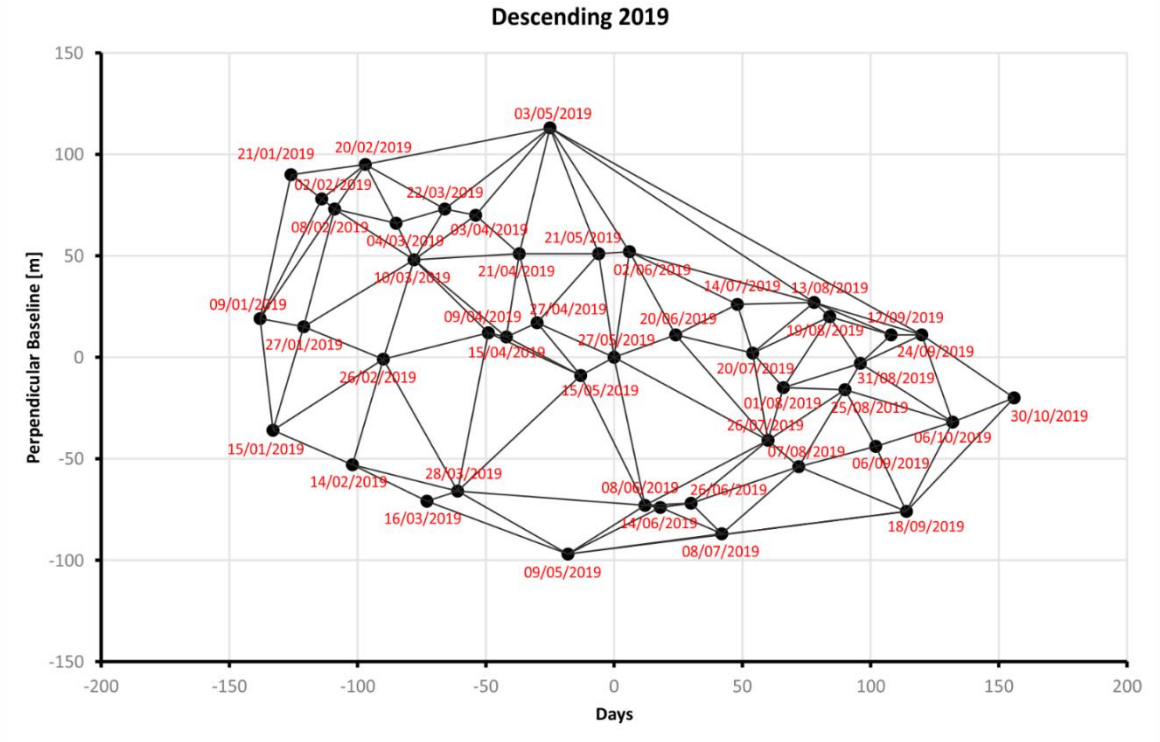

Figure 4. 9 - Distribution of the employed SAR dataset (Descending 2019) in the temporal/perpendicular baseline plane.

4.4 P-SBAS Results

The P-SBAS web tool produced a csv file, a metadata file and a georeferenced png file.

The csv file contains: i) the ID of the permanent scatter, ii) latitude, longitude and ellipsoid height in WGS84 reference frame for each pixel, iii) mean LOS velocity (cm/yr) as linear regression of the displacement time series, iv) temporal coherence, v) directional cosines and vi) displacement time series in LOS. The metadata file contains all the processing information like the interferograms and the parameters used for the processing.

From here on the raster bitmap image of the mean LOS velocity for each geometry and year are shown.

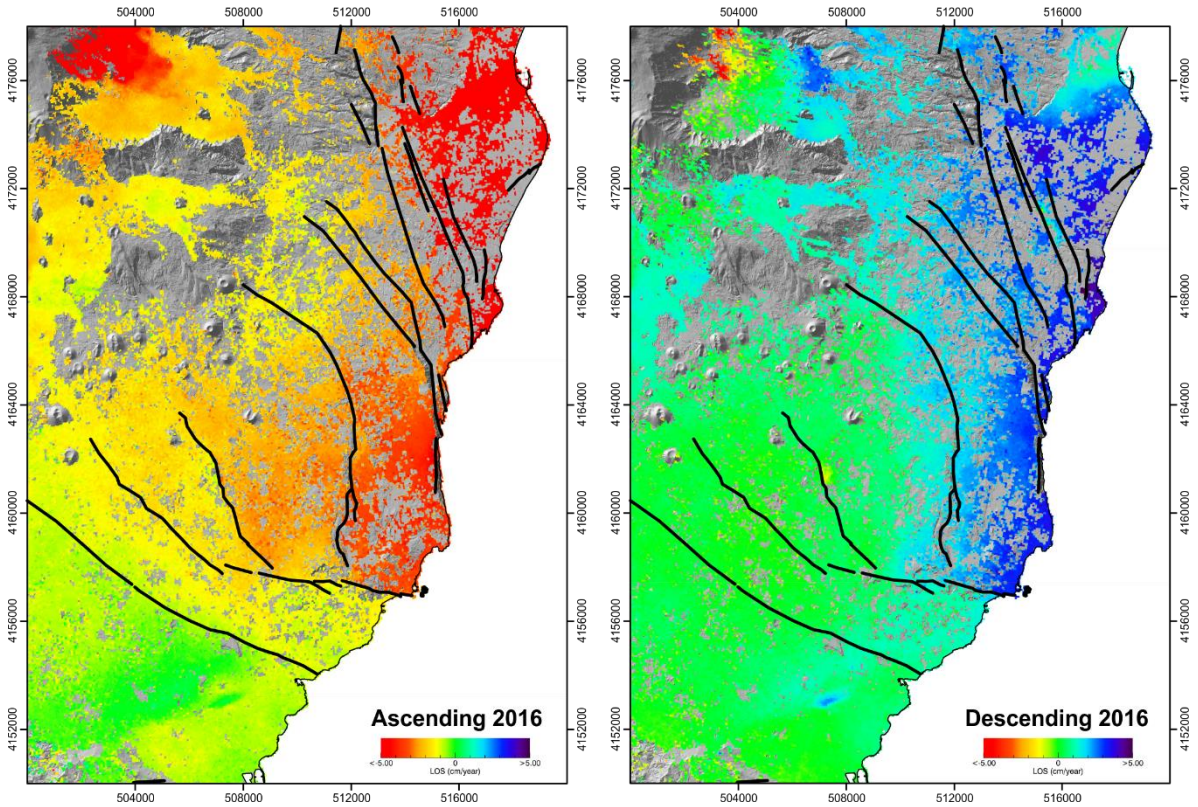

Figure 4. 10 – LOS mean deformation map (cm/yr) of eastern flank of Etna for Ascending orbit (on the left) and for Descending orbit (on the right) during the 2016.

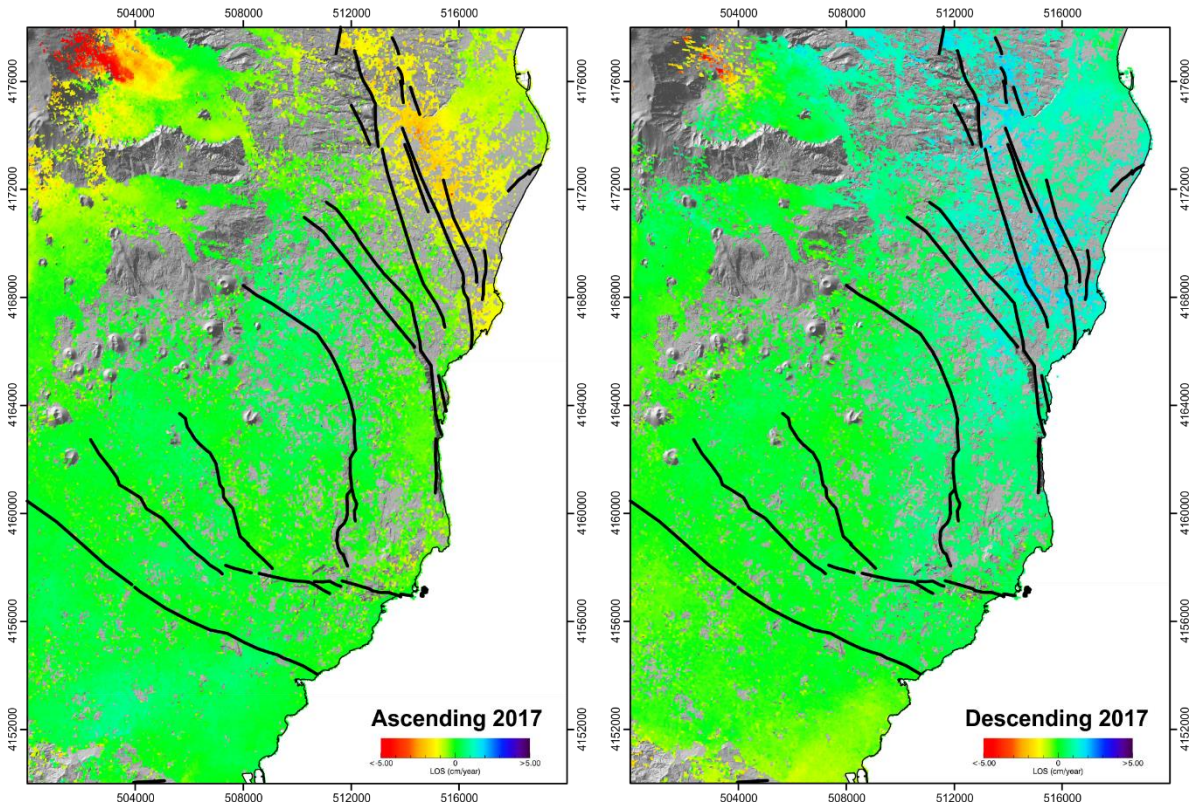

Figure 4. 11 - LOS mean deformation map (cm/yr) of eastern flank of Etna for Ascending orbit (on the left) and for Descending orbit (on the right) during the 2017.

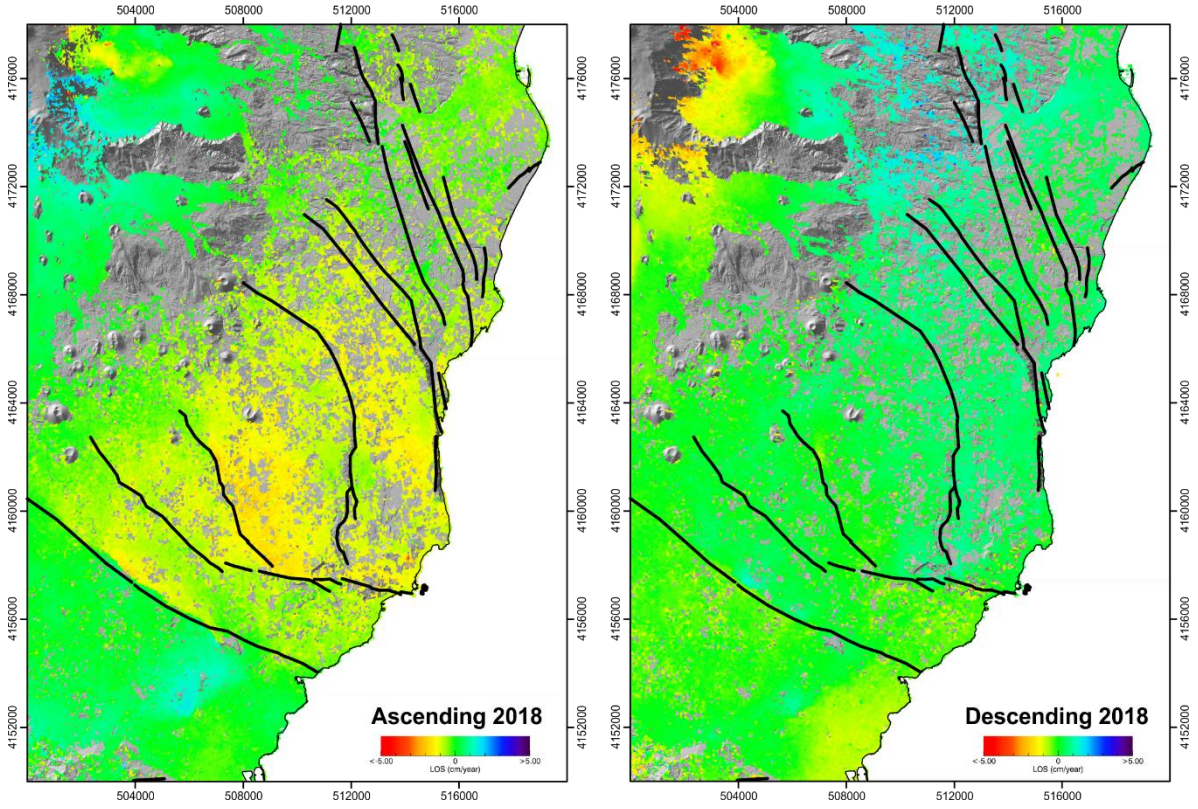

Figure 4. 12 - LOS mean deformation map (cm/yr) of eastern flank of Etna for Ascending orbit (on the left) and for Descending orbit (on the right) during the 2018.

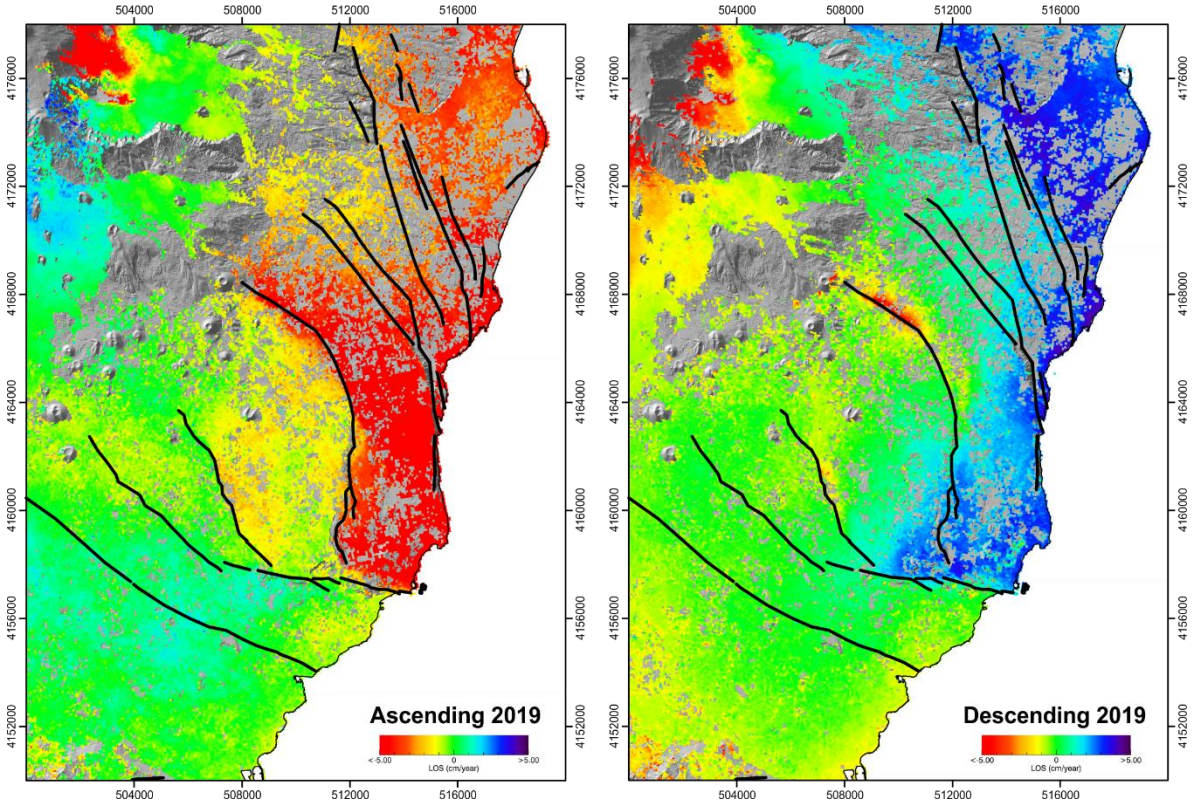

Figure 4. 13 - LOS mean deformation map (cm/yr) of eastern flank of Etna for Ascending orbit (on the left) and for Descending orbit (on the right) during the 2019.

4.5 PS-GNSS Alignment

In this paragraph the approach to convert the LOS displacement into the east and up displacement is show.

Initially, in order to tie the PS data to the coordinates of the GNSS permanent stations, the GNSS coordinate temporal variations (their North, East and Up component) were converted into LOS variations using the formula:

$$LOS_{ASC} = (E - E_O) * cosE_{ASC} + (N - N_O) * cosN_{ASC} + (U - U_O) * cosU_{ASC} \ ;$$

$$LOS_{DES} = (E - E_O) * cosE_{DESC} + (N - N_O) * cosN_{DESC} + (U - U_O) * cosU_{DESC} \ ;$$

where $cosE_{ASC}$, $cosN_{ASC}$, $cosU_{ASC}$, $cosE_{DESC}$, $cosN_{DESC}$ and $cosU_{DESC}$ are respectively the east, north and up directional cosines for the ascending and descending orbit; the terms in brackets represent the GNSS displacement for east, north, and up component respectively.

For the etnean area the following values of the directional cosines were used:

Ascending	cosE	-0.596
	cosN	-0.106
	cosU	0.796

Descending	cosE	0.581
	cosN	-0.104
	cosU	0.807

The pixels surrounding the GNSS permanent station were chosen to align the PS data to the GNSS data of the permanent station. The four years time series of each pixel were considered to align the LOS displacement time-series respect to LOS-projected GNSS time series.

The EIIV permanent station was used as reference point, so the LOS-projected GNSS measurements of the EIIV station were subtract to the LOS-projected GNSS measurements of other permanent station.

The station chosen to align the PS to the LOS-projected GNSS time series are: EBDA, ELAC, ENIC, EPED and ETEC. Each group of pixels that surrounding the GNSS permanent have a different correction for each year and for each station. The corrections used to align the PS and LOS-projected GNSS data are defined by a visual inspection of the time series, in order to make simple and easy the alignment between the two data sets. After that to verify their coherence, the residual values were computed together with the standard deviation.

For the permanent station EBDA the following corrections to the ascending orbit were applied:

	EBDA	
Ascending	Year	Correction [mm]
	2016	0
	2017	-15
	2018	-15
	2019	30

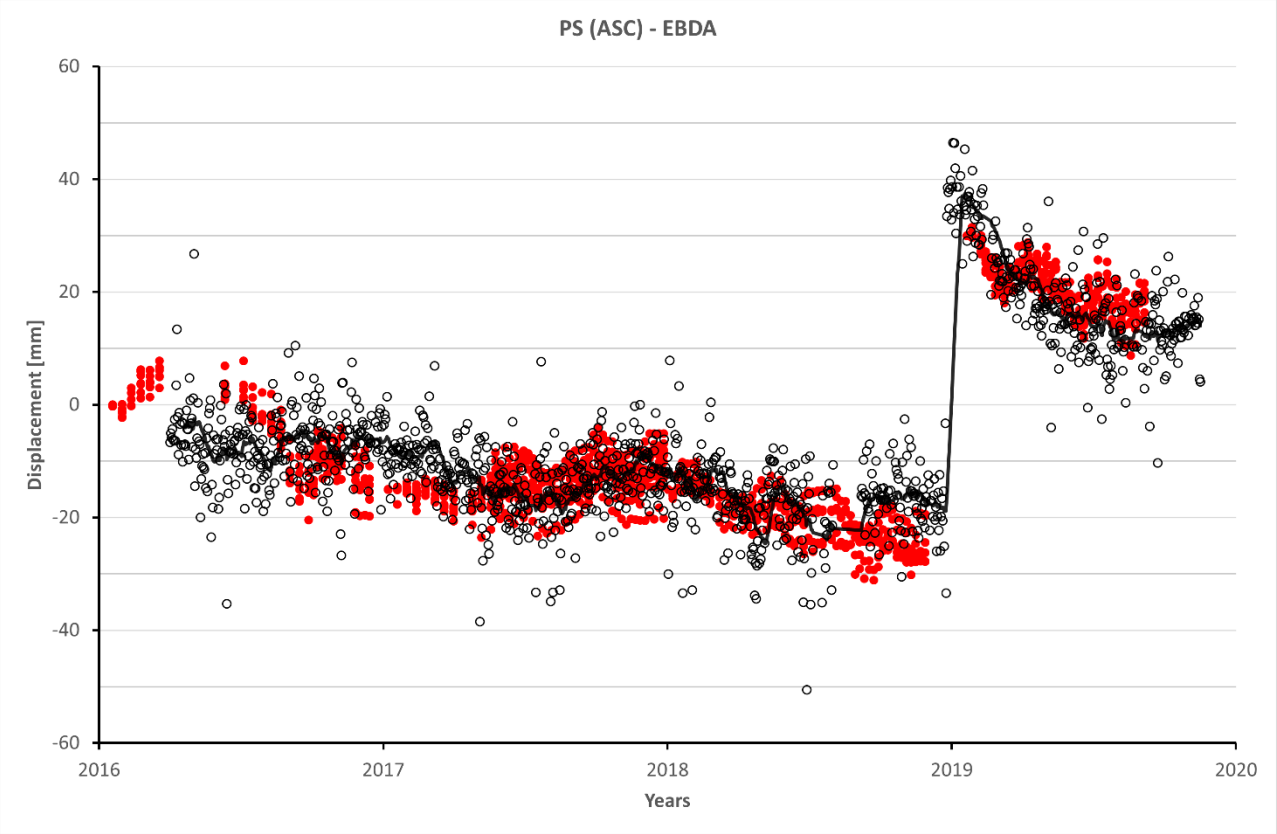

Figure 4. 14 – Comparison between the LOS projected displacement time series of the GNSS permanent station EBDA (black circles) and LOS displacement time series of the pixels around the GNSS station (red circles) for the Ascending orbit.

For the permanent station EBDA the following corrections to the descending orbit were applied:

	EBDA	
Descending	Year	Correction [mm]
	2016	-17
	2017	-4
	2018	5
	2019	-10

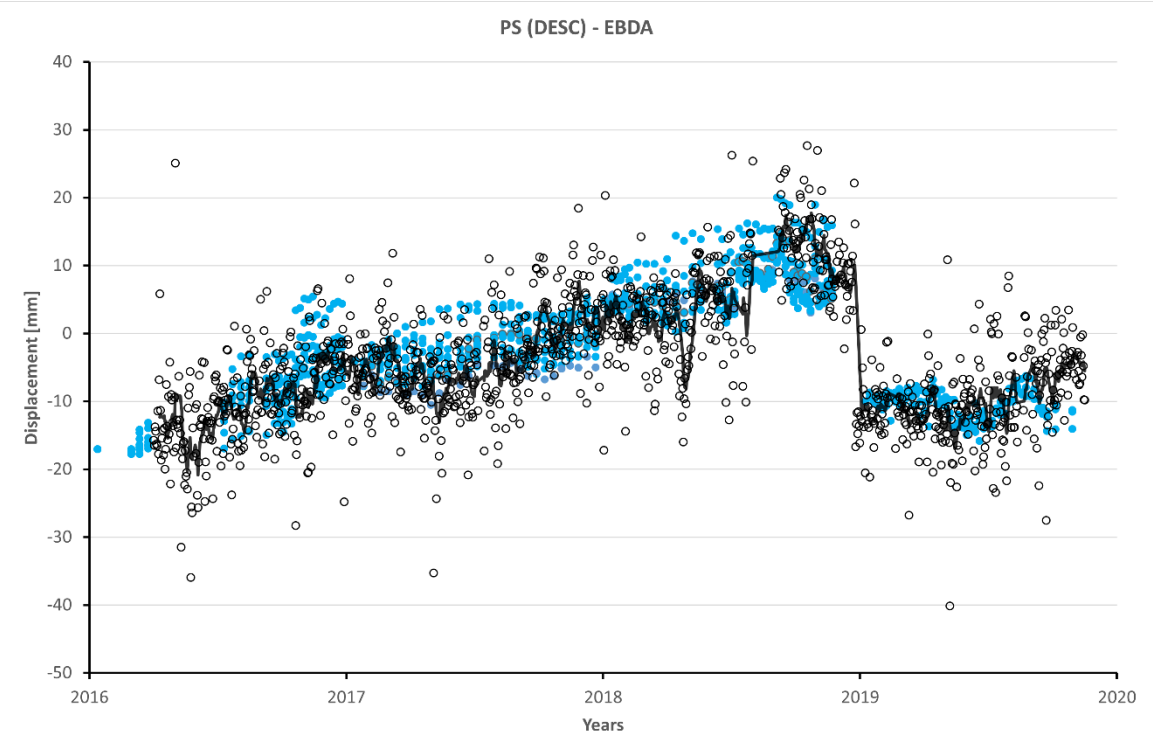

Figure 4. 15 - Comparison between the LOS projected displacement time series of the GNSS permanent station EBDA (black circles) and LOS displacement time series of the pixels around the GNSS station (blue circles) for the Descending orbit.

For the permanent station ELAC the following corrections to the ascending orbit were applied:

	ELAC	
Ascending	Year	Correction [mm]
	2016	0
	2017	-30
	2018	-37
	2019	-40

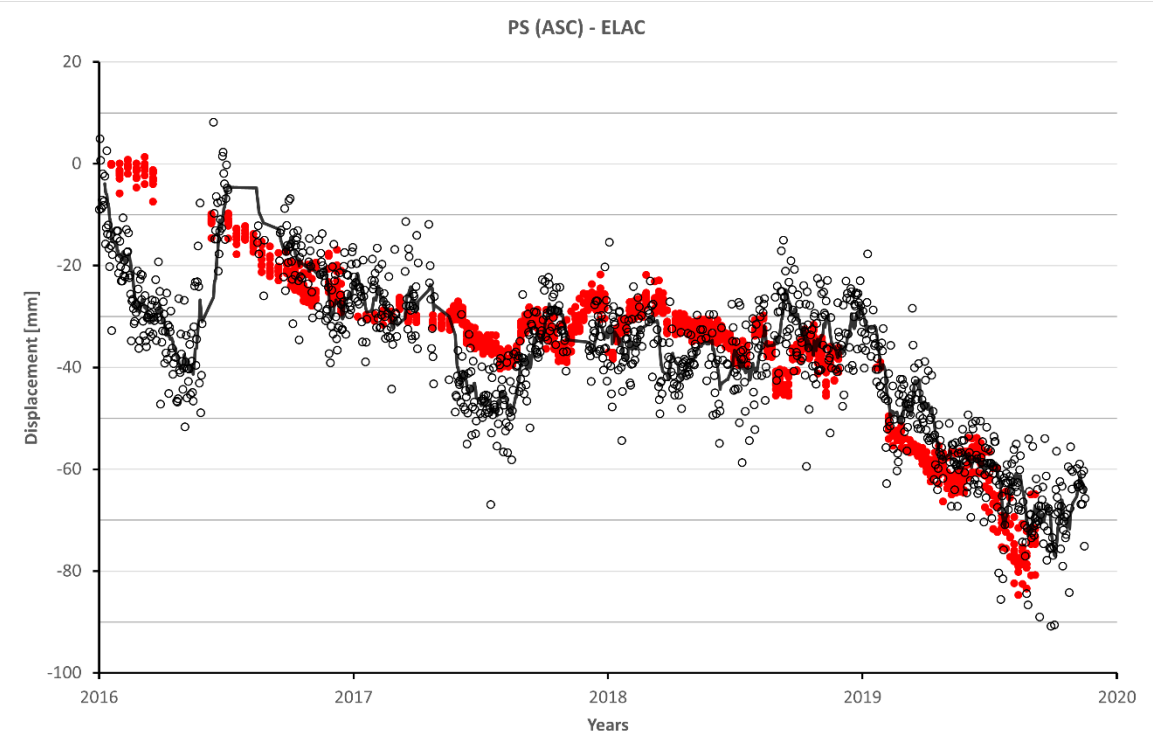

Figure 4. 16 - Comparison between the LOS projected displacement time series of the GNSS permanent station ELAC (black circles) and LOS displacement time series of the pixels around the GNSS station (red circles) for the Ascending orbit.

For the permanent station ELAC the following corrections to the descending orbit were applied:

	ELAC	
Descending	Year	Correction [mm]
	2016	5
	2017	30
	2018	40
	2019	50

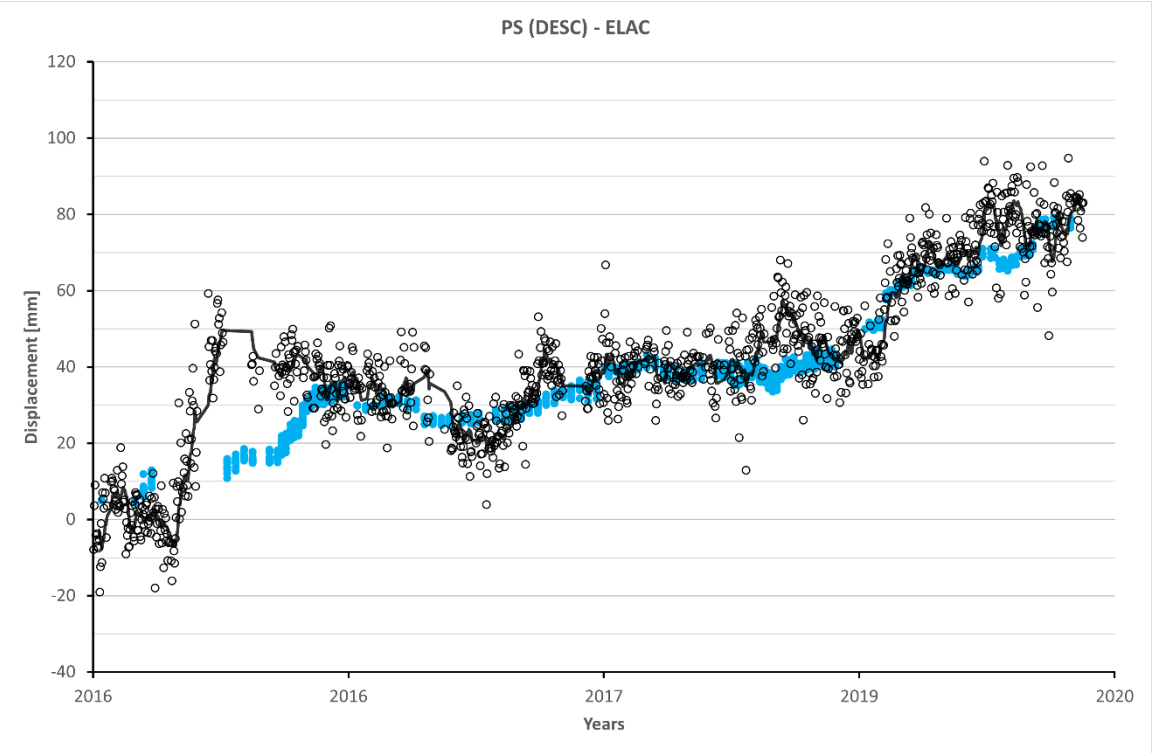

Figure 4. 17 - Comparison between the LOS projected displacement time series of the GNSS permanent station ELAC (black circles) and LOS displacement time series of the pixels around the GNSS station (blue circles) for the Descending orbit

For the permanent station ENIC the following corrections to the ascending orbit were applied:

	ENIC	
Ascending	Year	Correction [mm]
	2016	0
	2017	-15
	2018	-15
	2019	-17.5

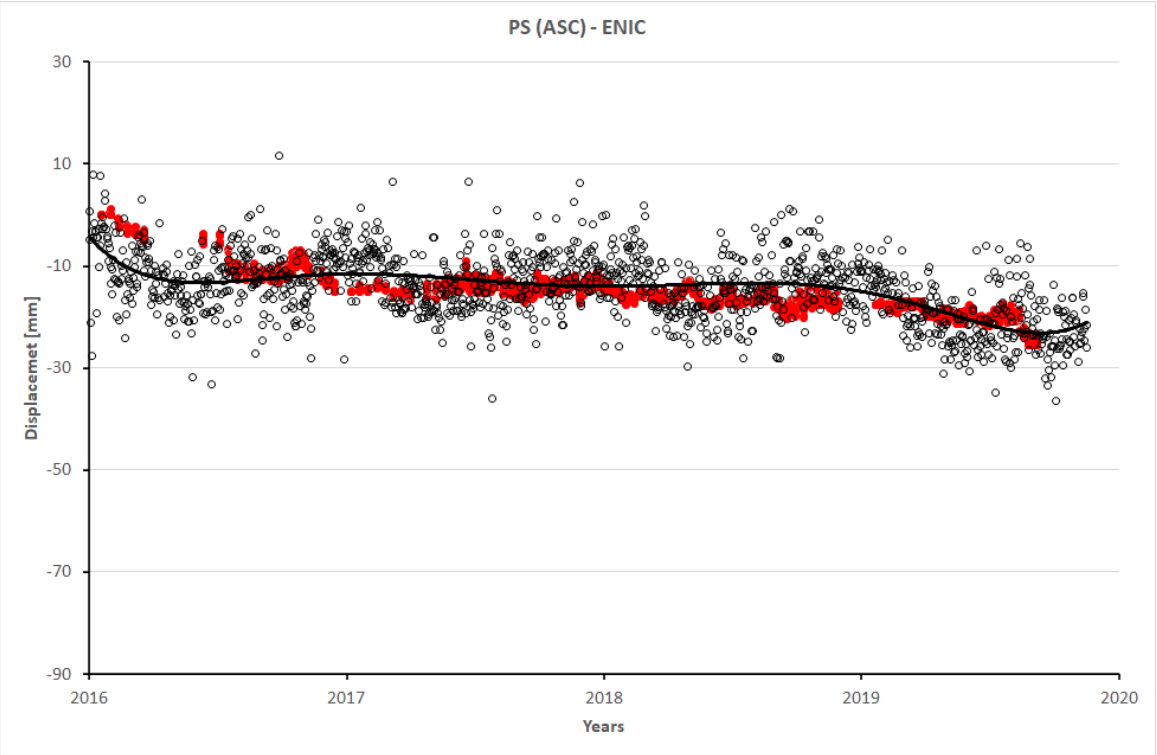

Figure 4. 18 - Comparison between the LOS projected displacement time series of the GNSS permanent station ENIC (black circles) and LOS displacement time series of the pixels around the GNSS station (red circles) for the Ascending orbit

For the permanent station ENIC the following corrections to the descending orbit were applied:

	ENIC	
Descending	Year	Correction [mm]
	2016	-7
	2017	-2
	2018	3.5
	2019	0

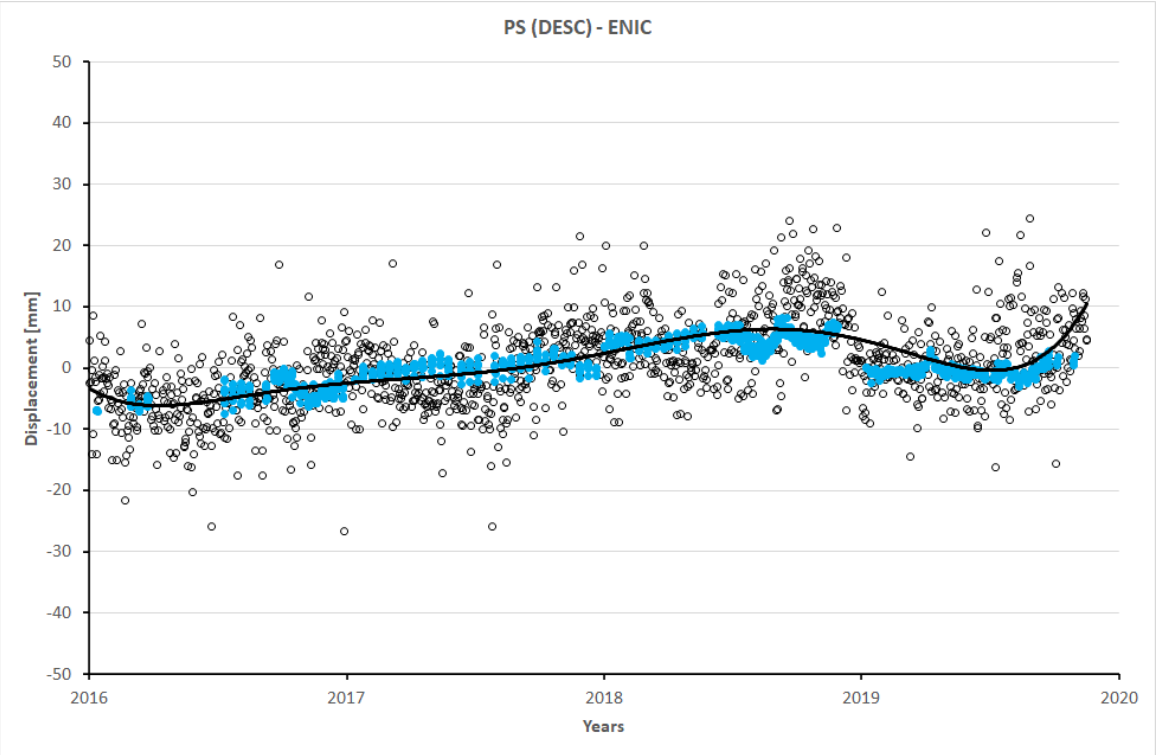

Figure 4. 19 - Comparison between the LOS projected displacement time series of the GNSS permanent station ENIC (black circles) and LOS displacement time series of the pixels around the GNSS station (blue circles) for the Descending orbit

For the permanent station EPED the following corrections to the ascending orbit were applied:

	EPED	
Ascending	Year	Correction [mm]
	2016	0
	2017	-15
	2018	-13
	2019	-20

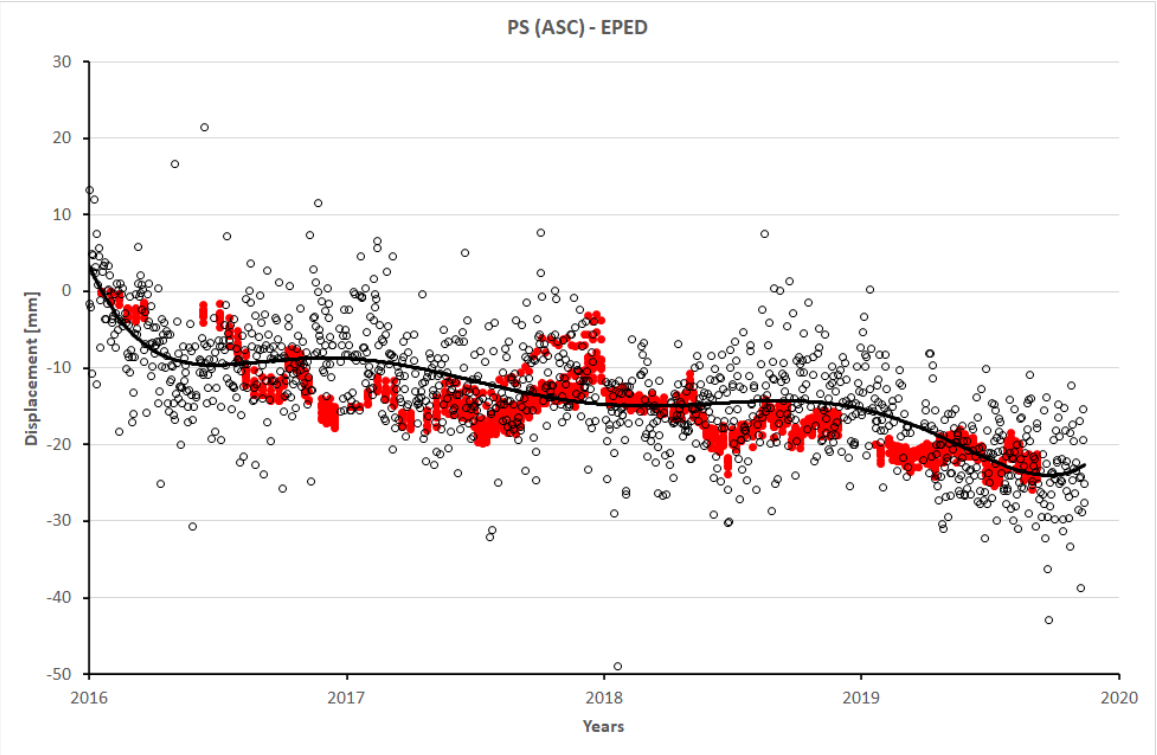

Figure 4. 20 - Comparison between the LOS projected displacement time series of the GNSS permanent station EPED (black circles) and LOS displacement time series of the pixels around the GNSS station (red circles) for the Ascending orbit

For the permanent station EPED the following corrections to the descending orbit were applied:

	EPED	
Descending	Year	Correction [mm]
	2016	-6
	2017	0
	2018	0
	2019	-2

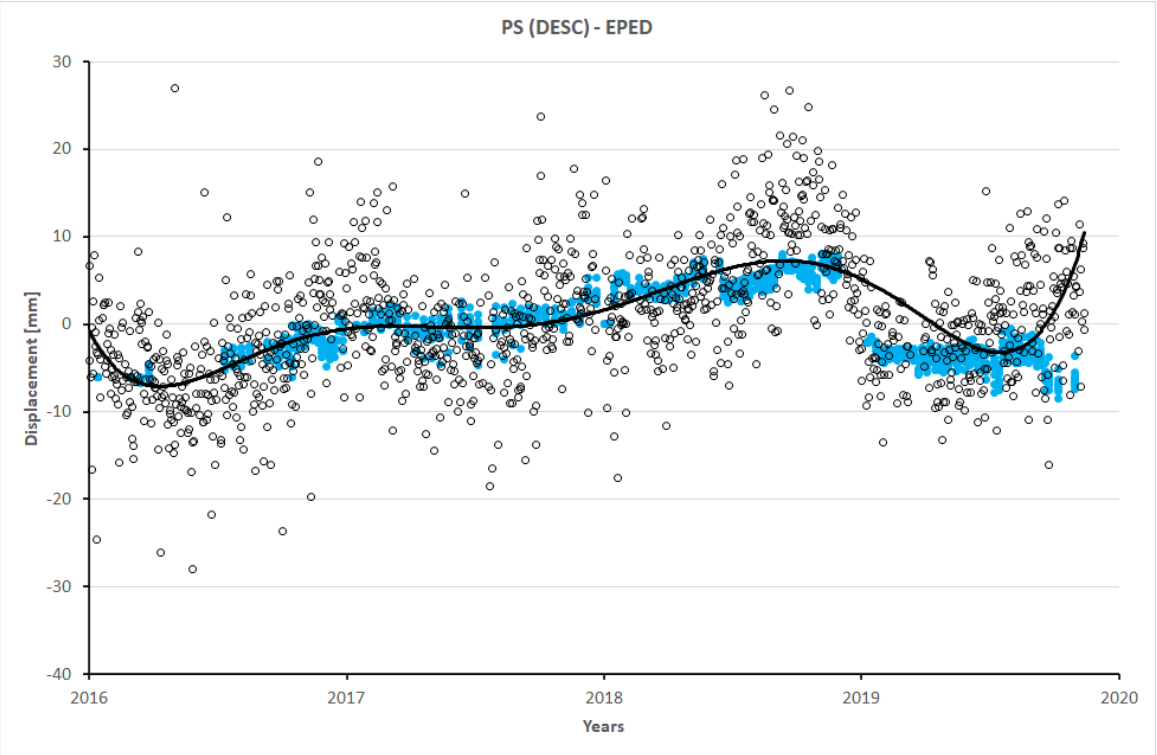

Figure 4. 21 - Comparison between the LOS projected displacement time series of the GNSS permanent station EPED (black circles) and LOS displacement time series of the pixels around the GNSS station (blue circles) for the Descending orbit

For the permanent station ETEC the following corrections to the ascending orbit were applied:

	ETEC	
Ascending	Year	Correction [mm]
	2016	-20
	2017	-39
	2018	-45
	2019	-100

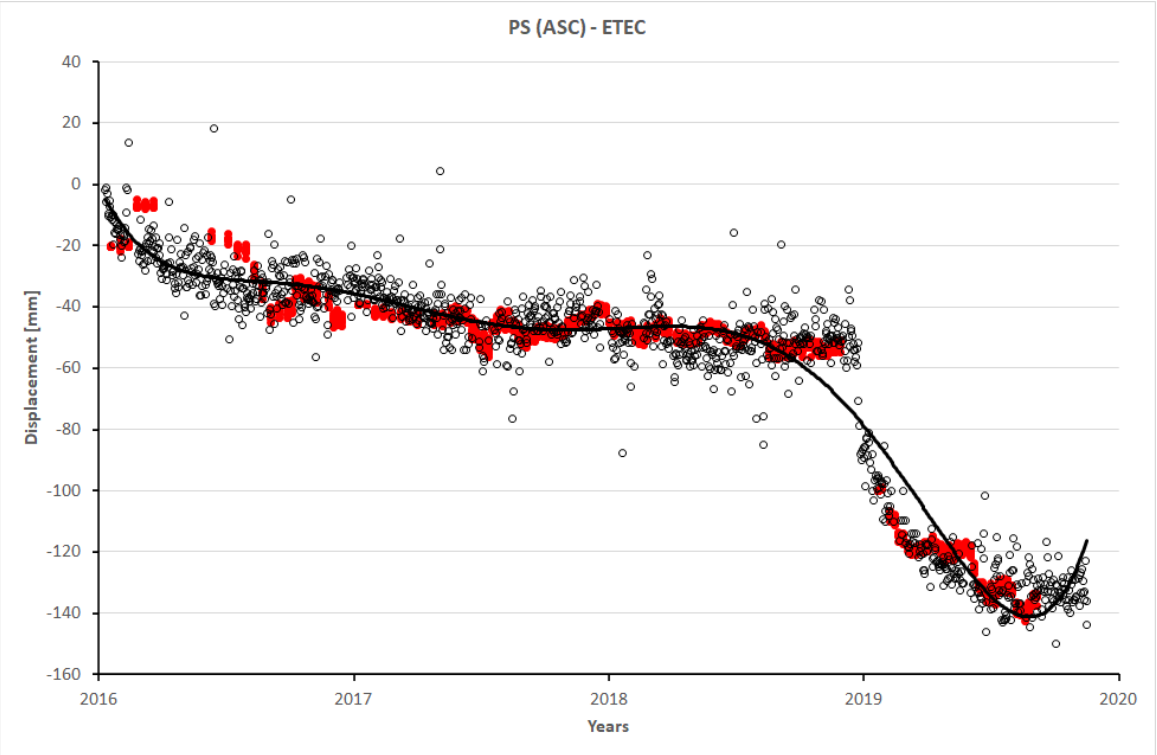

Figure 4. 22 - Comparison between the LOS projected displacement time series of the GNSS permanent station ETEC (black circles) and LOS displacement time series of the pixels around the GNSS station (red circles) for the Ascending orbit.

For the permanent station ETEC the following corrections to the descending orbit were applied:

	ETEC	
Descending	Year	Correction [mm]
	2016	0
	2017	30
	2018	50
	2019	100

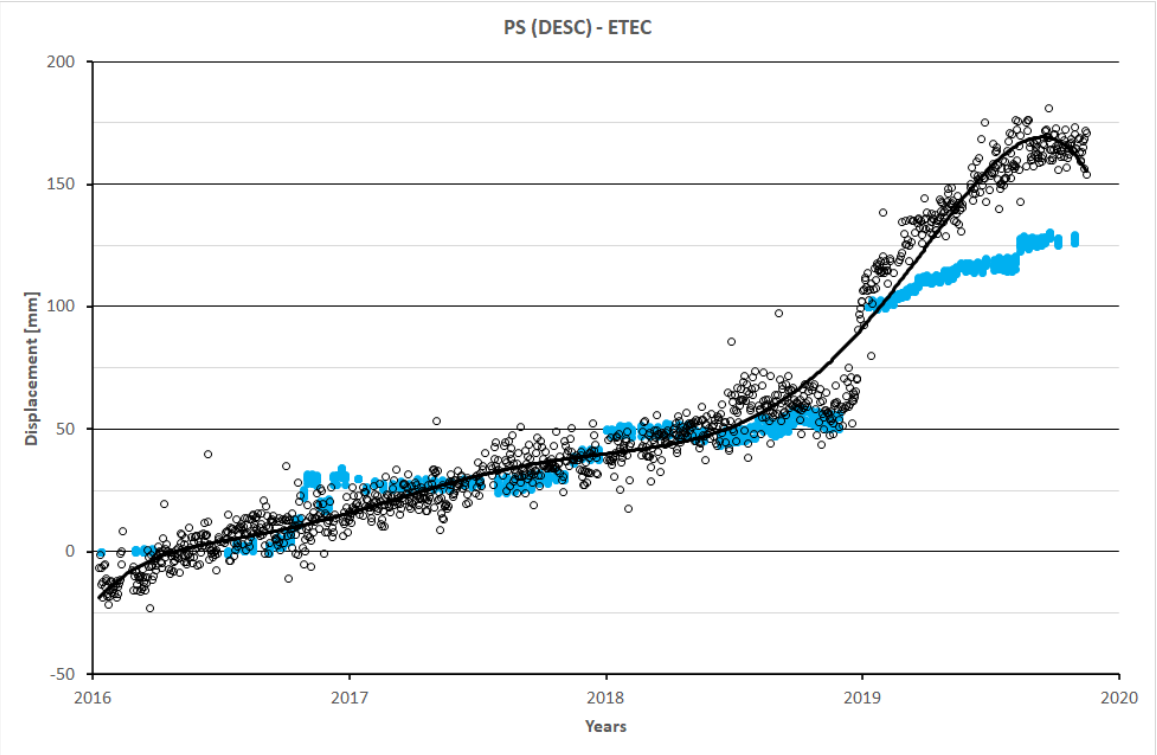

Figure 4. 23 - Comparison between the LOS projected displacement time series of the GNSS permanent station ETEC (black circles) and LOS displacement time series of the pixels around the GNSS station (blue circles) for the Descending orbit

It was not possible to align the pixel surrounding the campaign station EPEL, PDAP, EMSC, MDGR and ESGR of INGV-OE because those stations are occupied yearly so present an important gap in the data that makes impossible align the surrounding pixel to the LOS-projected GPS measurements.

There is a good agreement between the P-SBAS and LOS-projected GNSS measurements for each station of ETN@Net located in correspondence to a DInSAR pixels, to quantify the fitting between the two time series the standard deviation was computed.

Station	Orbit	Standard Deviation [mm]
EBDA	Asc	7.85
	Desc	8.33
ELAC	Asc	9.42
	Desc	8.14
ENIC	Asc	6.54
	Desc	6.11
EPED	Asc	6.06
	Desc	5.45
ETEC	Asc	8.75
	Desc	17.78

According to the values in the last table, the PS surrounding the station ENIC and EPED show the best agreement to the GNSS station, instead the PS located on the eastern area show higher values of standard deviation, in particular the pixels surrounding the station ETEC show the highest value of the standard deviation, probably due to the post-seismic deformation after the 26 December 2018 earthquakes. This means that the P-SBAS tool is unable to compute the real deformation that affect this area, in particular it is clear that at least one fringe in missing.
Moreover, the correction applied are different for each station (Figure 4. 24Figure 4. 24 – Correction applied to align the P-SBAS displacement time series to LOS-projected GNSS displacement time series for each GNSS permanent station on the south-eastern flank of Mount Etna.), it seems that there are two areas that are coherent each other: the first one, one the western part, that includes the station ENIC, EPED and EBDA, which show a similar correction value and the second one, on the eastern part, that includes the station ETEC and ELAC which show a very higher correction values.

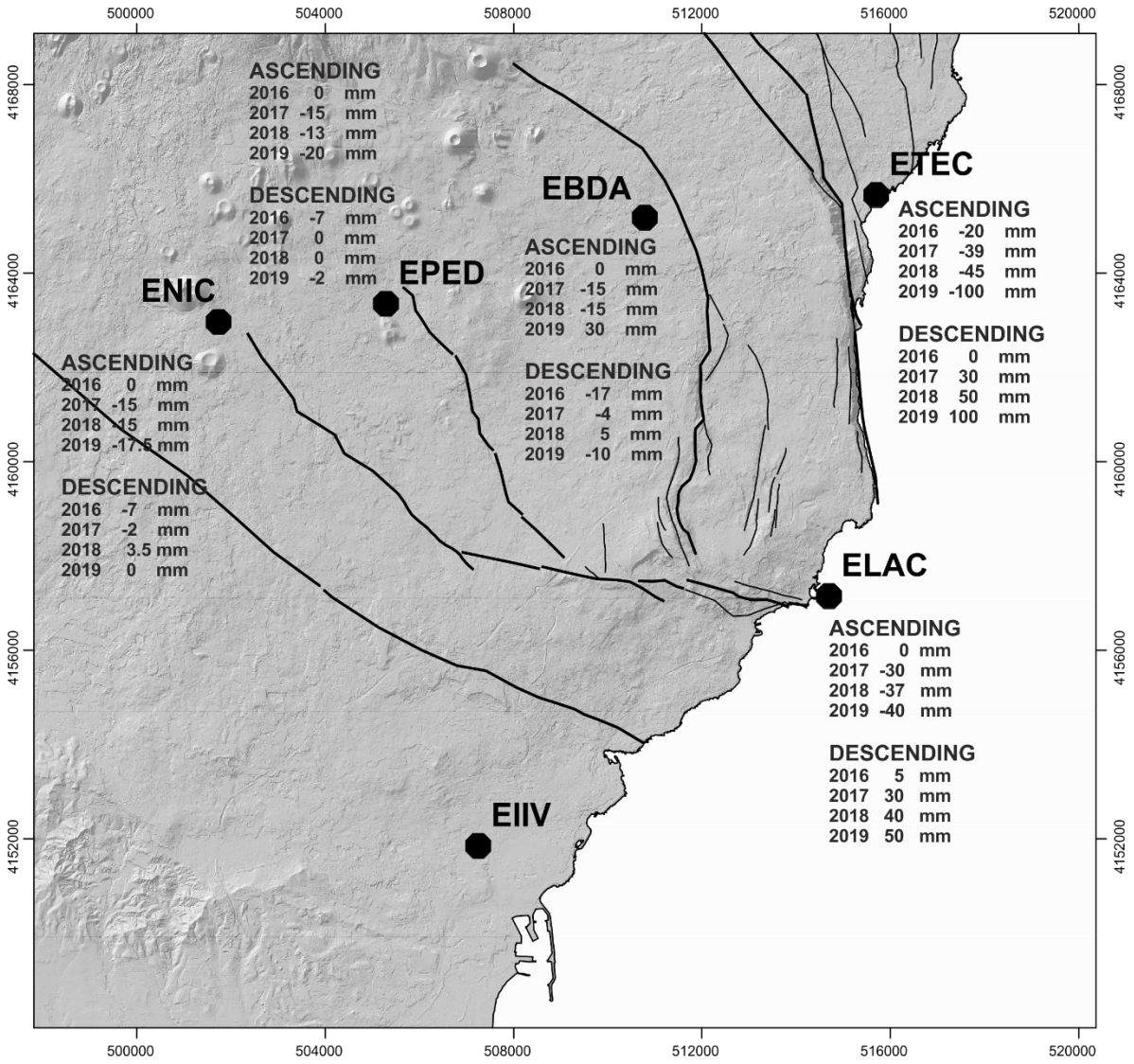

Figure 4. 24 – Correction applied to align the P-SBAS displacement time series to LOS-projected GNSS displacement time series for each GNSS permanent station on the south-eastern flank of Mount Etna.

Considering what has been written above, the conversion from LOS velocity to east and up velocities could be affected by error because the agreements between the PS and LOS-projected GNSS data is different for each station. In fig xxx the correction of each stations is shown.

4.6 East and Up Conversion

Assuming that the contribution of the north component of the displacement is negligible, the following formulas were used to convert the LOS displacement into east and up components:

$$UP_{DISPLACEMENT} = \frac{LOS_{DESC} * cosE_{ASC} - LOS_{ASC} * cosE_{DESC}}{cosU_{DESC} * cosE_{ASC} - cosU_{ASC} * cosE_{DESC}}$$

$$EAST_{DISPLACEMENT} = \frac{LOS_{ASC} * cosU_{DESC} - LOS_{DESC} * cosU_{ASC}}{cosU_{DESC} * cosE_{ASC} - cosU_{ASC} * cosE_{DESC}}$$

After the conversion, the east and up components of the PS and the GNSS station were compared. The standard deviation for each station was computed to estimate the quality of the conversion to the east and up components. From here on the graphs of the comparison between the east and up displacement of PS and GNSS are shown.

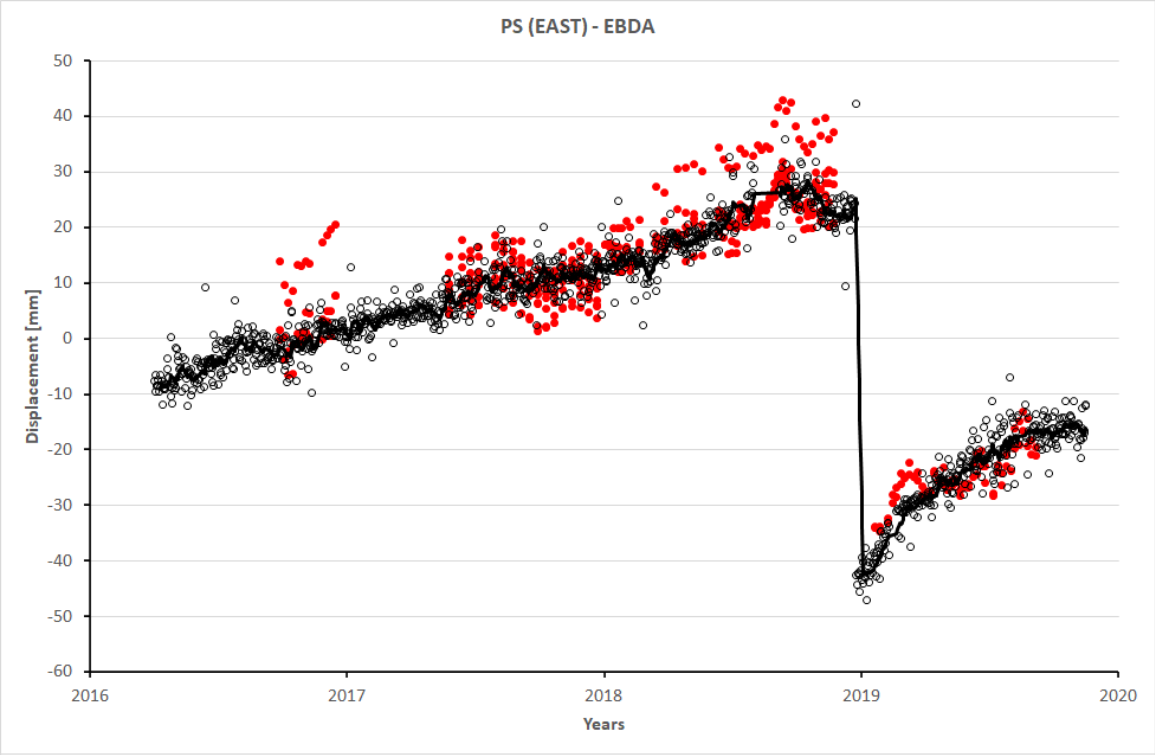

Figure 4. 25 - Comparison between the east displacement time series of the GNSS permanent station EBDA (black circles) and east displacement time series of the pixels around the GNSS station (red circles).

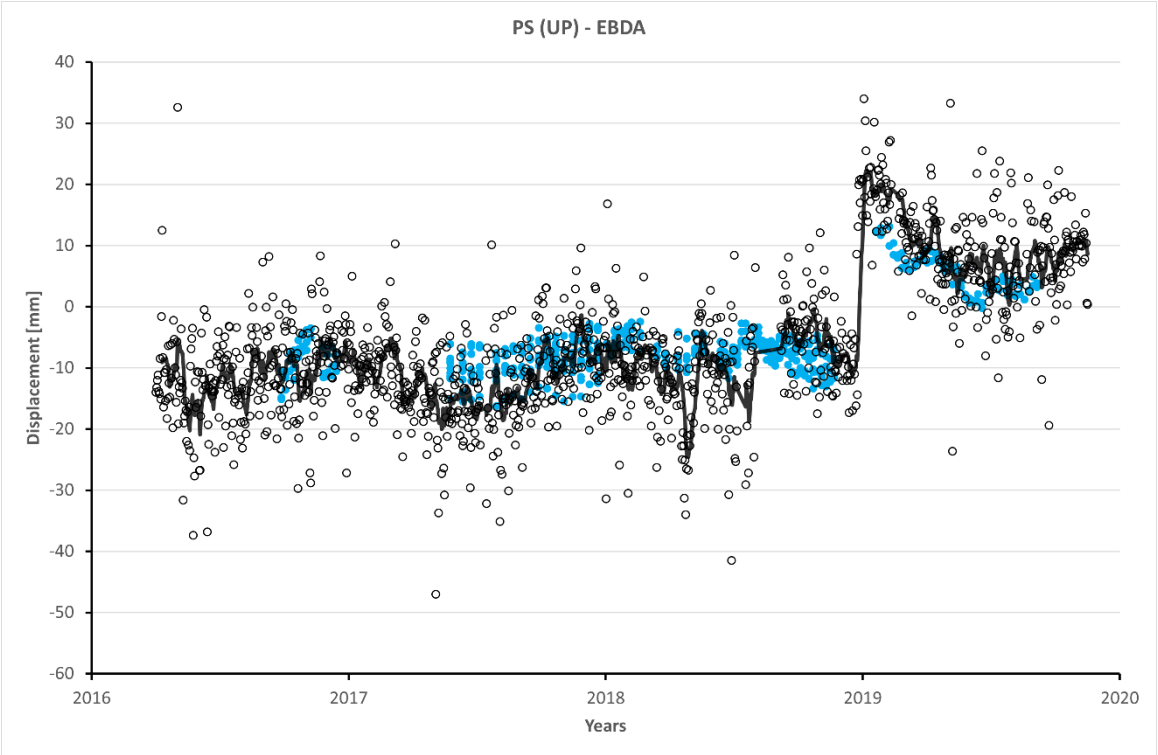

Figure 4. 26 - Comparison between the up displacement time series of the GNSS permanent station EBDA (black circles) and up displacement time series of the pixels around the GNSS station (blue circles).

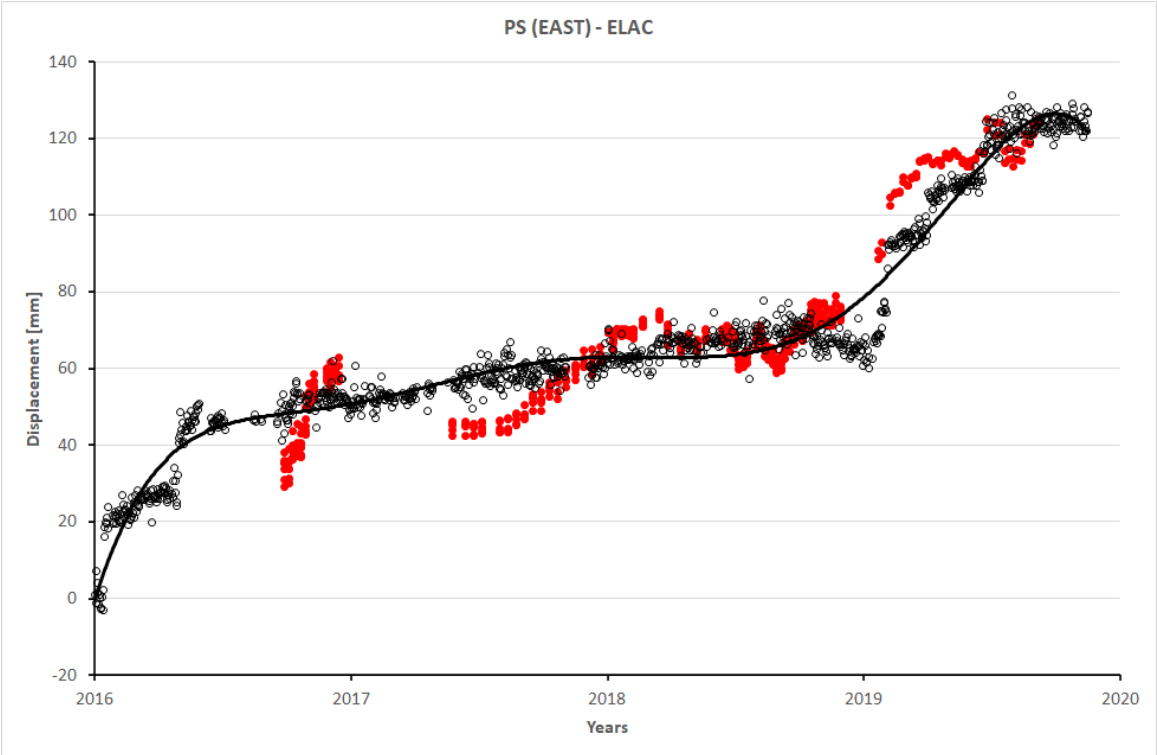

Figure 4. 27 - Comparison between the east displacement time series of the GNSS permanent station ELAC (black circles) and east displacement time series of the pixels around the GNSS station (red circles).

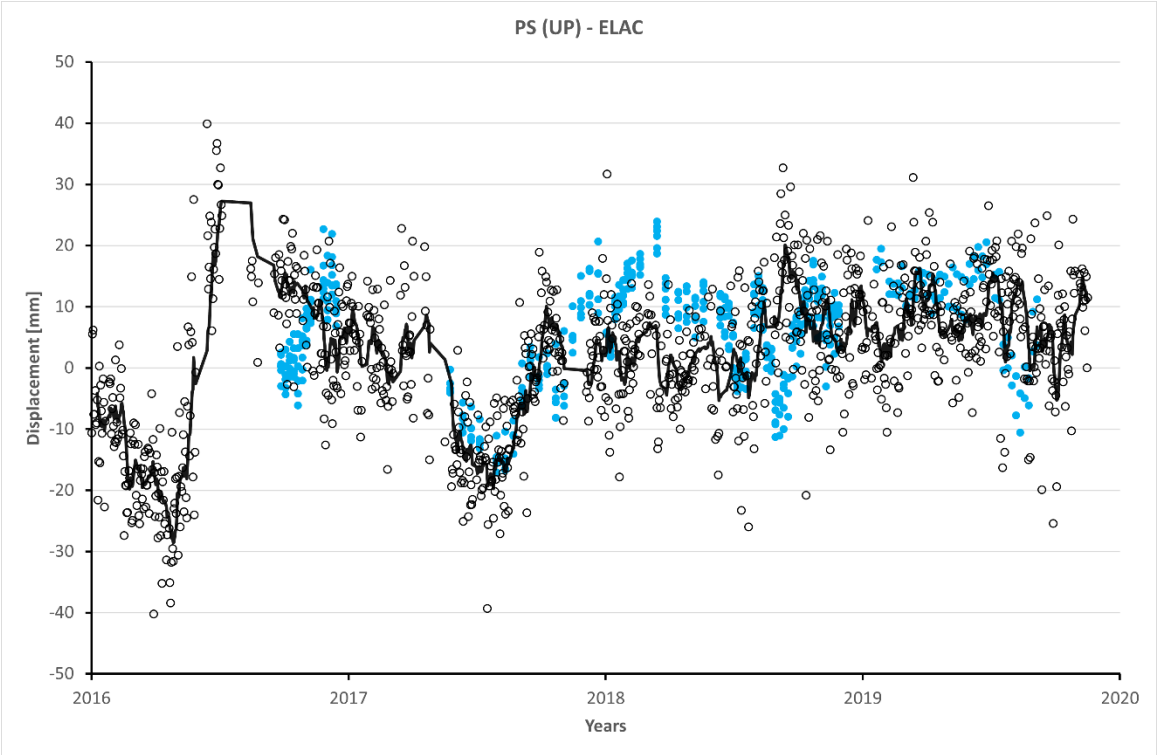

Figure 4. 28 - Comparison between the up displacement time series of the GNSS permanent station ELAC (black circles) and east displacement time series of the pixels around the GNSS station (blue circles).

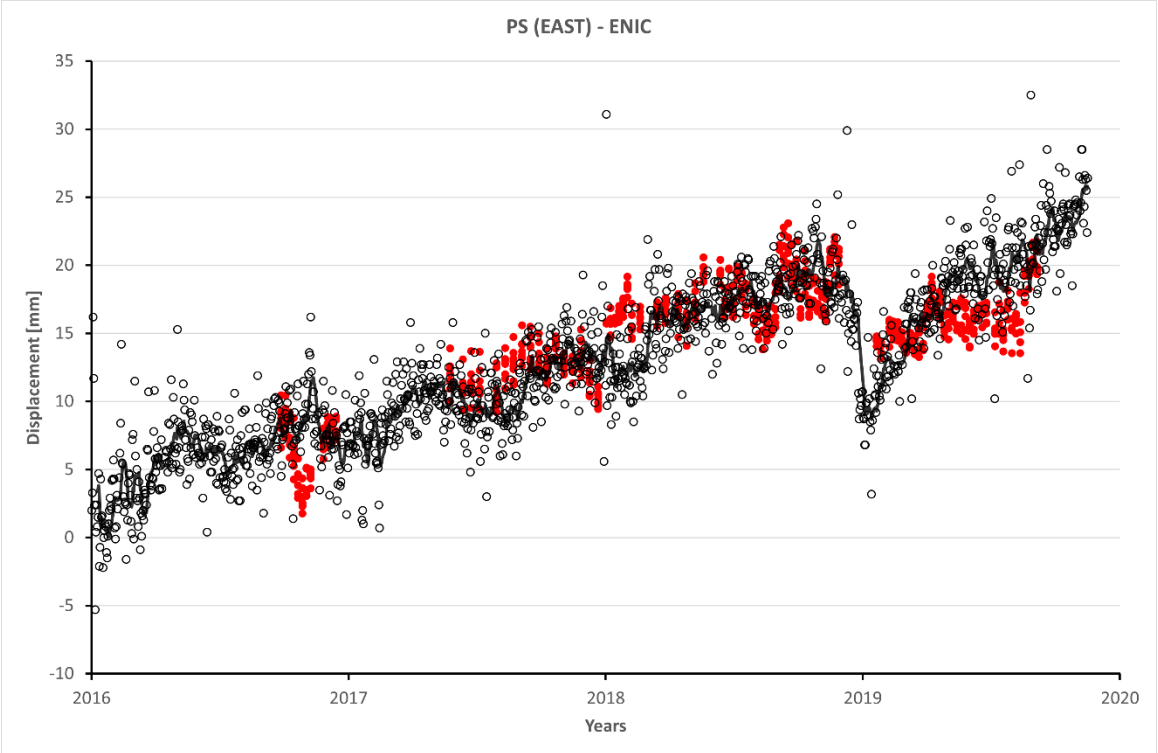

Figure 4. 29 - Comparison between the east displacement time series of the GNSS permanent station ENIC (black circles) and east displacement time series of the pixels around the GNSS station (red circles).

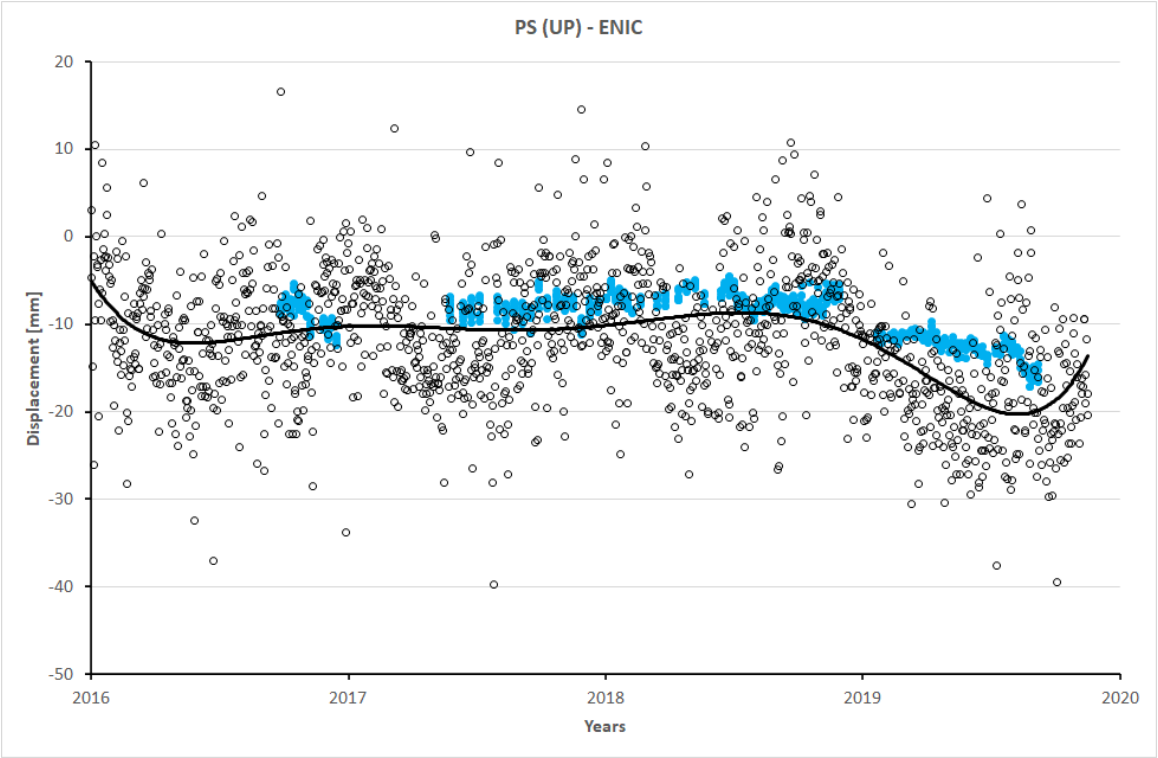

Figure 4. 30 - Comparison between the up displacement time series of the GNSS permanent station ENIC (black circles) and up displacement time series of the pixels around the GNSS station (blue circles).

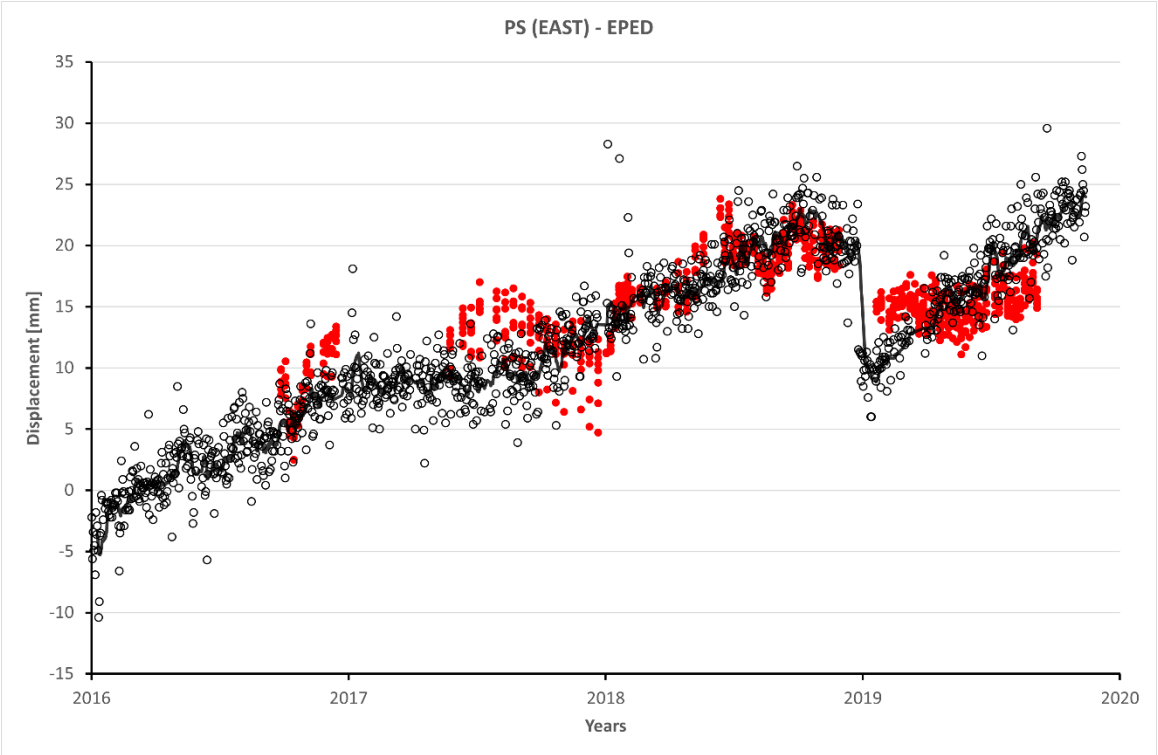

Figure 4. 31 - Comparison between the east displacement time series of the GNSS permanent station EPED (black circles) and east displacement time series of the pixels around the GNSS station (red circles).

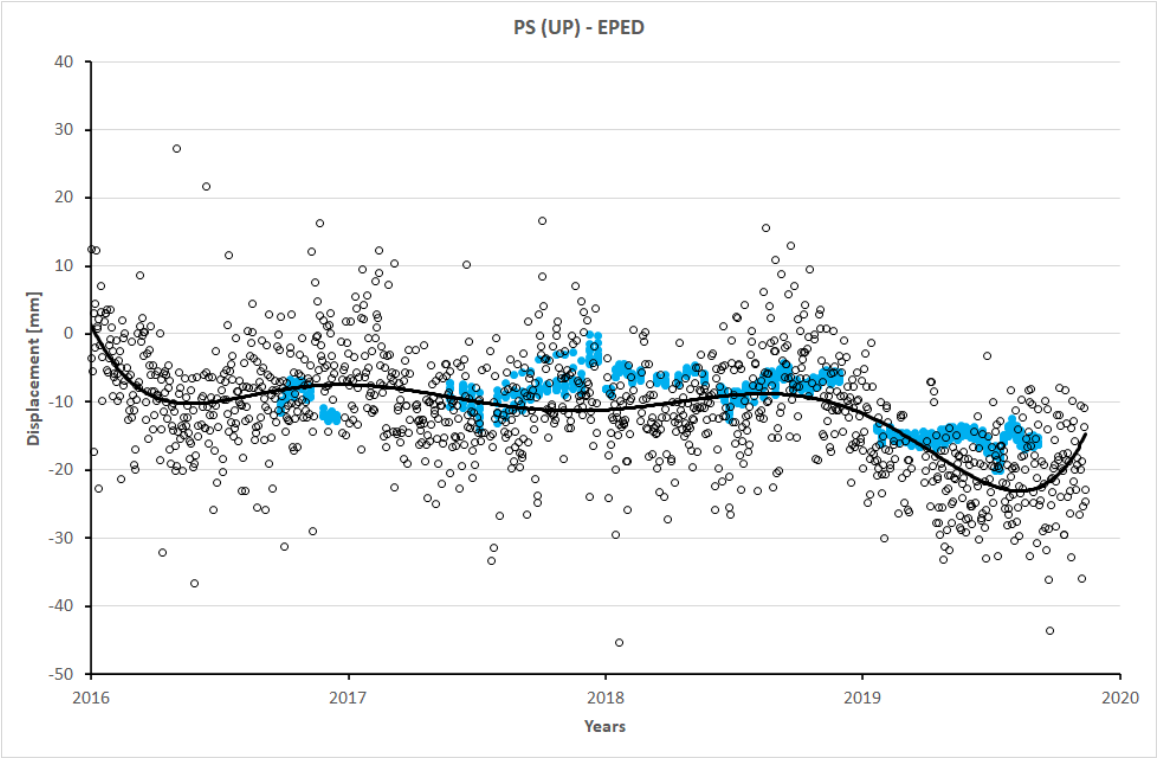

Figure 4. 32 - Comparison between the up displacement time series of the GNSS permanent station EPED (black circles) and up displacement time series of the pixels around the GNSS station (blue circles).

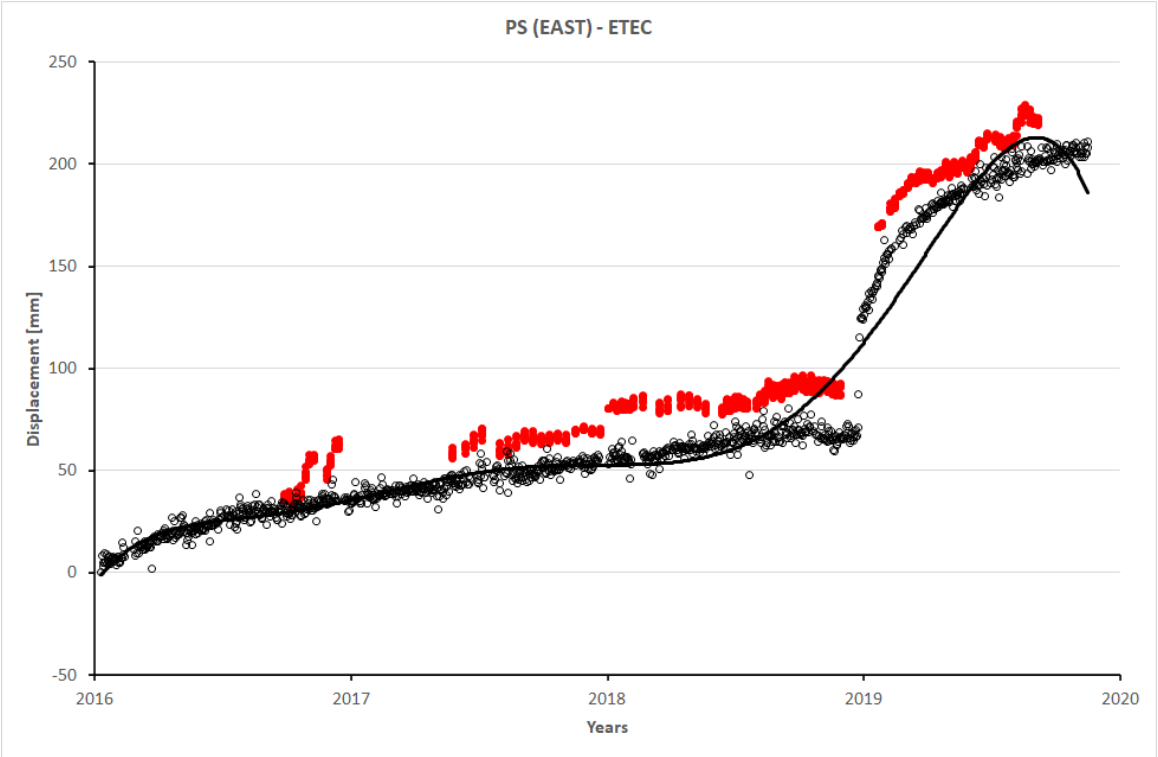

Figure 4. 33 - Comparison between the east displacement time series of the GNSS permanent station ETEC (black circles) and east displacement time series of the pixels around the GNSS station (red circles)

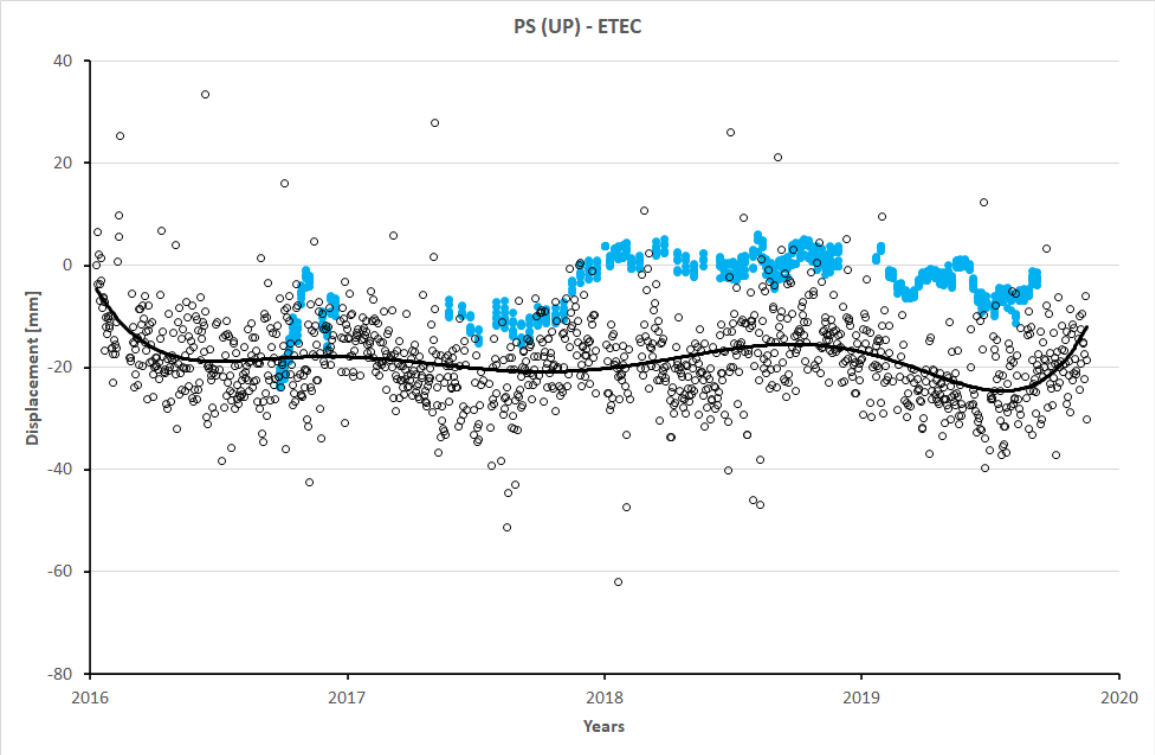

Figure 4. 34 - Comparison between the up displacement time series of the GNSS permanent station ETEC (black circles) and up displacement time series of the pixels around the GNSS station (blu circles)

Station	Component	Standard Deviation [mm]
EBDA	East	4.3
	Up	3.5
ELAC	East	8.7
	Up	11.5
ENIC	East	3.6
	Up	7.7
EPED	East	2.9
	Up	7.2
ETEC	East	5.8
	Up	11.7

As seen for the LOS displacement, the more reliable GNSS sites (in term of consistency GNSS v/s LOS) are located on western part of the analysed area; the stations EBDA, ENIC, and EPED have the lowest values of standard deviation both for the east and up component while the station ELAC and ETEC, located on the eastern area, have the highest value. In this case the P-SBAS web tool probably for the eastern part of the studied area, characterized by the highest velocity, is not able computed a reasonable time series.

4.7 EAST and UP Velocity

In this paragraph, for each year from 2016 until 2019, the east and up velocity maps are shown to create the anatomy of the deformation of the southern eastern flank of Etna volcano. The values of the velocity are relative to reference point which is located next to the EIIV GNSS permanent station located in Catania. The east and up velocity are generated by the combination of ascending and descending orbit for the same pixel common to both orbits.

4.7.1 Deformation in 2016

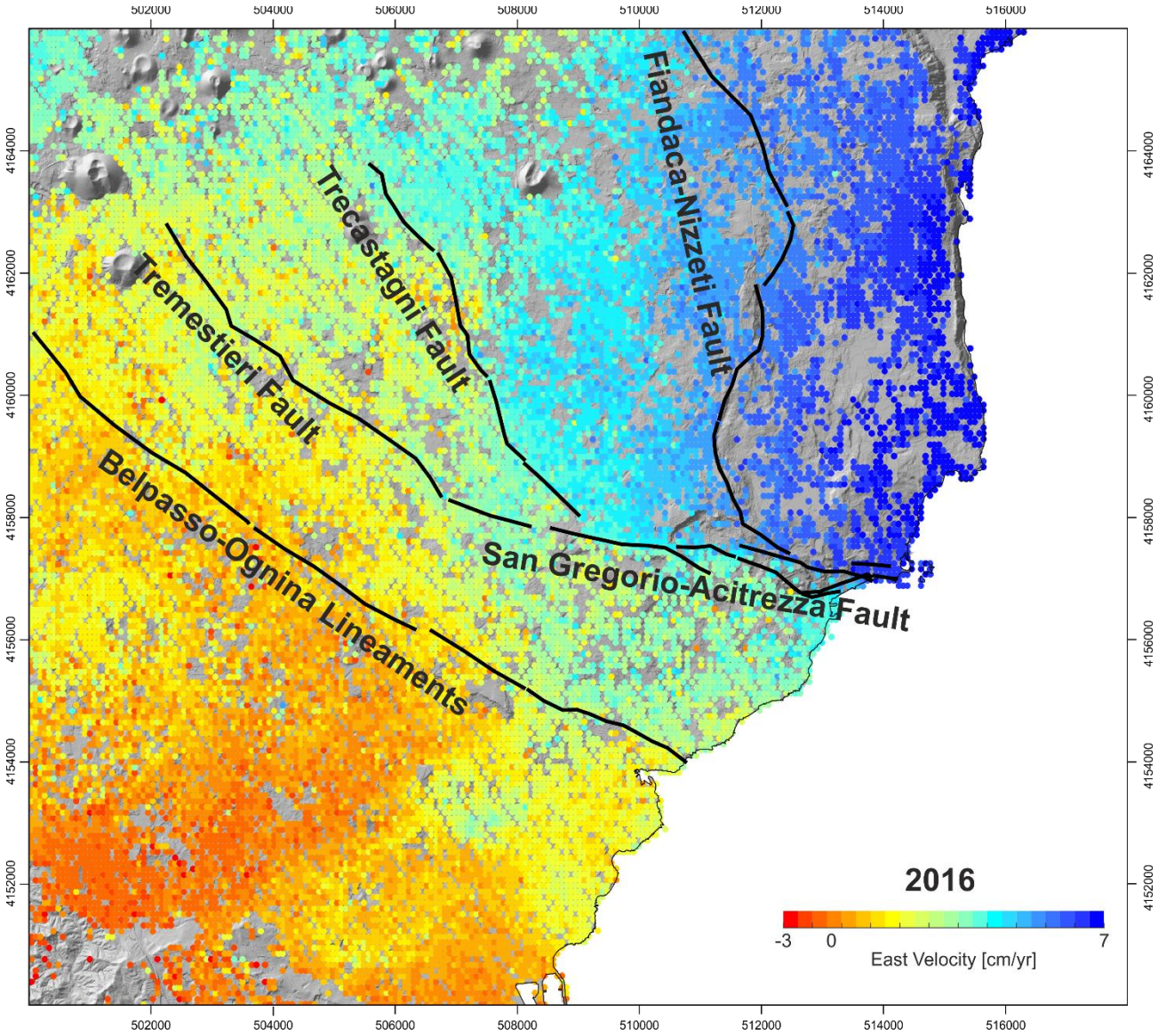

Figure 4. 35 – East velocity map (cm/yr) for the year 2016 and analysed structures of the south eastern flank of Mount Etna.

The Figure 4. 35 shows the east velocity map recorded by P-SBAS online tool during the year 2016. The most active faults in this period are the Trecastagni Fault and the San Gregorio-Acitrezza Fault that represent the margin of the eastern unstable flank. The east velocity suddenly increases from west to east after the Trecastagni fault. The Tremestieri fault and the Belpasso-Ognina Lineaments appear inactive in this period.

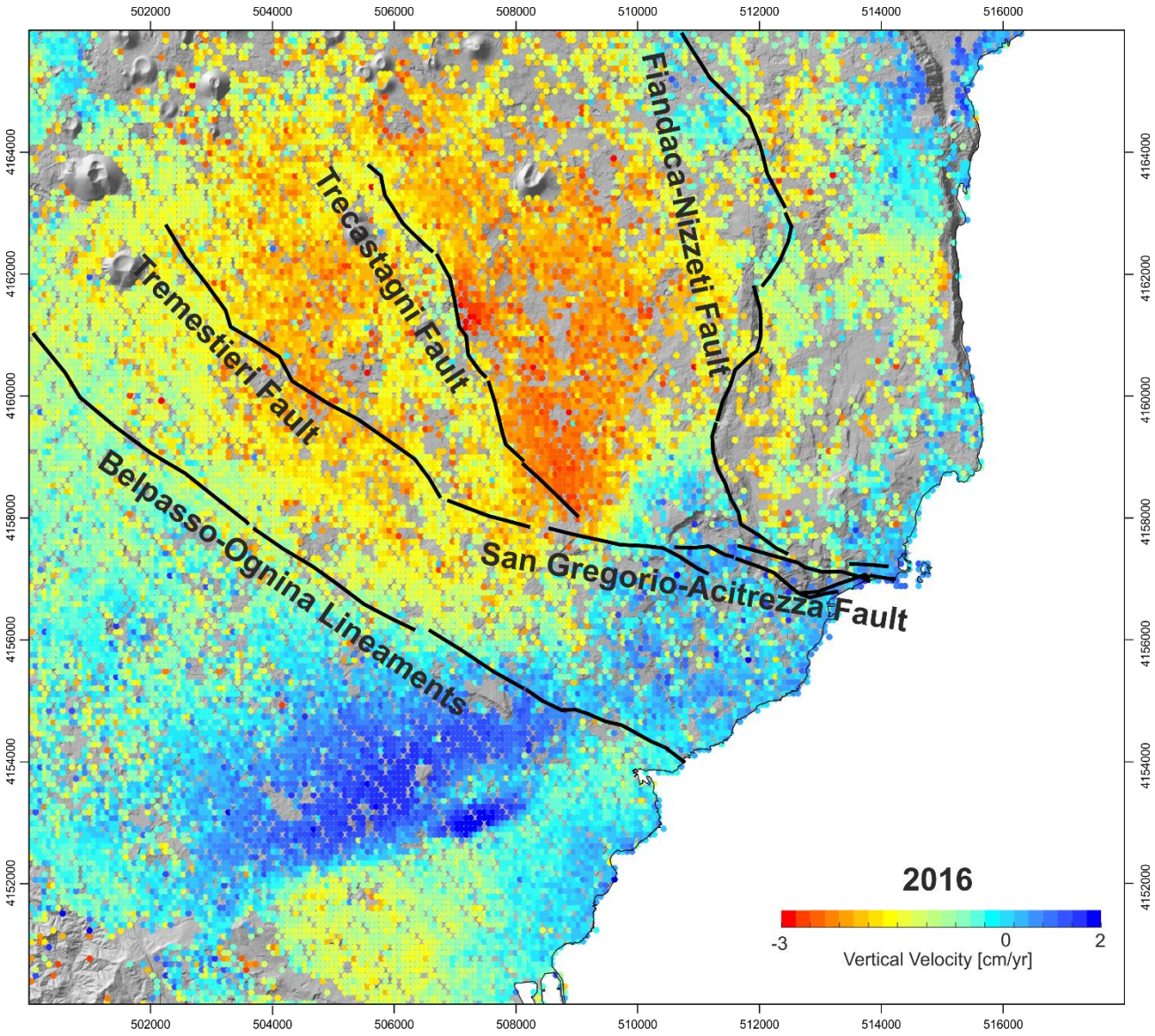

Figure 4. 36 – Up velocity map (cm/yr) for the year 2016 and analysed structures of the south eastern flank of Mount Etna.

The Figure 4. 36 shows the up velocity map that affected the eastern flank during the 2016. There are two areas that are affected by a vertical deformation: the first one is located at east side of the Trecastagni Fault and the second one is located at south of the Belpasso-Ognina Lineaments. The first area is deformed by the vertical displacement of the Trecastagni Fault

which is more active on the middle and southern part. The second area is affected by the uplift generated by the Anticlinal of Catania, with a maximum velocity of about 2 cm/yr during that year. It is important to note that the uplift deformation is continuing over the Belpasso-Ognina Lineaments, but the velocity is lower than the southern area and it is continuing until the San Gregorio-Acitrezza Fault.

4.7.2 Deformation in 2017

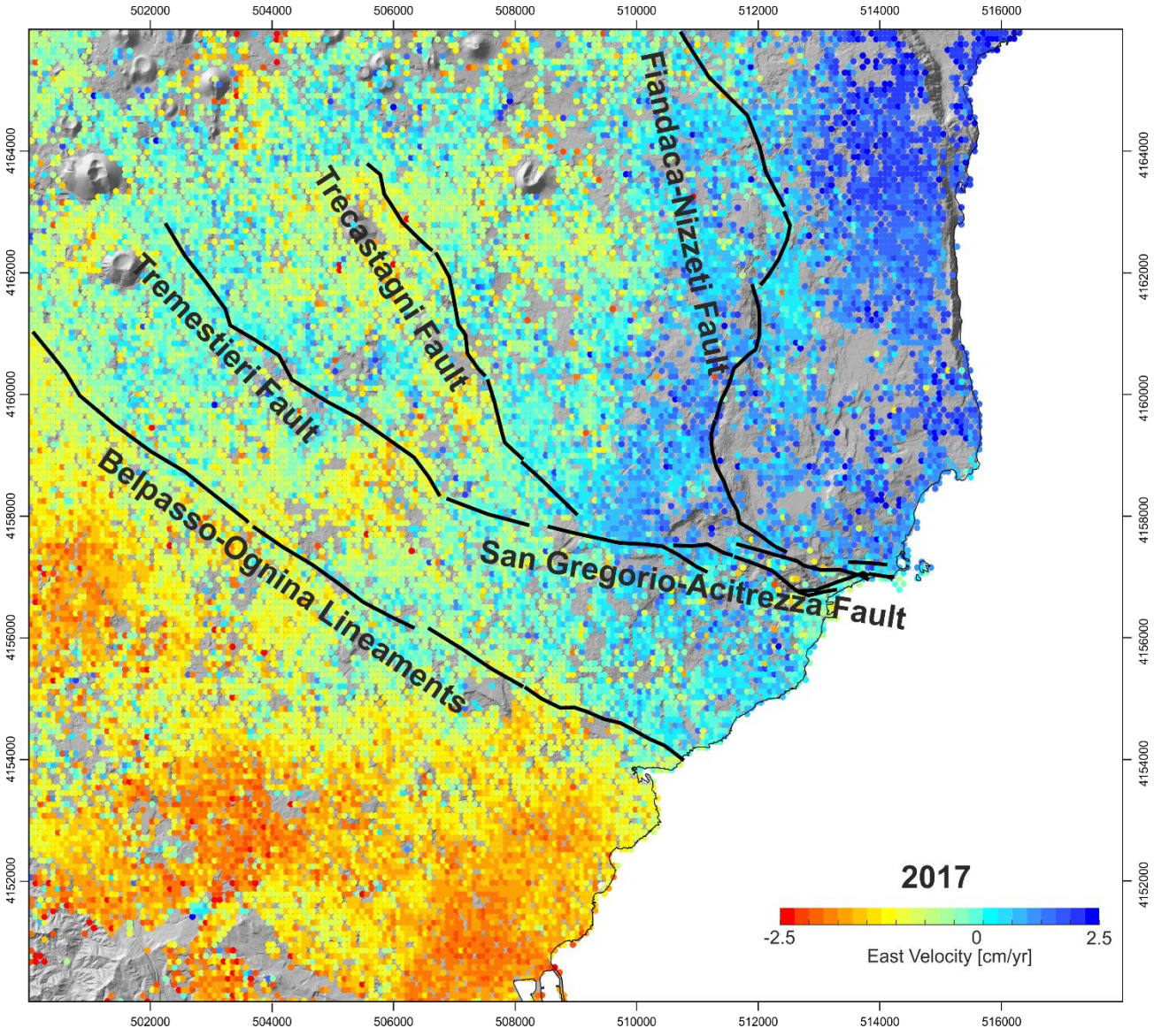

Figure 4. 37 - East velocity map (cm/yr) for the year 2017 and analysed structures of the south eastern flank of Mount Etna.

In Figure 4. 37 the east velocity map occurred during the 2017 are shown. The velocities reach during this year are the lowest from 2016 until 2019. Only the eastern part is moving toward

east with a maximum velocity of about 2.5 cm/yr. The Belpasso-Ognina Lineaments behaves as a barrier because on the south of this fault the east velocity is zero or negative.

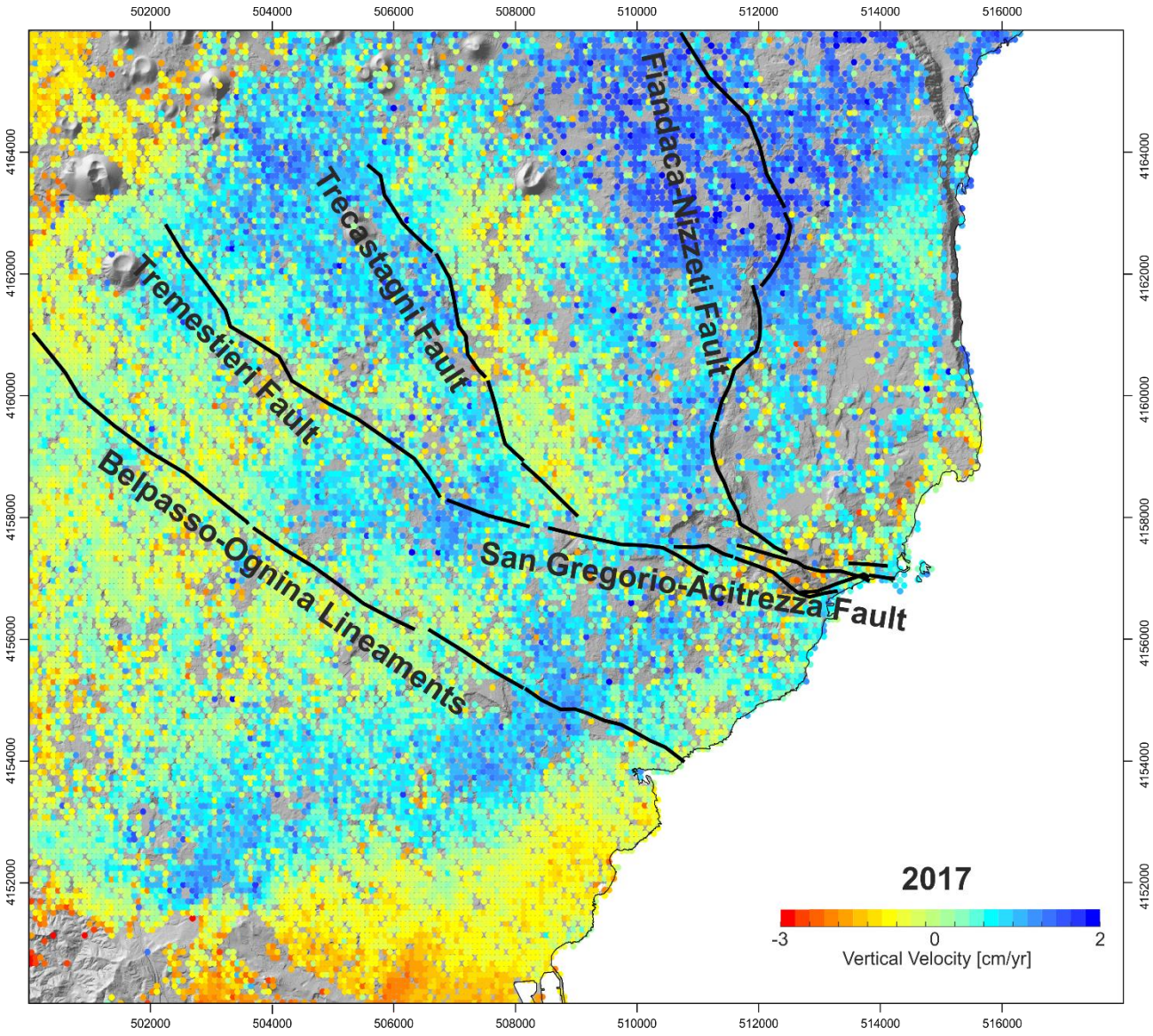

Figure 4. 38 - Up velocity map (cm/yr) for the year 2017 and analysed structures of the south eastern flank of Mount Etna.

In Figure 4. 38 the vertical deformation map in 2017 is shown. The Anticlinal of Catania is less active compare to the year 2016, moreover there is a general uplift, (1-2 cm/yr) that is affected almost all the eastern flank of Etna volcano.

4.7.3 Deformation in 2018

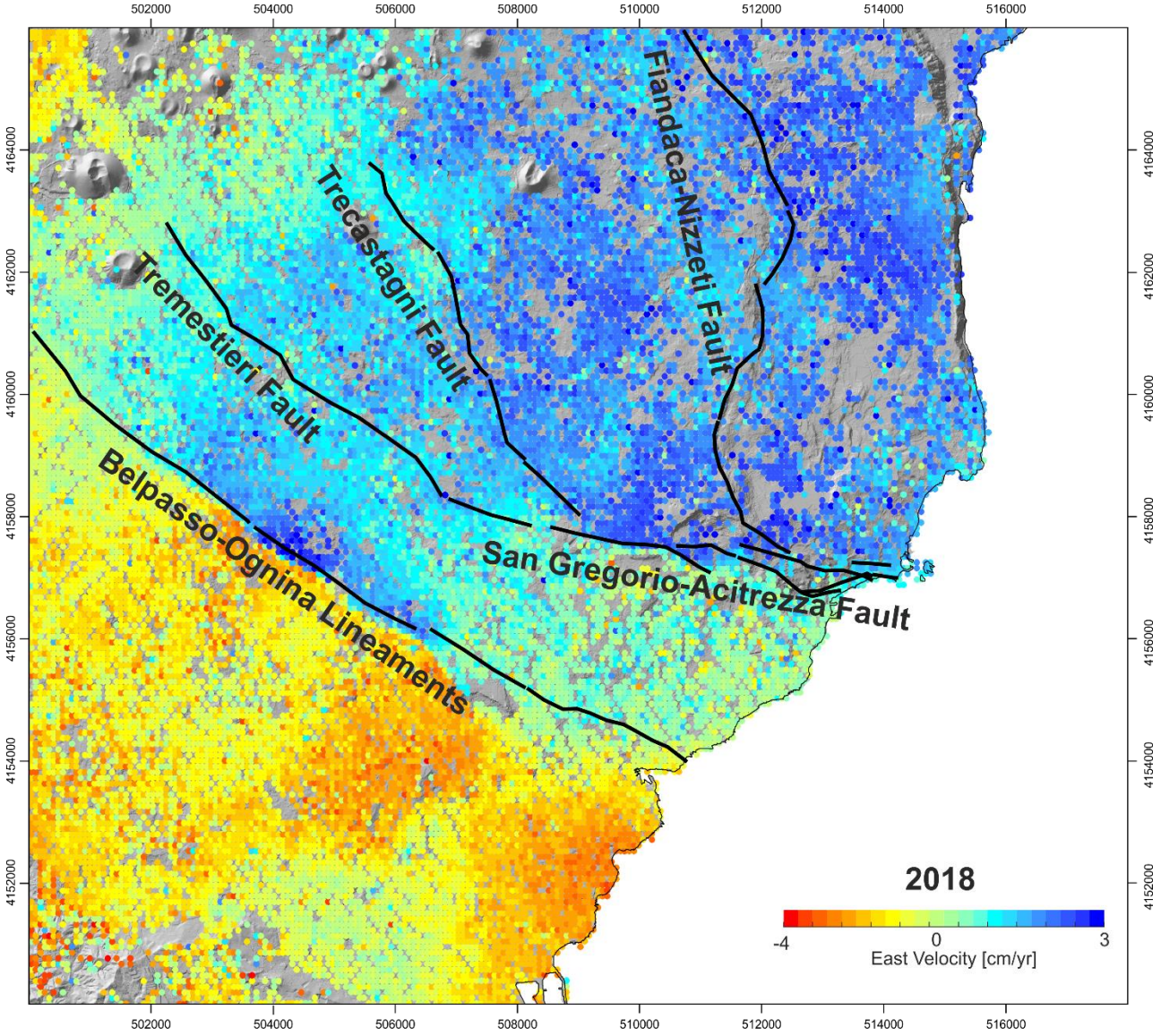

Figure 4. 39 - East velocity map (cm/yr) for the year 2018 and analysed structures of the south eastern flank of Mount Etna.

In Figure 4. 39 the east velocity map is shown. The most active fault in this period is the Belpasso-Ognina Lineaments on its middle part. Here the east velocity reaches the maximum values of about 3 cm/yr. This structure is behaving as a boundary between the stable southern side and the unstable northern side. The northern part moves entirely toward east as a single block.

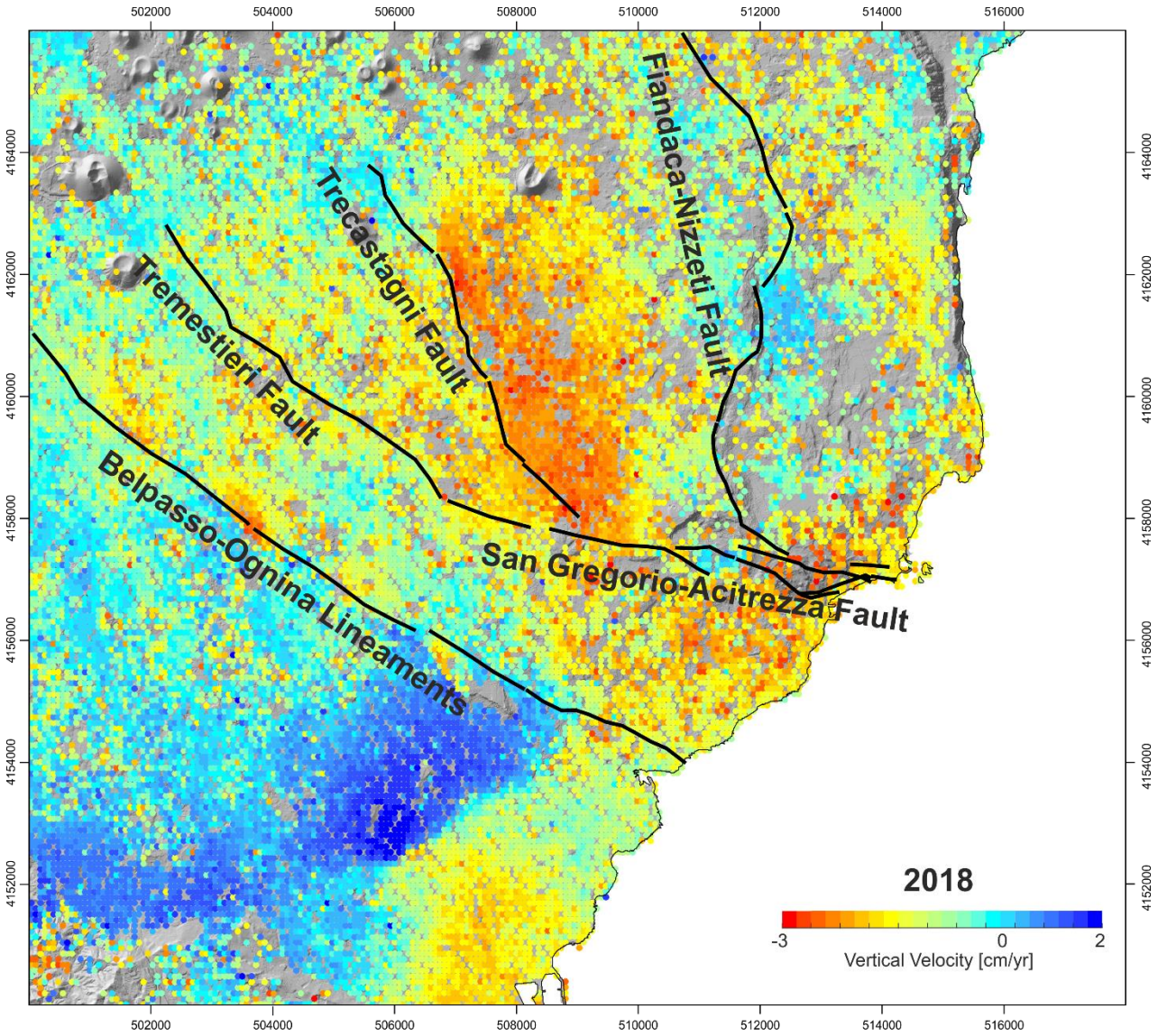

Figure 4. 40 - Up velocity map (cm/yr) for the year 2018 and analysed structures of the south eastern flank of Mount Etna.

In Figure 4. 40 the vertical velocity map is shown. During the 2018, on the hanging wall of Trecastagni Fault the highest vertical velocity of about -3 cm/yr occurs moreover the Anticlinal of Catania is active with a vertical velocity of about 2 cm/yr but in this case the uplift disappear on the north of Belpasso-Ognina Lineaments.

4.7.4 Deformation in 2019

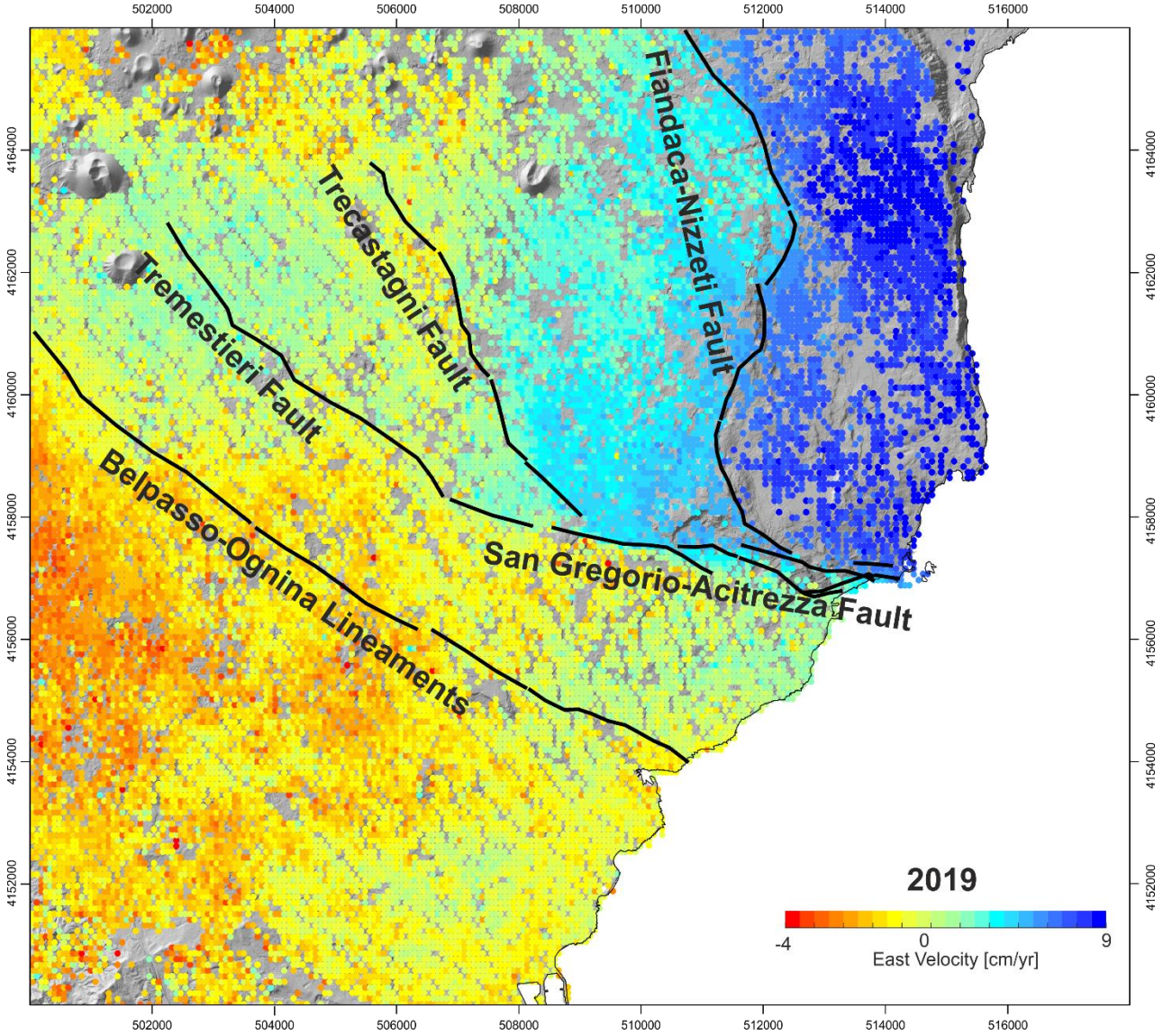

Figure 4. 41 - East velocity map (cm/yr) for the year 2019 and analysed structures of the south eastern flank of Mount Etna.

In Figure 4. 41 the east velocity recorded during the 2019 is shown. During this period the highest east velocity are reached, with a maximum value of about 9 cm/yr. The most active fault is the Fiandaca-Nizzeti Fault due the post-seismic deformation after the earthquake on 26 December 2018.

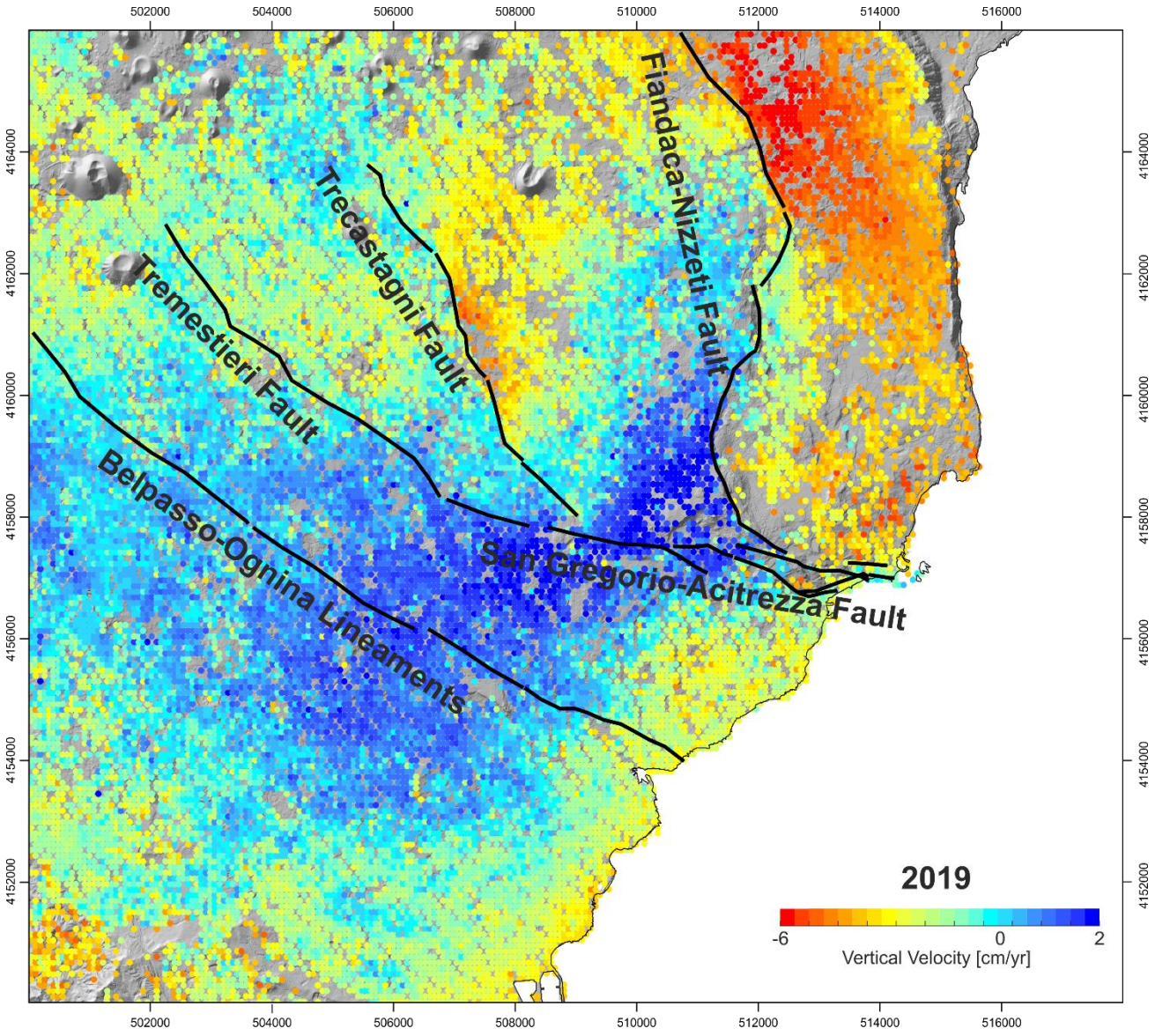

Figure 4. 42 - Up velocity map (cm/yr) for the year 2019 and analysed structures of the south eastern flank of Mount Etna.

In Figure 4. 42 the vertical velocity recorded during the 2019 is shown. The most active fault is the Fiandaca-Nizzeti Fault which show the highest vertical velocity of about -6 cm/yr on the hanging wall due to the post-seismic deformation after the 26 December Earthquake. Moreover the Trecastagni show a vertical velocity -4/-5 cm/yr on the middle part of the this fault.

4.8 East and Up Fault offset

After that, the permanent scatter's velocity had been converted into the east and up components. A distance of 500 meters from both sides of the fault was chosen to extract the

permanent scatters using ArcMap software of Esri. The permanent scatters were plotted to obtain the velocities of the various blocks divided by the faults and to analyse any acceleration or deceleration that might be occurred along the fault itself.

For this analysis: i) Belpasso-Ognina Lineaments, ii) Tremestieri - San Gregorio - Acitrezza Fault, iii) Trecastagni Fault and iv) Fiandaca-Nizzeti Fault, which has been considered as a single fault to simplify the graphic visualization, have been considered.

For each fault, two profiles were created according to the direction of the faults. For the faults with a predominantly E-W direction a north and a south profiles were created; for the faults with a predominantly N-S direction an east and a west profiles were created.

For the realization of the profiles a unique starting zero was considered for all profiles to calculate the distance along the profile calculated from this starting point (Figure 4. 43).

Finally, each profile has been realised for each year from 2016 to 2019 because the PS have been calculated for every single year.

Eight profile had been considered: Belpasso-Ognina Lineaments South (1) and North (2), Tremestieri-San Gregorio-Acitrezza Fault South (3) and North (4), Trecastagni fault West (5) and East (6), Fiandaca-Nizzeti West (7) and East (8) (Figure 4. 43).

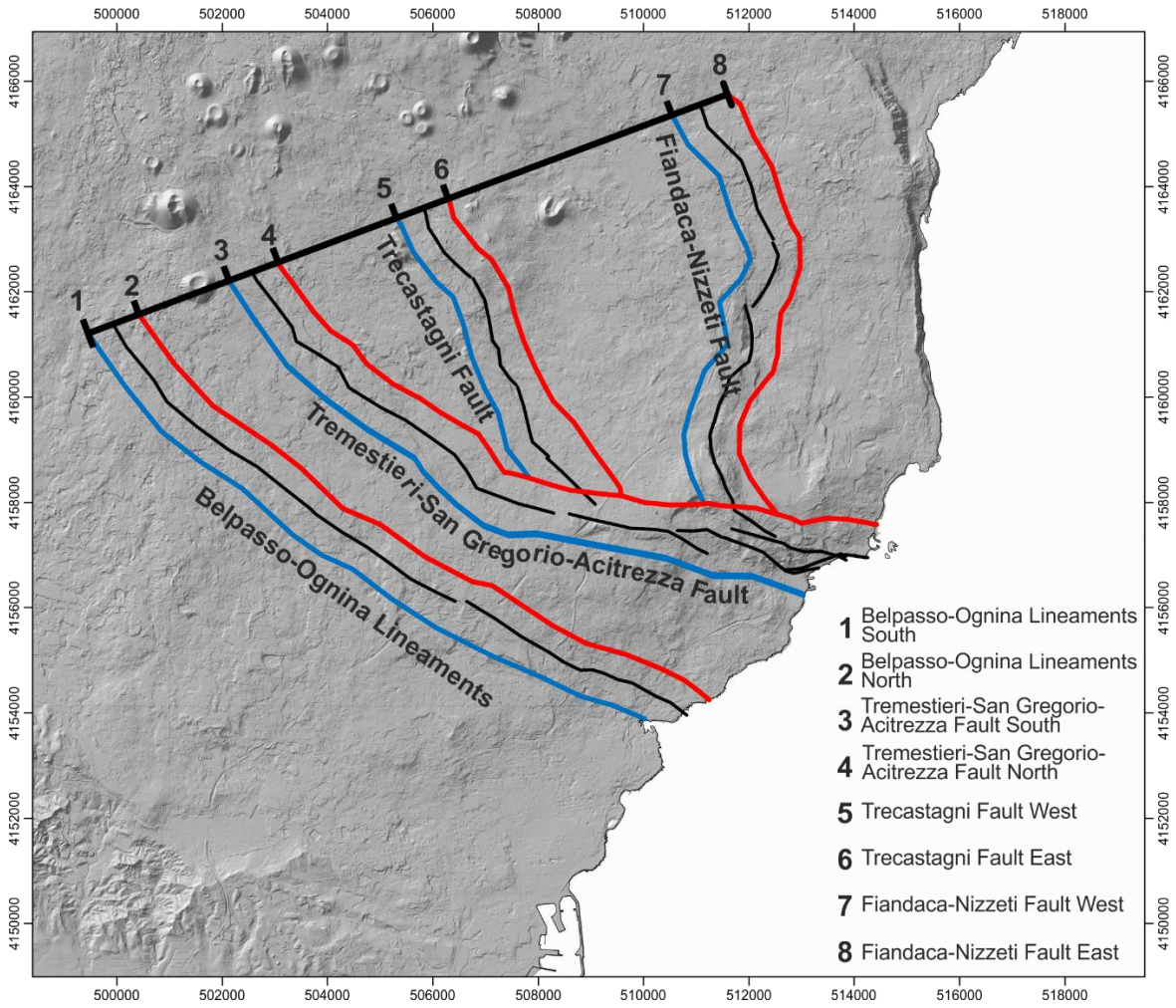

Figure 4. 43 – Trace of the profiles used to plot the permanent scatter. The coarser black line represents the zero common to all profiles. Red profiles are the east or north profiles for each fault. Blue profiles are the west or south profile for each fault.

4.8.1 Offset 2016

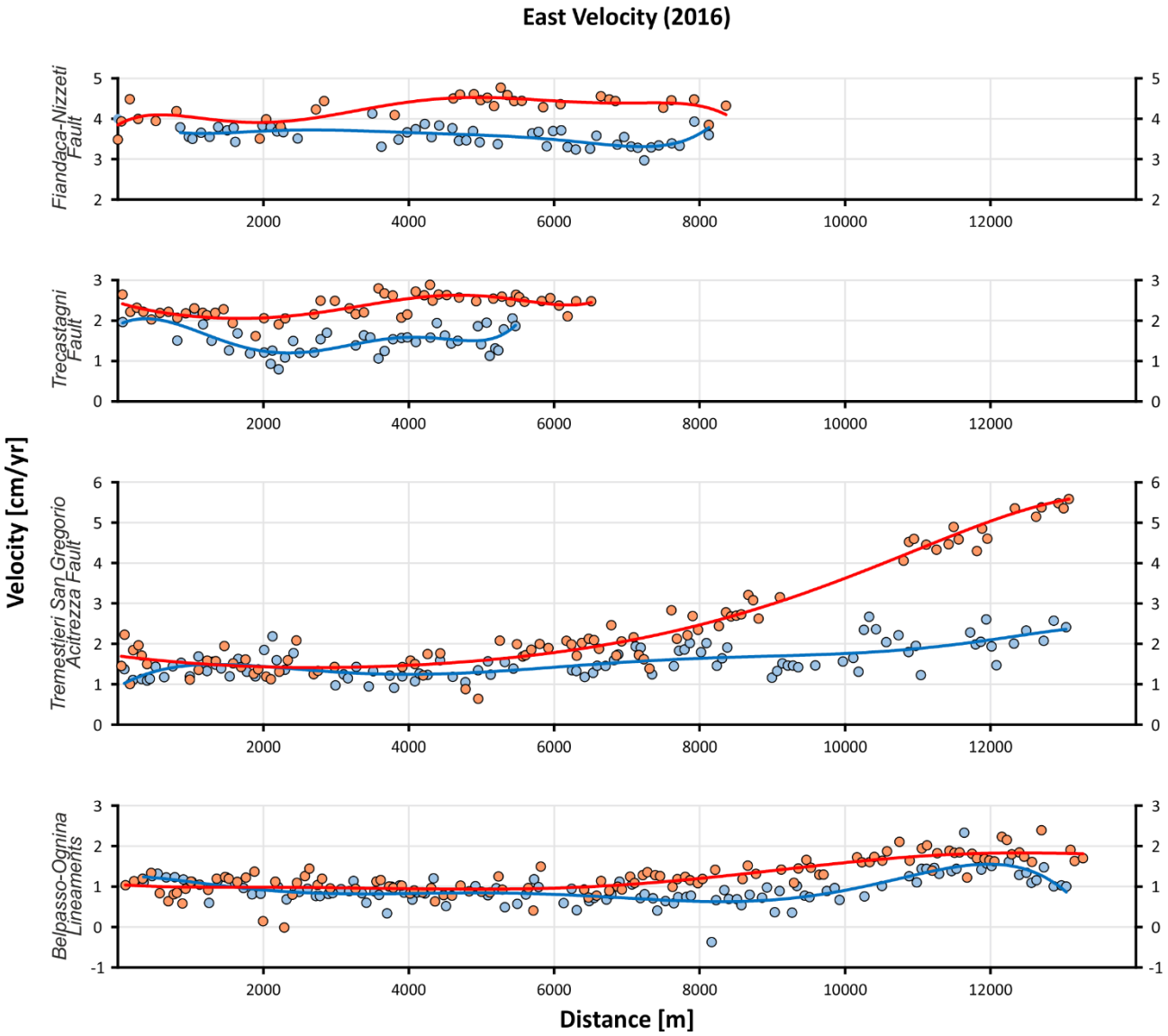

Figure 4. 44 – East velocity profiles of the selected PS for each fault considering for the year 2016. Blue dots are the south or west profiles. The red dots are the north and east profiles.

During the year 2016, all the faults are active on the east component (Figure 4. 44). The Tremestieri-San Gregorio-Acitrezza Fault shows an important east acceleration, up to almost 6 cm/yr, only on the northern side of the fault, showing also an offset between the two side of about 3.5 cm/yr. The Trecastagni Fault and the Nizzeti Fault show a constant offset of about 1 cm/yr for all their length. Belpasso-Ognina Lineaments shows an offset only in its final part of about 0.5 cm/yr.

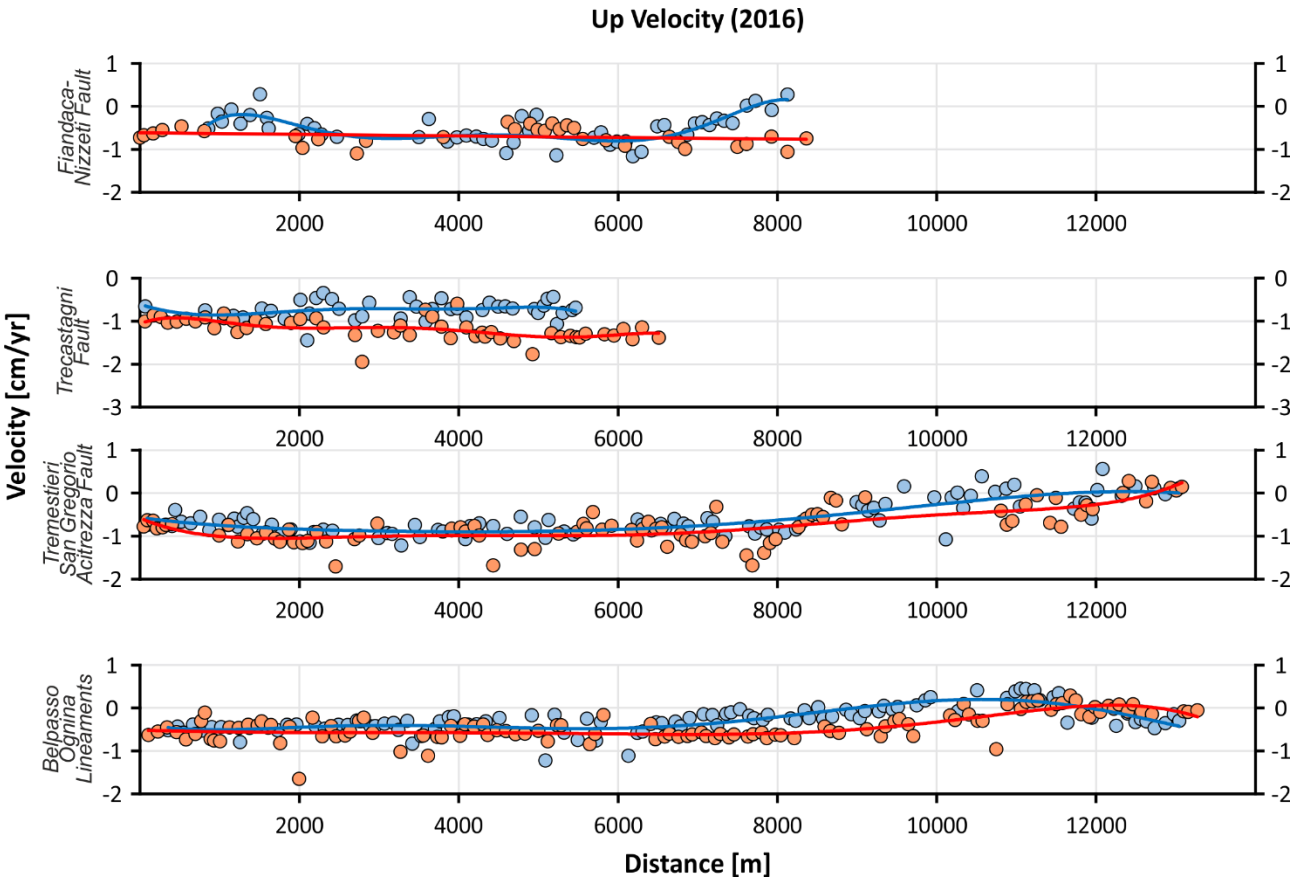

Figure 4. 45 - Up velocity profiles of the selected PS for each fault considering for the year 2016. Blue dots are the south or west profiles. The red dots are the north and east profiles.

For the up component (Figure 4. 45), there is an offset in the Trecastagni Fault of about 0.5 cm/yr and an offset 0.3 cm/yr on the final part of the Belpasso-Ognina Lineaments.

4.8.2 Offset 2017

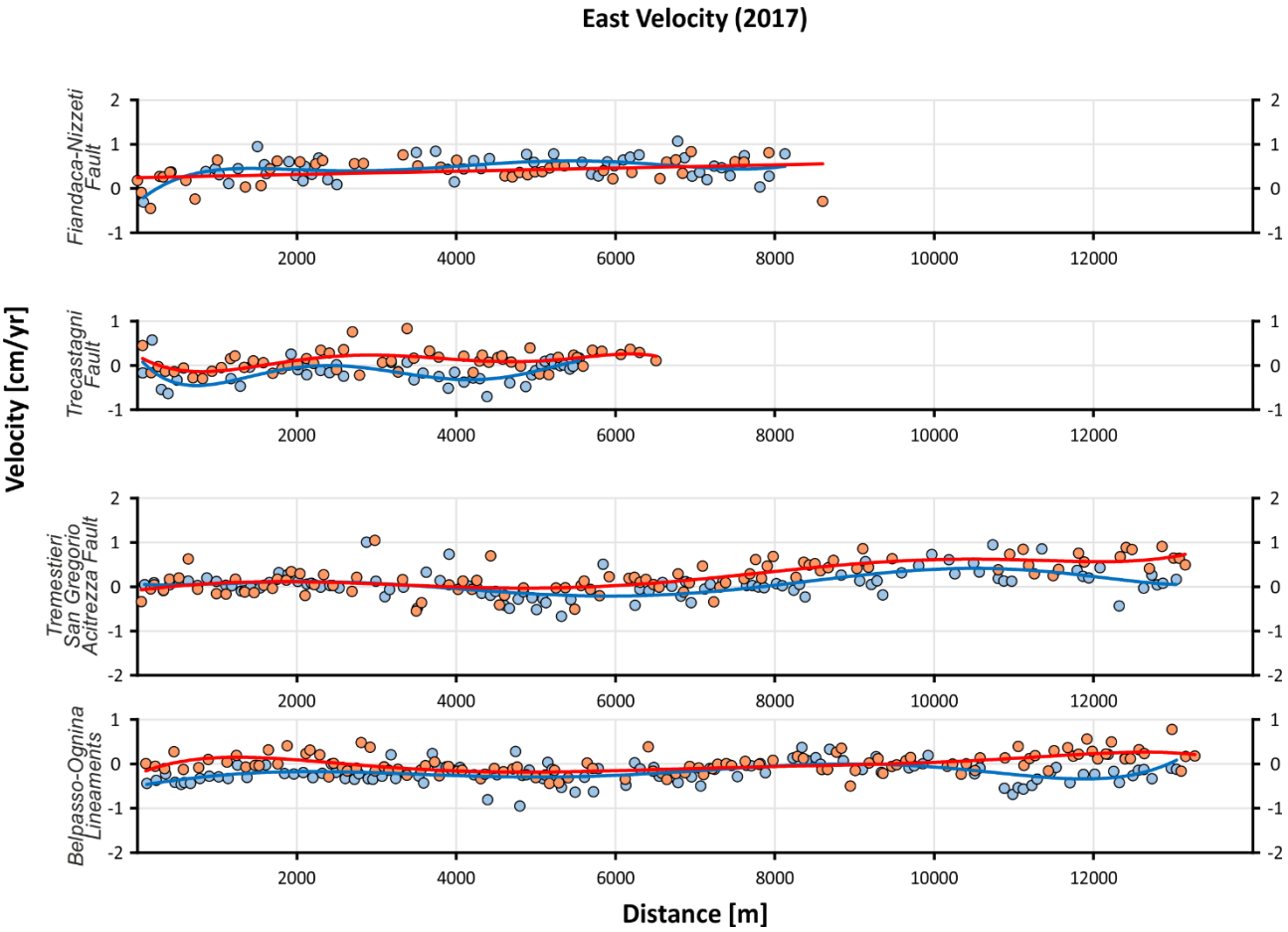

Figure 4. 46 - East velocity profiles of the selected PS for each fault considering for the year 2017. Blue dots are the south or west profiles. The red dots are the north and east profiles.

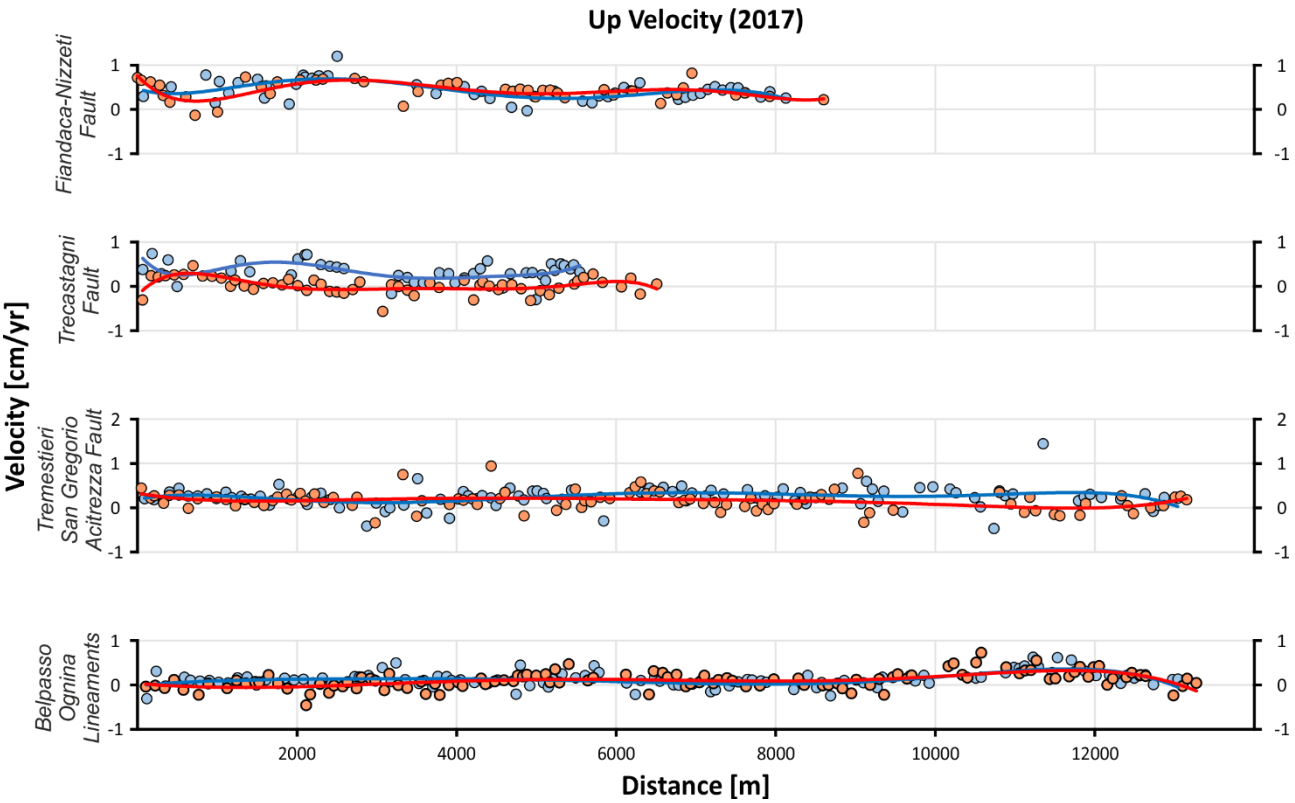

Figure 4. 47 - Up velocity profiles of the selected PS for each fault considering for the year 2017. Blue dots are the south or west profiles. The red dots are the north and east profiles.

During the 2017, there are not evident offset both for the east and the up component for each fault (Figure 4. 46 and Figure 4. 47).

4.8.3 Offset 2018

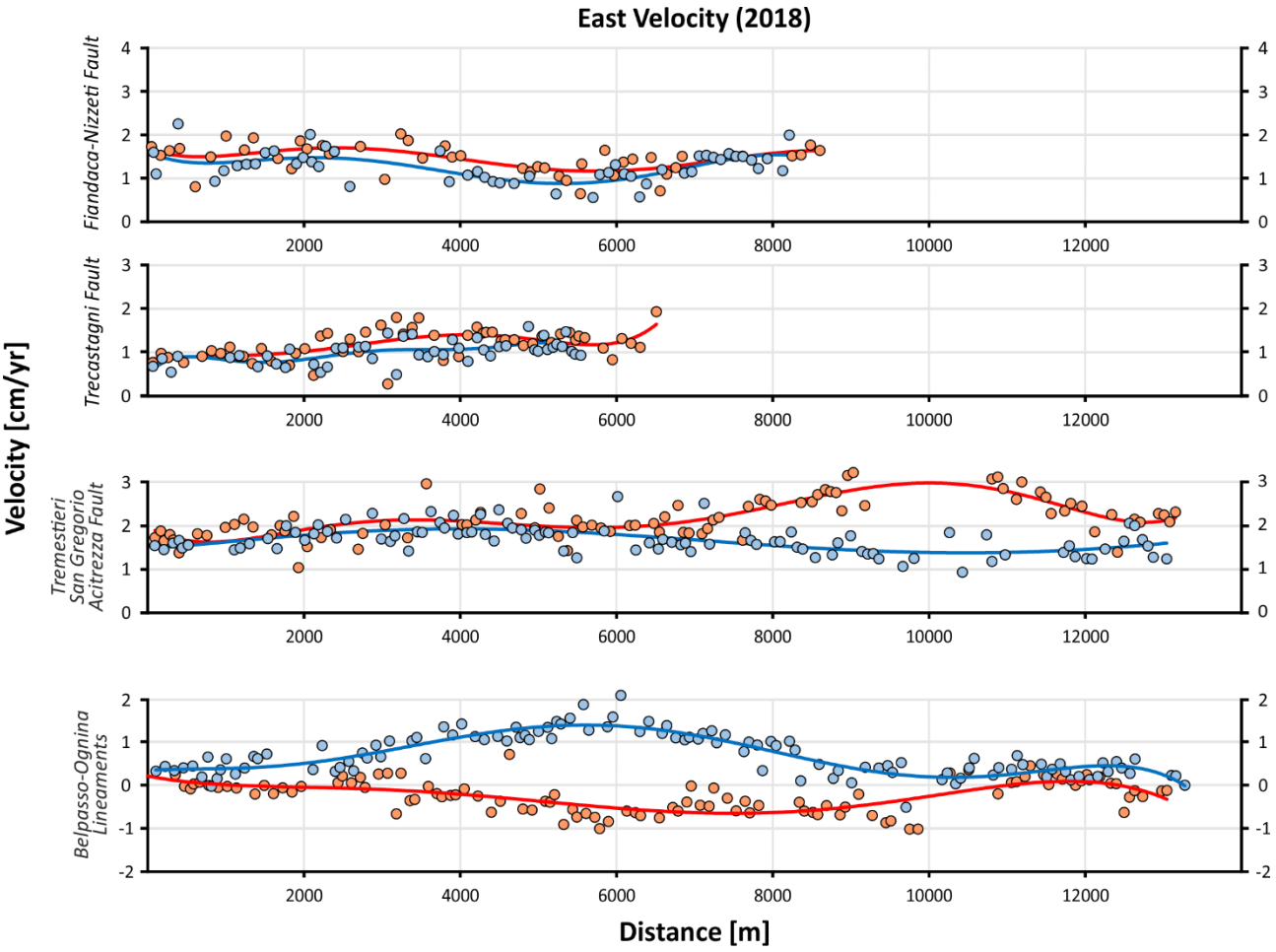

Figure 4. 48 - East velocity profiles of the selected PS for each fault considering for the year 2018. Blue dots are the south or west profiles. The red dots are the north and east profiles.

During the 2018, the southern part of the eastern flank of Etna is active, in particular the TSGA Fault and the Belpasso-Ognina Lineaments show an offset of about 2 cm/yr respectively. It is important to highlight that the terminal part of TSGA and the central part of Belpasso-Ognina Lineaments show the offset (Figure 4. 48).

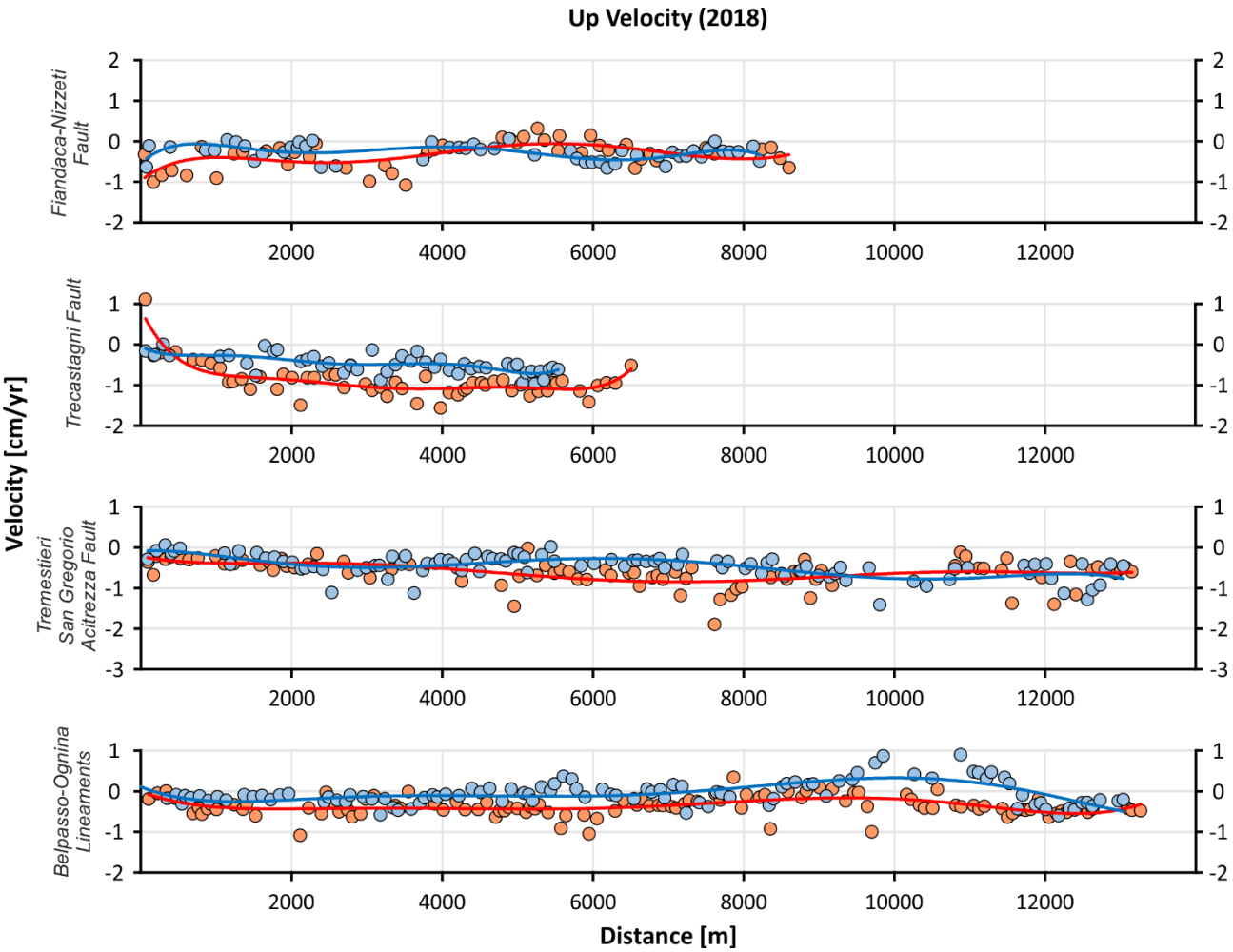

Figure 4. 49 - Up velocity profiles of the selected PS for each fault considering for the year 2018. Blue dots are the south or west profiles. The red dots are the north and east profiles.

For the up component (Figure 4. 49), only the Belpasso-Ognina Lineaments shows an offset of about 1 cm/yr that correspond to the intersection of this structure with the Catania anticlinal, which produce an uplift in the southern side of the Belpasso-Ognina Lineaments moreover this uplift disappears on the northern part.

4.8.4 Offset 2019

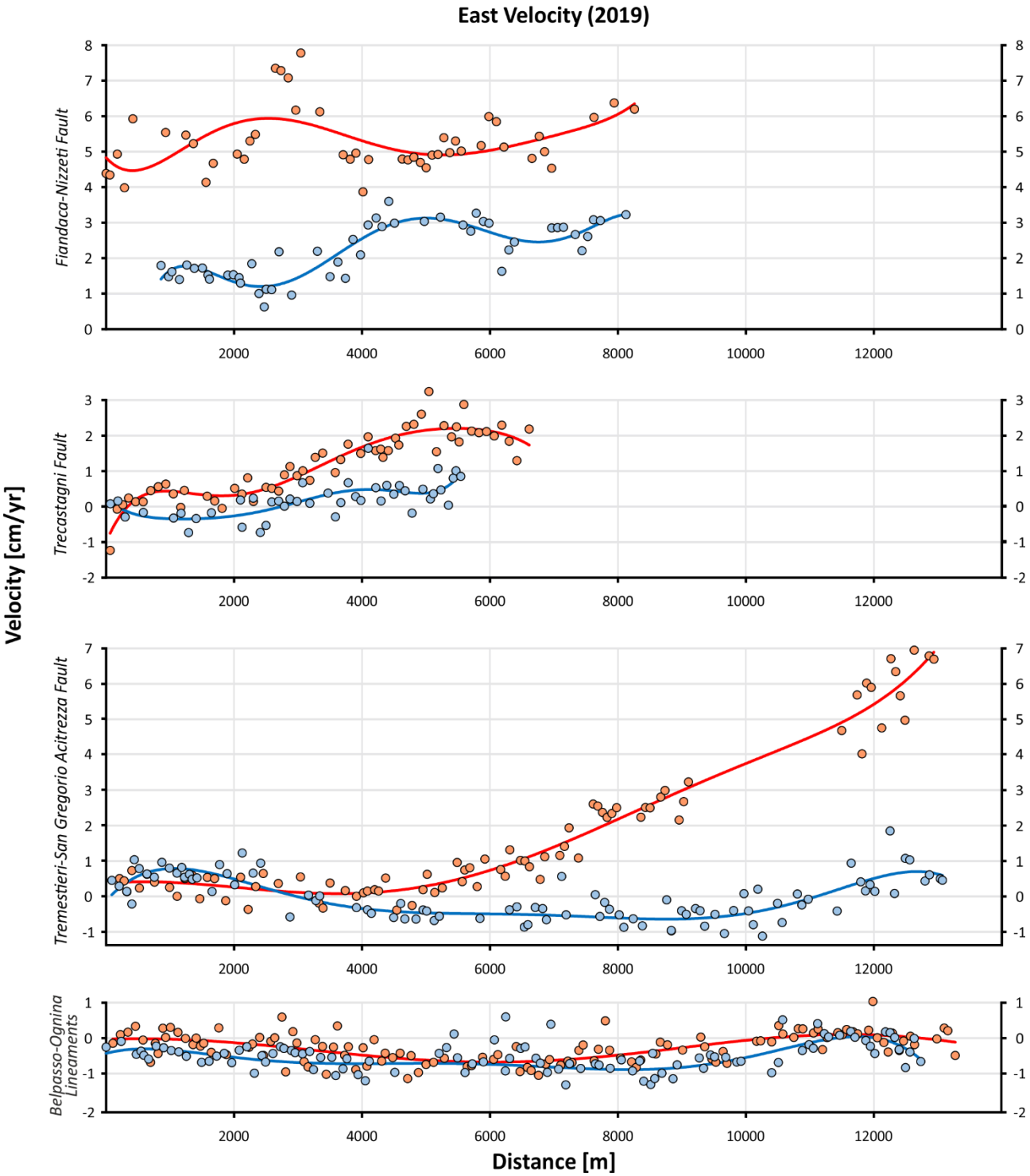

Figure 4. 50 - East velocity profiles of the selected PS for each fault considering for the year 2019. Blue dots are the south or west profiles. The red dots are the north and east profiles.

During the 2019, all the faults of the eastern flank of Etna were active due by the post-seismic deformation after the eruption and the earthquake occur on 24 and 26 December 2018 (Figure

4. 50). For the east component the Fiandaca-Nizzeti Fault is the most active, it shows an offset between 2-5 cm/yr. The offset is maximum on the northern part of the profile that corresponds to the Fiandaca Fault and it is decreasing to the south until to 2-3 cm/yr that corresponds to the Nizzeti Fault. The TSGA show a very important acceleration toward east, reachs the value of about 6 cm/yr as offset between the blocks. The Trecastagni Fault shows an offset of about 2 cm/yr in the southern part of the fault and the Belpasso-Ognina Lineaments show an unclear offset (Figure 4. 50).

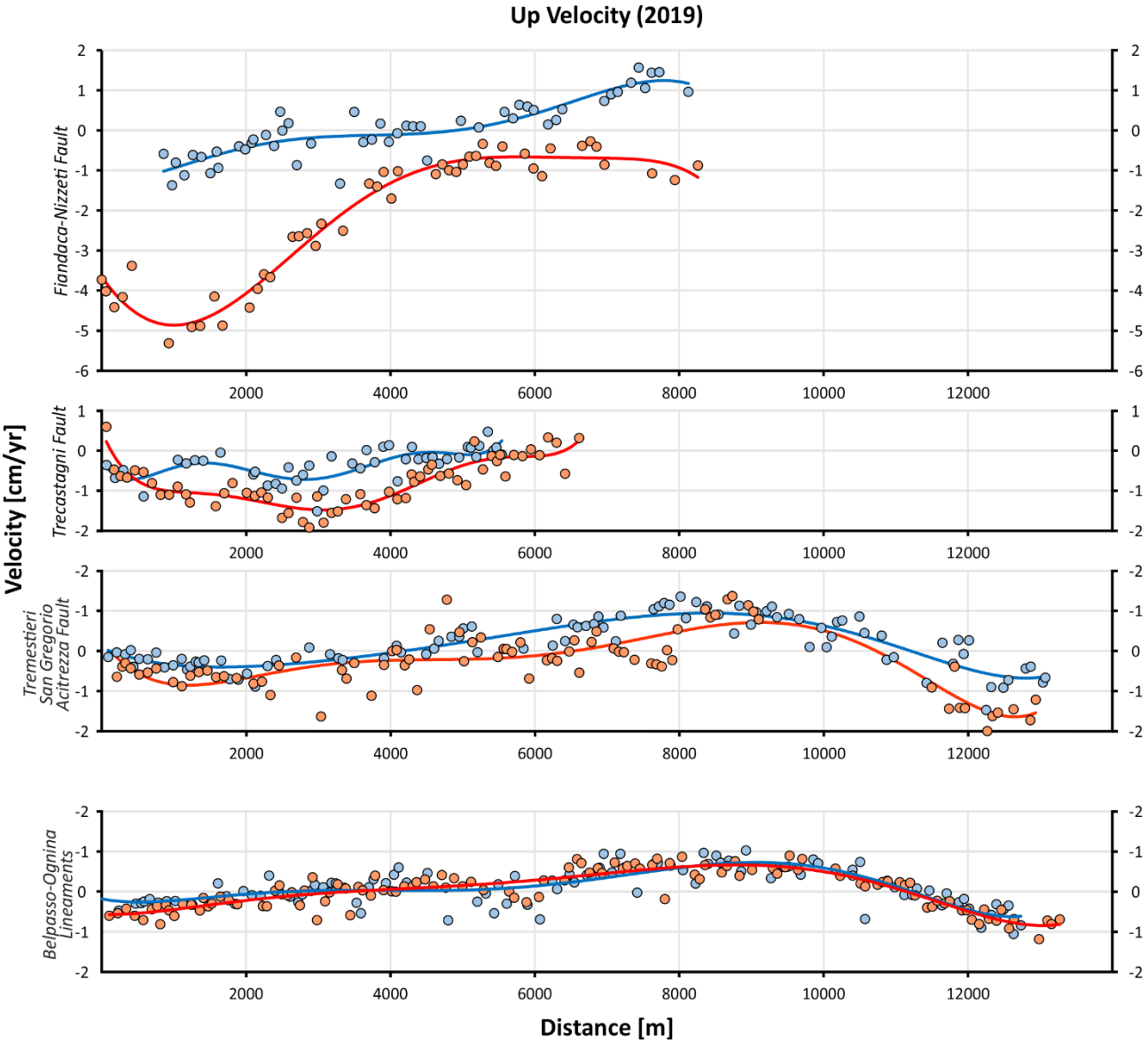

Figure 4. 51 - Up velocity profiles of the selected PS for each fault considering for the year 2019. Blue dots are the south or west profiles. The red dots are the north and east profiles.

For the up component (Figure 4. 51), the northern part of the Fiandaca-Nizzeti fault is the most active due by the post-seismic deformation after the earthquake of 26 December 2018. The

profile shows a maximum vertical offset of 4 cm/yr. The TSGA Fault and the Belpasso-Ognina Lineaments do not show an offset, but the Belpasso-Ognina Lineaments shows an uplift in the central part in both south and north blocks.

CHAPTER 5

DISCUSSION AND CONCLUSION

Mount Etna is located in an area where, at the broad scale, two dynamic tectonic regimes coexist: a compression oriented N-S and an extension oriented approximately WNW-ESE. At the local scale, the normal faults, as the Timpe faults, are due to the extensional tectonic while the active fold structures, immediately south west of the volcano complex, are linked to the compressional one, dynamics linked to the Africa Europa compression.

In this context, it is important to define a reference system relevant for the analysis of the velocity field of eastern Sicily.

In this thesis, the regional velocity field was defined by analysing the velocities of the permanent stations in eastern Sicily and then compared with the velocity of EIIV (Catania).

We have seen that considering only the stations located on the Hyblaean plateau or considering also the two stations located in north-eastern Sicily (MNOV and GALF), both cases lead to residues below the millimetre level. The EIIV station has a stable velocity, during the period from 2009 until 2015, of 1.2 mm/yr in the East component and of -1.8 mm/yr in the North component. This velocity has a N146° direction considering all the stations of eastern Sicily (HLNI, SSYX, HAGA, HMDC, HAV1, NOT1, GALF and MNOV) and a N150° direction considering only the GNSS stations on the Hyblaean plateau (HLNI, SSYX, HAGA, HMDC, HAV1 and NOT1).

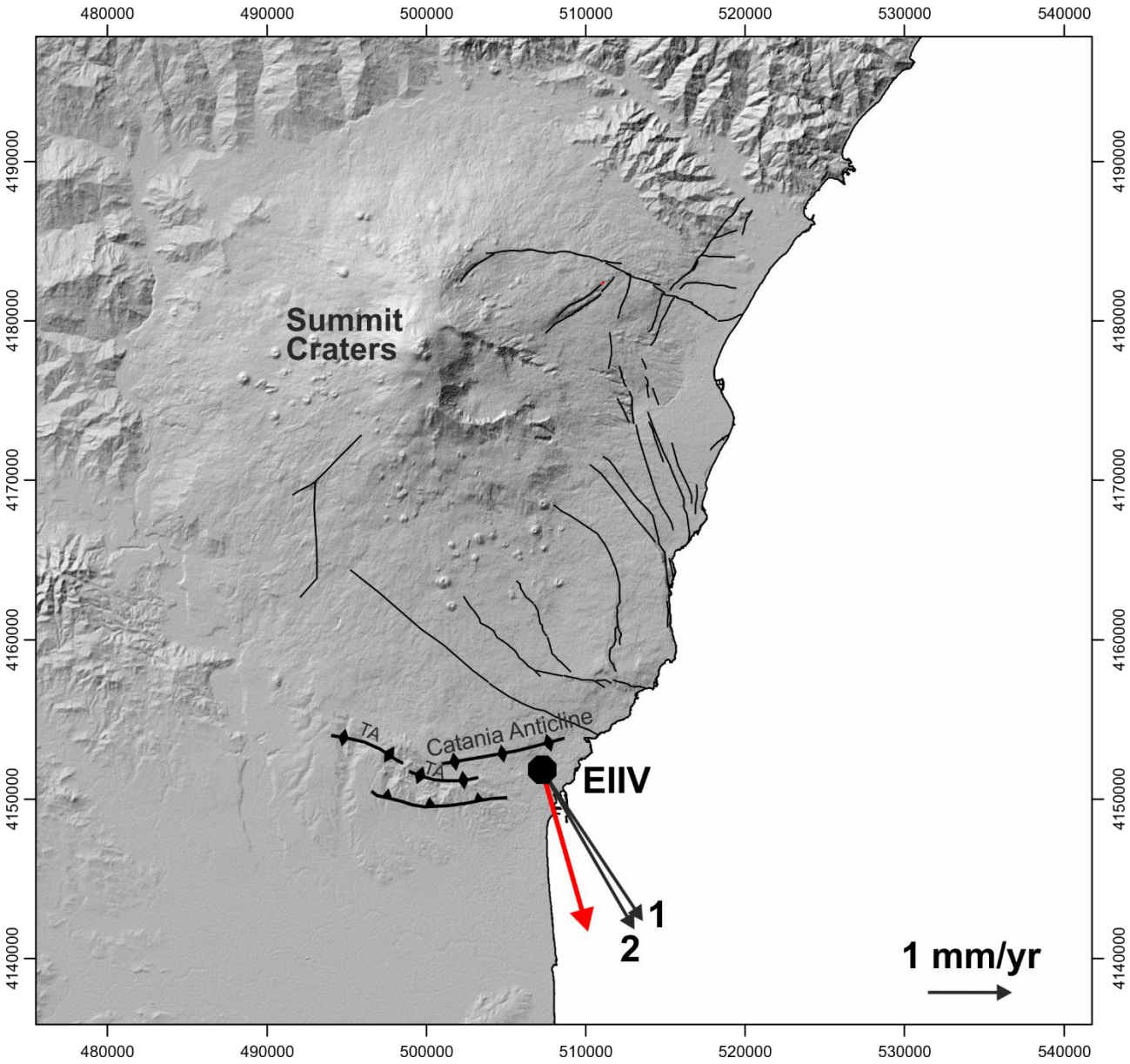

Figure 5. 1 – Velocity of EIIV referred to the Hyblaen plateau fixed (1) and to Eastern Sicily fixed (2). Red arrow represents the azimuth between the EIIV and the summit craters of Mount Etna. TA = Terreforti Anticline.

In both cases the azimuth of the anomaly is different from the direction N170° (azimuth between the EIIV and summit craters of Mount Etna), while it is consistent with the compressive plicative structures located beneath the north of the city of Catania (Figure 5. 1). Noteworthy, EIIV presents periods of departure to this trend before and after large eruptions like those of 2002 and 2018. We speculate that this linked to the phases of inflation and deflation of the volcano associated with those events. They correspond to velocity changes up to of 11 mm/yr as measured after the 2018 eruption.

The velocity field of eastern Sicily being precisely defined, it is subtracted from the velocity of the permanent GNSS stations located on the eastern side of Mount Etna (Figure 5. 2). The residual velocity field shows an clear south-east motion of the whole eastern slope of the volcano.

Figure 5. 2 shows that the stations located near the Ionian coast (ERIP, ETEC, EPOZ, ELEO and ETAC) present a higher east velocity than those located on the middle flank of Mount Etna (ESPC, EC10, EMFN, ENIC and EPED) confirming that the sliding process towards the east of the eastern slope is active and distributed. This acceleration towards east is accommodated by the normal faults on the middle eastern slope of Etna, in particular the Linera fault, the Santa Venerina fault, the San Leonardello fault, the Fiandaca fault and the Nizzeti fault.

The time series of the GNSS stations located on the middle flank of Mount Etna (ENIC and EPED) are less affected by the eastwards sliding. They also show the effect of the inflation and deflation cycles of the volcano, especially in the north and up component. ENIC and EPED show in their north component starting from mid-2018 a change of trend towards south due to the inflation phase that facilitated the 2018 eruption (Figure 5. 2). In November 2020, this inflation phase is still going on. Considering the period from 2001 to 2019, ENIC shows at least six fluctuations in the North component linked to the shorter inflation and deflation phases of the volcano.

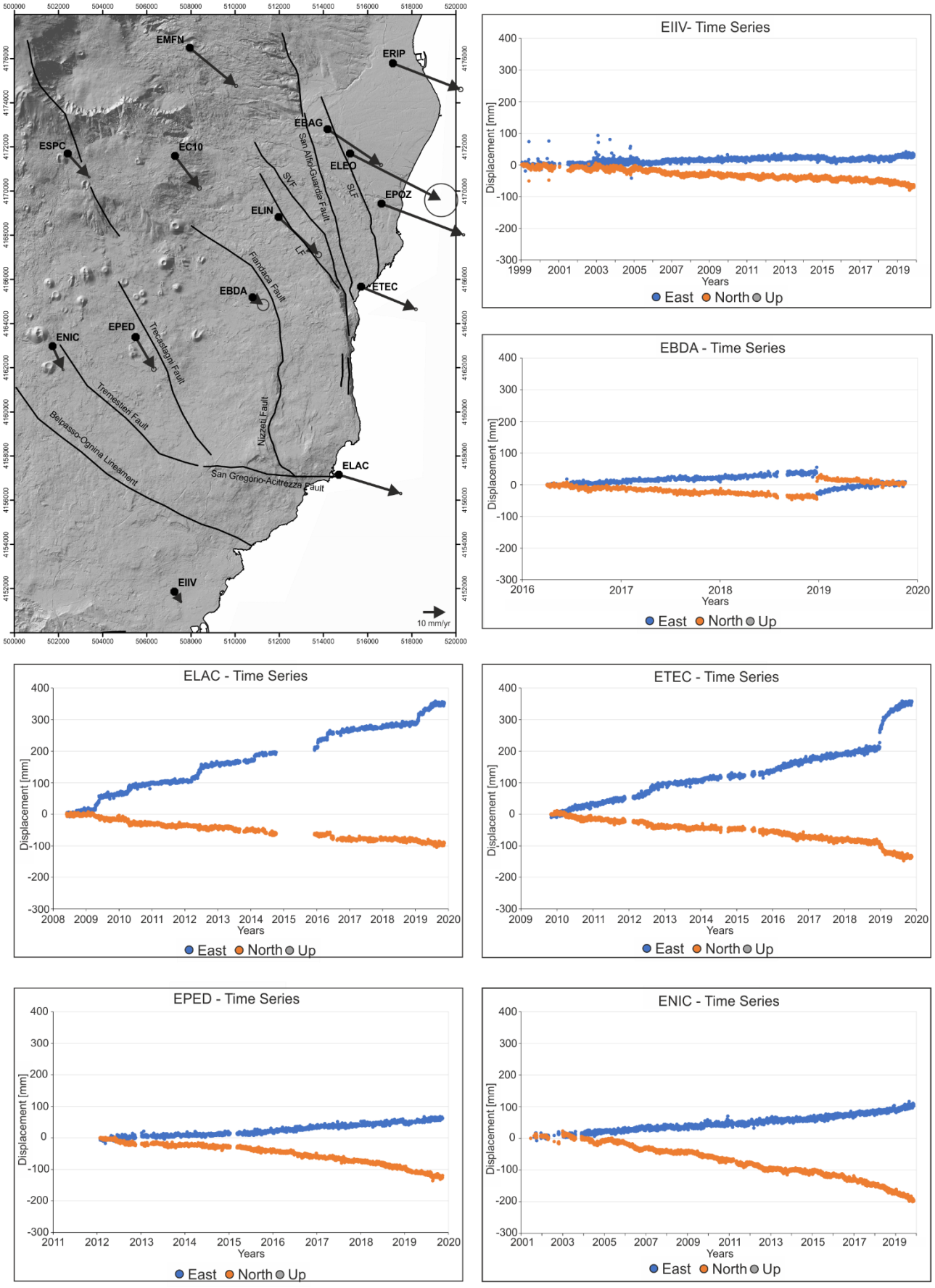

Figure 5. 2 – On the left velocity field of the eastern flank of Mount Etna. Time series (alienated to the east Sicily) of the GNSS permanent stations EIIV, EBDA, ELAC, ETEC, EPED and ENIC are shown.

The azimuth of the velocity of some permanent stations, e.g. ELIN, EBAG, ELEO, EPOZ, EIIV, are not parallel to the nearby structures. This suggests an inconsistency between deformation on the field and deformation caused by the faults of the middle slope of Mount Etna. The structures might be passively involved by the gravitational sliding of the eastern slope. This suggests that either the decollement surface is deeper than the structures or that the structures, even if linked to the regional extensional dynamic, are influenced by the gravitative sliding of the eastern slope of Mount Etna (Figure 5. 3). This question remains largely open.

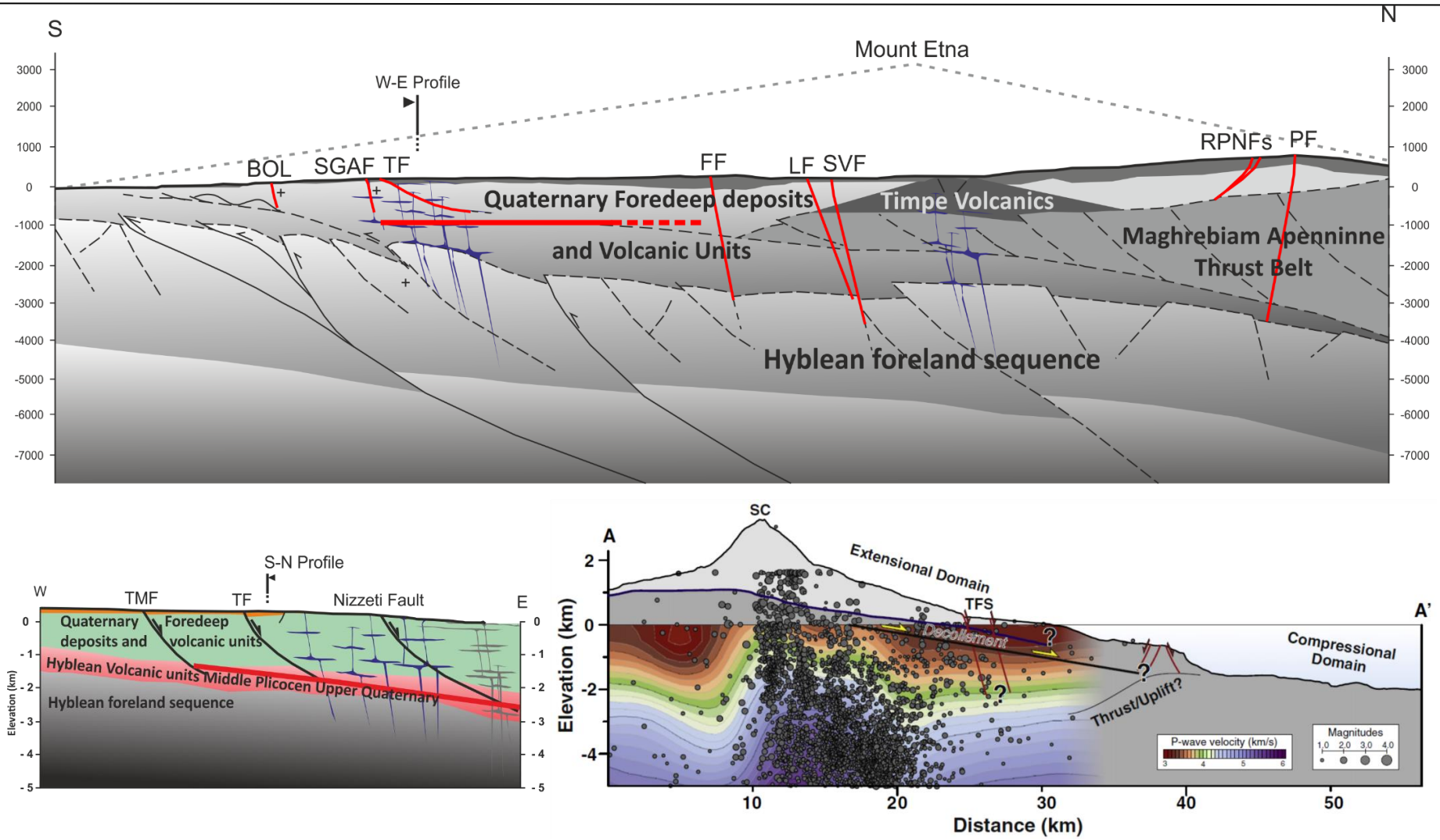

Figure 5. 3 – South - North (on the top) and West -East (on the bottom) schematic geological sections of the eastern flank of Mount Etna. On the right profile from Palano (2016). Red lines represent the decollement plan (black line on the right) modelled by Palano (2016). Based on the geological and geophysical interpretation of this thesis and according to Palano (2016) the Tremestieri fault (TMF), Trecastagni Fault (TF) and Nizzeti Fault join to the decollement plane. (BOL = Belpasso Ognina Lineaments; SGAF = San Gregorio-Acitrezza Fault; FF = Fiandaca Fault; LF = Linera Fault; SVF =Santa Venerina Fault).

Coseismic deformation associated with the event of December 2018 is recorded in all permanent stations on Etna. EPED and ENIC record a displacement of about 8 and 4 mm on the east component.

EBDA, which is close to the epicentre, registered the largest coseismic and post-seismic deformations. The time series shows a displacement of about 60 mm on the north component, -40 mm on the east component and about 15 mm on the vertical component, which confirm the large coseismic deformation caused by the volcano tectonic event.

The permanent station ETEC records a displacement of about 50 mm on the east component and about -40 mm on the north component. Moreover, immediately after the volcano-tectonic event it records a post-seismic deformation that lasts at least for the half of 2019 with an eastward velocity that is at least twice the long-term velocity of the station.

ELAC does not record a clear deformation but rather an increase in east velocity until mid-2019 with a trend very similar to the Slow Slip Events that have been recorded in the past by this station.

The PDAP and MDGR campaign stations also show a velocity increase in the east component compared with respect to the long term velocity.

The time series shows how the east velocity of the eastern flank was influenced by the volcano tectonic event at the end of December 2019, confirming the hypothesis that the stability of the eastern flank is extremely connected to the intrusion of dikes.

More specifically, the velocity field of the South-East sector obtained from both the permanent and campaign stations of the INGV-OE and the campaign stations of the UNICT-Net network was analysed to obtain the long-term deformation of the analysed sector.

In order to define the kinematics and the deformation of the San Gregorio – Acitrezza (SGA) lineament, the realization of a local reference system referred to the benchmark 02SG allows to analyse the offset generated by the fault. By grouping the stations located on the north of the structure, eastwards right - lateral motion of about 15±2 mm/yr towards is recorded (Figure 5. 4).

Moreover, grouping the stations of the Acitrezza Net to the north of the SGA fault, considering the 02SG stable point, a 23.5±3 mm/yr right - lateral motion between the blocks occurs, while grouping the stations to the south there is a residual with respect to 02SG of 3±6 mm/yr (Figure 5. 4).

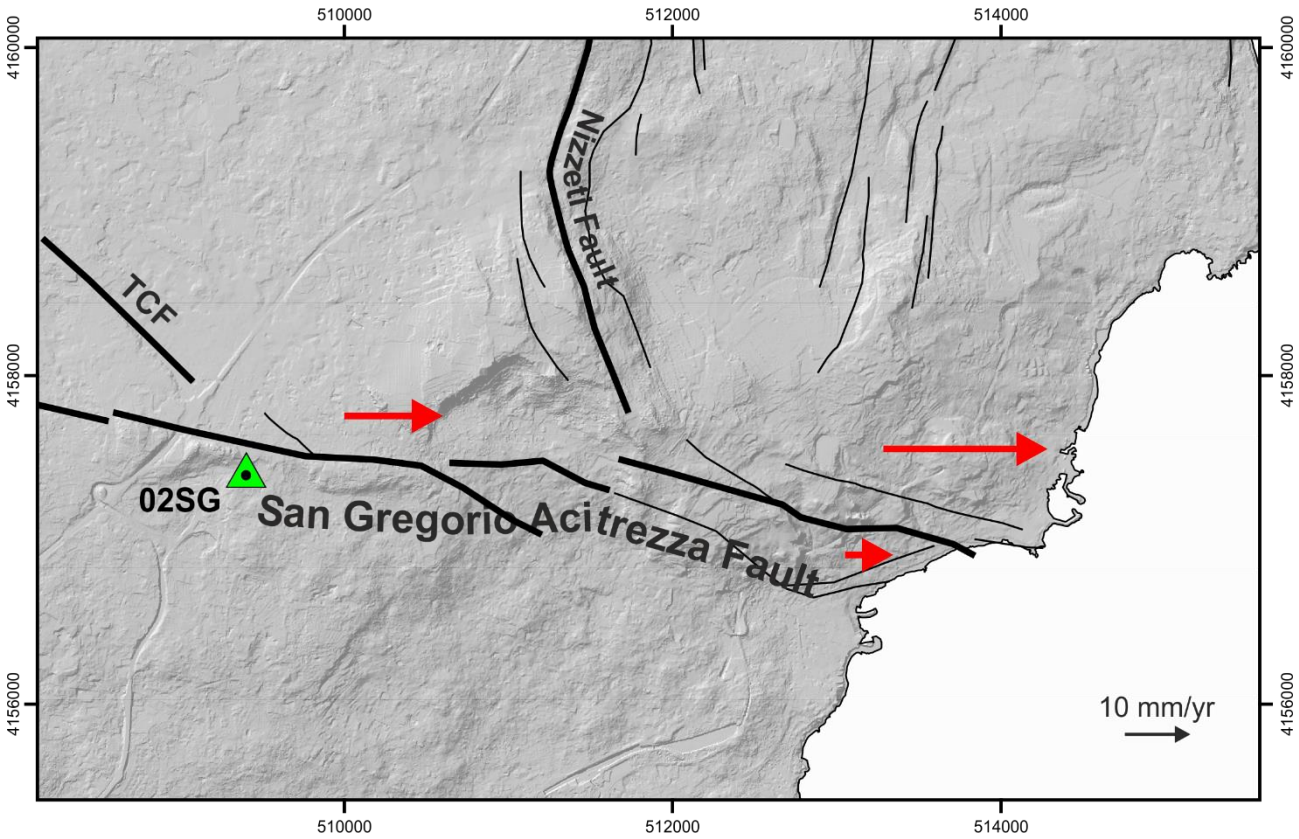

Figure 5. 4 – Velocity field along the San Gregorio – Acitrezza Fault. Red arrows are the velocities referred to the benchmark 02SG. TCF = Trecastagni Fault.

The data suggest that considering the block to the north of the SGA fault the eastward velocity increases of about 8 mm/yr between the network of San Gregorio and the Acitrezza. This result suggests that the Nizzeti Fault is involved in the sliding process of the unstable eastern flank of Mount Etna by accommodating this extension highlighted by westward decay of the velocity field rate observed along the SGA fault.

Together with the analysis of GNSS data, the P-SBAS technique developed by CNR-IREA and implemented in the GEP of ESA portal was used. This technique allows to obtain the time series of permanent scatters and therefore their velocity along the line of sight (LOS) of the satellite for ascending and descending orbit. By combining the ascending and descending LOS velocities, the east and vertical velocities of the permanent scatters have been obtained in order to compare them with the velocity obtained by processing GNSS data obtained through GipsyX. This is made assuming that the north velocity is small and can be neglected when combining the ascending and descending LOS measurements. The alignment of the two data sets, GNSS and InSAR, highlights the limits of the date and of the algorithm developed by CNR-IREA. Manunta et al. (2019) have shown that the algorithm works well on other parts of Italy, for

instance over Phlegraean Fields volcanic area west of Naples, where an excellent consistency between InSAR and GNSS is demonstrated.

As for the PS obtained on Mount Etna, the development of a single time series for the four years 2016 to 2019 is not systematically consistent with the GNSS data. In consequence, it was decided to implement an additional processing for each year from 2016 to 2019 aimed to align PS data with the GNSS data. It was noted that for GNSS stations showing a constant deformation rate, the alignment was good while for the stations with a non-constant deformation rate, the P-SBAS data were not always consistent with the GNSS data. This result shows that the IREA algorithm is always able to retrieve the actual deformation. This is particularly clear for the stations located near the Ionian coast, in particular ELAC and ETEC which show abrupt velocity changes in their time series, and with EBDA which shows the coseismic deformation following the December 2018 earthquake.

Despite this limitation, the P-SBAS Sentinel-1 web tool remains an excellent tool for ground deformation analysis when it is used with care and discrimination.

Using ArcMap software, the PS distant 500 metres away from the faults were selected in order to analyse the fault offset from 2016 to 2019. Through this methodology the anatomy of the deformation along various structures could be calculated.

The San Gregorio-Acitrezza fault constitutes the major southern border of the eastern unstable flank of Mount Etna. On this fault there is an increase of the east velocity from west to east. This property is clear for the 2016 and 2018 period. The forces that activate this fault could be: i) the gravitative sliding of the eastern flank ii) the intrusions of the dikes iii) the activity of the structures of the Etna flank iv) the plastic deformation of the clays that form the Etna basement, or all or part of these causes (Figure 5. 3). This behaviour is found only in this fault.

The Nizzeti Fault in its southern part shows a clear morphological escarpment that is abruptly interrupted at the intersection with the SGA fault. In its northern end it joins the Fiandaca Fault. In 2019 this structure shows the highest offset values of the entire eastern flank together with the Fiandaca Fault. It also shows an offset in the vertical component in 2016 and 2019. In 2016 only in its southern flank at the end with the SGAF and in 2019 for its entire length. This behaviour can be linked to at least two different phenomena: the activity of the SGAF and/or the activity of the normal structures of the Timpe system. The Nizzeti Fault can be considered an important major structure that accommodates the deformation due to the sliding of the Etna side and the tectonic structures linked to the extensional dynamics that characterises normal structures with NNW-SSE such as the Fiandaca Fault (Figure 5. 3).

The Fiandaca Fault was reactivated following the intrusion of the dike at the end of December 2018, that, in turn, triggered the earthquake of 26 December 2018. It is a NNW-SSE right-lateral normal fault. Historically, in 1984, it was reactivated generating the 25 October 1984 earthquake (Mm = 4.3) causing severe damages (Azzaro and D'Amico, 2019). In 2018, it was reactivated throughout its entire length until its southern end, generating ground fractures that continued to open even after the earthquake as a post-seismic deformation. In 2019 this structure shows the highest offset values recorded in the four years in both the east and vertical components. Considering the vertical component, there is a subsidence of about 4-5 cm/yr in the block to the east of the fault, while in the block to the west there is no corresponding uplift. This data suggests that the behaviour of this fault is not purely tectonic but corresponds to a behaviour linked to the gravitational sliding of the eastern flank of Mount Etna (see W-E and S-N profiles in chapter I).

The Belpasso-Ognina lineament is a structure that does not present any morphological evidence but that is well tracked in the InSAR images. It is a structures that developed at the southern border of the eastern flank of Mount Etna together with the San Gregorio-Acitrezza fault. According to the P-SBAS data the maximum offset recorded was about 2 cm/yr during the 2018. This structure interacts with the plicative structures on north-west of Catania (Catania Anticline; De Guidi et al., 2015). Observing the vertical velocity, this structure could act as a barrier for the uplift of the fold as in 2018 or as in 2016. Alternatively the uplift due to the folding continues after this structure. This double aspect is important to understand the nature of the fault itself because in case of this structure is considered as a part of the tectonic volcano dynamics, it should be passively involved in the regional tectonic dynamics. Conversely, as happened in 2016, this structure blocks the uplift created by the folds due to the regional compressional dynamics. Both the depth and the dynamic of this structure is still being studied (Figure 5. 3).

The Tremestieri and Trecastagni faults are well known in the literature and in the field. They present morphological evidence that made them easily recognizable. Together with the San Gregorio Acitrezza Fault, they form a fault system which plays the role of a southern junction of the unstable eastern flank of Etna. Both structures show a vertical offset (~0.5 cm/yr) and horizontal offset (~1 cm/yr). On average from 2016 to 2019, the Trecastagni fault is more active between the two as in 2016, 2018 and 2019. In 2019 it is involved in the deformation process generated by the Fiandaca fault while in the west the Tremestieri Fault does not seem to be involved in the deformation process. Considering the past InSAR data in the literature, the

activities of these two structures present alternate periods, for example in the early 2000s, the Tremestieri fault accommodated the deformation of the eastern flank more than Trecastagni fault, while from 2016 that Trecastagni accommodates most of the deformation. When analysing the vertical component we observe no corresponding uplift in the footwalls of the faults, as for the Fiandaca Fault, but rather they have a stepped behaviour.

In conclusion, in this thesis, the faults of the south-eastern slope of Mount Etna were analysed in detail using topographic and geodetic techniques in order to improve the knowledge and compression of tectonic and volcanic tectonic processes present in the Etna area. The use of GNSS and InSar data has become essential for a correct and deep analysis of the deformation acting in tectonically active areas.

The south-eastern flank of Mount Etna is a densely inhabited area, where about 700000 people are living. Therefore, the knowledge and understanding of volcano tectonic processes is important in that area in order to reduce the seismic and volcanic hazard and the related risks for the inhabitants.

This thesis highlights the strong need to increase the number of permanent GNSS stations across the major active faults of the volcano. This is particularly important along the major San Gregorio-Acitrezza fault, in order to better monitor the behaviour of this very active structure. It is important that across the Nizzeti fault there is another clear gap of the observation of the active structures.

It is also important evaluate the tectonic volcano process in terms of the deviatoric component induced by the ascent of the hydro-fractures which must alter the tensional state of the present features (Gudmundsson, 2006) (example the eruptions 2002, 2018). In fact, the measurements of GNSS campaign stations of the UNICT-Net performed before and after the 2018 event highlighted the effect caused by the intrusion of the dyke during post-event processing, which is the differential deformations in the relative footwall and hanging wall blocks. In this thesis, the effect of the deformation due to the volcano tectonic crisis of December 2018 can be seen both in the time series of the benchmarks belonging to Nizzeti Net and also in the InSAR time series during the 2019. A permanent local network between the Nizzeti fault is ongoing to be installed. The northern tip of the Nizzeti fault is arranged in a right stepping geometry with the southern end of Fiadanca fault activated on the 2018 event. Therefore, according to the models published in literature and the results highlighted in this thesis, the structure terminations, such as shear discontinuities, represent the areas of maximum concentration of elastic stress.

The second structure is the San Gregorio-Acitrezza fault. This structure has been associated with the slow slip events (SSEs) recorded by the permanent GNSS station ELAC, but the nature of these aseismic events, the surface involved and their relationship with the clayey outcropping in the area are still unknown. For this reason, it would be useful to install additional GNSS stations parallel and transversely to this structure, in order to map accurately the area affected by the aseismic creep phenomena and consequently evaluate its depth and extension. The same need exists for the area of San Gregorio village, because it is located where two structures merge with the SGA fault.

Another fault that must be in-depth studied is the Belpasso-Ognina Lineaments which is the less known structure of those analysed so far. The role of this structure in a geodynamic context as complicated as that of eastern Sicily is poorly understood because it is located on the border between an extensional volcanic zone and the convergence zone of Europe and Africa.

The web tool developed by CNR-IREA in Naples was precious for the realization of this thesis. It permitted the realization of time series of permanent scatters of high accuracy, once well understood the possibility of the presence of biases presumably due primarily to phase unwrapping errors in the constitution of time series. This tool has indeed technical limitations in the realization of time series in an active area such as Etna. It would be very useful if this tool could be improved in the future. It would become an even more indispensable tool for all scientists who analyse, model and interpret tectonically active areas all over the world.

REFERENCES

AA and VV: Carta geologica del Monte Etna. Scala 1:50000, edited by R. R. Ed., L.A.C., Firenze., 1979.

Aloisi, M., Bonaccorso, A., Gambino, S., Mattia, M. and Puglisi, G.: Etna 2002 eruption imaged from continuous tilt and GPS data, Geophys. Res. Lett., 30(23), n/a-n/a, doi:10.1029/2003GL018896, 2003.

Alparone, S., D'Amico, S., Gambino, S. and Maiolino, V.: Buried active faults in the Zafferana Etnea territory (south-eastern flank of Mt. Etna): Geometry and kinematics by earthquake relocation and focal mechanisms, Ann. Geophys., 56(1), 112, doi:10.4401/ag-5758, 2013a.

Alparone, S., Bonaccorso, A., Bonforte, A. and Currenti, G.: Long-term stress-strain analysis of volcano flank instability: The eastern sector of Etna from 1980 to 2012, J. Geophys. Res. Solid Earth, 118(9), 5098–5108, doi:10.1002/jgrb.50364, 2013b.

Altamimi, Z., Rebischung, P., Métivier, L. and Collilieux, X.: ITRF2014: A new release of the International Terrestrial Reference Frame modeling nonlinear station motions, J. Geophys. Res. Solid Earth, 121(8), 6109–6131, doi:10.1002/2016JB013098, 2016.

Antonioli, F., Kershaw, S., Rust, D. and Verrubbi, V.: Holocene sea-level change in Sicily and its implications for tectonic models: New data from the Taormina area, northeast Sicily, Mar. Geol., 196(1–2), 53–71, doi:10.1016/S0025-3227(03)00029-X, 2003.

Azzaro, R.: Earthquake surface faulting at Mount Etna volcano (Sicily) and implications for active tectonics, J. Geodyn., 28(2–3), 193–213, doi:10.1016/S0264-3707(98)00037-4, 1999.

Azzaro, R.: Seismicity and active tectonics in the Etna Region: Constraints for a seismotectonic model, in Geophysical Monograph Series, vol. 143, pp. 205–220, Blackwell Publishing Ltd., 2004.

Azzaro, R. and D'Amico, S.: INGV-OE: Catalogo Macrosismico dei Terremoti Etnei (CMTE)., 2019.

Azzaro, R., Carveni, P., Lo Giudice, E. and Rasà, R.: Il terremoto di Codavolpe (basso versante orientale etneo) del 29 Gennaio 1989: campo macrosismico e fratturazione cosismica. Boll. GNV 1989, 1–12., Bollettino, GNV 1989, 1–12, 1989.

Azzaro, R., Barbano, M. S., Antichi, B. and Rigano, R.: Macroseismic catalogue of Mt. Etna earthquakes from 1832 to 1998, Acta Vulcanol., 12, 3–36, 2000.

Azzaro, R., Branca, S., Gwinner, K. and Coltelli, M.: The volcano-tectonic map of Etna volcano, 1:100.000 scale: An integrated approach based on a morphotectonic analysis from high-resolution DEM constrained by geologic, active faulting and seismotectonic data, Ital. J. Geosci., 131(1), 153–170, doi:10.3301/IJG.2011.29, 2012.

Azzaro, R., Bonforte, A., Branca, S. and Guglielmino, F.: Geometry and kinematics of the fault systems controlling the unstable flank of Etna volcano (Sicily), J. Volcanol. Geotherm. Res., 251, 5–15, doi:10.1016/j.jvolgeores.2012.10.001, 2013.

Barreca, G., Corradino, M., Monaco, C. and Pepe, F.: Active Tectonics along the South East Offshore Margin of Mt. Etna: New Insights from High-Resolution Seismic Profiles, Geosciences, 8(2), 62, doi:10.3390/geosciences8020062, 2018a.

Barreca, G., Branca, S. and Monaco, C.: Three-Dimensional Modeling of Mount Etna Volcano: Volume Assessment, Trend of Eruption Rates, and Geodynamic Significance, Tectonics, 37(3), 842–857, doi:10.1002/2017TC004851, 2018b.

Barreca, G., Scarfì, L., Gross, F., Monaco, C. and De Guidi, G.: Fault pattern and seismotectonic potential at the south-western edge of the Ionian Subduction system (southern Italy): New field and geophysical constraints, Tectonophysics, 761(September 2018), 31–45, doi:10.1016/j.tecto.2019.04.020, 2019.

Battaglia, M., Di Bari, M., Acocella, V. and Neri, M.: Dike emplacement and flank instability at Mount Etna: Constraints from a poro-elastic-model of flank collapse, J. Volcanol. Geotherm. Res., 199(1–2), 153–164, doi:10.1016/j.jvolgeores.2010.11.005, 2011.

Berardino, P., Fornaro, G., Lanari, R. and Sansosti, E.: A new algorithm for surface deformation monitoring based on small baseline differential SAR interferograms, IEEE Trans. Geosci. Remote Sens., 40(11), 2375–2383, doi:10.1109/TGRS.2002.803792, 2002.

Berrino, G., Corrado, G., Luongo, G. and Toro, B.: Ground deformation and gravity changes accompanying the 1982 Pozzuoli uplift, Bull. Volcanol., 47(2), 187–200, doi:10.1007/BF01961548, 1984.

Bertiger, W., Bar-Sever, Y., Dorsey, A., Haines, B., Harvey, N., Hemberger, D., Heflin, M., Lu, W., Miller, M., Moore, A. W., Murphy, D., Ries, P., Romans, L., Sibois, A., Sibthorpe, A., Szilagyi, B., Vallisneri, M. and Willis, P.: GipsyX/RTGx, a new tool set for space geodetic operations and research, Adv. Sp. Res., 66(3), 469–489, doi:10.1016/j.asr.2020.04.015, 2020.

Bianca, M., Monaco, C., Tortorici, L. and Cernobori, L.: Quaternary normal faulting in

southeastern Sicily (Italy): a seismic source for the 1693 large earthquake, Geophys. J. Int., 139(2), 370–394, doi:10.1046/j.1365-246x.1999.00942.x, 1999.

Bigi, G., Castellarin, A., Coli, M., Dal Piaz, G. V., Sartori, R., Scandone, P. and Vai, G. B.: Structural Model of Italy scale 1:500.000, in C.N.R.Progetto Finalizzato Geodinamica, edited by S. Firenze., 1992.

Boehm, J., Niell, A., Tregoning, P. and Schuh, H.: Global Mapping Function (GMF): A new empirical mapping function based on numerical weather model data, Geophys. Res. Lett., 33(7), L07304, doi:10.1029/2005GL025546, 2006.

Bonaccorso, A., Aloisi, M. and Mattia, M.: Dike emplacement forerunning the Etna July 2001 eruption modeled through continuous tilt and GPS data, Geophys. Res. Lett., 29(13), 1624, doi:10.1029/2001GL014397, 2002.

Bonforte, A., Gambino, S. and Neri, M.: Intrusion of eccentric dikes: The case of the 2001 eruption and its role in the dynamics of Mt. Etna volcano, Tectonophysics, 471(1–2), 78–86, doi:10.1016/j.tecto.2008.09.028, 2009.

Bonforte, A., Guglielmino, F., Coltelli, M., Ferretti, A. and Puglisi, G.: Structural assessment of Mount Etna volcano from Permanent Scatterers analysis, Geochemistry, Geophys. Geosystems, 12(2), doi:10.1029/2010GC003213, 2011.

Bonforte, A., Carnazzo, A., Gambino, S., Guglielmino, F., Obrizzo, F. and Puglisi, G.: A multidisciplinary study of an active fault crossing urban areas: The Trecastagni Fault at Mt. Etna (Italy), J. Volcanol. Geotherm. Res., 251, 41–49, doi:10.1016/j.jvolgeores.2012.05.001, 2013a.

Bonforte, A., Guglielmino, F. and Puglisi, G.: Interaction between magma intrusion and flank dynamics at Mt. Etna in 2008, imaged by integrated dense GPS and DInSAR data, Geochemistry, Geophys. Geosystems, 14(8), 2818–2835, doi:10.1002/ggge.20190, 2013b.

Bonforte, A., Federico, C., Giammanco, S., Guglielmino, F., Liuzzo, M. and Neri, M.: Soil gases and SAR measurements reveal hidden faults on the sliding flank of Mt. Etna (Italy), J. Volcanol. Geotherm. Res., 251, 27–40, doi:10.1016/j.jvolgeores.2012.08.010, 2013c.

Bonforte, A., Guglielmino, F. and Puglisi, G.: Large dyke intrusion and small eruption: The December 24, 2018 Mt. Etna eruption imaged by Sentinel-1 data, Terra Nov., (March), ter.12403, doi:10.1111/ter.12403, 2019.

Borgia, A., Lanari, R., Sansosti, E., Tesauro, M., Berardino, P., Fornaro, G., Neri, M. and Murray, J. B.: Actively growing anticlines beneath catania from the distal motion of Mount Etna's

Decollement measured by SAR interferometry and GPS, Geophys. Res. Lett., 27(20), 3409–3412, doi:10.1029/1999GL008475, 2000.

Bottari, A. and Riuscetti, M.: La stazione sismica di Serra la Nave sull'Etna, Ann. Geophys., 20(3), 243–264, 1967.

Bousquet, J.-C. and Lanzafame, G.: Déformations compressives quaternaires au bord sud de l'Etna, Comptes rendus l'Académie des Sci. Série 2, Mécanique, Phys. Chim. Sci. l'univers, Sci. la Terre, 303(3), 1986.

Bousquet, J. C. and Lanzafame, G.: The tectonics and geodynamics of Mt. Etna: Synthesis and interpretation of geological and geophysical data, Geophys. Monogr. Ser., 143, 29–47, doi:10.1029/143GM03, 2004.

Branca, S. and Ferrara, V.: The morphostructural setting of Mount Etna sedimentary basement (Italy): Implications for the geometry and volume of the volcano and its flank instability, Tectonophysics, 586, 46–64, doi:10.1016/j.tecto.2012.11.011, 2013.

Branca, S., Coltelli, M. and Groppelli, G.: Geological evolution of etna volcano, Geophys. Monogr. Ser., 143, 49–63, doi:10.1029/143GM04, 2004.

Branca, S., Coltelli, M., De Beni, E. and Wijbrans, J.: Geological evolution of Mount Etna volcano (Italy) from earliest products until the first central volcanism (between 500 and 100 ka ago) inferred from geochronological and stratigraphic data, Int. J. Earth Sci., 97(1), 135–152, doi:10.1007/s00531-006-0152-0, 2008.

Branca, S., Coltelli, M. and Groppelli, G.: Geological evolution of a complex basaltic stratovolcano: Mount Etna, Italy Volcan Project View project Intregrated geophysics for Archaeology View project, Ital. J. Geosci., 130(3), 306–317, doi:10.3301/IJG.2011.13, 2011a.

Branca, S., Coltelli, M., Groppelli, G. and Lentini, F.: Geological map of Etna volcano, 1:50,000 scale, Ital. J. Geosci., 130(3), 265–291, doi:10.3301/IJG.2011.15, 2011b.

Branca, S., De Guidi, G., Lanzafame, G. and Monaco, C.: Holocene vertical deformation along the coastal sector of Mt. Etna volcano (eastern Sicily, Italy): Implications on the time–space constrains of the volcano lateral sliding, J. Geodyn., 82, 194–203, doi:10.1016/j.jog.2014.07.006, 2014.

Briole, P., Gaulon, R., Nunnari, G., Puglisi, G. and Ruegg, J. C.: Measurements of Ground Movement on Mount Etna, Sicily: A Systematic Plan to Record Different Temporal and Spatial Components of Ground Movement Associated with Active Volcanism, pp. 120–129., 1992.

Bruno, V., Mattia, M., Montgomery-Brown, E., Rossi, M. and Scandura, D.: Inflation Leading to a Slow Slip Event and Volcanic Unrest at Mount Etna in 2016: Insights From CGPS Data, Geophys. Res. Lett., 44(24), 12,141-12,149, doi:10.1002/2017GL075744, 2017.

Caloi, P., Lo Surdo, A. and Ponte, G.: Agitazioni macrosismiche originate da attività vulcanica, Ann. Geophys., 1(1), 5–9, 1948.

Calvari, S., Tanner, L. H., Groppelli, G. and Norini, G.: Valle del Bove, Eastern Flank of Etna Volcano: a Comprehensive Model for the Opening of the Depression and Implications for Future Hazards, Geophys. Monogr. Ser., 143, 65–75 [online] Available from: https://www.earth-prints.org/handle/2122/3121 (Accessed 30 October 2020), 2004.

Castellano, M., Ferrucci, F., Patanè, G., Imposa, S., Hirn, A. and Dorel, J.: Monitoring seismicity and volcanic activity at Mt. Etna Volcano (southern Italy) by means of three-component temporary arrays., 1989.

Castellano, M., Ferrucci, F., Godano, C., Imposa, S. and Milano, G.: Upwards migration of seismic focii: A forerunner of the 1989 eruption of Mt Etna (Italy), Bull. Volcanol., 55(5), 357–361, doi:10.1007/BF00301146, 1993.

Casu, F., Elefante, S., Imperatore, P., Zinno, I., Manunta, M., De Luca, C. and Lanari, R.: SBAS-DInSAR parallel processing for deformation time-series computation, IEEE J. Sel. Top. Appl. Earth Obs. Remote Sens., 7(8), 3285–3296, doi:10.1109/JSTARS.2014.2322671, 2014.

Catalano, S. and De Guidi, G.: Late Quaternary uplift of northeastern Sicily: Relation with the active normal faulting deformation, J. Geodyn., 36(4), 445–467, doi:10.1016/S0264-3707(02)00035-2, 2003.

Catalano, S., De Guidi, G., Romagnoli, G., Torrisi, S., Tortorici, G. and Tortorici, L.: The migration of plate boundaries in SE Sicily: Influence on the large-scale kinematic model of the African promontory in southern Italy, Tectonophysics, 449(1–4), 41–62, doi:10.1016/j.tecto.2007.12.003, 2008.

Catalano, S., Torrisi, S., Tortorici, G. and Romagnoli, G.: Active folding along a rift-flank: The Catania region case history (SE Sicily), J. Geodyn., 51(1), 53–63, doi:10.1016/j.jog.2010.08.001, 2011.

Chiarabba, C., Amato, A., Boschi, E. and Barberi, F.: Recent seismicity and tomographic modeling of the Mount Etna plumbing system, J. Geophys. Res. Solid Earth, 105(B5), 10923–10938, doi:10.1029/1999jb900427, 2000.

Chouet, B. A.: Long-period volcano seismicity: Its source and use in eruption forecasting, Nature, 380(6572), 309–316, doi:10.1038/380309a0, 1996.

Clocchiatti, R., Schiano, P., Ottolini, L. and Bottazzi, P.: Earlier alkaline and transitional magmatic pulsation of Mt Etna volcano, Earth Planet. Sci. Lett., 163(1–4), 399–407, doi:10.1016/S0012-821X(98)00170-8, 1998.

Cocina, O., Neri, G., Privitera, E. and Spampinato, S.: Seismogenic stress field beneath Mt. Etna (South Italy) and possible relationships with volcano-tectonic features, J. Volcanol. Geotherm. Res., 83(3–4), 335–348, doi:10.1016/S0377-0273(98)00026-2, 1998.

Coltelli, M., Del Carlo, P. and Vezzoli, L.: Stratigraphic constraints for explosive activity in the past 100 ka at Etna Volcano, Italy, Int. J. Earth Sci., 89(3), 665–677, doi:10.1007/s005310000117, 2000.

Corsaro, R. A. and Cristofolini, R.: Origin and differentiation of recent basaltic magmas from Mount Etna, Mineral. Petrol., 57, 1–21 [online] Available from: https://www.earth-prints.org/handle/2122/6695 (Accessed 30 October 2020), 1996.

Corsaro, R. A. and Pompilio, M.: Dynamics of Magmas at Mount Etna, Geophys. Monogr. Ser., 143, 91–110, 2004.

Corsaro, R. A., Neri, M. and Pompilio, M.: Paleo-environmental and volcano-tectonic evolution of the southeastern flank of Mt. Etna during the last 225 ka inferred from the volcanic succession of the 'Timpe', Acireale, Sicily, J. Volcanol. Geotherm. Res., 113(1–2), 289–306, doi:10.1016/S0377-0273(01)00262-1, 2002.

Cristofolini, R., Ghisetti, F., Ruschetti, M. and Vezzani, L.: Neotectonics, seismicity and volcanic activity in northeasstern Sicily, in VI Colloq. Geol. Aegean Reg., pp. 757–766, Athens., 1977.

Crosetto, M., Crippa, B. and Biescas, E.: Early detection and in-depth analysis of deformation phenomena by radar interferometry, Eng. Geol., 79(1–2), 81–91, doi:10.1016/j.enggeo.2004.10.016, 2005.

Curlander, J. C. and McDonough, R. N.: Synthetic aperture radar, Vol. 11., Wiley, New York., 1991.

D'Agostino, N. and Selvaggi, G.: Crustal motion along the Eurasia-Nubia plate boundary in the Calabrian Arc and Sicily and active extension in the Messina Straits from GPS measurements, J. Geophys. Res. Solid Earth, 109(11), 1–16, doi:10.1029/2004JB002998, 2004.

D'Agostino, N., Avallone, A., Cheloni, D., D'Anastasio, E., Mantenuto, S. and Selvaggi, G.: Active

tectonics of the Adriatic region from GPS and earthquake slip vectors, J. Geophys. Res. Solid Earth, 113(12), 1–19, doi:10.1029/2008JB005860, 2008.

De Beni, E., Branca, S., Coltelli, M., Groppelli, G. and Wijbrans, J. R.: 40Ar/ 39Ar isotopic dating of Etna volcanic succession, Ital. J. Geosci., 130(3), 292–305, doi:10.3301/IJG.2011.14, 2011.

De Guidi, G., Catalano, S., Monaco, C. and Tortorici, L.: Morphological evidence of Holocene coseismic deformation in the Taormina region (NE Sicily), J. Geodyn., 36(1–2), 193–211, doi:10.1016/S0264-3707(03)00047-4, 2003.

De Guidi, G., Scudero, S. and Gresta, S.: New insights into the local crust structure of Mt. Etna volcano from seismological and morphotectonic data, J. Volcanol. Geotherm. Res., 223–224(April), 83–92, doi:10.1016/j.jvolgeores.2012.02.001, 2012.

De Guidi, G., Imposa, S., Scudero, S. and Palano, M.: New evidence for Late Quaternary deformation of the substratum of Mt. Etna volcano (Sicily, Italy): Clues indicate active crustal doming, Bull. Volcanol., 76(5), 1–13, doi:10.1007/s00445-014-0816-8, 2014.

De Guidi, G., Barberi, G., Barreca, G., Bruno, V., Cultrera, F., Grassi, S., Imposa, S., Mattia, M., Monaco, C., Scarfì, L. and Scudero, S.: Geological, seismological and geodetic evidence of active thrusting and folding south of Mt. Etna (eastern Sicily): Revaluation of “seismic efficiency” of the Sicilian Basal Thrust, J. Geodyn., 90, 32–41, doi:10.1016/j.jog.2015.06.001, 2015.

De Guidi, G., Vecchio, A., Brighenti, F., Caputo, R., Carnemolla, F., Di Pietro, A., Lupo, M., Maggini, M., Marchese, S., Messina, D., Monaco, C. and Naso, S.: Brief communication: Co-seismic displacement on 26 and 30 October 2016 (Mw = 5.9 and 6.5) – earthquakes in central Italy from the analysis of a local GNSS network, Nat. Hazards Earth Syst. Sci., 17(11), 1885–1892, doi:10.5194/nhess-17-1885-2017, 2017.

De Guidi, G., Brighenti, F., Carnemolla, F., Imposa, S., Marchese, S. A., Palano, M., Scudero, S. and Vecchio, A.: The unstable eastern flank of Mt. Etna volcano (Italy): First results of a GNSS-based network at its southeastern edge, J. Volcanol. Geotherm. Res., 357, 418–424, doi:10.1016/j.jvolgeores.2018.04.027, 2018.

de Luca, C., Cuccu, R., Elefante, S., Zinno, I., Manunta, M., Casola, V., Rivolta, G., Lanari, R. and Casu, F.: An on-demand web tool for the unsupervised retrieval of earth’s surface deformation from SAR data: The P-SBAS service within the ESA G-POD environment, Remote Sens., 7(11), 15630–15650, doi:10.3390/rs71115630, 2015.

De Novellis, V., Atzori, S., De Luca, C., Manzo, M., Valerio, E., Bonano, M., Cardaci, C., Castaldo, R.,

Di Bucci, D., Manunta, M., Onorato, G., Pepe, S., Solaro, G., Tizzani, P., Zinno, I., Neri, M., Lanari, R. and Casu, F.: DInSAR Analysis and Analytical Modeling of Mount Etna Displacements: The December 2018 Volcano-Tectonic Crisis, Geophys. Res. Lett., 46(11), 5817–5827, doi:10.1029/2019GL082467, 2019.

Doglioni, C., Innocenti, F. and Mariotti, G.: Why Mt Etna?, Terra Nov., 13(1), 25–31, doi:10.1046/j.1365-3121.2001.00301.x, 2001.

Ellis, M. and King, G.: Structural control of flank volcanism in continental rifts, Science (80-.)., 254(5033), 839–842, doi:10.1126/science.254.5033.839, 1991.

ESA: Geohazards-Thematic Exploitation Platform, [online] Available from: https://geohazards-tep.eu (Accessed 2 October 2020), 2015.

ESA: Sentinel online, [online] Available from: https://sentinel.esa.int/web/sentinel/missions/sentinel-1 (Accessed 6 October 2020), 2020.

Estey, L. H. and Meertens, C. M.: TEQC: The Multi-Purpose Toolkit for GPS/GLONASS Data, GPS Solut., 3(1), 42–49, doi:10.1007/PL00012778, 1999.

Faccenna, C., Molin, P., Orecchio, B., Olivetti, V., Bellier, O., Funiciello, F., Minelli, L., Piromallo, C. and Billi, A.: Topography of the Calabria subduction zone (southern Italy): Clues for the origin of Mt. Etna, Tectonics, 30(1), doi:10.1029/2010TC002694, 2011.

Ferretti, A., Prati, C. and Rocca, F.: Permanent scatterers in SAR interferometry, IEEE Trans. Geosci. Remote Sens., 39(1), 8–20, doi:10.1109/36.898661, 2001.

Firth, C., Stewart, I., Mcguire, W. J., Kershaw, S. and Vita-Finzi, C.: Coastal elevation changes in eastern Sicily: Implications for volcano instability at Mount Etna, Geol. Soc. Spec. Publ., 110(1), 153–167, doi:10.1144/GSL.SP.1996.110.01.12, 1996.

Franceschetti, G. and Lanari, R.: Synthetic Aperture Radar Processing, CRC Press., 2018.

Froger, J. L., Merle, O. and Briole, P.: Active spreading and regional extension at Mount Etna imaged by SAR interferometry, Earth Planet. Sci. Lett., 187(3–4), 245–258, doi:10.1016/S0012-821X(01)00290-4, 2001.

Gabriel, A. K., Goldstein, R. M. and Zebker, H. A.: Mapping small elevation changes over large areas: differential radar interferometry, J. Geophys. Res., 94(B7), 9183–9191, doi:10.1029/JB094iB07p09183, 1989.

Gambino, S.: High-precision locations of the microseismicity preceding the 2002–2003 Mt. Etna

eruption, Geophys. Res. Lett., 31(18), L18604, doi:10.1029/2004GL020499, 2004.

Gambino, S., Bonforte, A., Carnazzo, A., Falzone, G., Ferrari, F., Ferro, A., Guglielmino, F., Laudani, G., Maiolino, V. and Puglisi, G.: Displacement across the Trecastagni Fault (Mt. Etna) and induced seismicity: The October 2009 to January 2010 episode, Ann. Geophys., 54(4), 414–423, doi:10.4401/ag-4841, 2011.

Goes, S., Jenny, S., Hollenstein, C., Kahle, H. G. and Geiger, A.: A recent tectonic reorganization in the south-central Mediterranean, Earth Planet. Sci. Lett., 226(3–4), 335–345, doi:10.1016/j.epsl.2004.07.038, 2004.

Govers, R. and Wortel, M. J. R.: Lithosphere tearing at STEP faults: response to edges of subduction zones, Earth Planet. Sci. Lett., 236(1–2), 505–523, doi:10.1016/j.epsl.2005.03.022, 2005.

Gresta, S. and Patané, G.: Review of seismological studies at Mount Etna, Pure Appl. Geophys., 125(6), 951–970, doi:10.1007/BF00879362, 1987.

Gresta, S., Bella, D., Musumeci, C. and Carveni, P.: Some efforts on active faulting processes (earthquakes and aseismic creep) acting on the eastern flank of Mt. Etna (Sicily). Acta Vulcanol. 9 (1/2), 101–108., Acta Vulcanol., 9(1/2), 101–108, 1997.

Gresta, S., Peruzza, L., Slejko, D. and Distefano, G.: Inferences on the main volcano-tectonic structures at Mt. Etna (Sicily) from a probabilistic seismological approach, J. Seismol., 2(2), 105–116, doi:10.1023/A:1008096020808, 1998.

Gross, F., Krastel, S., Geersen, J., Behrmann, J. H., Ridente, D., Chiocci, F. L., Bialas, J., Papenberg, C., Cukur, D., Urlaub, M. and Micallef, A.: The limits of seaward spreading and slope instability at the continental margin offshore Mt Etna, imaged by high-resolution 2D seismic data, Tectonophysics, 667, 63–76, doi:10.1016/j.tecto.2015.11.011, 2016.

Gruppo Analisi Dati Sismici: Catalogo dei terremoti della Sicilia Orientale - Calabria Meridionale (1999-2020), INGV, Catania [online] Available from: http://sismoweb.ct.ingv.it/maps/eq_maps/sicily/catalogue.php (Accessed 24 October 2020), 2020.

Gudmundsson, A.: How local stresses control magma-chamber ruptures, dyke injections, and eruptions in composite volcanoes, Earth-Science Rev., 79(1–2), 1–31, doi:10.1016/j.earscirev.2006.06.006, 2006.

Guest, J. E., Chester, D. K. and Duncan, A. M.: The valle del bove, Mount Etna: Its origin and

relation to the stratigraphy and structure of the volcano, J. Volcanol. Geotherm. Res., 21(1–2), 1–23, doi:10.1016/0377-0273(84)90013-1, 1984.

Gutscher, M. A., Dominguez, S., De Lepinay, B. M., Pinheiro, L., Gallais, F., Babonneau, N., Cattaneo, A., Le Faou, Y., Barreca, G., Micallef, A. and Rovere, M.: Tectonic expression of an active slab tear from high-resolution seismic and bathymetric data offshore Sicily (Ionian Sea), Tectonics, 35(1), 39–54, doi:10.1002/2015TC003898, 2016.

Gvirtzman, Z. and Nur, A.: The formation of Mount Etna as the consequence of slab rollback, Nature, 401(6755), 782–785, doi:10.1038/44555, 1999.

Hirn, A., Nicolich, R., Gallart, J., Laigle, M., Cernobori, L., Accaino, F., Avedik, F., Bianca, M., Diaz, J., Lépine, J. C., Metton, G., Monaco, C., Nercessian, A., Petronio, L., Pou, S., Romanelli, M., Gallares, V., Sapin, M., Tortorici, L., Marson, I., Sachpazi, M. and Della Vedova, B.: Roots of Etna volcano in faults of great earthquakes, Earth Planet. Sci. Lett., 148(1–2), 171–191, doi:10.1016/s0012-821x(97)00023-x, 1997.

Hooper, A., Zebker, H., Segall, P. and Kampes, B.: A new method for measuring deformation on volcanoes and other natural terrains using InSAR persistent scatterers, Geophys. Res. Lett., 31(23), doi:10.1029/2004GL021737, 2004.

Houlié, N., Briole, P., Bonforte, A. and Puglisi, G.: Large scale ground deformation of Etna observed by GPS between 1994 and 2001, Geophys. Res. Lett., 33(2), L02309, doi:10.1029/2005GL024414, 2006.

Imposa, S., De Guidi, G., Grassi, S., Scudero, S., Barreca, G., Patti, G. and Boso, D.: Applying geophysical techniques to investigate a segment of a creeping fault in the urban area of San Gregorio di Catania, southern flank of Mt. Etna (Sicily - Italy), J. Appl. Geophys., 123, 153–163, doi:10.1016/j.jappgeo.2015.10.008, 2015.

INGV-OE: SismoWeb, [online] Available from: http://sismoweb.ct.ingv.it/index.php (Accessed 21 October 2020), 2018.

ISIDe Working Group: Italian Seismological Instrumental and Parametric Database (ISIDe), Ist. Naz. di Geofis. e Vulcanol., doi:10.13127/ISIDe, 2007.

Kampes, B.: Radar interferometry: Persistent scatterers technique, The Netherlands: Springer, 2006.

Kershaw, S.: Quaternary Reefs of Northeastern Sicily: Structure and Growth Controls in an Unstable Tectonic Setting, J. Coast. Res., 16(4), 1037–1062 [online] Available from:

https://www.jstor.org/stable/4300121 (Accessed 3 November 2020), 2000.

Kieffer, G.: Évolution structurale et dynamique d'un grand Vulcan polygénique: stade d'édification et activité actuelle de l'Etna., Université de Clermont-Ferrand., 1985.

Labaume, P., Claude Bousquet, J. and Lanzafame, G.: Early deformations at a submarine compressive front: the quaternary Catania foredeep south of Mt. Etna, Sicily, Italy, Tectonophysics, 177(4), 349–366, doi:10.1016/0040-1951(90)90395-O, 1990.

Lanari, R., Mora, O., Manunta, M., Mallorquí, J. J., Berardino, P. and Sansosti, E.: A small-baseline approach for investigating deformations on full-resolution differential SAR interferograms, IEEE Trans. Geosci. Remote Sens., 42(7), 1377–1386, doi:10.1109/TGRS.2004.828196, 2004.

Lanzafame, G., Neri, M. and Rust, D.: Active tectonics affecting the eastern flank of Mount Etna: structural interactions at a regional and local scale, Etna fifteen years, 25–33, 1996.

Lavecchia, G., Ferrarini, F., de Nardis, R., Visini, F. and Barbano, M. S.: Active thrusting as a possible seismogenic source in Sicily (Southern Italy): Some insights from integrated structural-kinematic and seismological data, Tectonophysics, 445(3–4), 145–167, doi:10.1016/j.tecto.2007.07.007, 2007.

Lentini, F. and Carbone, S.: Geology of Sicily, Mem. Descr. della Cart. Geol. d'Italia, 95, 7–414 [online] Available from: https://www.isprambiente.gov.it/it/pubblicazioni/periodici-tecnici/memorie-descrittive-della-carta-geologica-ditalia/memdes_95_intro.pdf (Accessed 3 November 2020), 2014.

Lo Giudice, E. and Rasà, R.: The role of the NNW structural trend in the recent geodynamic evolution of north-eastern sicily and its volcanic implications in the etnean area, J. Geodyn., 5(3–4), 309–330, doi:10.1016/0264-3707(86)90012-8, 1986.

Lo Giudice, E. and Rasà, R.: Very shallow earthquakes and brittle deformation in active volcanic areas: The Eatnean region as an example, Tectonophysics, 202(2–4), 257–268, doi:10.1016/0040-1951(92)90111-I, 1992.

Luongo, G., Del Gaudio, C., Obrizzo, F. and Ricco, C.: Movimenti lenti del suolo all'Etna mediante livellazioni di precisione, Boll. Grup. Naz. Vulc, CNR, 1989.

Makris, J., Nicolich, R. and Weigel, W.: A seismic study in the western Ionian Sea., Ann. Geophys. Ser. B, 4 B(6), 665–678 [online] Available from: https://pascal-francis.inist.fr/vibad/index.php?action=getRecordDetail&idt=7962145 (Accessed 9 November 2020), 1986.

Manunta, M., De Luca, C., Zinno, I., Casu, F., Manzo, M., Bonano, M., Fusco, A., Pepe, A., Onorato, G., Berardino, P., De Martino, P. and Lanari, R.: The Parallel SBAS Approach for Sentinel-1 Interferometric Wide Swath Deformation Time-Series Generation: Algorithm Description and Products Quality Assessment, IEEE Trans. Geosci. Remote Sens., 57(9), 6229–6281, doi:10.1109/TGRS.2019.2904912, 2019.

Massonnet, D. and Feigl, K. L.: Radar interferometry and its application to changes in the earth's surface, Rev. Geophys., 36(4), 441–500, doi:10.1029/97RG03139, 1998.

Massonnet, D., Rossi, M., Carmona, C., Adragna, F., Peltzer, G., Feigl, K. and Rabaute, T.: The displacement field of the Landers earthquake mapped by radar interferometry, Nature, 364(6433), 138–142, doi:10.1038/364138a0, 1993.

Mattia, M., Bruno, V., Cannavò, F. and Palano, M.: Evidences of a contractional pattern along the northern rim of the Hyblean plateau (Sicily, Italy) from GPS data, Geol. Acta, 10(1), 63–70, doi:10.1344/105.000001705, 2012.

Mattia, M., Bruno, V., Caltabiano, T., Cannata, A., Cannavò, F., D'Alessandro, W., Di Grazia, G., Federico, C., Giammanco, S., La Spina, A., Liuzzo, M., Longo, M., Monaco, C., Patanè, D. and Salerno, G.: A comprehensive interpretative model of slow slip events on Mt. Etna's eastern flank, Geochemistry, Geophys. Geosystems, 16(3), 635–658, doi:10.1002/2014GC005585, 2015.

Mogi, K.: Relations between the eruptions of various volcanoes and the deformations of the ground surfaces around them, Bull. Earthq. Res. Inst., 36, 99–134, 1958.

Monaco, C. and Tortorici, L.: Active faulting in the Calabrian arc and eastern Sicily, J. Geodyn., 29(3–5), 407–424, doi:10.1016/S0264-3707(99)00052-6, 2000.

Monaco, C., Petronio, L. and Romanelli, M.: Tettonica estensionale nel settore orientale del Monte Etna (Sicilia): dati morfotettonici e sismici, Stud. Geol. camerti, Speciale, 363–374, doi:10.15165/studgeocam-103, 1995.

Monaco, C., Tapponnier, P., Tortorici, L. and Gillot, P. Y.: Late Quaternary slip rates on the Acireale-Piedimonte normal faults and tectonic origin of Mt. Etna (Sicily), Earth Planet. Sci. Lett., 147(1–4), 125–139, doi:10.1016/s0012-821x(97)00005-8, 1997.

Monaco, C., Catalano, S., Cocina, O., De Guidi, G., Ferlito, C., Gresta, S., Musumeci, C. and Tortorici, L.: Tectonic control on the eruptive dynamics at Mt. Etna Volcano (Sicily) during the 2001 and 2002-2003 eruptions, J. Volcanol. Geotherm. Res., 144(1-4 SPEC. ISS.), 211–233,

doi:10.1016/j.jvolgeores.2004.11.024, 2005.

Monaco, C., De Guidi, G. and Ferlito, C.: The Morphotectonic map of Mt. Etna, Ital. J. Geosci., 129(3), 408–428, doi:10.3301/IJG.2010.11, 2010.

Mora, O., Mallorqui, J. J. and Broquetas, A.: Linear and nonlinear terrain deformation maps from a reduced set of interferometric sar images, IEEE Trans. Geosci. Remote Sens., 41(10), 2243–2253, doi:10.1109/TGRS.2003.814657, 2003.

Murray, J. B.: Elastic model of the actively intruded dyke feeding the 1991–1993 eruption of Mt. Etna, derived from ground deformation measurements., Acta Vulcanol., 4, 97–99, 1994.

Murray, J. B. and Guest, J. E.: Vertical ground deformation on Mount Etna, 1975-1980 (Sicily)., Geol. Soc. Am. Bull., 93(11), 1160–1175, doi:10.1130/0016-7606(1982)93<1160:VGDOME>2.0.CO;2, 1982.

Murray, J. B., Guest, J. E. and Butterworth, P. S.: Large ground deformation on Mount Etna volcano, Nature, 266(5600), 338–340, doi:10.1038/266338a0, 1977.

Neri, G., Marotta, A. M., Orecchio, B., Presti, D., Totaro, C., Barzaghi, R. and Borghi, A.: How lithospheric subduction changes along the Calabrian Arc in southern Italy: Geophysical evidences, Int. J. Earth Sci., 101(7), 1949–1969, doi:10.1007/s00531-012-0762-7, 2012.

Neri, M., Guglielmino, F. and Rust, D.: Flank instability on Mount Etna: Radon, radar interferometry, and geodetic data from the southwestern boundary of the unstable sector, J. Geophys. Res. Solid Earth, 112(4), doi:10.1029/2006JB004756, 2007.

Nicolich, R., Laigle, M., Hirn, A., Cernobori, L. and Gallart, J.: Crustal structure of the ionian margin of Sicily: Etna volcano in the frame of regional evolution, Tectonophysics, 329(1–4), 121–139, doi:10.1016/S0040-1951(00)00192-X, 2000.

Omori, F.: No Title, Bull. Imp. Earthq. Investig. Committe, 8(323), 1911.

Palano, M.: Episodic slow slip events and seaward flank motion at Mt. Etna volcano (Italy), J. Volcanol. Geotherm. Res., 324, 8–14, doi:10.1016/j.jvolgeores.2016.05.010, 2016.

Palano, M., Puglisi, G. and Gresta, S.: Ground deformation patterns at Mt. Etna from 1993 to 2000 from joint use of InSAR and GPS techniques, J. Volcanol. Geotherm. Res., 169(3–4), 99–120, doi:10.1016/j.jvolgeores.2007.08.014, 2008.

Palano, M., Rossi, M., Cannavò, F., Bruno, V., Aloisi, M., Pellegrino, D., Pulvirenti, M., Siligato, G. and Mattia, M.: Etn@ref: A geodetic reference frame for Mt. Etna GPS networks, Ann. Geophys.,

53(4), 49–57, doi:10.4401/ag-4879, 2010.

Palano, M., Ferranti, L., Monaco, C., Mattia, M., Aloisi, M., Bruno, V., Cannav, F., Siligato, G., Cannavò, F. and Siligato, G.: GPS velocity and strain fields in Sicily and southern Calabria, Italy: Updated geodetic constraints on tectonic block interaction in the central Mediterranean, J. Geophys. Res. Solid Earth, 117(7), 1–12, doi:10.1029/2012JB009254, 2012.

Patanè, D., Ferrucci, F. and Gresta, S.: Spectral Features of Microearthquakes in Volcanic Areas: Attenuation in the Crust and Amplitude Response of the Site at Mt. Etna, Italy. [online] Available from: http://pubs.geoscienceworld.org/ssa/bssa/article-pdf/84/6/1842/2708098/BSSA0840061842.pdf (Accessed 24 October 2020), 1994.

Patanè, D., Ferrucci, F., Giampiccolo, E. and Scaramuzzino, L.: Source scaling of microearthquakes at Mt. Etna Volcano and in the Calabrian Arc (southern Italy), Geophys. Res. Lett., 24(15), 1879–1882, doi:10.1029/97GL01745, 1997.

Patanè, D., De Gori, P., Chiarabba, C. and Bonaccorso, A.: Magma ascent and the pressurization of Mount Etna's volcanic system, Science (80-.)., 299(5615), 2061–2063, doi:10.1126/science.1080653, 2003a.

Patanè, D., Privitera, E., Gresta, S., Akinci, A., Alparone, S., Barberi, G., Chiaraluce, L., Cocina, O., De Gori, P., Di Grazia, G., Falsaperla, S., Ferrari, F., Gambino, S., Giampiccolo, E., Langer, H., Maiolino, V., Moretti, M., Mostaccio, A., Musumeci, C., Piccinini, D., Reitano, D., Scarfì, L., Spampinato, S., Ursino, A. and Zuccarello, L.: Seismological constraints for the dike emplacement of July-August 2001 lateral eruption at Mt. Etna volcano, Italy., 2003b.

Patanè, D., Cocina, O., Falsaperla, S., Privitera, E. and Spampinato, S.: Mt. Etna volcano: A seismological framework, in Geophysical Monograph Series, vol. 143, pp. 147–165., 2004.

Patanè, D., Mattia, M. and Aloisi, M.: Shallow intrusive processes during 2002-2004 and current volcanic activity on Mt. Etna, Geophys. Res. Lett., 32(6), 1–4, doi:10.1029/2004GL021773, 2005.

Patanè, G., La Delfa, S. and Tanguy, J. C.: Volcanism and mantle-crust evolution: The Etna case, Earth Planet. Sci. Lett., 241(3–4), 831–843, doi:10.1016/j.epsl.2005.10.039, 2006.

Pepe, A. and Lanari, R.: On the extension of the minimum cost flow algorithm for phase unwrapping of multitemporal differential SAR interferograms, IEEE Trans. Geosci. Remote Sens., 44(9), 2374–2383, doi:10.1109/TGRS.2006.873207, 2006.

Polonia, A., Torelli, L., Artoni, A., Carlini, M., Faccenna, C., Ferranti, L., Gasperini, L., Govers, R.,

Klaeschen, D., Monaco, C., Neri, G., Nijholt, N., Orecchio, B. and Wortel, R.: The Ionian and Alfeo-Etna fault zones: New segments of an evolving plate boundary in the central Mediterranean Sea?, Tectonophysics, 675, 69–90, doi:10.1016/j.tecto.2016.03.016, 2016.

Puglisi, G., Briole, P. and Bonforte, A.: Twelve years of ground deformation studies on Mt. Etna volcano based on GPS surveys, Geophys. Monogr. Ser., 143, 321–341, doi:10.1029/143GM20, 2004.

Rasà, R., Azzaro, R. and Leonardi, O.: Aseismic creep on faults and flank instability at Mount Etna volcano, Sicily, Geol. Soc. Spec. Publ., 110(110), 179–192, doi:10.1144/GSL.SP.1996.110.01.14, 1996.

Ristuccia, G. M., Di Stefano, A., Gueli, A. M., Monaco, C., Stella, G. and Troja, S. O.: OSL chronology of quaternary terraced deposits outcropping between Mt. Etna volcano and the Catania Plain (Sicily, southern Italy), Phys. Chem. Earth, 63, 36–46, doi:10.1016/j.pce.2013.03.002, 2013.

Rust, D. and Kershaw, S.: Holocene tectonic uplift patterns in northeastern Sicily: Evidence from marine notches in coastal outcrops, Mar. Geol., 167(1–2), 105–126, doi:10.1016/S0025-3227(00)00019-0, 2000.

Sansosti, E., Casu, F., Manzo, M. and Lanari, R.: Space-borne radar interferometry techniques for the generation of deformation time series: An advanced tool for Earth's surface displacement analysis, Geophys. Res. Lett., 37(20), n/a-n/a, doi:10.1029/2010GL044379, 2010.

Scandone, P.: Mesozoic and Cenozoic rocks from the Malta Escarpment (central Mediterranean)., Am. Assoc. Pet. Geol. Bull., 65(7), 1299–1319, doi:10.1306/03b5949f-16d1-11d7-8645000102c1865d, 1981.

Scarfi, L., Messina, A. and Cassisi, C.: Sicily and southern Calabria focal mechanism database: A valuable tool for local and regional stress-field determination, Ann. Geophys., 56(1), 109, doi:10.4401/ag-6109, 2013.

Schellart, W. P. P.: Mount Etna–Iblean volcanism caused by rollback-induced upper mantle upwelling around the Ionian slab edge: An alternative to the plume model, Geology, 38(8), 691–694, doi:10.1130/G31037.1, 2010.

Scudero, S., Guidi, G. De, Imposa, S., Currenti, G., De Guidi, G., Imposa, S. and Currenti, G.: Modelling the long-term deformation of the sedimentary substrate of Mt. Etna volcano (Italy), Terra Nov., 27(5), 338–345, doi:10.1111/ter.12165, 2015.

Solaro, G., Acocella, V., Pepe, S., Ruch, J., Neri, M. and Sansosti, E.: Anatomy of an unstable volcano

from InSAR: Multiple processes affecting flank instability at Mt. Etna, 1994-2008, J. Geophys. Res. Solid Earth, 115(10), 1994–2008, doi:10.1029/2009JB000820, 2010.

Spampinato, C. R., Scicchitano, G., Ferranti, L. and Monaco, C.: Raised Holocene paleo-shorelines along the Capo Schisò coast, Taormina: New evidence of recent co-seismic deformation in northeastern Sicily (Italy), J. Geodyn., 55, 18–31, doi:10.1016/j.jog.2011.11.007, 2012.

Stewart, I. S., Cundy, A., Kershaw, S. and Firth, C.: Holocene coastal uplift in the taormina area, northeastern sicily: Implications for the southern prolongation of the calabrian seismogenic belt, J. Geodyn., 24(1–4), 37–50, doi:10.1016/S0264-3707(97)00012-4, 1997.

Tanguy, J. C. and Kieffer, G.: Les éruptions de l'Etna et leurs mécanismes, Mémoires la Société géologique Fr., 163, 239–252 [online] Available from: http://pascal-francis.inist.fr/vibad/index.php?action=getRecordDetail&idt=3749578, 1993.

Tanguy, J. C., Condomines, M. and Kieffer, G.: Evolution of the Mount Etna magma: Constraints on the present feeding system and eruptive mechanism, J. Volcanol. Geotherm. Res., 75(3–4), 221–250, doi:10.1016/S0377-0273(96)00065-0, 1997.

Torelli, L., Grasso, M., Mazzoldi, G. and Peis, D.: Plio-Quaternary tectonic evolution and structure of the Catania foredeep, the northern Hyblean Plateau and the Ionian shelf (SE Sicily), Tectonophysics, 298(1–3), 209–221, doi:10.1016/S0040-1951(98)00185-1, 1998.

Tortorici, L., Monaco, C., Tansi, C. and Cocina, O.: Recent and active tectonics in the Calabrian arc (Southern Italy), Tectonophysics, 243(1–2), 37–55, doi:10.1016/0040-1951(94)00190-K, 1995.

UNAVCO and GPS Reflections Research Group: GPS Data, [online] Available from: https://spotlight.unavco.org/how-gps-works/gps-and-tectonics/gps-data.html (Accessed 25 September 2020), 2020.

Villari, L.: How do the summit of Etna deform during alternating phases of its persisten ativity? A four months geodimeter survey on the Etna summit area, , 15, 1977.

Wadge, G.: Deformation of Mount Etna, 1971-1974, J. Volcanol. Geotherm. Res., 1(3), 237–263, doi:10.1016/0377-0273(76)90010-X, 1976.

Wadge, G.: The storage and release of magma on Mount Etna, J. Volcanol. Geotherm. Res., 2(4), 361–384, doi:10.1016/0377-0273(77)90021-X, 1977.

Wadge, G., Horsfall, J. A. C. and Brander, J. L.: Tilt and strain monitoring of the 1974 eruption of

Mount Etna, Nature, 254(5495), 21–23, doi:10.1038/254021a0, 1975.

Walter, T. R.: Feedback processes between magmatic events and flank movement at Mount Etna (Italy) during the 2002–2003 eruption, J. Geophys. Res., 110(B10), B10205, doi:10.1029/2005JB003688, 2005.

Werner, C., Wegmuller, U., Strozzi, T. and Wiesmann, A.: Interferometric point target analysis for deformation mapping, in IGARSS 2003. 2003 IEEE International Geoscience and Remote Sensing Symposium. Proceedings (IEEE Cat. No.03CH37477), vol. 7, pp. 4362–4364, IEEE., 2003.

Westaway, R.: Quaternary uplift of southern Italy, J. Geophys. Res., 98(B12), 21741–21772, doi:10.1029/93jb01566, 1993.